Product Sound: Acoustically pleasant motor drives

Mathe, Laszlo

Publication date:
2010

Document Version
Accepted author manuscript, peer reviewed version

Product sound: Acoustically pleasant motor drives

By

László Máthé

Dissertation submitted to the Faculty of Engineering, Science & Medicine at Aalborg University in partial fulfillment of the requirements for the degree of Doctor of Philosophy in Electrical Engineering

Aalborg University, Denmark
Institute of Energy Technology
June, 2010

Aalborg University
Department of Energy Technology
Pontoppidanstraede 101
DK-9220 Aalborg East
Denmark
Web address: http://www.et.aau.dk

Printed in Denmark by UniPrint
ISBN: 978-87-89179-94-0

Preface

This thesis is written under the framework of the Danish PhD Research school EnergyLab DK. The project is entitled *Project sound: Acoustically pleasant motor drives,* and it is partly supported by Danfoss Drives.

The research project was carried out under the supervision of Associate Prof. Peter Omand Rasmussen and Associate Prof. John K. Pedersen from Department of Energy Technology (DET) at Aalborg University; and respectively Dr. Henrik Andersen Rosendal and Dr. Niels Gade from Danfoss Drives. My deepest gratefulness goes to my steering committee for their guidance and professional support during the elaboration of this thesis.

I would like to thank to Dantherm for providing the ventilation system, absolutely necessary for the experimental tests.

I would like to express my sincere thanks to Prof. Maria Imecs from Technical University of Cluj, Romania for all the support she gave during my bachelor and masters studies.

I'm also grateful to Florin Lungeanu for his professional support.

Horea Cornean from the Department of Mathematical Sciences AAU is to be acknowledged for his mathematical support.

Special thanks for all my colleges from DET for their friendly companionship, especially to Dezso Sera, Mihai Ciobotaru, RamKrishan Maheshwari, Tamas Kerekes, Uffe Jakobsen and Yash Veer Singh.

Finally, I would like to thank to my wife Eszter and our two kids Arnika and Boldizsar for their patience, and continuous support during the elaboration of this work.

László Máthé
June 2010; Aalborg

Abstract

The work in this thesis is focused on the acoustic noise generated by electrical motors driven by a pulse width modulated (PWM) power electronic inverter. In a usual inverter based electrical drive, the modulation uses fixed switching frequency; that introduces a set of harmonics in the acoustic spectra transforming the acoustic noise generated by the motor in a strong whistling noise. To maintain high efficiency for the entire drive, the switching frequency is typically kept around 4 kHz. However, this is the range where the human ear is the most sensitive. The main goal of this thesis is to ameliorate this whistling acoustic noise, while maintaining the efficiency of the drive.

The first chapter of the report is an introductory chapter where the motivation, objectives, limitations and an overview on electrical motor acoustics are presented. A list of main contributions of this PhD project is also presented here. The second chapter starts with an overview of the most widely used two level inverters and presentation of the basic modulation principles. A theoretical elaboration of the line-to-line voltage and vibration spectrum is presented in the next chapter, where a new unified analytical solution is proposed. The proposed unified analytical solution can be used for most of the carrier based PWM techniques. Starting from the unified analytical solution of the line-to-line voltage, a mathematical equation is proposed which describes the spectral components of the acoustical noise generated by the motor.

A cost effective solution to reduce the annoyance of the acoustic noise generated by the modulation in an inverter-fed electric motor, is the random PWM. After the presentation of the existing random modulation methods in Chapter 4, a new random PWM technique is proposed. The advantage of the new modulation method is that it can be easily retrofit in a prior implemented open- or closed-loop control algorithm, without adding any extra hardware components.

Typically, for application in heating ventilation and air condition (HVAC), the main focus is on cost, efficiency and *acoustic noise*, while high performance is not required for shaft-torque dynamics. In order to investigate the acoustic performance of the new proposed random modulation method, a ventilation system has been used. In Chapter 5, various methods to measure the frequency response of the ventilation system were evaluated. The first method was based on exciting the system with a force impulse. The second excitation method was based on injection of a sinusoidal current

with variable frequency into the motor. The third, most promising method to measure the frequency response of the ventilation system, was based on random PWM.

Chapter 6 presents the acoustic measurements of the ventilation system using various modulation techniques. A new trend in HVAC is to use permanent magnet synchronous motor (PMSM) instead of the asynchronous motor, in order to increase the efficiency of the electrical drive. In this chapter, the acoustic performance of the two different motor structures is also analyzed.

A relatively new cost effective solution for HVAC applications is to decrease the size of the capacitance form the DC-link of the inverter. This will cause a large DC-link voltage ripple, and resonances between the line inductance and DC link capacitor can appear. These effects decrease the acoustic performance of the drive. A new compensation method for the DC-link voltage fluctuation is proposed in Chapter 7. The compensation removes the main frequency component introduced by the DC-link voltage ripple from the acoustic spectra.

The last chapter of this report presents the conclusions based on the theoretical and experimental results performed during the PhD work. Finally, a list of future work is proposed.

Dansk resumé

Denne afhandling fokuserer på akustisk støj fra elektriske motorer som er drevet af en effektelektronisk inverter som anvender puls bredde modulation (PWM). En almindelig inverter baseret elektrisk drev, anvender en fast switch frekvens. Denne switch frekvens introducerer harmoniske i det akustiske spektra, som for den elektriske motors vedkommende lyder som en markant hyletone. For at opnå en høj effektivitet for det samlede drev, er switch frekvensen typisk sat til 4 kHz, hvor det menneskelige øre er mest følsomt. Hoved motivationen for denne afhandling er at dćmpe den markante hyletone, men samtidig bevare effektiviteten.

Det første kapitel indeholder introduktionen, som beskriver det motivationen for afhandlingen, mål, afgrćsninger og et overblik over akustisk motor støj. Derudover indeholder kapitlet også en liste over de vigtigste videnskabelige bidrag som er gjort i projekt perioden. Det andet kapitel starter med et overblik over de mest anvendte to niveau invertere og en prćsentation af grundlćggende modulations principper. Det nćste kapitel prćsenterer en teoretisk beskrivelse forbindelsen mellem linje til linje spćndingen og vibrations spektret, sammen med en ny analytisk løsning. Den foreslåede analytiske løsning kan anvendes på de fleste bćrebølge baserede PWM. Baseret den analytiske løsning prćsenteres en ligning der beskriver de spektrale komponenter af den akustiske støj dannet af den elektriske motor.

En billig metode til at reducere ubehaget af den akustiske støj fra PWM anvendt på en inverter drevet elektrisk motor er at anvende tilfćldighedsbaseret pulsebredde modulation (random PWM). Udover at prćsentere eksisterende random PWM metoder, introduceres også en ny metode til random PWM i kapitel 4. Fordelen ved den nye metode er at den nemt kan anvendes med eksisterende åben eller lukket sløjfe reguleringssystemer uden at det er nødvendigt at tilføje ekstra hardware komponenter.

Når anvendelsesområdet er varme og klimateknik (HVAC), er der ofte fokus på pris, effektivitet og akustisk stćj, hvorimod der er mindre fokus på de dynamiske forhold. Et ventilations system blev anvendt for at kunne undersøge ydelsen af den foreslåede ny random PWM metode. I kapitel 5 er forskellige metoder til at måle frekvensresponset af ventilationssystemet uddybet. Den første metode anslår systemet med en kraftimpuls. Den anden anslagsmetode anvender sinusoidale strømme med

forskellige frekvenser på motoren. Den mest lovende måde at måle frekvensresponset af ventilationssystemet er baseret på random PWM.

Kapitel 6 prćsenterer de akustiske målinger af ventilationssystemet under anvendelse af forskellige modulationsteknikker. For at øge effektiviteten af elektriske motor er der en tendens til at udskifte rotoren i induktionsmotoren med en passende permanent magnet motor rotor. I dette kapitel analyseres også effekten af hvad en sådan rotor udskiftning har på den akustiske støj.

En omkostningsbesparelse for tre fasede invertere er formindske størrelse på kondensatoren i DC-leddet af inverteren. En mindre kondensator øger udsvinget i DC-spćndingen i inverteren, som blandt andet foringer den akustiske ydelse af drevet. En ny kompensationsmetode der stabiliserer oscillationstendensen i DC-spćndingen. Kompensationen er udført på en sådan måde at hoved komponenterne, introduceret af udsvingene i DC-link spćndingen, er fjernet fra det akustiske spektrum.

Det sidste kapitel konkluderer afhandlingen baseret på de teoretiske og eksperimentelle resultater opnået gennem PhD-perioden. Endelig prćsenteres forslag til yderligere forskning.

Table of contents

List of abbreviations

AC-RPWM	Asymmetric Carrier Random Pulse Width Modulation
ADC	Analog to Digital Conversion
cmv	common mode voltage
CR	Compare Register
DFT	Discrete Fourier Transformation
DPWM	Discontinuous PWM
DSP	Digital Signal Processor
EMC	Electro-Magnetic Compatibility
EMI	Electro-Magnetic Interference
FCF	Fixed Carrier Frequency
FCF-RPWM	Fixed Carrier Frequency Random Pulse Width Modulation
FEM	Finite Element Modeling
FOC	Field Oriented Control
HPWM	Hybrid PWM
HVAC	Heating Ventilation and Air-Condition
mi	modulation index
MPW	Minimum Pulse Width
PMSM	Permanent Magnet Synchronous Motor
PR	Period Register
PWHD	Partial Weighted Harmonic Distortion
PWM	Pulse Width Modulation
RCF-PWM	Random Carrier Frequency Pulse Width Modulation
RLL-PWM	Random Lead Leg PWM
RPM	Revolution Per Minutes
RPP-PWM	Random Pulse Position
RPWM	Random Pulse Width Modulation
ST-PWM	Sine-Triangular PWM
SVM	Space Vector Modulation
THD	Total Harmonic Distortion
VSC	Voltage Source Converter

Chapter 1

Introduction

This chapter describes the background and motivation of the thesis, and presents a short overview of acoustics in electrical drives. This is followed by the project's objectives and limitations. Next, the main contributions are presented. Finally, the outline of the thesis is provided.

1.1 Background and motivation

Power electronic converters for drives are now a mature technology with noteworthy and dynamic worldwide markets. The improvements that were made with this technology, with respect to industrial motion, torque, speed, and position control, are impressive, fulfilling all expectations regarding performance and quality in electric drives. Unfortunately, power electronics converters have also unwanted consequences that come along with, like current and voltage distortion, extra power losses (conduction and switching), thermal stress, electromagnetic interference (EMI), torque ripple in rotating machines, mechanical vibrations, and radiation of *acoustic noise*.

Recent endeavors in research in electrical drives have been motivated by desire to eliminate the above mentioned side effects while maintaining the performance of the application. The power electronic converters are usually using PWM technique to convert rectified input DC voltage into a voltage with adjustable amplitude and frequency. The optimal modulation frequency to maintain minimal losses for the whole electrical drive system is typically around 4kHz (in case of a drive in range of kW) [1]. This switching frequency of 4kHz cause a strong whistling noise in the electrical motors in the frequency range where the human ear is the most sensitive.
The focus of this thesis is to develop and implement modulation techniques that can decrease or ameliorate the acoustic noise generated by the electrical motors controlled by a PWM based inverter.

1.1.1 Overview of acoustic noise sources in electrical motors

The acoustic noise sources in electrical motors can be classified in four main categories: magnetic, mechanical, aerodynamic and electronic [2, 3]. Figure 1-1 presents the various acoustic noise sources.

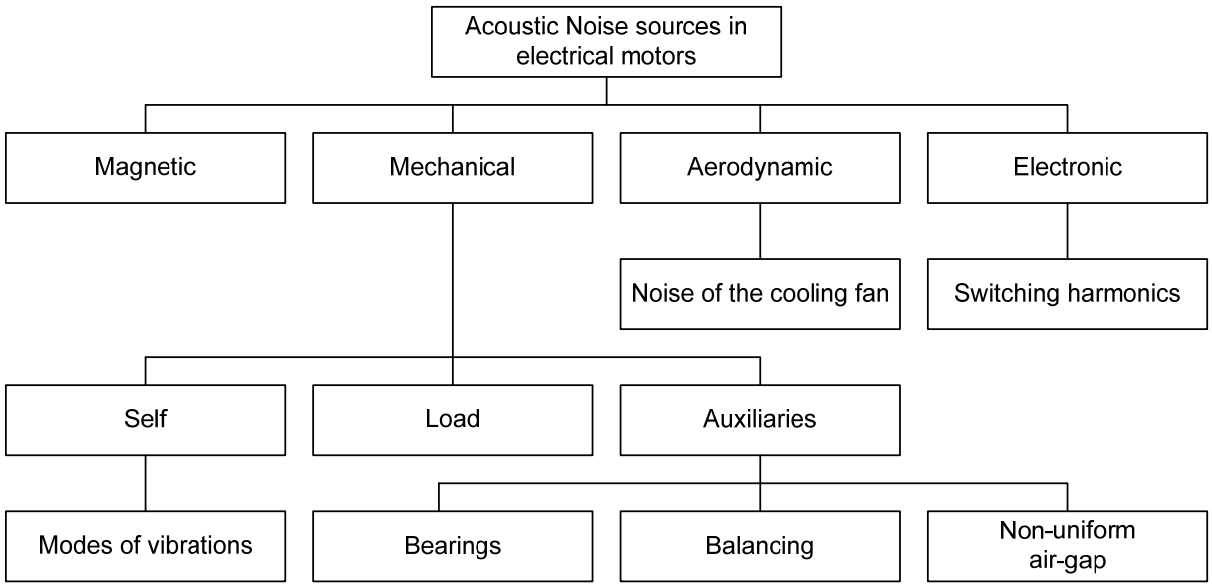

Figure 1-1 Acoustic noise sources in electrical motor [2]

The acoustic noise generated by the mechanical and aerodynamic sources is mainly connected to the mechanical structure of the electric motor. The magnetic force acting on the cores of the stator and rotor may produce troublesome noise and vibration, especially when the frequencies of the exciting forces are equal or near to the natural frequencies of the machine concerned. In most of the practical cases, the predominant acoustic noise is produced by the radial force [4]. In case of inverter fed drives the radial force contains the switching frequency components, which are transformed by the motor into acoustic noise. There is no clear boundary between the pleasant acoustic environment, like music, and the acoustic noise. In general the acoustic noise can be defined as an undesired sound for the recipient [4]. By analyzing the spectrum of the acoustic noise generated by the inverter fed motors it can be found that it contains discrete components usually in the frequency range where the human ear is the most sensitive. These discrete components from the acoustic spectra are very far to be sensed as a pleasant sound. Moreover, for the people who work close to drives above few kilowatts, these discrete components from the acoustic spectra can cause partial deafness. The A-weighting curve from Figure 1-2 shows that the human ear is very sensitive to frequency components from the acoustic spectra in the range between 1 kHz and 5 kHz. The obvious solution to get rid of the acoustic noise generated by the switching frequency is to increase the switching frequency above the human audible

boundary of 20 kHz [5-7]. However, the converter losses will increase, sharply decreasing the efficiency of the whole drive.

Another solution is to use filters between the inverter and the electrical motor [8]. The disadvantage of this technique is that the costs are increased, extra power loss is introduced, and the acoustic noise might still be present in the filter.

From costs point of view the most promising method to decrease the annoyance of the switching frequency noise is to transform the whistling noise into a white noise. This can be achieved by randomly varying the switching frequency, modulation method called random PWM (RPWM). It is very important to mention here that the acoustic noise level is not reduced by RPWM, only the spectral distribution of the acoustic noise is modified [9]. In general speaking, the humans perceive time-invariant sounds (whistling noise) more annoying than the sounds which are variable in intensity or frequency. The goal is not necessarily the elimination of the undesired acoustic noise; the aim is to make it more pleasant for the human ear.

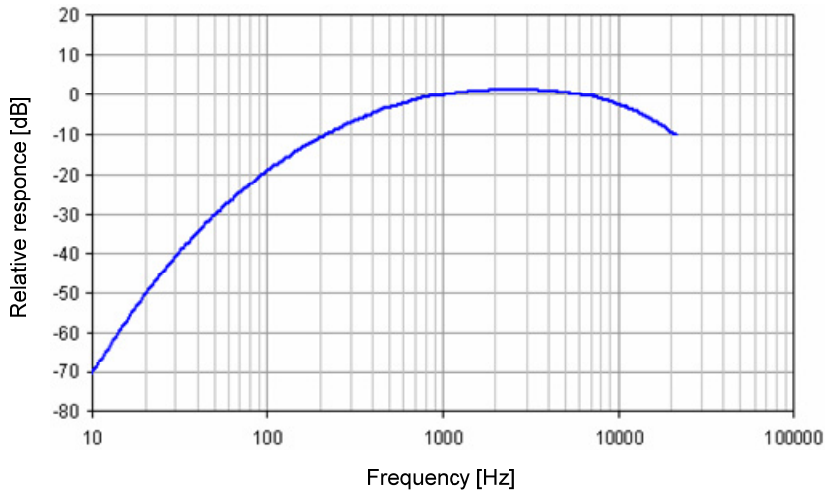

Figure 1-2 Internationally standardized A-weighting curve, used to emulate the perception of sound by humans [10]

1.2 Objectives and Limitations

1.2.1 Objectives

The primary goals of this project were:

- to develop new control/modulation strategies where the main focus is on the acoustic noise
- to analyze the acoustic noise generated by real applications, like ventilation systems
- to compare the acoustic performance of the induction motor and permanent magnet synchronous motor used in HVAC applications
- to analyze the acoustic performance of Slim DC-link inverter driven HVAC applications

1.2.2 Project Limitations

This thesis focuses on the acoustic noise generated by the PWM inverter fed electrical drives, the rest of the acoustic noise sources like cooling fan, bearings etc. were not considered.
The acoustic measurements were not made in an anechoic chamber; as a consequence, the reflections and exterior noises are not entirely eliminated.
The experimental tests of the proposed modulation technique were tested only on a ventilation system.

1.2.3 Tools used

The control algorithms developed along this thesis were created using a simulation platform based on MATLAB®/Simulink [11], and for simulation of the electrical components, the PLECS® toolbox was used [12]. The control algorithms code was written in C programming language; the same C code was used for real time implementation and simulation. For the experimental implementation, a Danfoss VLT® FC302 was used, which was controlled by a Texas Instruments TMS320F28355 floating point DSC. A ventilation system produced by Dantherm (Figure 1-3) was used for testing the acoustical performance of the different modulation techniques.

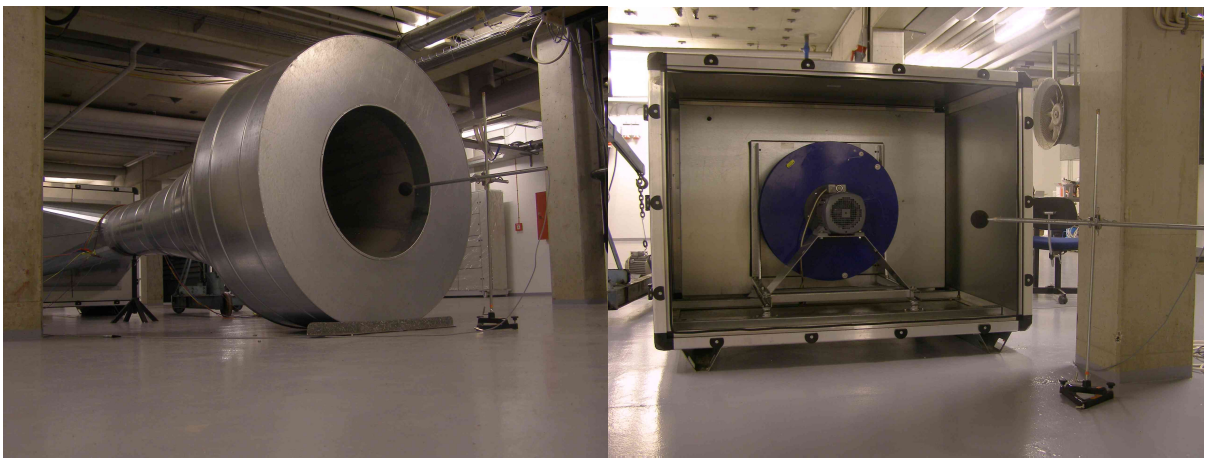

(*a*) (*b*)

Figure 1-3 Ventilation system used for the experimental tests, (a) anechoic termination used to simulate the propagation of the acoustic noise in the duct, (b) inlet of the ventilator

Two 4kW motors produced by VEM with similar stators - one equipped with squirrel cage rotor and the second with a permanent magnet rotor - were used in the drive for the ventilation system (motor data in Appendix A). The acoustic noise and vibrations has been measured using a Bruel and Kjaer Pulse Multianalyzer type 3560. The motor and line currents were measured using Tektronics TDS 3014B oscilloscope.

1.3 Main contributions

The main contributions of this PhD research project are presented in the following, in the order they appear in the thesis.

In Chapter 3 a **new unified analytical equation is derived** that describes the spectrum of the line-to-line voltage of a PWM controlled inverter, where an arbitrary signal is injected into the common mode voltage. Although in the literature can be found various analytical solutions for the popular modulation methods (like SVM, discontinuous PWM etc.) [13], these solutions are valid only for the specific modulation method they were developed for. The new unified analytical equation is valid for any modulation method.

Starting from the unified analytical solution of the line-to-line voltage, **a new analytical solution that approximates the spectral components from the acoustic spectra, generated by a PWM inverter fed motor,** is also proposed in the same chapter.

In Chapter 4, a **new fixed carrier frequency RPWM method** is proposed which has similar performances to those of the random carrier frequency PWM method, but with the added advantage of easy integration in closed loop applications. A **new fixed carrier frequency RPWM method which can shape the spectra of the vibrations on the frame of the motor**, avoiding in this way the excitation of the resonances from the drive system, is also proposed in this chapter.

In Chapter 6 a **comparison between a synchronous and an asynchronous motor from acoustical point of view** is presented.

In Chapter 7 a **new compensation method for the DC-link voltage** for the slim DC-link drives is proposed. The compensation is able to damp the oscillation between the line inductance and the DC-link capacitor thus eliminating the strong 300Hz component from the acoustic spectra caused by the rectification of the three phase grid voltage.

1.4 Outline of the thesis

The thesis is structured in eight chapters. A brief outline of each chapter follows below.

Chapter 1, Introduction: The current chapter where the background, motivation, objectives, limitations and the main contributions are presented.

Chapter 2, Conversion of a DC voltage into an AC voltage using power switches: In this chapter the basic hardware configurations used for energy conversion, especially the three phase voltage source inverter is presented. The basics of modulation and the implementation of various modulation schemes are also described in this chapter.

Chapter 3, Analytic expression for the two-level PWM waveform spectra: The focus in this chapter is on derivation of a mathematical equation which determines the line-to-line voltage and the acoustic spectra.

Chapter 4, Random Pulse Width Modulation: presents the basics of random PWM. In the first part of the chapter the random carrier frequency PWM methods with their advantages and disadvantages are presented. The second part of the chapter presents the fixed carrier random PWM modulation methods.

Chapter 5, Modeling of the ventilation system: presents three methods to model the frequency response of a complex structure like the ventilation system. The first method uses a force impulse (hammer excitation) to excite the structure. The second method is base on injection of a sinusoidal current in one phase of the motor with variable frequency. The third method is based on random PWM.

Chapter 6, Acoustic noise measurement of the ventilation system: presents the measurement results of the proposed modulation technique on a ventilation system. A comparison between an asynchronous and synchronous motor from acoustic point of view is also presented.

Chapter 7, Acoustic noise analysis of Slim DC-link drives: deals with the acoustic noise generated by a slim DC-link driven motor. In this chapter a DC-link voltage compensation method is proposed, method which reduces the oscillation between the line inductance and DC-link capacitor. Moreover, using the proposed modulation method the 300Hz component from the acoustic spectra caused by the low DC-link capacitor is eliminated.

Chapter 8, Conclusions: In this chapter based on the theoretical and experimental work the main conclusions are highlighted. Additionally, suggestions for future work are given.

1.5 List of publications derived from this thesis

1. **L. Mathe**, U. Jakobsen, P. O. Rasmussen, and J. K. Pedersen, "Analysis of the vibration spectrum based on the input voltage spectrum," in Energy Conversion Congress and Exposition, 2009. ECCE 2009. IEEE, 2009, pp. 220-225.

2. **L. Mathe**, P. R. Omand, and J. K. Pedersen, "Shaping the spectra of the line-to-line voltage using signal injection in the common mode voltage," Industrial Electronics, 2009. IECON '09. 35th Annual Conference of IEEE, pp. 1288-1293

3. **L. Mathe**, H. R. Andersen, R. Lazar, M. Ciobotaru, "DC-Link Compensation Method for Slim DC-Link Drives Fed by Soft Grid" Industrial Electronics, 2010. ISIE '10. Annual Conference of IEEE

4. **L. Mathe**, F. Lungeanu, P. O. Rasmussen, J. K. Pedersen, "Asymmetric Carrier Random PWM" Industrial Electronics, 2010. ISIE '10. Annual Conference of IEEE

5. **L. Mathe**, H. Cornean, P. O. Rasmussen, D. Sera, J. K. Pedersen, "Unified analytical equation for theoretical determination of the harmonic components of modern PWM Strategies" Transaction in Power Electronics submitted for review

Chapter 2

Conversion of a DC voltage into an AC voltage using power switches

In this chapter the basic hardware configurations used for energy conversion, especially the three phase voltage source inverter is presented. The basics of modulation and the implementation of various modulation schemes are also described in this chapter.

2.1 Introduction

The semiconductor-based power electronic components that allow the transformation of a DC voltage into an AC voltage, with the desired amplitude, frequency and phase, are called converters. In ideal case the power electronic transistors are operating like ideal switches having one of the two possible states: fully ON or fully OFF. The converters based on switching devices can operate from low power range (milli-watt) to the high power range (hundreds of mega-watt), maintaining high efficiency and reliability.

The strategy of switching the power electronic components is called *modulation.* Modulation is the main element of a control scheme for those applications where power electronic converters are employed. This being the fact why, for more than 30 years the modulation theory has been a major research area in power electronics.

One of the most often used modulation method in electrical drives is the pulse-width modulation (PWM). To find the optimal modulation strategy and topology for a special application, several PWM methods can be found in the literature. This chapter presents the fundamentals of the two level inverter topologies and the basics of PWM strategies. A very comprehensive overview about inverter topologies and PWM modulation can be found in [1, 13].

2.2 Basic inverter topologies

A very efficient way to decrease a DC voltage level is to use a power switch between the DC source and the load like is presented in the left side from Figure 2-1. By switching the switch *on* and *off* the load can be connected or disconnected from the DC source.

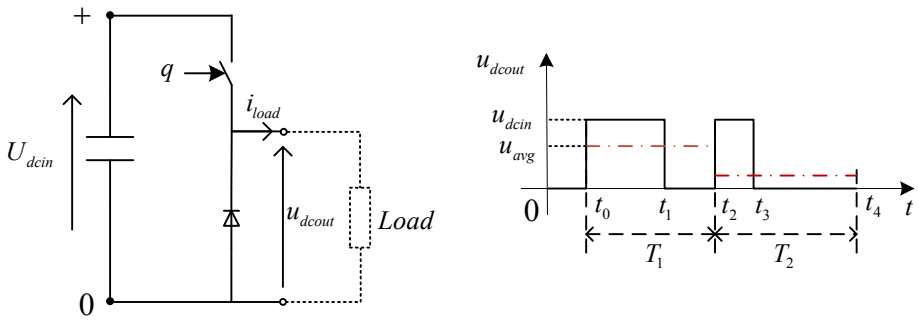

Figure 2-1 Step-down converter topology (left), and waveform of the output voltage (right)

The aim is to control this *on-off* switching in such a way to maintain the same volt-second average per carrier cycle as the target reference waveform has at same instance. A drawback of the *on-off* control is that the output voltage contains unwanted harmonic components which should be minimized [14]. Considering a time interval T where the switch has one *on* and one *off* state the average voltage can be calculated during this time interval with:

$$u_{avg} = \int_{t_0}^{t_0+T} u_{dc\ in} \cdot q(t)dt \tag{2.1}$$

where *q(t)* is the *on-off* state of the switch in time called switching function. Equation (2.1) shows that the average output voltage during the T period of time can vary linearly between zero (switch is off) and U_{dcin} (switch is on). The average voltage can also be expressed as a duty ratio, which can be calculated as the ratio between the time period when the switch is *on* and the switch is *off*. The duty ratio can vary between zero (fully *off*) and one (fully *on*), and it can be expressed as:

$$d = \frac{1}{T}\int_{t_0}^{t_0+T} q(t)dt \tag{2.2}$$

By using PWM technique, any kind of signal which varies between zero and U_{dcin} with a period larger than the modulation period T, can be reproduced. Naturally, the output voltage is always only an approximation of the reference voltage. Nevertheless, by decreasing the modulation period (increase the switching frequency), this approximation becomes closer and closer to the reference voltage. By installing a low pass filter between the load and the step-down converter can also reduce the difference between the reference and output voltage.

A simple circuit which transforms a DC voltage into an AC voltage, called half-bridge inverter, is shown in Figure 2-2. The topology is constructed from two power switches, each of them equipped with a free-wheeling diode, and a load.

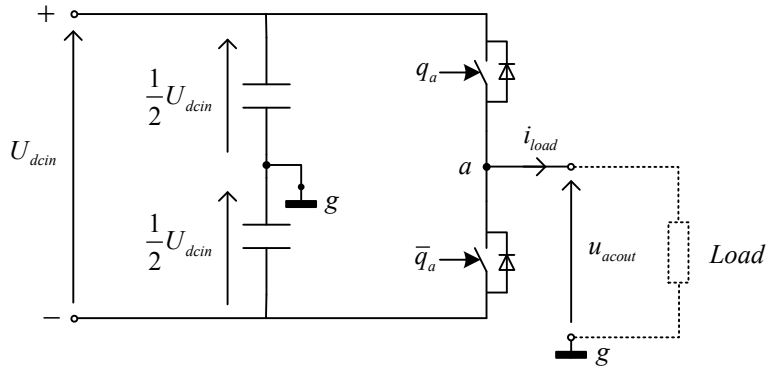

Figure 2-2 Hardware configuration of a classic half-bridge voltage source inverter

The half-bridge topology has a DC input voltage with center-tap point, considered as ground or reference point. The output voltage can be positive, (q_a switch is on) or negative ($\overline{q}_a$ switch is on) compared to the reference point. The maximum amplitude of the output voltage u_{acout} is half of the input voltage U_{dcin}. There are some hardware limitations regarding to the control of the power switches from the half-bridge.

In order to avoid creating a shoot-through for the input voltage U_{dcin}, it is not allowed to switch *on* both of the power transistors at the same time. By using complementary logic for the two power switches the shoot-through can be avoided, maintaining the full control on the current through the load. The current will increase when the q_a switch is *on* and $\overline{q}_a$ switch is *off*, respectively the current will decrease when q_a is *off* and $\overline{q}_a$ is *on*.

The *on-off* switching of the power transistors takes a short period of time, which means in a real application a simple complementary logic is not enough to avoid shoot-through. It should be always inserted a short delay after one switch change its state from *on* to *off*, or vice versa. For this short period of time both of the switches should be switched *off*. In the literature this delay is called *dead time*. The dead time introduces a modulation error; [4-6] presents compensation methods for the dead-time caused error.

The generation of narrow pulses (the pulse width is less than the length of the dead time) for the power switches should be avoided in order to not create turn-on or turn off failures [15]. In the literature it is referred to as Minimum Pulse Width (MPW).

The free-wheeling diodes enable bi-directional energy flow, which is necessary for those applications when the load can act as a current source. For example in case of an inductive load the power switches can be damaged, because when both of the switches are off (example dead time period) without the free-wheeling diodes the voltage on the load would increase to high values.

In many industrial applications, usually for AC electrical motors, three-phase voltage is used as power supply. Connecting three half-bridges to a DC voltage, like in Figure 2-3, a three phase voltage with desired amplitude\frequency\phase can be created. This topology is the most often used power converter topology for AC motor drive in the industry [1].

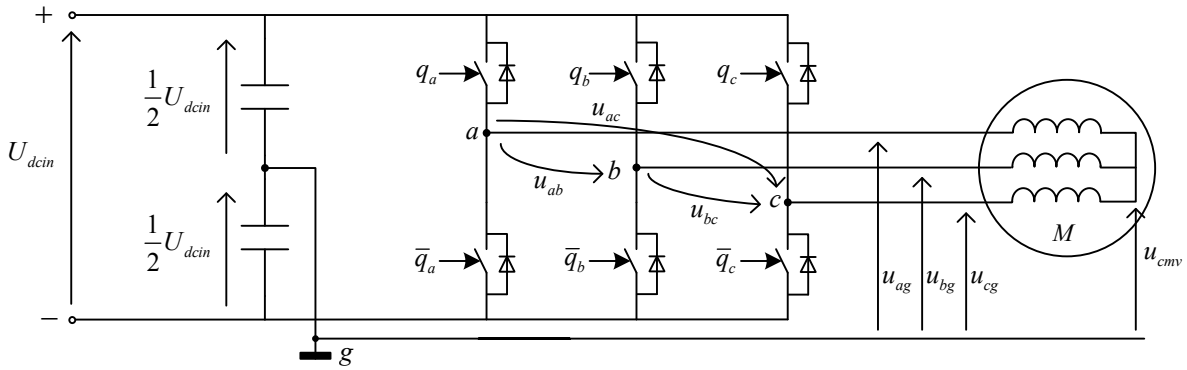

Figure 2-3 Hardware configuration of a three phase voltage source inverter drive

In most of the cases the AC motors require balanced three-phase currents where the amplitudes and frequencies are equal, and the phase displacement between the three phases is 120^0. To create the balanced three phase current with this topology it is not necessary to connect the star point to the ground. In this way two sets of three phase voltages can be defined: the line voltages noted with u_{ab}, u_{bc} and u_{ac} in Figure 2-3 and the phase voltages noted with u_{ag}, u_{bg} and u_{cg} in Figure 2-3. The line voltages can be expressed in function of the phase voltages like:

$$\begin{cases} u_{ab} = u_{ag} - u_{bg} \\ u_{bc} = u_{bg} - u_{cg} \\ u_{ac} = u_{ag} - u_{cg} \end{cases} \tag{2.3}$$

The voltage between the star point and the ground is called common mode voltage or zero sequence voltage and it can be expressed:

$$u_{cmv} = \frac{u_{ag} + u_{bg} + u_{cg}}{3} \tag{2.4}$$

2.3 Pulse generation for the power switches

The pulse generation for the power switches can be done in open-loop or in closed-loop. The open-loop method, also called carrier-based PWM, generates a train of pulses based on a comparison between a reference signal and a high frequency triangular wave, as it is shown in Figure 2-4. The high frequency triangular wave is also called carrier wave. The generated PWM signal modifies its state at every match of the reference signal and the triangular carrier wave, when the reference waveform is greater

than the carrier wave the switching function is set to one (the load is connected to positive DC rail); when the reference signal is smaller than the carrier the switching function is set to zero (the load is connected to negative DC rail). In case when the amplitude of the reference signal is higher or lower than the amplitude of the carrier wave, the output voltage will be limited to the input DC voltage.

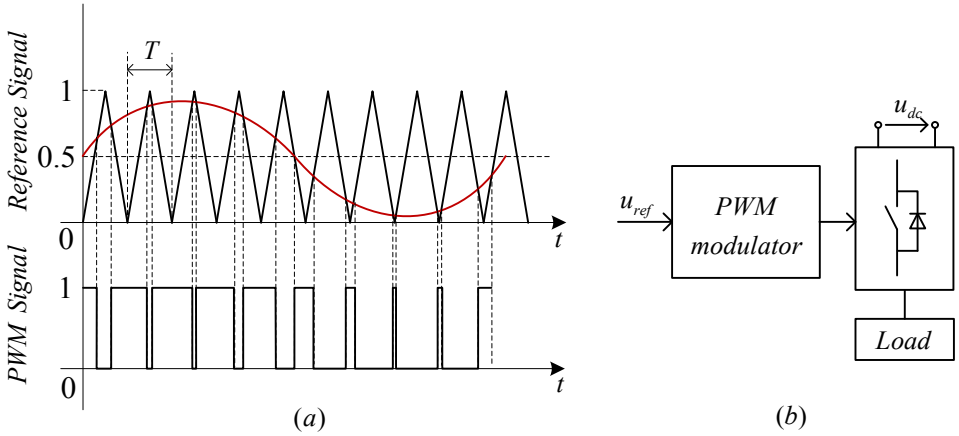

Figure 2-4 PWM pulse train generation by comparing the source signal with a high frequency carrier wave (a) and PWM scheme of the open-loop voltage control (b)

An example for closed-loop PWM method is to use as feed-back the measured load current. The DC voltage is switched in *on-off* manner in a way to maintain this current close to the reference current. A solution is to define a hysteresis band around the reference current signal (dotted line around the reference signal from Figure 2-5). The power transistors are switched when the current through the load is leaving the hysteresis band around the reference, as it can be seen in Figure 2-5. A disadvantage of this method is the uncontrolled switching frequency which can vary in a large domain.

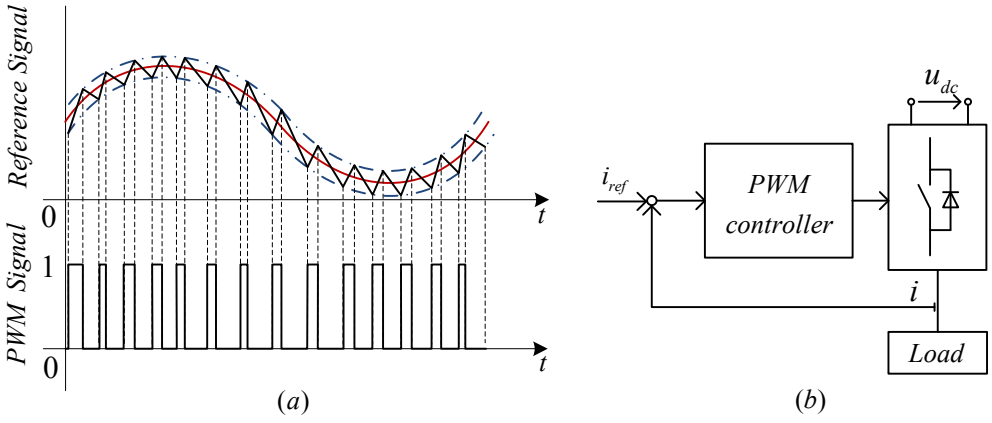

Figure 2-5 Closed-loop current control PWM waveform generation (a), and block diagram (b)

In most of the practical applications the carrier-based modulation methods are preferred due to their low-harmonic distortion, fixed switching frequency, well-defined

harmonic spectrum and implementation simplicity [16]. In this work the open–loop (carrier-based) PWM methods are analyzed.

2.3.1 Modulation of Three-Phase Voltage using Carrier-Based PWM

The carrier-based PWM method presented in the previous section can be extended to generate the pulse train for a three-phase voltage source inverter based on half-bridge topology (Figure 2-3). To generate the switching function for each phase, a three-phase reference voltage is compared with a carrier wave. Usually in digital implementation the carrier wave is generate by a counter which has only positive values. For this reason in this work the amplitude of the carrier wave and the reference signals are considered to vary between 0 and 1. The use of such a carrier wave has the advantage to simplify the conversion of the reference signals into compare values for the PWM unit (a simple multiplication with the value of the PR register). To maintain the reference signal between zero and one an offset of 0.5 is added. The modulation where sinusoidal signals are compared with a triangular carrier wave is called sine-triangle method (ST-PWM) [17]. Figure 2-6 (a) presents a fundamental period of the balanced three phase sinusoidal reference signals on macroscopic scale, which can be defined in mathematical form like:

$$\begin{cases} u_{ag} = \dfrac{M}{2} \cdot \cos\left(\omega_0 t\right) + 0.5 \\ u_{bg} = \dfrac{M}{2} \cdot \cos\left(\omega_0 t + \dfrac{2\pi}{3}\right) + 0.5 \\ u_{cg} = \dfrac{M}{2} \cdot \cos\left(\omega_0 t - \dfrac{2\pi}{3}\right) + 0.5 \end{cases} \tag{2.5}$$

where M is the modulation index, and ω_0 is the fundamental frequency. The modulation index is the normalized fundamental voltage [18] which can be expressed as:

$$M = \frac{U_0}{\left(\dfrac{2}{\pi}\right) U_{dc}} \tag{2.6}$$

where U_0 is the fundamental voltage. Figure 2-6 (b) presents the pulse generation mechanism for the three phase inverter based on half-bridges on microscopic scale. It should be noted here again the pulse generation for the two power switches for the same leg is made in complementary logic. All the hardware limitations presented in section 2.2 should be respected.

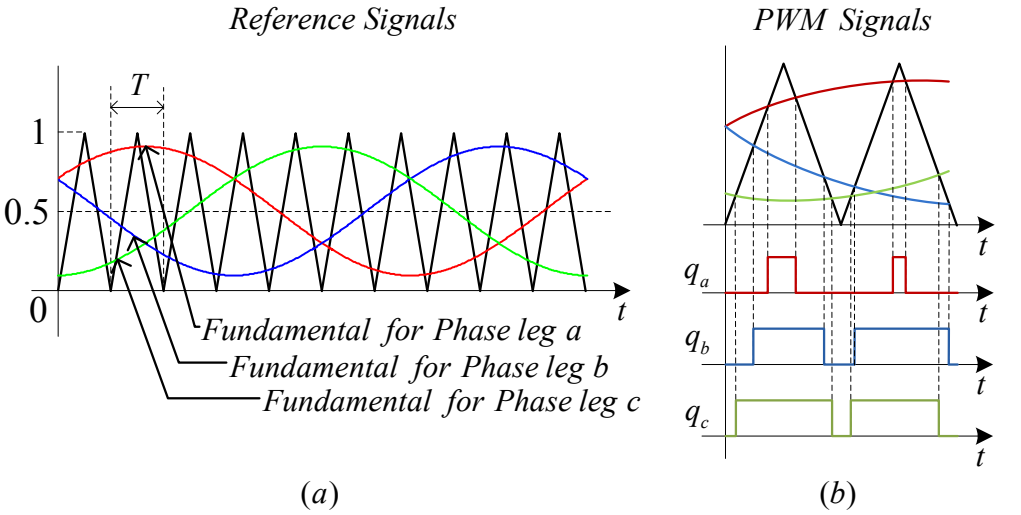

Figure 2-6 Reference voltages and carrier wave for a three-phase voltage source inverter using carrier-based PWM method over one fundamental period (a), pulse generation in micro scale (b)

2.3.2 Space Vector Modulation PWM

The space vector modulation strategy is based on the graphical representation of the possible voltage vectors in *d-q* plane [19, 20]. With a conventional three phase inverter (Figure 2-3) six active and two zero sequence basic voltage vectors can be generated. The six active voltage vectors represented in ***d-q*** plane (Figure 2-7 *(a)*) form a hexagon, where each active vector points to the corner of the hexagon. When one of the six active vectors is generated the load takes the energy from the DC-link, forming a circuit from the load impedances like is shown in Figure 2-7 *(a)*. The generation of the zero sequence vectors is done by connection of all three legs of the load to the plus (v_{111}) or minus (v_{000}) of the DC rail.

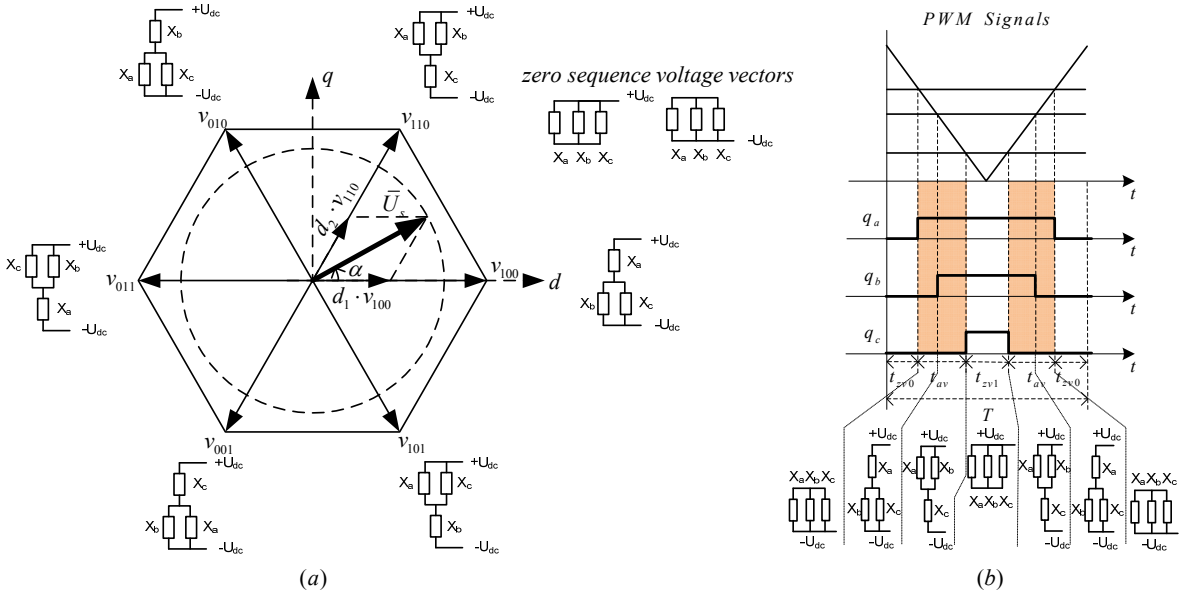

Figure 2-7 Voltage space vector representation in d-q plane (a), and pulse generation in one modulation period (b)

In each half carrier period a voltage vector $\bar{U}_s$ with desired length and position in ***d-q*** can be generated. The position of a voltage vector $\bar{U}_s$ in ***d-q*** plane is defined by the ratio between the applied time-length for the two adjacent active vectors. The zero sequence vectors are responsible to reduce the length of the resultant voltage vector $\bar{U}_s$. The amplitude of the active switching vectors is $\left|v_x\right| = 2/3 U_{dc}$. Generation of the zero sequence vectors and the active vectors in time can be tracked in Figure 2-7 *(b)* where the active region (when the load takes the energy from the DC-link) was highlighted.
The mathematical relation between the voltage vector $\bar{U}_s$ duty ratio and the time-length of the active vectors can be expressed as:

$$\begin{aligned} &\bar{U}_s = d_1 \cdot \bar{v}_x + d_2 \cdot \bar{v}_y \\ &d_1 = \sqrt{3}\frac{|U_s|}{U_{dc}}\sin(\alpha) \qquad t_{av1} = d_1 \cdot T \\ &d_2 = \sqrt{3}\frac{|U_s|}{U_{dc}}\sin(\frac{\pi}{3}-\alpha) \qquad t_{av2} = d_2 \cdot T \end{aligned} \tag{2.7}$$

where the duty ratios d_1 and d_2 are the ratio between the time-length of the applied basic voltage vector and the modulation period T, $\bar{v}_x$ and $\bar{v}_y$ are the adjacent basic voltage vectors, and α is the position angle of the resultant voltage vector. The most popular method to calculate the timing for the zero sequence vectors is to distribute them equally during a modulation period (t_{zv0}=t_{zv1}). This equally distributed zero sequence vectors method is also called as space vector modulation (SVM).
The sine-triangle PWM (ST-PWM) and SVM modulation methods were considered as two different PWM methods. In [21] the author described the correlation between the ST-PWM and SVM. The difference between the two modulation methods is only the distribution of the time-length of the zero-sequence voltage vectors. With other words, the difference is in the common mode voltage waveform.

2.3.3 Redistribution of the zero sequence vectors

As it was presented in the previous section, the replacement of the zero-sequence vectors can extend the linear range of ST-PWM, and it can significantly reduce the switching losses [22, 23].
In the inverter topology presented in Figure 2-3 the star point connection from the load is not connected to the ground. In case of ST-PWM the voltage between the star point and ground (u_{cmv}) can be expressed from (2.4) and (2.5) in macro scale:

$$u_{cmv} = \frac{u_{ag} + u_{bg} + u_{cg}}{3} = \frac{M}{3} \cdot \left(\cos\left(\omega_0 t\right) + \cos\left(\omega_0 t + \frac{2\pi}{3}\right) + \cos\left(\omega_0 t - \frac{2\pi}{3}\right)\right) = 0 \tag{2.8}$$

From Eq. (2.8) can be seen that the average common mode voltage is always zero in case of ST-PWM. In micro scale the common mode voltage vary between $\pm U_{dc}$. The ST-PWM method has a narrow linear range, the linear range ends when $M_{\max} = \pi/4 = 0.785$ [1]. Publication [24] presents the third-harmonic reference injection

PWM method, which increases the linear range to $M_{\max} = \pi/2\sqrt{3} = 0.907$. The method is based on the statement: by adding a signal with triple frequency to the phase voltages has no effect on the line-to-line voltage. However, the redistribution of the zero-sequence vector significantly influences the spectra of the line-to-line voltage in the range of the switching frequency. This statement can easily be proved; in (2.3) the line voltage is expressed as a difference between the two phase voltages, therefore, the presence of the same signal in the phase voltages will be eliminated by the subtraction. Figure 2-8 *(a)* presents the phase voltage waveforms obtained by adding the third harmonic to the sinusoidal reference signals.

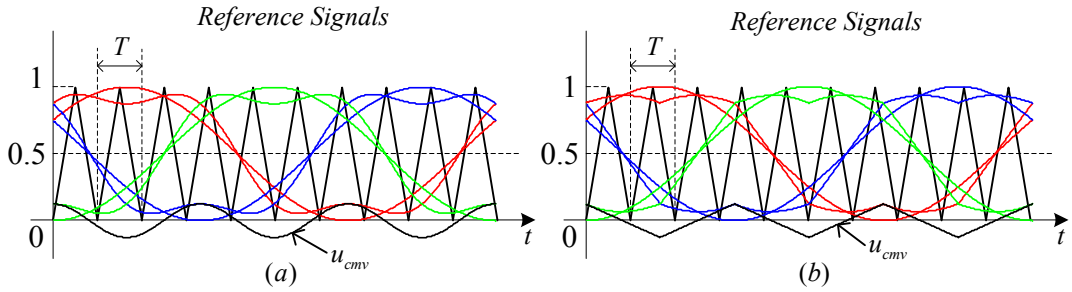

Figure 2-8 Generation of the reference signals by using: third harmonic injected modulation method (a), and space vector modulation (b)

By analyzing the third harmonic injection modulation technique from the pulse generation point of view, it can be observed that the distribution between the time-length of the two zero sequence vectors is changed during a fundamental period. In case of SVM (Figure 2-8 *(b)*) the time-length of the two zero sequence vectors was set to be always equal, resulting a triangular signal into the common mode voltage with a frequency three times larger than the fundamental.

An alternative modulation strategy is to use only one zero sequence voltage vector, which is called 120^0 discontinuous PWM (120^0 DPWM). This modulation method is based on moving the active vector region in successive half carrier intervals to join together, eliminating in this way one from the zero sequence voltage vectors. From phase voltage point of view, the discontinuous modulation method can be characterized as one leg clamped to the positive or negative DC rail for 120^0 segments of the fundamental period. By eliminating the pulse generation for one leg, the number of switching is reduced with 33% in case of DPWM.

Improved discontinuous modulation methods are the 30^0 and 60^0 PWM. For this modulation techniques the two zero sequence vectors are eliminated alternatively for successive 30^0 and respectively 60^0 segments during the fundamental period [13].

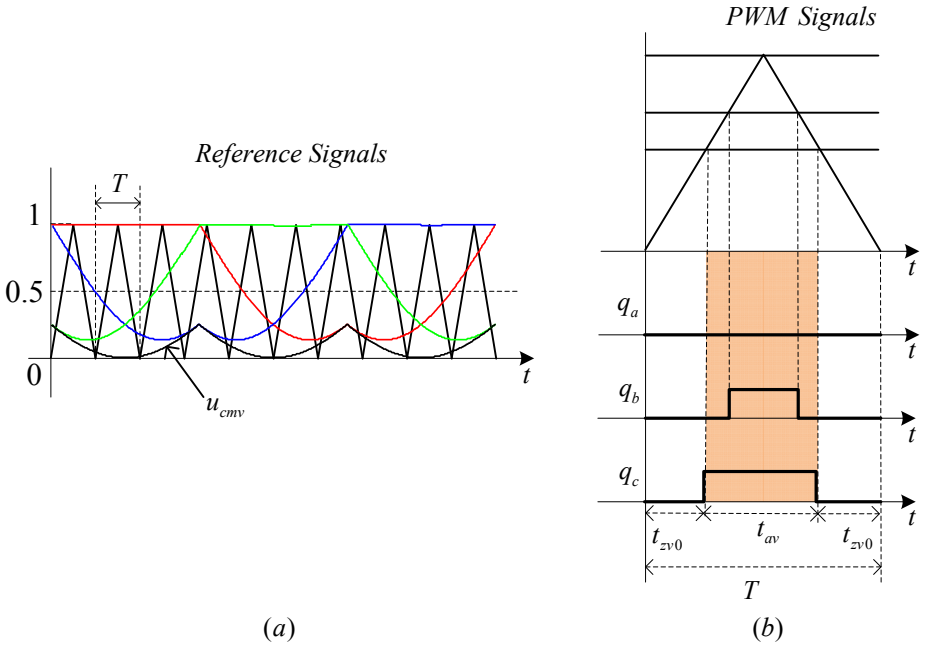

Figure 2-9 120^0 Discontinuous PWM: reference signal waveforms (a), and pulse generation mechanism (b)

The advantage of these methods is that the switching losses are balanced, the unmodulated leg is connected to the upper or lower DC-rail only for 30^0 and respectively 60^0 from the fundamental period. The space vector representation of the generated voltage vector from Figure 2-7 does not show the time distribution between the two zero sequence vectors. A graphical interpretation of the phase voltages, where the distribution of the zero sequence vectors can be tracked is presented in [25]. Figure 2-10 *(a)* presents one fundamental period of the normalized reference voltages and the carrier wave in Cartesian coordinates. The zero sequence vectors are generated when the carrier wave has higher or lower value than the positive and negative peak of the reference signals. By converting the Cartesian coordinates to polar coordinates the reference signals are describing closed curves like in Figure 2-10 *(b)*.

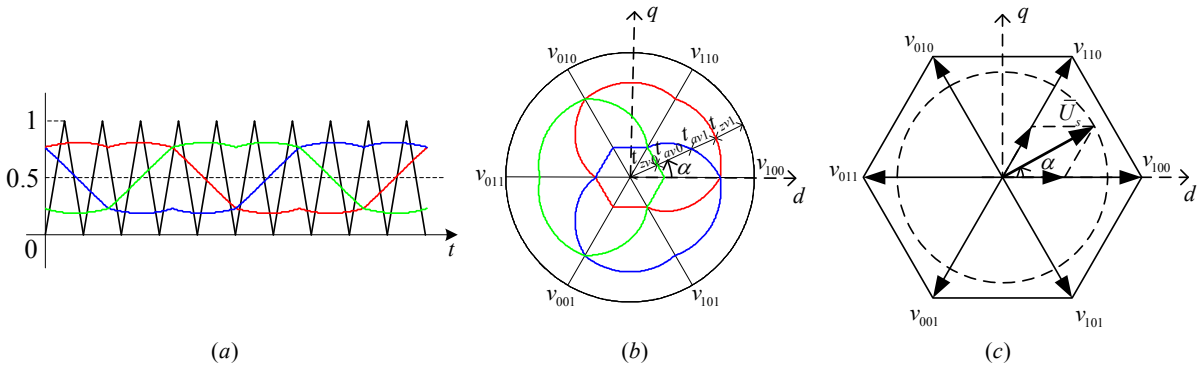

Figure 2-10 Graphical interpretation of the reference voltage in Cartesian coordinates (a), polar coordinates (b), and space vector representation (c)

In polar coordinate representation, the intersection of the radius at an angle α with the curves drawn by the three phase voltages gives the individual time components (t_{zv0}, t_{av1}, t_{av2}, t_{zv1}) for the basic voltage vectors. The relation between time components obtained by the intersection of the radius with the reference signals and the resultant voltage vector is given by (2.7). This relation between a rotating radius and the rotating voltage vector shows analogy between polar coordinates and SVM representation in *d-q* plane.

2.3.4 Saw-tooth carrier versus triangular carrier

Usually saw-tooth or triangular waveforms are used as carrier waves for PWM. Figure 2-11 *(a)* and *(b)* presents the saw-tooth respectively the triangular carrier waveforms during a fundamental period. Figure 2-11 *(c)* presents the pulse generation mechanism using the two different carrier waveforms. The main difference between the two carrier waveforms is the position of the generated pulses. From the point of view of the voltage vectors, seven vectors are generated during a modulation period, in case of the triangular carrier, while only four voltage vectors in a period in case of the saw-tooth carrier. During a modulation period, the active vector region (highlighted in Figure 2-11 *(c)*) is reduced from two to one in case of saw-tooth carrier.

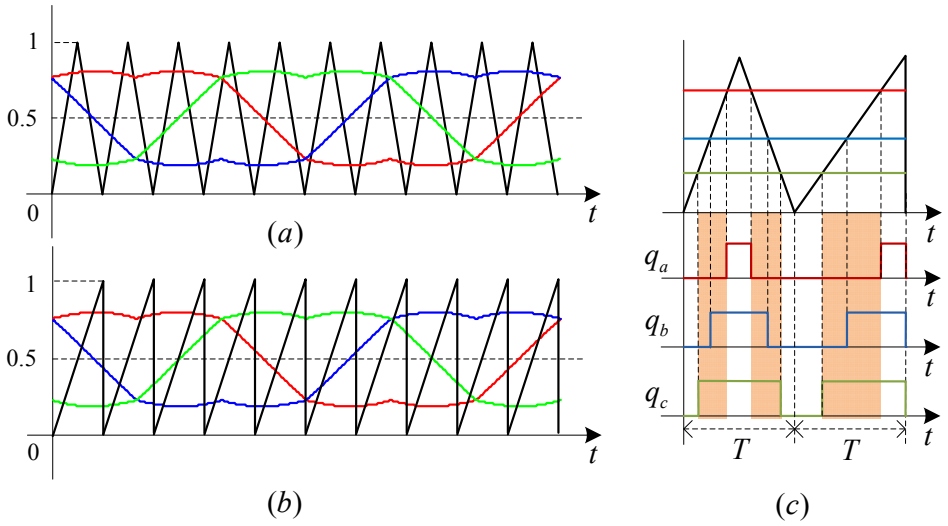

Figure 2-11 Pulse generation by using triangular or saw-tooth carrier wave

This means the time-length spent for each voltage vector is approximately double in case of saw-tooth carrier, which result a larger current ripple during one modulation period. With other words, when the triangular carrier is used, in both, the rising and at the falling edge of the triangular are voltage vectors generated. In case of saw-tooth modulation voltage vectors are generated only in the rising period. This means when the switches are switched off there is no voltage vector generated only the switching losses are increased.

Finally it can be concluded that triangular carrier is preferable for the three phase voltage source converters due to the lower current ripple per modulation period.

2.4 Implementation of the PWM schemes

Two alternatives exist for implementation of the PWM methods: by using analog or by using digital electronic components. For analog implementation the so called *naturally sampled* PWM is the most suitable, for digital implementation the *regular sampled* PWM is usually used. By using analog comparator the switch of the power transistor can be done exactly on the intersection point between the triangular carrier wave and the reference signal (Figure 2-12 *(a)*).

The appearance of cheap microcontroller makes the digital implementation more attractive. The calculation of the intersection point in case of the digital implementation can gives difficulties. To overcome this limitation the reference signal is sampled and then held constant for the carrier period (Figure 2-12 (b)). Being both the carrier and the reference signal a digital number, the comparison can be done easily in digital environment. The microcontrollers used for motor control are usually equipped with a PWM unit which consists: an up-down counter, three Compare Registers (CR), and a Period Register (PR). By using this dedicated PWM module the load on the microcontroller calculation power is minimal. In digital environment the carrier wave is generated by employing an up-down counter like is shown in Figure 2-12. By resetting the counter after the value from the period register is reached, the saw-tooth carrier wave can be generated.

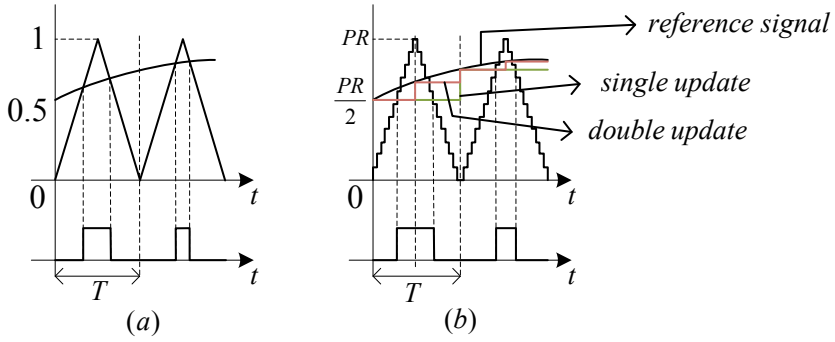

Figure 2-12 (a) naturally sampled PWM, (b) regular sampled PWM

The reference signal which is expressed as modulation index (vary between 0 and 1) is converted into compare value by multiplication of the value with the value of PR. The switching frequency is set by the PR value which can be expressed as:

$$f_{sw} = \frac{1}{2 \cdot PR \cdot T_{clk}} \tag{2.9}$$

where f_{sw} is the switching frequency, T_{clk} is the time base for the counter.
The output pin will change it state each time the number stored into the compare register match with the actual value of the counter. In this way each half modulation period a voltage vector $\bar{U}_s$ can be generated. The sampling of the reference signal can be done once (single update) or twice (double update) during a carrier period. The

double update technique gives better approximation for the time instance when switching should occur. However, in the case at high switching frequency it can cause over-overloading for the microcontroller.

2.5 Summary

In this chapter the basics of the voltage source converter topologies and the principle of carrier based modulation has been reviewed. By using the presented pulse width modulation methods, variable frequency and amplitude AC voltage supply can be built, which are suitable to be used for AC motor control. The concept of the space vector was also introduced, concept which helps understanding the theory behind the modern modulation techniques. Finally, implementation techniques for the presented modulation methods are presented.

Chapter 3

Analytic expression for the two-level PWM waveform spectra

The focus in this chapter is on derivation of a mathematical equation which determines the line-to-line voltage and the acoustic spectra.

3.1 Introduction

In most of the practical applications the carrier-based PWM methods are preferred due to their low-harmonic distortion, fixed switching frequency, well-defined harmonic spectra and implementation simplicity [16]. As described in the previous chapter, the carrier-based PWM method generates the variable-width train of pulses based on comparison between a low frequency reference signal and a high frequency triangular carrier wave. Most AC motor drives require a balanced three phase sinusoidal current. The balance can be ensured by not connecting the neutral point (star point) to the ground, leaving it floating; this offers an extra degree of freedom for the modulation. As a consequence, by adding the same signal (which appears in the common mode voltage (*cmv*)) to the three phase reference signals (phase voltages), the fundamental component of the line-to-line voltages (u_{ab}, u_{ab}, and u_{bc}) will not be affected. However, it does have an influence on the high frequency content of the line-to-line voltage spectra. One of the prime advantages of signal injection in the *cmv* is that the output voltage amplitude can be extended by 15% [24]. Several modulation methods that propose different signals to be injected into the common mode voltage can be found in the literature [18, 22].

The standard approach for harmonic analysis of the line-to-line voltage is to use discrete Fourier transform (DFT) on the measured signals, rather than an analytical solution to find the spectral components. However, the determination of an analytical equation for the PWM strategies was one of the main topics for the researchers in the

last decades, developing analytical solution for almost any PWM strategy [13]. The drawback of using DFT is that it is limited by its inputs: windowing will introduce side lobes in the frequency domain, and aliasing will introduce non-existing frequency components. The magnitude of the measured signal will be influenced by the limits of the analogue to digital conversion, the physical setup of the measurements, and external noise. An analytical solution is not affected by the previously mentioned factors in its prediction of the spectral components. The first analytical study of the modulated signals appears in [26, 27], which was adopted for PWM for power electronics in [28]. The analysis of modulation methods like sine-triangular modulation (ST-PWM), space vector modulation (SVM), and discontinuous PWM (DPWM), also called as modern modulation methods, can be found in [29-32]. A modulation method, which injects a sinusoidal signal with arbitrary frequency and amplitude into the common mode voltage is investigated in [25], showing that a well defined group of harmonics appear in the line-to-line and phase voltage spectrum with controllable amplitude.

The acoustic noise from an electric machine may arise due to mechanical, aerodynamic, electronic and magnetic sources [33]. The magnetic source and the mechanical structure interact due to the magnetic forces and the frequency response of the mechanical structure [34, 35]. It is well known that the normal components of the current dependent forces are significantly larger than the tangential components [34]. A previous analytical approach for describing pulse width modulation (PWM) effects on AC-drives was presented in [14], however radial forces were not considered in that paper. The radial forces were considered also regarding harmonics in the magnetic air gap flux in [36], without an evaluation of the effects from PWM. However, at low speed, switching frequency is the dominant source of the acoustic noise generated by the machine [37, 38]. The effects from PWM were considered with regards to the radial force in [37], but the authors did not treat analytically the relationship between PWM and radial force. Radial force prediction and calculation for a PWM driven asynchronous motor using finite-element method (FEM) can be found in [39-41]. Based on the analytical expression of the line-to-line voltage spectra, there is a possibility to predict the vibration spectra on the motor shell [42] which helps the identification of the mechanical noise sources in a drive system.

This chapter first presents the traditional analytic method, based on double Fourier integral calculation, of one phase leg for the ST-PWM which is the simplest modulation method. Next a generalization of the ST-PWM method is proposed, where a unified analytical solution, valid for all the PWM strategies with any kind of waveform injected in the common mode voltage, is deducted. This equation can be used also for the prediction of the spectra when a voltage ripple is present in the DC-link voltage, as well as for the case when the inverter works in over-modulation. In the last section an analytical solution is derived for prediction of the vibrations on the motor shell.

3.2 Analytical expression of the line-to-line voltage spectra using sine-triangular modulation method

As a starting point, the analytical method to determine the theoretical spectra of ST-PWM method is presented. However, the ST-PWM modulation method has poor waveform quality, and it is rarely used in real application, having 15% lower linear range than the modern modulation methods its simplicity eases the analytical calculation for the first step.

Any PWM signal can be described as an interaction of two independent time variable functions $\tilde{f}(t)=f\big(x(t),y(t)\big)$, where *x(t)* is considered as the carrier signal (usually triangular) with a frequency of ω_c and phase of θ_c; and *y(t)* is considered to be the reference signal (sinusoidal in case of ST-PWM) with a frequency of ω_0 and phase of θ_0. Based on the PWM theory presented in [13], an arbitrarily modulated waveform can be expressed with the double Fourier series expansion as:

$$\tilde{f}(t)=\frac{A_{00}}{2}+\sum_{m=0}^{\infty}\sum_{n=-\infty}^{\infty}\Big(A_{mn}\cos\big((m\omega_c+n\omega_0)t+(m\theta_c+n\theta_0)\big)+B_{mn}\sin\big((m\omega_c+n\omega_0)t+(m\theta_c+n\theta_0)\big)\Big)$$
$$A_{mn}=\frac{1}{2\pi^2}\int_{-\pi}^{\pi}\int_{-\pi}^{\pi}f(t)\cos(mx+ny)\,dxdy;\ B_{mn}=\frac{1}{2\pi^2}\int_{-\pi}^{\pi}\int_{-\pi}^{\pi}f(t)\sin(mx+ny)\,dxdy \tag{3.1}$$

where m is the carrier modulation index, n is the baseband index, and A_{mn} and B_{mn} are the magnitudes of each individual harmonic component from the spectrum. The $(m\omega_c+n\omega_0)$ gives the frequency, and $(m\theta_c+n\theta_0)$ gives the phase of each A_{mn} and B_{mn} magnitude values from (3.1). By setting the carrier index $m=0$ equation (3.1) gives the fundamental and the baseband harmonic components; by setting $n=0$ the equation gives the carrier harmonics.

The function *f(x(t),y(t))* can be graphically represented in *x-y* plane as it is shown in Figure 3-1 (a). Considering that the reference signal and the carrier wave are periodic functions, *f(x(t),y(t))* can be described as an infinite repetition of the unit cell in x and y axis direction. The unit cell, which contains one period from the reference signal and carrier wave, is marked with red contour in Figure 3-1 (a). The carrier wave theoretically can be interpreted as a straight line with a slope of ω_0/ω_c in the repetitive representation of the unit cell. This straight line becomes a triangular carrier wave when the reference signal is unfold in time like in Figure 3-1 *(c)*. As it was presented in the previous chapter, the PWM signal takes the value of 0 (white part of the unit cell from Figure 3-1 *(a)*) when the carrier wave is higher than the reference signal, and U_{dc} (gray part of the unit cell from Figure 3-1 (a)) in case when the reference signal is lower than the carrier wave.

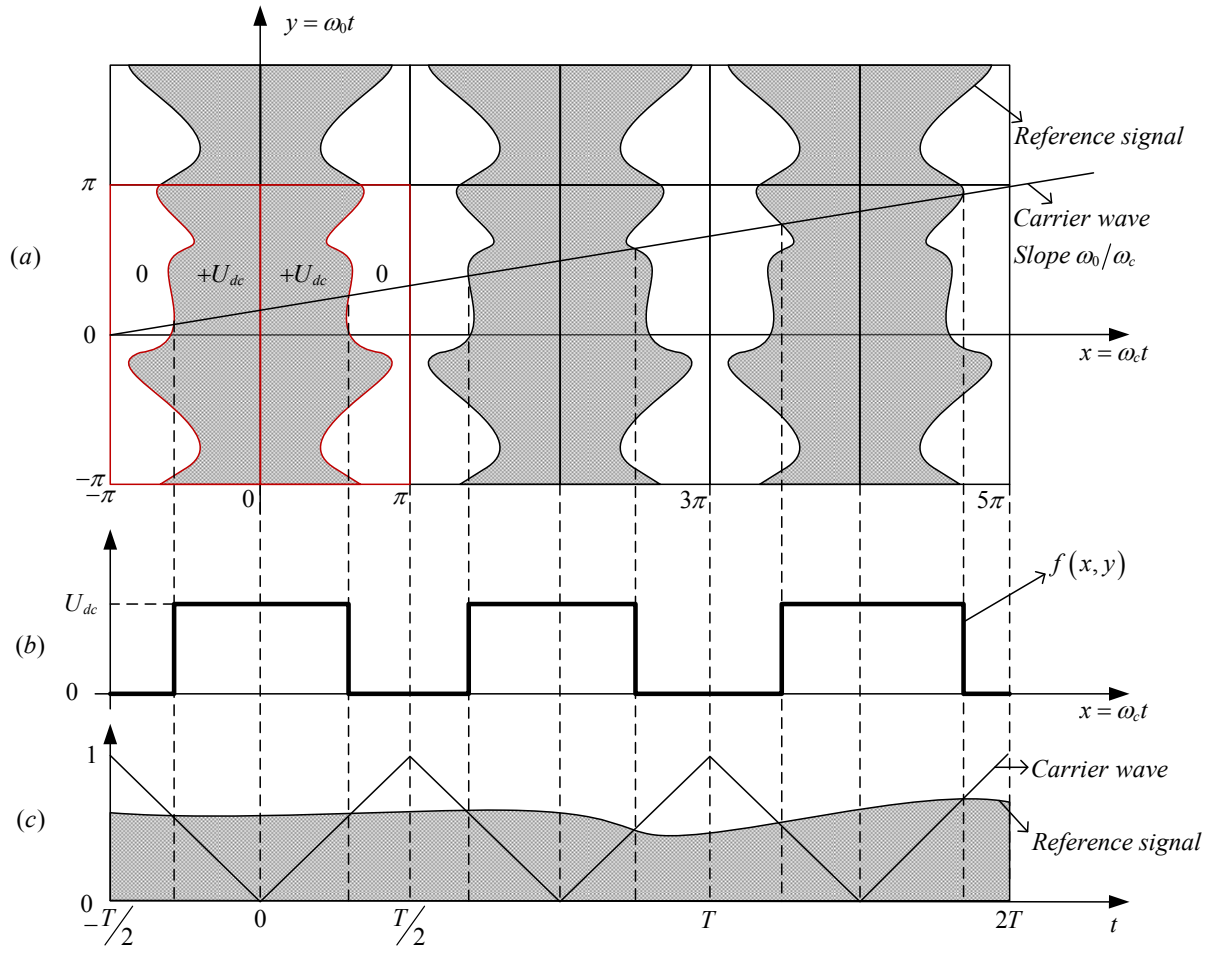

Figure 3-1 The x-y plane representation of the double-edge PWM signal generation: replicated unit cell (red frame) representation of modulation in x-y plane (a), resultant PWM signal (b), and pulse generation by comparison between the triangular carrier wave and the reference signal (c)

The intersection of this line with the reference signal and its mirror results similar switching instants like the triangular carrier wave intersection point and the unfold reference signal in time.

The magnitude values of the harmonic components from (3.1) can be calculated using the double Fourier integral, which is different for each modulation method. In case of ST-PWM method, the reference signal can be expressed as:

$$u_{ref} = M\cos(\omega_0 t + \theta_0) = M\cos(y) \tag{3.2}$$

where M is the modulation index. The representation of the ST-PWM method in x-y plane is shown in Figure 3-2:

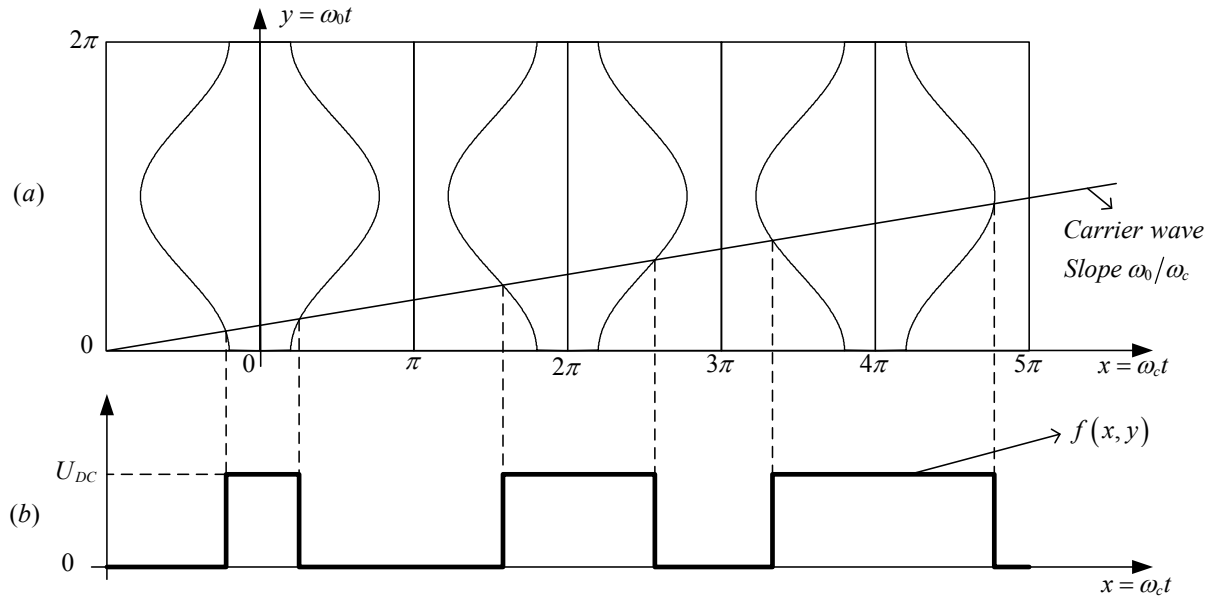

Figure 3-2 The x, y plane representation of the double-edge ST-PWM: sinusoidal reference signal and the carrier wave (a), and resultant PWM signal (b)

The switching instants for ST-PWM will take place when the carrier wave intersects the reference voltage, which can be mathematically expressed such that:

$$x = 2\pi p - \frac{\pi}{2}\left(1 + M\cos\left(y\right)\right) \quad p = 0,1,2,...,\infty \tag{3.3}$$

for switching from *0* to $+U_{dc,}$ and

$$x = 2\pi p + \frac{\pi}{2}\left(1 + M\cos\left(y\right)\right) \quad p = 0,1,2,...,\infty \tag{3.4}$$

for switching from $+U_{dc}$ to *0*.

The magnitudes of the spectral components of the phase voltage in case of ST-PWM can be expressed as:

$$\bar{C}_{mn} = A_{mn} + jB_{mn} = \frac{U_{dc}}{2\pi^2}\int_{-\pi}^{\pi}\int_{-\frac{\pi}{2}(1+M\cos(y))}^{\frac{\pi}{2}(1+M\cos(y))} e^{j(mx+ny)}dxdy \tag{3.5}$$

where U_{dc} is the DC-link voltage. The limits of the inner integral describe one period of the reference signal; the outer integral limits correspond to the carrier wave. The closed form solution of (2), based on [5], is expressed as:

$$\bar{C}_{mn} = \frac{1}{m}J_n\left(m\frac{\pi}{2}M\right)\sin\left(\left(m+n\right)\frac{\pi}{2}\right) \tag{3.6}$$

where $J_n(\beta)$ denotes the n-th order Bessel function of the first kind with the argument of β.

The complete solution can be found by substituting $\bar{C}_{mn}$ from Eq. (3.1) with its expression from Eq. (3.6):

$$u_{ag} = \frac{U_{dc}}{2}\left(\begin{array}{l}1 + M\cos(\omega_0 t + \theta_0) + \\ \frac{4}{\pi}\sum_{m=1}^{\infty}\sum_{n=\infty}^{\infty}\left(\frac{1}{m}J_n\left(m\frac{\pi}{2}M\right)\sin\left((m+n)\frac{\pi}{2}\right)\cos\left((m\omega_c + n\omega_c)t + (m\theta_c + n\theta_0)\right)\right)\end{array}\right) \tag{3.7}$$

3.3 Analytical expression of the line-to-line voltage spectra for PWM methods using redistributed zero sequence vectors

In case of ST-PWM modulation, both the phase voltages and the line-to-line voltages are sinusoidal signals. As described in the previous chapter, the fundamental frequency of the motor current, is not affected if an arbitrary signal is added to the reference voltages. The approach to develop an analytical solution for the modulation method where the zero sequence vectors are redistributed, presented in [13], is to decompose the reference signal in segments. The disadvantage of this method is that for each modulation method a unique equation has to be derived. For those modulation methods where the fundamental signal has to be decomposed in many segments the derivation of a new solution becomes cumbersome.

The unified analytical method is based on the decomposition of the reference signal into its harmonics, and derivation of an analytical solution for the case when the reference signal contains multiple frequency components. In this case a unique equation can describe the spectral components of a PWM signal, where the reference is an arbitrary signal.

Based on Fourier series decomposition any periodic signal can be expressed as the sum of its harmonic components:

$$y(t) = a_0 + \sum_{m=1}^{\infty} a_m \cos(m\omega t) + b_m \sin(m\omega t) = a_0 + \sum_{m=1}^{\infty} c_m \cos(m\omega t + \xi_m) \tag{3.8}$$

After applying the Fourier analysis on the reference signal, which contains the sinusoidal reference and the arbitrary signal injected in *cmv*, it can be characterized as a set of frequency and amplitude components:

$$U_{ref} = off_{ref} + \sum_{z=1}^{\infty} M_z \cos(zy + \xi_z) \tag{3.9}$$

where the first element from the infinite sum characterizes the fundamental frequency,(M_1) is the modulation index and ξ_1 is the phase of the fundamental frequency; the rest of the harmonic components describe the arbitrary signal injected into *cmv*. For numerical calculations, the number of considered harmonics from the reference voltage spectrum is limited to the *N*-th order. Moreover, in case of regular sampled PWM, the maximum frequency that can be injected into the common mode voltage is limited by the switching frequency.

The double Fourier integral that defines the magnitudes of the spectral components for the reference signal which consists of multiple harmonic components - becomes:

$$\bar{C}_{mn} = \frac{U_{dc}}{2\pi^2}\int_{-\pi}^{\pi}\int_{-\frac{\pi}{2}\left(off+\sum_{z=1}^{N} M_z\cos(zy+\xi_z)\right)}^{\frac{\pi}{2}\left(off+\sum_{z=1}^{N} M_z\cos(zy+\xi_z)\right)} e^{j(mx+ny)}dxdy \tag{3.10}$$

where the offset is $off = 1 + off_{ref}$.

First Eq. (3.10) is evaluated for the case when $m=0$, then the equation becomes:

$$\begin{aligned}\bar{C}_{0n} &= \frac{U_{dc}}{2\pi^2}\int_{-\pi}^{\pi}\int_{-\frac{\pi}{2}\left(off+\sum_{z=1}^{N} M_z\cos(zy+\xi_z)\right)}^{\frac{\pi}{2}\left(off+\sum_{z=1}^{N} M_z\cos(zy+\xi_z)\right)} e^{jny}dxdy = \\ &\frac{U_{dc}}{2\pi^2}\int_{-\pi}^{\pi}\left(off+\sum_{z=1}^{N} M_z\cos\left(zy+\xi_z\right)\right)e^{jny}dy\end{aligned} \tag{3.11}$$

by rearranges with some manipulation:

$$\bar{C}_{0n} = \frac{U_{dc}}{4\pi^2}off\int_{-\pi}^{\pi} e^{j(ny)}dy + M_z\sum_{z=1}^{N}\left(e^{j\xi_z}\int_{-\pi}^{\pi} e^{j(z+n)y}dy + e^{-j\xi_z}\int_{-\pi}^{\pi} e^{-j(z+n)y}dy\right) \tag{3.12}$$

by using

$$\begin{cases}\int_{-\pi}^{\pi} e^{jpy}dy = 0 \ for \ p \neq 0 \\ \int_{-\pi}^{\pi} e^{jpy}dy = 2\pi \ for \ p = 0\end{cases} \quad for \quad p \in \mathbb{Z} \tag{3.13}$$

Reduces (3.12) to:

$$\bar{C}_{0n} = \frac{U_{dc}}{2\pi}\left(\sum_{z=1}^{N} e^{j\xi_z}M_z\right)\Bigg|_{z=|n|} \tag{3.14}$$

for $n \neq 0$, and for $n = 0$

$$\bar{C}_{00} = \frac{U_{dc}off}{2\pi} \tag{3.15}$$

For the case when $m > 0$, the inner integral from (3.10) can be evaluated to:

$$\bar{C}_{mn} = \frac{U_{dc}}{2jm\pi^2}\int_{-\pi}^{\pi}\left(e^{jny}\left(e^{j\cdot off\cdot m\frac{\pi}{2}}e^{\sum_{z=1}^{N} jm\frac{\pi}{2}M_z\cos(zy+\xi_z)} - e^{-j\cdot off\cdot m\frac{\pi}{2}}e^{-\sum_{z=1}^{N} jm\frac{\pi}{2}M_z\cos(zy+\xi_z)}\right)\right)dy \tag{3.16}$$

by substituting:

$$s_z = \frac{m\pi M_z}{2} \tag{3.17}$$

Equation (3.16) becomes:

$$\bar{C}_{mn} = \frac{U_{dc}}{2jm\pi^2}\int_{-\pi}^{\pi}\left(e^{jny}\left(e^{j\cdot off\cdot m\frac{\pi}{2}}\prod_{z=1}^{N} e^{js_z\cos(zy+\xi_z)} - e^{-j\cdot off\cdot m\frac{\pi}{2}}\prod_{z=1}^{N} e^{-js_z\cos(zy+\xi_z)}\right)\right)dy \tag{3.18}$$

Using Jacobi-Anger and Bessel function relationship:

$$\begin{aligned}&e^{\pm j\gamma\cos(\theta)} = J_0(\gamma) + 2\sum_{k=1}^{\infty} j^{\pm k}J_k(\gamma)\cos(k\theta) = 2\sum_{k=0}^{\infty} j^{\pm k}\tilde{J}_k(\gamma)\cos(k\theta) \\ &where \quad \begin{cases}\tilde{J}_k(\gamma) = \frac{J_0(\gamma)}{2} \quad for \quad k = 0 \\ \tilde{J}_k(\gamma) = J_k(\gamma) \quad for \quad k \neq 0\end{cases}\end{aligned} \tag{3.19}$$

Equation (3.18) can be expressed as:

$$\bar{C}_{mn} = \frac{2^N U_{dc}}{2jm\pi^2} \int_{-\pi}^{\pi} \left(e^{jny} \begin{pmatrix} e^{j\cdot off\cdot m\frac{\pi}{2}} \prod_{z=1}^{N} \left(\sum_{k=0}^{\infty} j^k \tilde{J}_k(s_z) \cos(kzy + k\xi_z) \right) - \\ e^{-j\cdot off\cdot m\frac{\pi}{2}} \prod_{z=1}^{N} \left(\sum_{k=0}^{\infty} j^{-k} \tilde{J}_k(s_z) \cos(kzy + k\xi_z) \right) \end{pmatrix} \right) dy \tag{3.20}$$

The product of a sum can be transformed in sum of products with:

$$\prod_{z=1}^{N} \left(\sum_{k=0}^{\infty} j^k \tilde{J}_k(s_z) \cos(kzy + k\xi_z) \right) = \sum_{k_1=0}^{\infty} \sum_{k_2=0}^{\infty} \dots \sum_{k_N=0}^{\infty} \left(\prod_{z=1}^{N} \left(j^{k_z} \tilde{J}_{k_z}(s_z) \cos(k_z zy + k_z \xi_z) \right) \right) \tag{3.21}$$

From the above, Eq. (3.20) becomes:

$$\bar{C}_{mn} = \frac{2^{N-1} U_{dc}}{jm\pi^2} \begin{pmatrix} \int_{-\pi}^{\pi} e^{jny} e^{j\cdot off\cdot m\frac{\pi}{2}} \left(\sum_{k_1=0}^{\infty} \sum_{k_2=0}^{\infty} \dots \sum_{k_N=0}^{\infty} \left(\prod_{z=1}^{N} \left(j^{k_z} \tilde{J}_{k_z}(s_z) \cos(k_z zy + k_z \xi_z) \right) \right) \right) dy - \\ - \int_{-\pi}^{\pi} e^{jny} e^{-j\cdot off\cdot m\frac{\pi}{2}} \left(\sum_{k_1=0}^{\infty} \sum_{k_2=0}^{\infty} \dots \sum_{k_N=0}^{\infty} \left(\prod_{z=1}^{N} \left(j^{-k_z} \tilde{J}_{k_z}(s_z) \cos(k_z zy + k_z \xi_z) \right) \right) \right) dy \end{pmatrix} \tag{3.22}$$

Rearranging (3.22) with some manipulation yields:

$$\bar{C}_{mn} = \frac{2^{N-1} U_{dc}}{jm\pi^2} \left(\sum_{k_1=0}^{\infty} \sum_{k_2=0}^{\infty} \dots \sum_{k_N=0}^{\infty} \prod_{z=1}^{N} \left(\tilde{J}_{k_z}(s_z) \right) \int_{-\pi}^{\pi} e^{jny} \begin{pmatrix} \left(e^{j\cdot off\cdot m\frac{\pi}{2}} \prod_{z=1}^{N} \left(j^{k_z} \cos(k_z zy + k_z \xi_z) \right) \right) - \\ \left(e^{-j\cdot off\cdot m\frac{\pi}{2}} \prod_{z=1}^{N} \left(j^{-k_z} \cos(k_z zy + k_z \xi_z) \right) \right) \end{pmatrix} dy \right) \tag{3.23}$$

By using the relation $j^{\pm k_z} = e^{\pm jk_z\frac{\pi}{2}}$, Eq. (3.23) can be further rearranged to:

$$\bar{C}_{mn} =$$

$$\frac{2^{N-1} U_{dc}}{jm\pi^2} \sum_{k_1=0}^{\infty} \sum_{k_2=0}^{\infty} \dots \sum_{k_N=0}^{\infty} \left(\prod_{z=1}^{N} \left(\tilde{J}_{k_z}(s_z) \right) \int_{-\pi}^{\pi} \left(e^{jny} \prod_{z=1}^{N} \left(\cos(k_z zy + k_z \xi_z) \right) \begin{pmatrix} e^{j\frac{\pi}{2}(off\cdot m)} \prod_{z=1}^{N} e^{jk_z\frac{\pi}{2}} - \\ e^{-j\frac{\pi}{2}(off\cdot m)} \prod_{z=1}^{N} e^{-jk_z\frac{\pi}{2}} \end{pmatrix} \right) dy \right) \tag{3.24}$$

Transforming the product of cosine functions into sum of cosine function:

$$\prod_{z=1}^{N} \cos(k_z zy + k_z \xi_z) = \frac{1}{2^{N-1}} \sum_{\varepsilon_1=0}^{1} \sum_{\varepsilon_2=0}^{1} \dots \sum_{\varepsilon_{N-1}=0}^{1} \cos\left(\sum_{z=2}^{N} \left(\left(k_1 + zk_z(2\varepsilon_{z-1} - 1) \right) y + k_1\xi_1 + k_z\xi_z(2\varepsilon_{z-1} - 1) \right) \right) \tag{3.25}$$

and by using Euler formula for sine function, Eq. (3.24) becomes:

$$\bar{C}_{mn} =$$

$$\frac{2^{N-1} U_{dc}}{2^{N-1} jm\pi^2} \sum_{k_1=0}^{\infty} \sum_{k_2=0}^{\infty} \dots \sum_{k_N=0}^{\infty} \begin{pmatrix} \prod_{z=1}^{N} \left(\tilde{J}_{k_z}(s_z) \right) 2j \sin\left(\frac{\pi}{2} \left(off\cdot m + \sum_{z=1}^{N} k_z \right) \right) \\ \int_{-\pi}^{\pi} e^{jny} \sum_{\varepsilon_1=0}^{1} \sum_{\varepsilon_2=0}^{1} \dots \sum_{\varepsilon_{N-1}=0}^{1} \cos\left(\sum_{z=2}^{N} \begin{pmatrix} \left(k_1 + zk_z(2\varepsilon_{z-1} - 1) \right) y + \\ k_1\xi_1 + k_z\xi_z(2\varepsilon_{z-1} - 1) \end{pmatrix} \right) dy \end{pmatrix} \tag{3.26}$$

By using Euler formula for the cosine function:

$$\bar{C}_{mn} =$$

$$\frac{2U_{dc}}{m\pi^2}\sum_{k_1=0}^{\infty}\sum_{k_2=0}^{\infty}\cdots\sum_{k_N=0}^{\infty}\left(\begin{array}{l}\prod_{z=1}^{N}\left(\tilde{J}_{k_z}(s_z)\right)\sin\left(\frac{\pi}{2}\left(off\cdot m+\sum_{z=1}^{N}k_z\right)\right)\\ \sum_{\varepsilon_1=0}^{1}\sum_{\varepsilon_2=0}^{1}\cdots\sum_{\varepsilon_{N-1}=0}^{1}\left(\begin{array}{l}e^{j\left(k_1\xi_1+\sum_{z=2}^{N}k_z\xi_z(2\varepsilon_{z-1}-1)\right)}\int_{-\pi}^{\pi}\frac{e^{j\left(n+\sum_{z=2}^{N}\left(k_1+zk_z(2\varepsilon_{z-1}-1)\right)\right)y}}{2}dy+\\ e^{-j\left(k_1\xi_1+\sum_{z=2}^{N}k_z\xi_z(2\varepsilon_{z-1}-1)\right)}\int_{-\pi}^{\pi}\frac{e^{-j\left(-n+\sum_{z=2}^{N}\left(k_1+zk_z(2\varepsilon_{z-1}-1)\right)\right)y}}{2}dy\end{array}\right)\end{array}\right) \quad (3.27)$$

Considering (3.13), equation (3.27) will have solution when $n+\sum_{z=2}^{N}\left(k_1+zk_z(2\varepsilon_{z-1}-1)\right)=0$ or $n-\sum_{z=2}^{N}\left(k_1+zk_z(2\varepsilon_{z-1}-1)\right)=0$ for each combination of ε_{N-1}. By transforming the exponential with Euler formula in sum of sine and cosine functions the solution for the outer integral becomes:

$$\bar{C}_{mn}=\frac{2U_{dc}}{m\pi}\times$$

$$\sum_{k_1=0}^{\infty}\sum_{k_2=0}^{\infty}\cdots\sum_{k_N=0}^{\infty}\left(\begin{array}{l}\prod_{z=1}^{N}\left(\tilde{J}_{k_z}(s_z)\right)\left(\sin\left(\frac{\pi}{2}\left(off\cdot m+\sum_{z=1}^{N}k_z\right)\right)\right)\times\\ \left(\begin{array}{l}\cos\left(\sum_{\varepsilon_1=0}^{1}\sum_{\varepsilon_2=0}^{1}\cdots\sum_{\varepsilon_{N-1}=0}^{1}\left(k_1\xi_1+\sum_{z=2}^{N}k_z\xi_z(2\varepsilon_z-1)\right)\right)\pm\\ j\sin\left(\sum_{\varepsilon_1=0}^{1}\sum_{\varepsilon_2=0}^{1}\cdots\sum_{\varepsilon_{N-1}=0}^{1}\left(k_1\xi_1+\sum_{z=2}^{N}k_z\xi_z(2\varepsilon_{z-1}-1)\right)\right)\end{array}\right)\end{array}\right)\left|\begin{array}{l}k_1+\\ \sum_{z=2}^{N}\left(zk_z(2\varepsilon_{z-1}-1)\right)\end{array}\right|=\mp n \quad (3.28)$$

for $n\neq 0$; in case when $n=0$ both of the integrals are equal with 2π, (3.27) becoming:

$$\bar{C}_{m0} =$$

$$\frac{4U_{dc}}{m\pi}\sum_{k_1=0}^{\infty}\sum_{k_2=0}^{\infty}\cdots\sum_{k_N=0}^{\infty}\left(\begin{array}{l}\prod_{z=1}^{N}\left(\tilde{J}_{k_z}(s_z)\right)\sin\left(\frac{\pi}{2}\left(off\cdot m+\sum_{z=1}^{N}k_z\right)\right)\\ \sum_{\varepsilon_1=0}^{1}\sum_{\varepsilon_2=0}^{1}\cdots\sum_{\varepsilon_{N-1}=0}^{1}\left(\cos\left(k_1\xi_1+\sum_{z=2}^{N}k_z\xi_z(2\varepsilon_{z-1}-1)\right)\right)\end{array}\right)\left|\begin{array}{l}k_1+\\ \sum_{z=2}^{N}\left(zk_z(2\varepsilon_{z-1}-1)\right)\end{array}\right|=0 \quad (3.29)$$

The conditional limitation can be interpreted as a summation of the harmonic components of the reference voltage. For example in case of SVM the reference voltage can be approximated the first four sinusoidal components from the signal spectrum like:

$$y(t)=M_1\cos(\omega_0 t)-0.2M_1\cos(3\omega_0 t)+0.047M_1\cos(9\omega_0 t)-0.02M_1\cos(15\omega_0 t) \quad (3.30)$$

where the first component is the fundamental. The conditional limitation for this case will be:

$$\begin{aligned}
k_1 + 3k_2 + 9k_3 + 15k_4 &= |n| \\
k_1 + 3k_2 + 9k_3 - 15k_4 &= |n| \\
k_1 + 3k_2 - 9k_3 + 15k_4 &= |n| \\
k_1 + 3k_2 - 9k_3 - 15k_4 &= |n| \\
k_1 - 3k_2 + 9k_3 + 15k_4 &= |n| \\
k_1 - 3k_2 + 9k_3 - 15k_4 &= |n| \\
k_1 - 3k_2 - 9k_3 + 15k_4 &= |n| \\
k_1 - 3k_2 - 9k_3 - 15k_4 &= |n|
\end{aligned} \tag{3.31}$$

Taking in consideration the rapid roll off of the Bessel function, it is enough to calculate for the first 10 terms [13]. For those cases where the reference signal can be described as a sum of sine and cosine functions with phase equal to zero (in most of the cases for modern modulation methods presented in [22]), Eq. (3.27) can be reduced to:

$$\bar{C}_{mn} =$$

$$\frac{2U_{dc}}{m\pi}\sum_{k_1=0}^{\infty}\sum_{k_2=0}^{\infty}\cdots\sum_{k_N=0}^{\infty}\left(\prod_{z=1}^{N}\left(\tilde{J}_{k_z}\left(s_z\right)\right)\left(\sin\left(\frac{\pi}{2}\left(off\cdot m+\sum_{z=1}^{N}k_z\right)\right)\right)\right)\left|\begin{pmatrix}k_1+\\ \sum_{z=2}^{N}\left(zk_z\left(2\varepsilon_{z-1}-1\right)\right)\end{pmatrix}=|n|\right. \tag{3.32}$$

In most of the cases for digital applications, symmetrical regular sampled PWM is used. Figure 3-3 (a) presents the sampled reference signal and the solution trajectory in *x-y* plane, where the intersection between the solution trajectory and the sampled reference signal gives the switching instants for the power transistors. A different approach is presented in Figure 3-3 (b), where the reference signal is maintained smooth and the solution trajectory is held constant for the modulation period. The outcome is similar in both cases, the only advantage of the second approach is that it eases the mathematically calculations. In case of regular sampled PWM, where a staircase solution trajectory is considered, the solution can be found by replacing y with $y = y' + (\omega_0/\omega_c)x$ in (3.10), becoming:

$$\bar{C}_{mn} = \frac{U_{dc}}{2\pi^2}\int_{-\pi}^{\pi}\int_{-\frac{\pi}{2}\left(off+\sum_{z=1}^{N}M_z\cos\left(zy'+\xi_z\right)\right)}^{\frac{\pi}{2}\left(off+\sum_{z=1}^{N}M_z\cos\left(zy'+\xi_z\right)\right)} e^{j\left(mx+n\left(y'+(\omega_0/\omega_c)x\right)\right)}dxdy \tag{3.33}$$

which transforms Eq. (3.32) into:

$$\bar{C}_{mn} =$$

$$\frac{2U_{dc}}{q\pi}\sum_{k_1=0}^{\infty}\sum_{k_2=0}^{\infty}\cdots\sum_{k_N=0}^{\infty}\left(\prod_{z=1}^{N}\left(\tilde{J}_{k_z}\left(\tilde{s}_z\right)\right)\left(\sin\left(\frac{\pi}{2}\left(off\cdot q+\sum_{z=1}^{N}k_z\right)\right)\right)\right)\left|\begin{pmatrix}k_1+\\ \sum_{z=2}^{N}\left(zk_z\left(2\varepsilon_{z-1}-1\right)\right)\end{pmatrix}=|n|\right. \tag{3.34}$$

$$where\ \tilde{s}_z = \frac{q\pi M_z}{2},\ q = m + n\left(\omega_0/\omega_c\right)$$

For the case of symmetrical regular sampled PWM.

The line-to-line voltage can be calculated by subtracting the two phase voltages, which have a phase difference of 120^0. The subtraction of the phase voltages expressed as a sum of harmonics (using Eq. (3.1)), and considering that the phase of *x(t)* and *y(t)* zero, is:

$$f(t)=\left(\frac{A_{00}}{2}+\sum_{m=0}^{\infty}\sum_{n=-\infty}^{\infty}\left(A_{mn}\cos\left(\left(m\omega_c+n\omega_0\right)t\right)+B_{mn}\sin\left(\left(m\omega_c+n\omega_0\right)t\right)\right)\right)- \\ \left(\frac{A_{00}}{2}+\sum_{m=0}^{\infty}\sum_{n=-\infty}^{\infty}\left(A_{mn}\cos\left(\left(m\omega_c+n\omega_0\right)t+n\frac{2\pi}{3}\right)\right)+B_{mn}\sin\left(\left(m\omega_c+n\omega_0\right)t+n\frac{2\pi}{3}\right)\right) \tag{3.35}$$

which can be simplified by using trigonometric identities to:

$$u_{ab}=2\sum_{m=0}^{\infty}\sum_{n=-\infty}^{\infty}\left(A_{mn}\sin\left(n\frac{\pi}{3}\right)\cos\left(\left(m\omega_c+n\omega_0\right)t-n\frac{\pi}{2}+\frac{\pi}{2}\right)+B_{mn}\sin\left(-n\frac{\pi}{3}\right)\cos\left(\left(m\omega_c+n\omega_0\right)t-n\frac{\pi}{3}\right)\right) \tag{3.36}$$

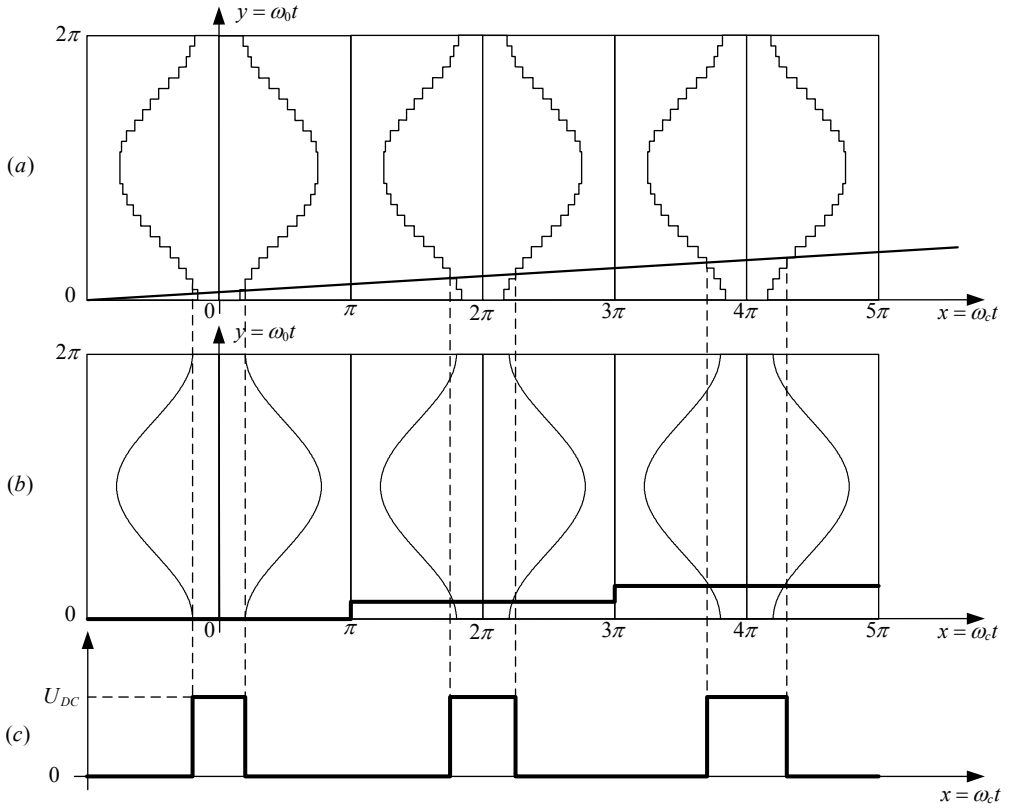

Figure 3-3 x-y plane representation of the regular sampled double-edge ST-PWM: sampled sinusoidal reference signal with continuous carrier wave (solution trajectory)((a), sampled carrier wave (solution trajectory) with continuous reference signal (b), (c) resultant PWM signal

In case of digital applications where usually regular sampled PWM is used, it is difficult to set the exact $2\pi/3$ radian (120^0) phase shift between the phases. For the analytical calculations, a quantization error of 0.02 radians (app. 1^0), was added to the ideal $2\pi/3$ radian phase shift. This quantization error causes a delay of $\pm 0.1ms$ at the 25Hz fundamental, which corresponds to a half modulation period at a switching frequency of 4kHz. By having this small phase error, the harmonic sideband will not be

completely cancelled around the odd carrier multiples as it will be show later in the measured and analytically calculated spectra.

Two double-edge symmetrical regularly sampled PWM methods were analyzed for experimental validation; the very common SVM and the 120^0 DPWM, modulation methods that are rich in harmonics. The switching frequency has been set to 4 kHz, while the fundamental frequency was set to 25 Hz with a modulation index of 0.5. For the entire measured and calculated spectrum, the magnitude values have been referenced to the magnitude of the fundamental frequency component.

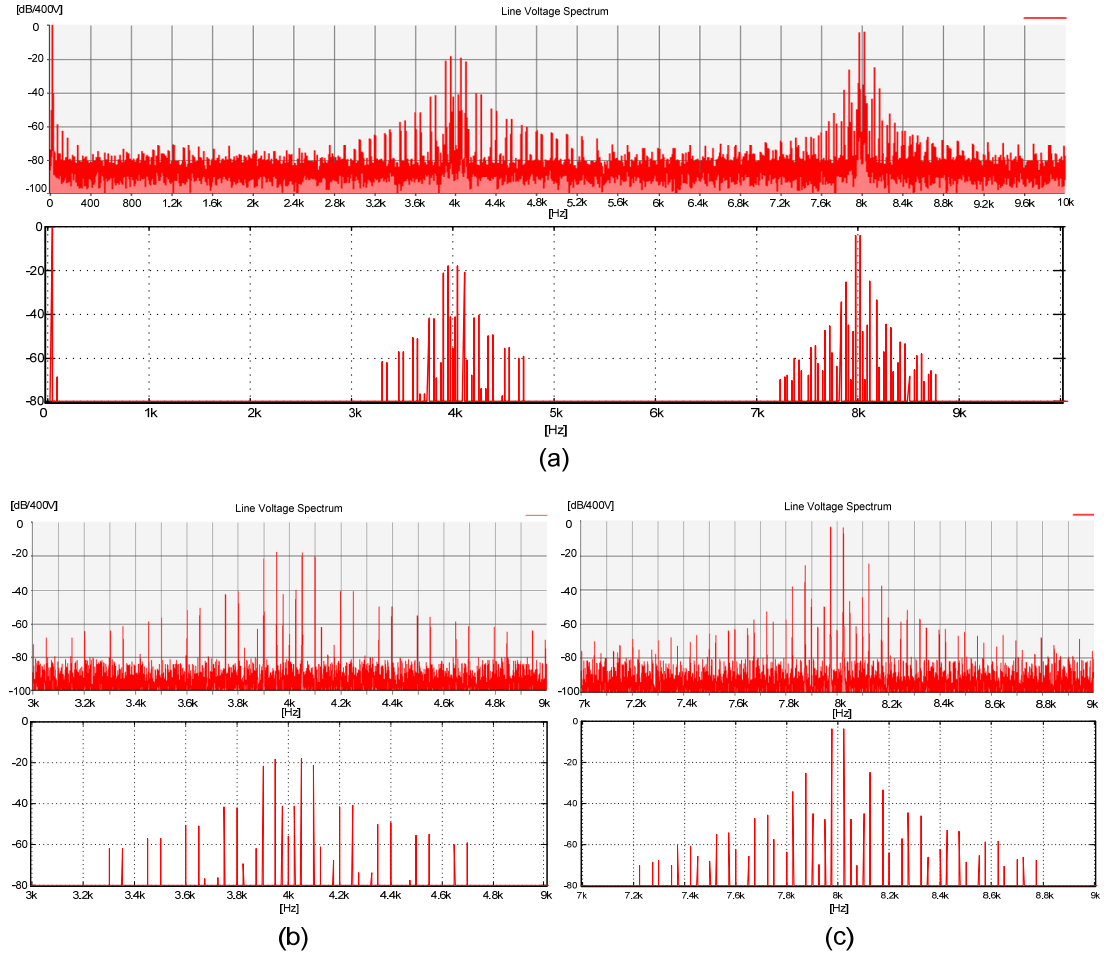

Figure 3-4 Spectra of the line-to-line voltage using SVM method: measured full spectra ((a), top), calculated full spectra, ((a), bottom). Subfigure (b) shows the zoom in the spectra around the switching frequency (measured ((b), top), and calculated ((b), bottom)), while Subfigure (c) shows a zoom in spectra around the double switching frequency (measured ((c), top), and calculated ((c), bottom)).

The theoretical line-to-line voltage and the measured line-to-line voltage spectrum are presented in Figure 3-4, where the modulator was SVM technique. The first 5 harmonics from the reference signal's spectral components have been considered for the analytical calculations, and the Bessel function run-out was set to be 10.Figure 3-5

presents the line-to-line spectrum obtained with 120^0 DPWM. Five harmonics of the reference signal were considered, the run-out of the Bessel function was also set to 10.

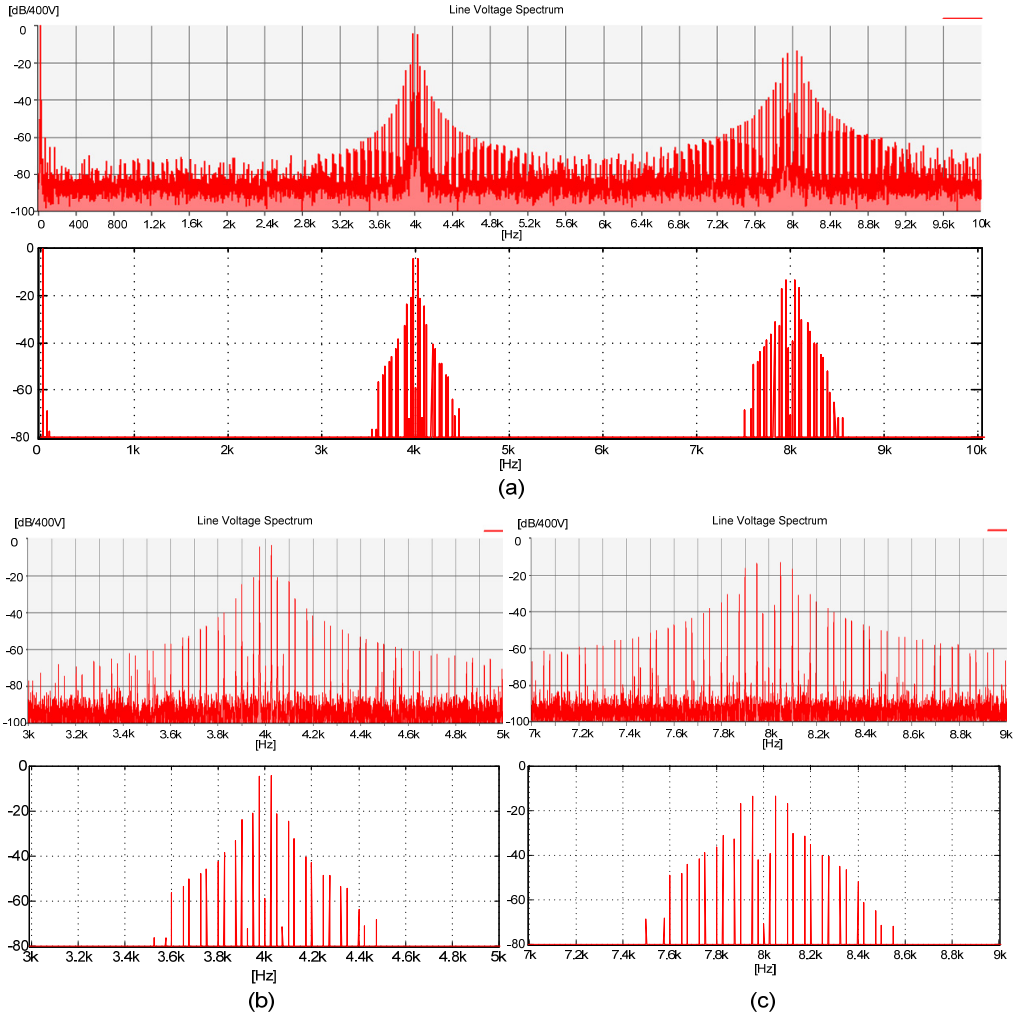

Figure 3-5 Spectra of the line-to-line voltage using 120^0 DPWM method: measured full spectra ((a), top), calculated full spectra, ((a), bottom). Subfigure (b) shows the zoom in the spectra around the switching frequency (measured ((b), top), and calculated ((b), bottom)), while Subfigure (c) shows a zoom in spectra around the double switching frequency (measured ((c), top), and calculated ((c), bottom)).

3.4 Analytical determination of the radial force spectra

In order to isolate the vibration spectral component caused by modulation from the resonances due to the complex mechanical structure of the motor, a simplified setup with no moving parts was used. The behavior of the normal force in the induction motor can be approximated with a single coil shown in Figure 3-6, as it was done similarly in [43], for a switched reluctance motor.

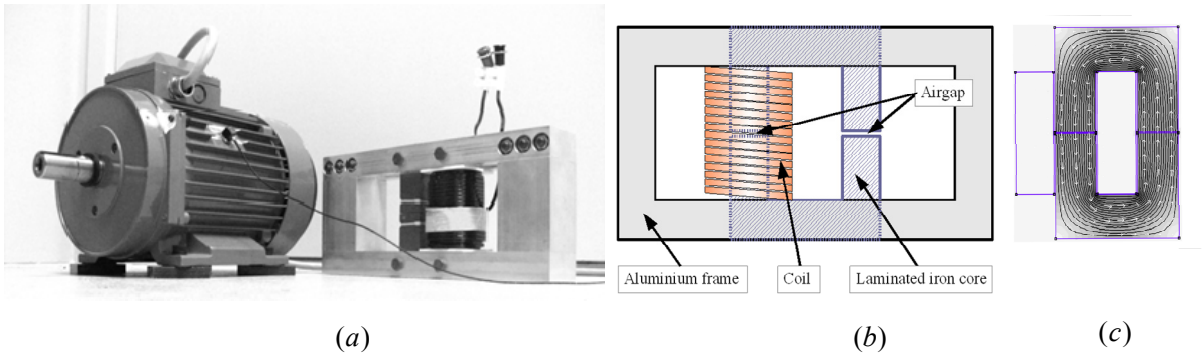

Figure 3-6 Motor and coil used for measurements (a), and two u-cores with a 0.8 mm air-gap, and a coil with 80 turns and 3 mH inductance to excite these cores, with cross-sections of 6 cm^2.(b). The acceleration sensor is placed on the aluminum frame. On (c), a result from a FEM simulation of the magnetic circuit is shown.

In order to have approximately the same spectrum for the current through the coil as in one phase of an induction motor, the coil was connected to the inverter together with two resistors as shown in Figure 3-7.

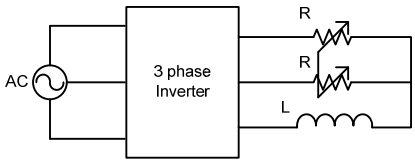

Figure 3-7 Experimental setup schematic for the coil fed by an inverter

The frequency response of this structure to the current through the coil mainly depends on the mechanical structure of the coil. This frequency response can be determined by using Random PWM (RPWM) [44]; the frequency response of the motors in Chapter 5 was measured in similar way. RPWM has the property to distribute the discrete frequency components from the current spectrum creating a spectrum close to white noise. The current with a spectrum like white noise equally excites all the frequency components, giving the response of the mechanical structure in term of vibrations. The frequency response of the vibrations to the phase current of the asynchronous motor is presented in Figure 3-8. The advantage of determining the frequency response of the mechanical structure by using measurements is that it gives a real picture about the entire mechanical system.

To calculate the normal force acting on the laminated iron core of the coil in the air gap, FEM simulation was set up as shown in Figure 3-7. Stepping through various current levels a look up table was generated. Since vibrations are caused by the acceleration of a mass respecting $F = m \cdot a$ means the force is proportional to the vibrations. Assuming that there are no resonances in the mechanical structure, the normalized force spectrum is thus equal to the normalized acceleration spectrum.

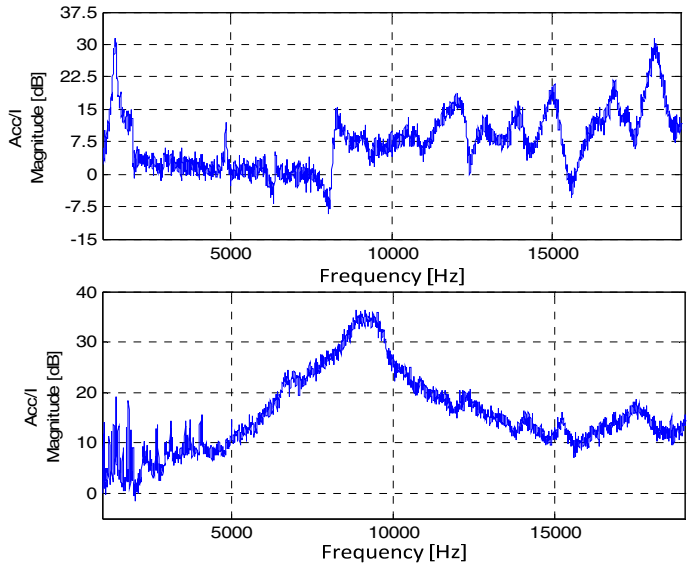

Figure 3-8 Measured transfer function between current and acceleration of the mechanical structure: in the top for the coil, in the bottom for the motor

Using equation (3.36) the analytical form of the spectrum of the normal force can be approximated. The normal force f in a not saturated coil is given by:

$$f = \frac{\psi^2}{2\mu_0 AN^2} = \frac{L^2}{2\mu_0 AN^2} \cdot i^2 = k \cdot i^2 \tag{3.37}$$

where ψ - magnetic flux, μ_0 - magnetic permeability, A - cross sectional area of the magnetic path, N - number of wire turns, L - inductance, k - constant in time;
Since from the right side of (3.37) only the current vary in function of time, the parameters can be noted as k and represented as a normalized spectrum. The flux can be expressed in function of the line voltage, ignoring nonlinearities and the phase resistances:

$$\psi(t) \simeq \int V_{ll}(t)dt \tag{3.38}$$

Expressing the flux by integrating the voltage equation (3.36) in function of time for the case when the reference signal has only cosine components:

$$\psi = 2\sum_{m=0}^{\infty}\sum_{n=-\infty}^{\infty}\left(A_{mn}\sin\left(n\frac{\pi}{3}\right)\int\cos\left(\left(m\omega_c + n\omega_0\right)t - n\frac{\pi}{2} + \frac{\pi}{2}\right)dt\right) \tag{3.39}$$

By substituting:

$$A^*_{mn} = 2A_{mn}\sin\left(n\frac{\pi}{3}\right); \omega_{mn} = \left(m\omega_c + n\omega_0\right); \xi_1 = -n\frac{\pi}{2} + \frac{\pi}{2}; \tag{3.40}$$

And integrating (3.39), results:

$$\psi = \sum_{m=0}^{\infty}\sum_{n=-\infty}^{\infty}\left(\frac{A^*_{mn}}{\omega_{mn}}\sin\left(\omega_{mn}t + \xi_1\right)\right) \tag{3.41}$$

Substituting the flux equation (3.39) in (3.37), the force equation becomes:

$$F = \frac{\psi^2}{2\mu AN^2} = \frac{1}{2\mu AN^2}\left(\sum_{m=0}^{\infty}\sum_{n=-\infty}^{\infty}\frac{A^*_{mn}}{\omega_{mn}}\sin\left(\omega_{mn}t + \xi_1\right)\right)^2 \tag{3.42}$$

By noting with N, and M the considered number of harmonics, the square of a double sum can be expanded as:

$$\left(\sum_{m=0}^{M}\sum_{n=-N}^{N}\left(Z_{mn}\right)\right)^2=\sum_{m=0}^{M}\sum_{n=-N}^{N}\left(\left(Z_{mn}\right)^2\right)+2\sum_{m=0}^{M}\sum_{n=-N}^{N}\sum_{i=0}^{m-1}\sum_{j=-N}^{N}\left(Z_{mn}\cdot Z_{ij}\right)+2\sum_{m=0}^{M}\sum_{n=-N}^{N}\sum_{j=n+1}^{N}\left(Z_{mn}\cdot Z_{mj}\right)=$$
$$\sum_{m=0}^{M}\sum_{n=-N}^{N}\left(\left(Z_{mn}\right)^2+2\sum_{i=0}^{m-1}\sum_{j=-N}^{N}\left(Z_{mn}\cdot Z_{ij}\right)+2\sum_{j=n+1}^{N}\left(Z_{mn}\cdot Z_{mj}\right)\right) \tag{3.43}$$

Substituting (3.43) in (3.42) becomes:

$$F=\frac{1}{2\mu AN^2}\sum_{m=0}^{M}\sum_{n=-N}^{N}\left(\begin{array}{l}\frac{1}{\omega_{mn}{}^2}\left(A_{mn}^{*\,2}\sin^2\left(\omega_{mn}t+\xi_1\right)\right)+\\ \sum_{i=0}^{m-1}\sum_{j=-N}^{N}\frac{2A_{mn}^{*}A_{ij}^{*}}{\omega_{mn}\omega_{ij}}\left(\sin\left(\omega_{mn}t+\xi_1\right)\sin\left(\omega_{ij}t+\xi_1\right)\right)\\ \sum_{j=n+1}^{N}\frac{2A_{mn}^{*}A_{mj}^{*}}{\omega_{mn}\omega_{mj}}\left(\sin\left(\omega_{mn}t+\xi_1\right)\sin\left(\omega_{mj}t+\xi_1\right)\right)\end{array}\right) \tag{3.44}$$

Eq. (3.44) can be rewritten by using trigonometric identities to:

$$F=\frac{1}{4\mu AN^2}\sum_{m=0}^{M}\sum_{n=-N}^{N}\left(\begin{array}{l}\frac{A_{mn}^{*\,2}}{\omega_{mn}{}^2}\left(\left(1+\cos\left(2\omega_{mn}t-n\pi+\pi\right)\right)\right)+\\ \sum_{i=0}^{m-1}\sum_{j=-N}^{N}\frac{A_{mn}^{*}A_{ij}^{*}A}{\omega_{mn}\omega_{ij}}\left(\cos\left(\left(\omega_{mn}-\omega_{ij}\right)t+\varsigma\right)\right)\\ \sum_{j=n+1}^{N}\frac{A_{mn}^{*}A_{mj}^{*}A}{\omega_{mn}\omega_{mj}}\left(\cos\left(\left(\omega_{mn}-\omega_{mj}\right)t+\varsigma\right)\right)\end{array}\right) \tag{3.45}$$

$$where\ \varsigma=arctg\left(\frac{\sin\left(-n\pi+\pi\right)}{1+\cos\left(-n\pi+\pi\right)}\right);A=4\left(1+\cos^2\left(-n\pi+\pi\right)\right)$$

The force equation for those modulation methods where the reference signal contains multiple frequency components can be deduced in similar way.

For experimental tests, the 2.2 kW asynchronous motor and the coil presented in Figure 3-7, was used, driven by a 2.2 kW Danfoss FC302 VLT three phase inverter. The current and vibrations on the motor/coil frame were measured with a Bruel and Kjaer Pulse Multi-analyzer type 3560. Asymmetrical regular sampled sine-triangular modulation was used for the measurements. The switching frequency was set to 5 kHz, while the fundamental frequency of the current was 35 Hz. Figure 3-9 presents the results of the vibration spectra obtained by different methods: calculated analytically, using a current to force look-up table and by measuring the vibration on the frame of the coil. To compare the calculated and measured spectra, the frequency response of the mechanical structure of the coil is shown in Figure 3-9 (c) and (d).

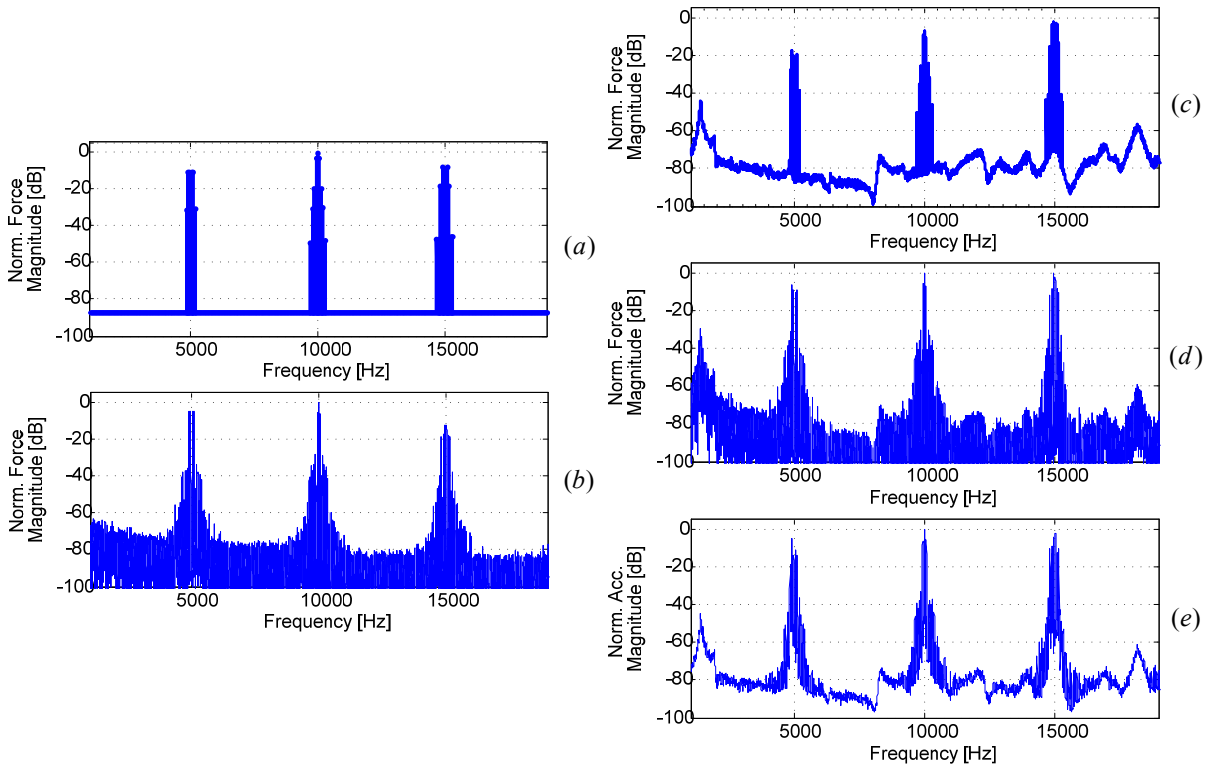

Figure 3-9 The normalized vibration spectra on the frame of the coil: analytical calculated spectra (a), spectra derived using the measured current to force look-up table (b), analytical calculated spectra adjusted with the transfer function of the mechanical structure (c), Simulation using force look-up table adjusted with the transfer function of the mechanical structure (d), and measured vibration spectra (e)

To show the correlation between the calculated and measured spectra, Figure 3-10 presents a zoom in the spectra around 5 and 10 kHz, respectively. Figure 3-11 presents the calculated and measured spectra for the asynchronous motor. For the spectra given by the analytical calculations (Figure 3-11 and Figure 3-12), the frequency response of vibrations to the motor current has been considered. The prediction of the force spectra in the asynchronous motor using (3.37) is shown in Figure 3-11 (b). Using (3.37) with the measured phase current from the rotating asynchronous motor as input, the equivalent force in the air gap of an imaginary coil was calculated and normalized.

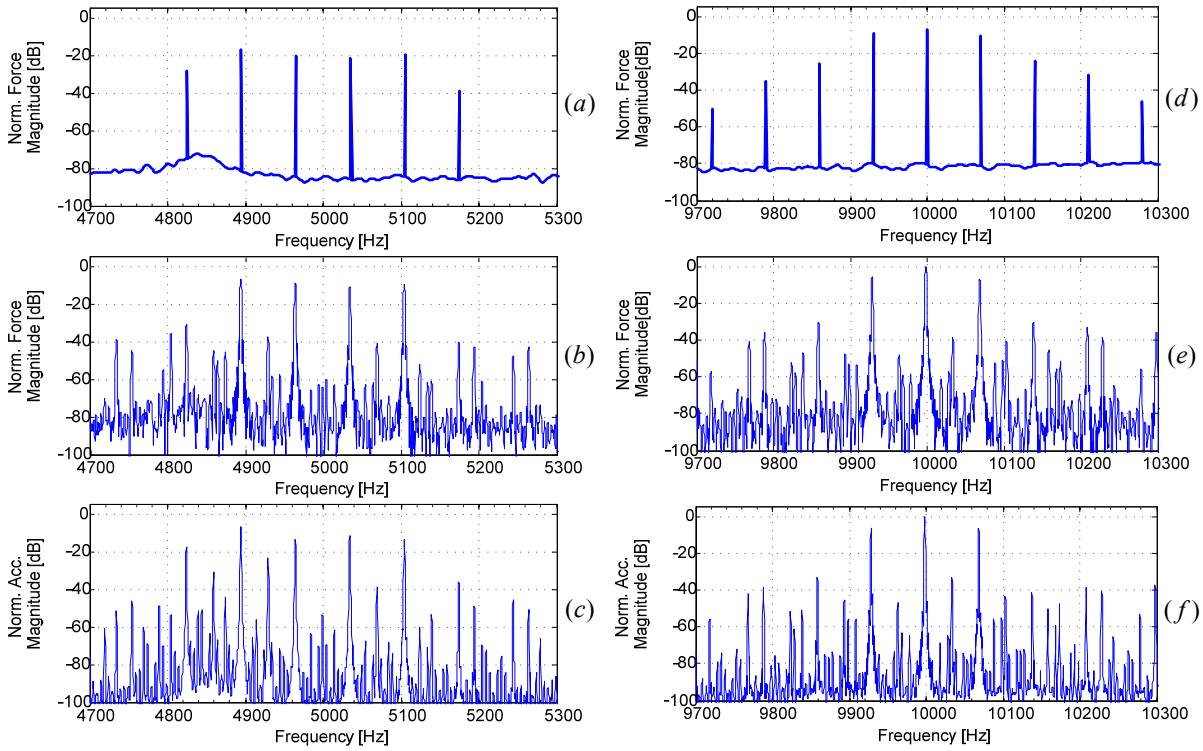

Figure 3-10 Zoom in vibration spectra of the coil: analytically calculated spectra at 5 kHz (a), vibration spectra using force look-up table at 5kHz (b), measured vibration spectra at 5kHz (c), analytically calculated spectra at 10kHz (d), vibration spectra using force look-up table at 10kHz (e), and measured vibration spectra at 10kHz (f)

The spectrum of the force from Figure 3-11(b) was calculated using DFT with a Hanning windowing function, the same as was used in vibration measurements on the motor shell. As it can be seen on Figure 3-11 and Figure 3-12, the spectra predicted by the analytical solution and by the FEM model show good agreement with the measured acceleration on the shell of the induction motor. Although the mechanical structure of the motor is completely different from the structure of the coil used for FEM model, the spectra of the vibration around the switching frequency shows very good match.

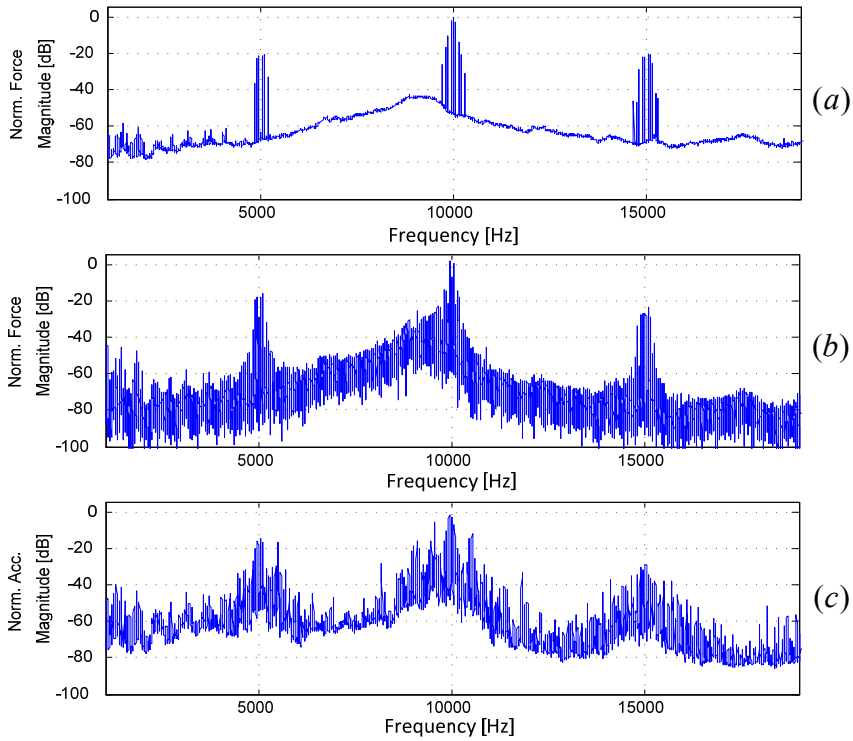

Figure 3-11 The normalized spectra of vibrations on the motor shell: (a) analytically calculated spectra, (b) vibration spectra using force look-up table, (c) measured vibration spectra

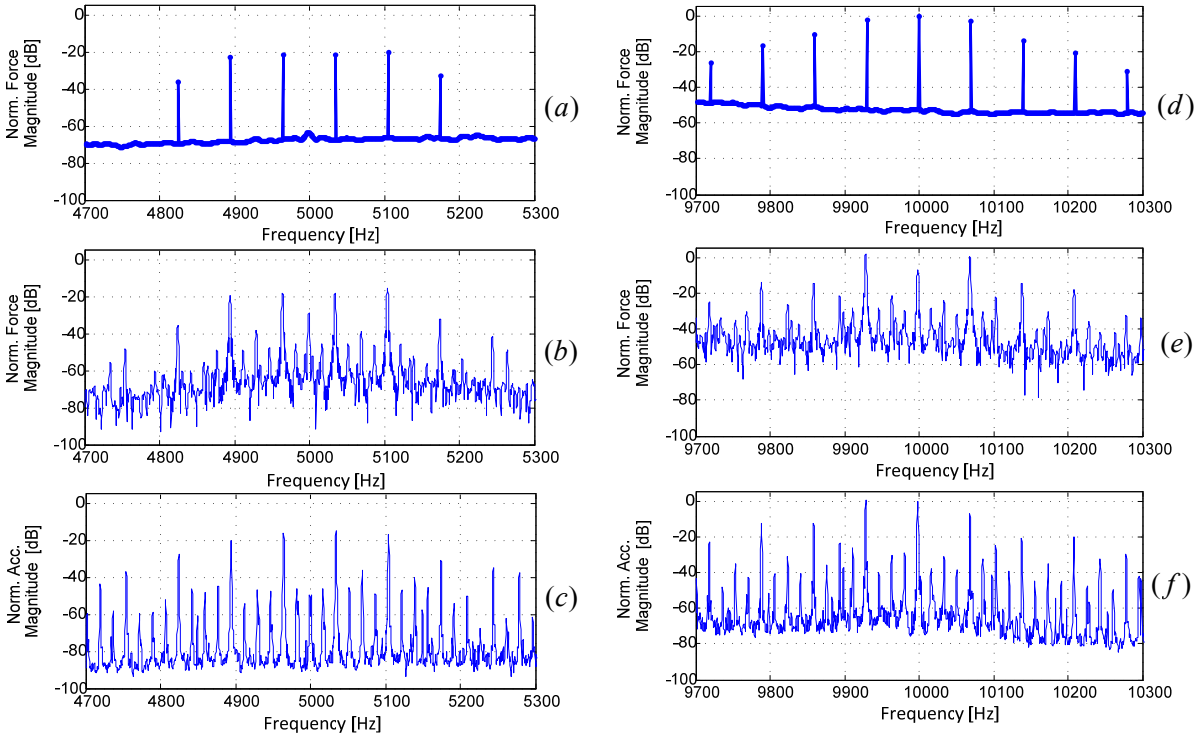

Figure 3-12 Zoom in vibration spectra on the motor shell: analytically calculated spectra at 5 kHz (a), vibration spectra using force look-up table at 5 kHz (b), measured vibration spectra at 5 kHz (c), analytically calculated spectra at 10kHz (d), vibration spectra using force look-up table at 10kHz (e), and measured vibration spectra at 10kHz (f)

3.5 Summary

A unified analytical method for theoretical calculation of the harmonic components of the phase, line-to-line voltage and the normal force has been proposed and presented in this chapter. One single equation is derived, which can be used for prediction of the spectra of any carrier-based modulation method. The line-to-line voltage spectrum determined by the analytical calculations has been compared with the experimental measurements showing excellent agreement for all the considered modulation techniques, such as SVM, 120^0 DPWM. It can be concluded that every frequency component present in the spectrum of the phase voltage introduces a well defined group of harmonic components (in amplitude and in frequency) into the line-to-line voltage spectra.

The measurements show that the dominant spectral components in the vibrations of an asynchronous motor are mainly caused by the modulation, which agrees well with the results obtained from the analytical solution and simulations based on the current to force look-up table. The advantage of the analytical method is that it allows isolating spectral components caused by the PWM even in mechanically complex drive system. The method can be applied to other than sine-triangular PWM strategies to evaluate their performance in terms of radial force. The experiments show that vibrations caused by the PWM are dominant irrespective if the PWM was applied to the coil or the induction motor.

Chapter 4

Random Pulse Width Modulation

In the first part of the chapter the random carrier frequency PWM methods with their advantages and disadvantages are presented. The second part presents the fixed carrier random PWM modulation methods.

4.1 Introduction

The concept of random PWM is mainly related to acoustic and electromagnetic noise generated by an inverter controlled electric drive. As it was presented in the previous chapter, the carrier based PWM methods have a well defined line-to-line and phase voltage spectrum, whit a group of harmonics around the multiples of the switching frequency. Similar group of harmonics appear in the motor current spectra, current which generates a radial force. The acoustic noise is mainly generated by the radial force [37, 45], which transforms the surface of the stator in a membrane, similar with the membrane of a loudspeaker. Finally, the acoustic spectra generated by the motor will contain similar discrete components in its spectra as the line-to-line voltage, mainly caused by the switching frequency. Being the optimal switching frequency from efficiency point of view at around 3-4kHz (in case of a 2.2kW drive) [1], a strong whistling noise in the frequency range where the human ear is the most sensitive will be generated. The random PWM technique does not solve totally the acoustical problems of the electrical drives, but it gives a cost effective solution to eliminate the tonality of generated acoustic noise. The fundamental idea behind RPWM is to vary the switching frequency in random manner, spreading in this way the discrete components from the acoustic spectra. As a result of randomly varying switching frequency, the whistling noise is transformed into a white noise, said more pleasant for the human ear [44]. It is important to mention here that the usage of RPWM technique will not reduce the acoustic noise generated by the motor; rather, slightly increases the sound pressure level of the acoustic noise.

From the switching frequency point of view the RPWM can mainly be classified as: Random Carrier Frequency PWM (RCF-PWM) [46], and Fixed Carrier Frequency Random PWM (FCF-RPWM) [47]. Usually the switching period gives the time base for the motor control algorithm; therefore randomly varying the switching period creates difficulties in closed loop applications. The limitation of the number of the switching frequencies can be a solution [48]. An idea to maintain a fixed update frequency is presented in [49], where a random delay is inserted on such a way to maintain the resultant switching period constant (a long delay in one sampling cycle is followed by a short delay in the next cycle).The FCF-RPWM methods are easy to synchronize with the control algorithm. However, other problems like current sampling, calculation overhead and spreading effectiveness appears.

In this chapter the RCF-PWM is analyzed first, which is followed by the analysis of the FCF- PWM.

4.2 Random Carrier Frequency PWM

RCF-PWM method is based on random selection of the carrier frequency for each carrier period [9, 46, 50, 51]. The only requirement for RCF-PWM is to maintain the volt-second balance during a carrier period, ensuring that the fundamental frequency component is not affected by the randomization. Figure 4-1 *(b)* presents three consecutive modulation periods where the time-length of each period (T_1, T_2, and T_3) was selected randomly. During a modulation period from Figure 4-1 *(b),* two similar resultant voltage vectors can be generated. Figure 4-1 *(a)* presents each instance of the applied voltage vectors to the motor in *d-q* plane, vectors which were generated with different switching frequencies.

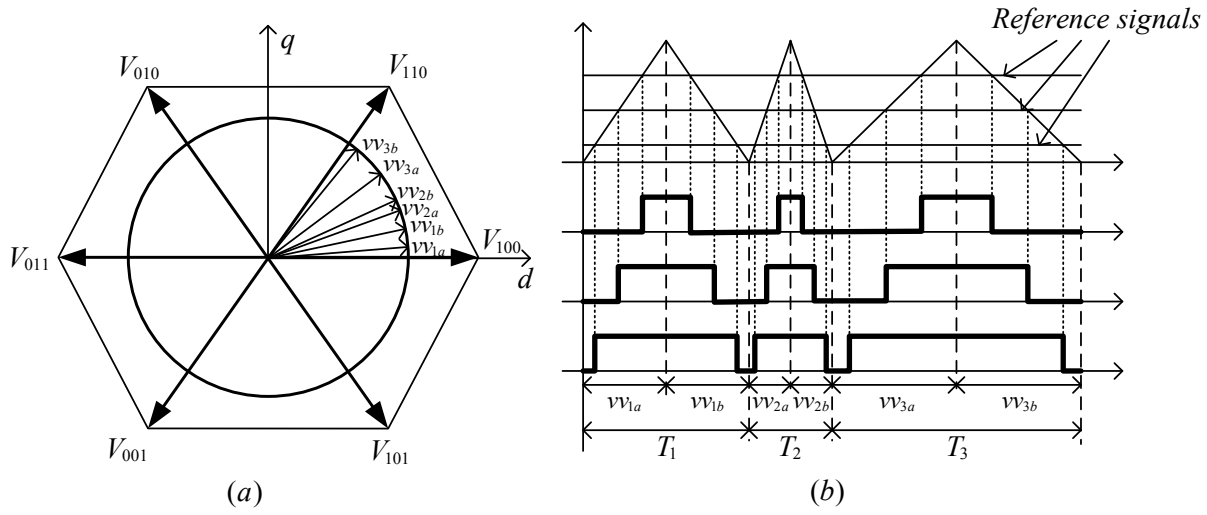

Figure 4-1 SVM representation of the generated voltage vector (a), and pulse generation mechanism using RCF-PWM (b)

The upper and lower limits for the pool from which the actual value for the switching frequency is selected, is mainly given by the hardware parameters of the entire drive. The very high switching frequency (above 10kHz) causes high switching losses in the inverter, the low switching frequency (under 2kHz) will increase the motor current ripple creating unacceptable losses on the motor side. Having the optimal switching frequency around 3-4 kHz for a drive in the kilo-watt range, a good spread effect of the discrete components from the acoustic spectra can be achieved by setting a pool of ± 1 kHz around the desired average switching frequency. Figure 4-2 and Figure 4-3 present the spectrum of the line-to-line voltage, motor current, vibration on the motor shell and the acoustic noise by using SVM method and RCF-PWM method. The average switching frequency was selected to be 4 kHz, the pool from where the actual switching frequency is selected becoming 3-5 kHz.

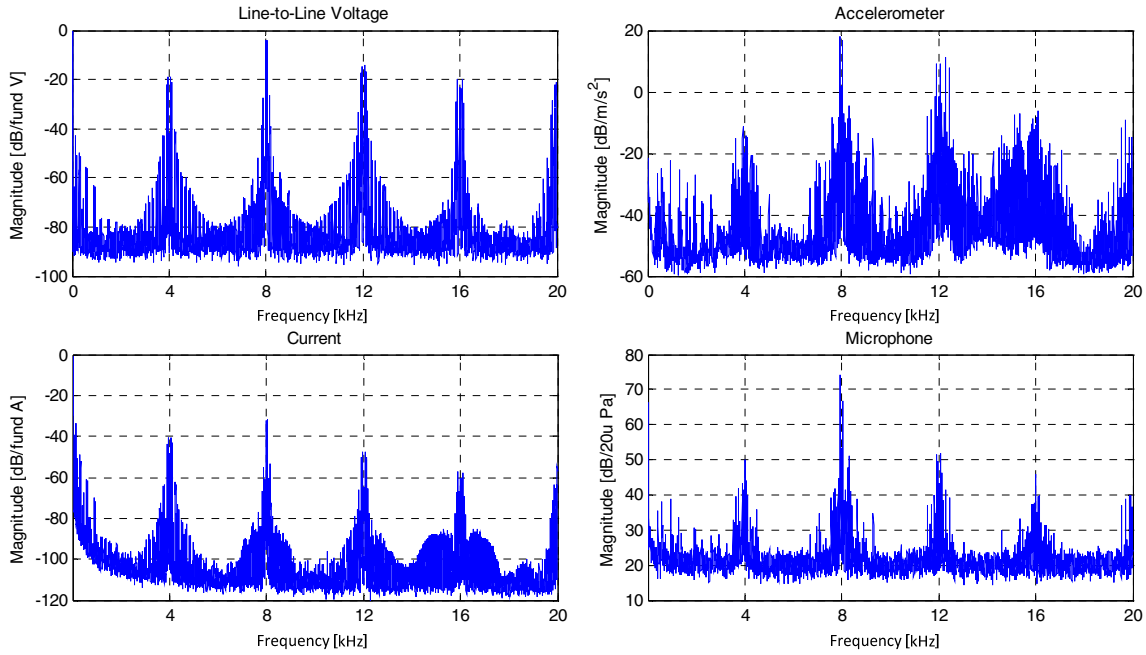

Figure 4-2 Measured spectrum of the line-to-line voltage (top-left), vibrations on the motor shell (top-right), motor current (bottom-left), and acoustic noise (bottom-right), by using SVM modulation method

From sound pressure level point of view, the SVM is slightly better (64dBA), compared to RCF-RPWM where the sound pressure level was measured to be 66dBA. As it is shown in Figure 4-3, the distribution of the frequency components in case of SVM is concentrated around the switching frequency component and its upper harmonics (mainly around the first upper harmonic) resulting a strong whistling. In case of RCF-PWM the peak amplitude is reduced with around 20db and is spread to a wider range.

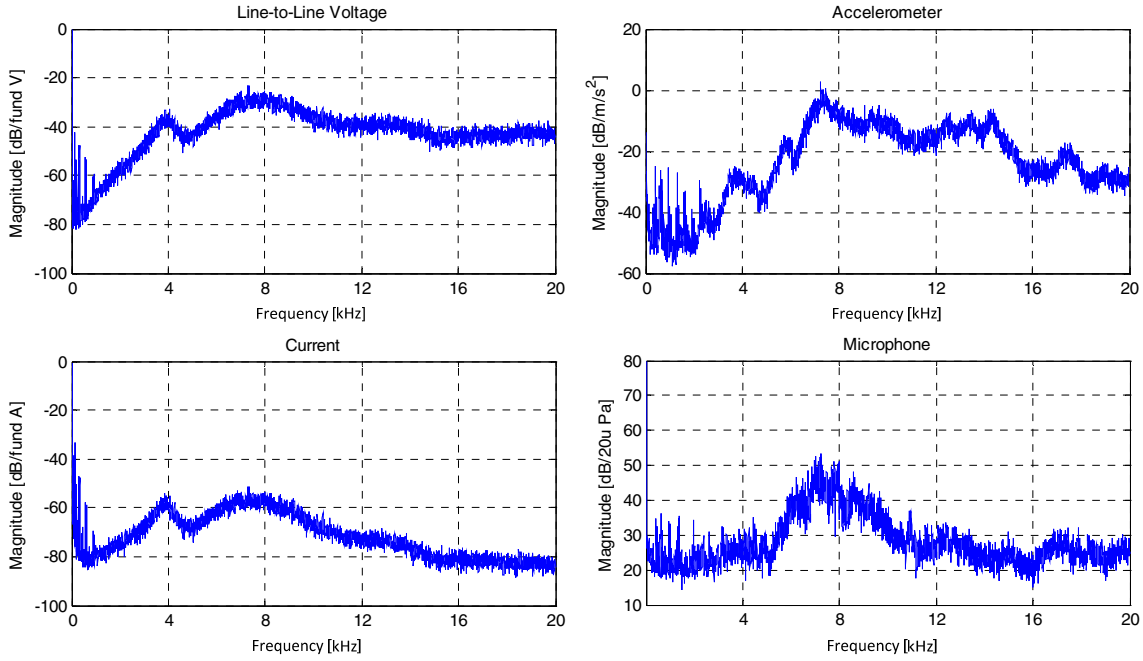

Figure 4-3 Measured spectrum of the line-to-line voltage (top-left), vibrations on the motor shell (top-right), motor current (bottom-left), and acoustic noise (bottom-right), by using randomly two switching frequencies (3.5 and 4.5kHz)Measured spectrum of the vibrations on the motor shell (left), and acoustic noise (right), RCF-PWM modulation method

By varying the switching frequency in such a way to play the musical notes from a melody, the whistling noise can be transformed to music [52, 53]. However, the music effect is usually less than satisfactory.

The RCF-RPWM method work very well in open loop applications, but it gives difficulties for implementation in closed loop applications like field-oriented control [54]. Usually the control algorithm is synchronized with the switching frequency, which means every time the switching frequency is changed the sample time used in the control algorithm, will have to be modified as well. As a consequence the parameters for the controllers, filters, observers etc. will have to be recalculated every time the switching frequency is modified. The recalculation of these parameters gives a computational overhead for the digital implementation. The limitation of the number of switching frequencies together with the usage of off-line calculated parameters can be a solution [48, 55]. However, by decreasing the number of possible switching frequency values it will decrease the spread effect under the discrete components from the acoustic spectra. By randomly selecting one from two switching frequencies for every carrier period, has the advantage of using only two sets of off-line calculated parameters. For the experimental results (Figure 4-4), the two switching frequencies were selected in such a way to have the same number of switching per second as in case of SVM at 4 kHz. The two selected frequencies were 3.5 kHz and 4.5 kHz. By using this modulation method, the discrete components are eliminated from the vibration spectra; however, they are still present in the acoustic spectra around the average switching frequency (4

kHz). The main conclusion is that the acoustic noise generated by two frequencies is very close to the acoustic noise generated by RCF-PWM.

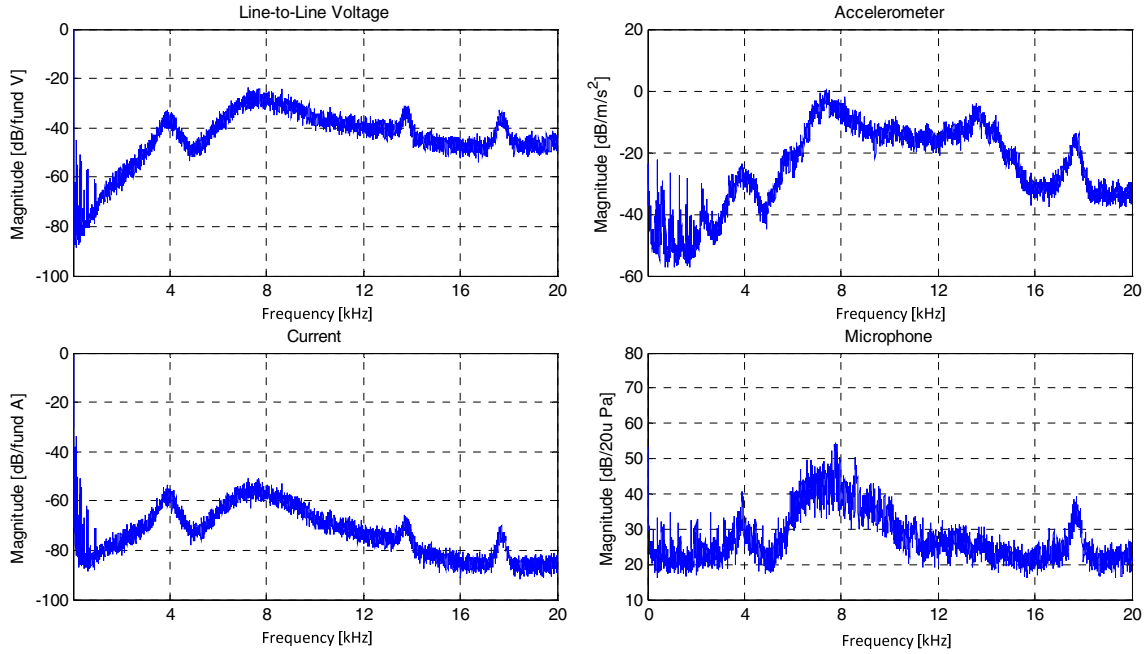

Figure 4-4 Measured spectrum of the line-to-line voltage (top-left), vibrations on the motor shell (top-right), motor current (bottom-left), and acoustic noise (bottom-right), by using randomly two switching frequencies (3.5 and 4.5kHz)

The creation of different sequences for several carrier periods where few switching frequencies are altering, is proposed in [56]. According to the presented idea, for example in case of two carrier periods with time-lengths of T_1 and T_2, a sequence of 6 carrier periods like T_1, T_2, T_2, T_1, T_1, T_2 can be set up. This pattern of the 6 carrier periods is repeated infinitely. This modulation scheme was tested in practice; the spectrum of the line-to-line voltage, motor current, vibration and acoustic noise is presented in Figure 4-5. The discrete components are not totally disappeared from the acoustic spectrum, but many new frequency components are introduced in the spectrum which decreases the tonality of the sound. Compared to the previously presented method, where one from the two switching frequency are chosen randomly, this method has no advantage.

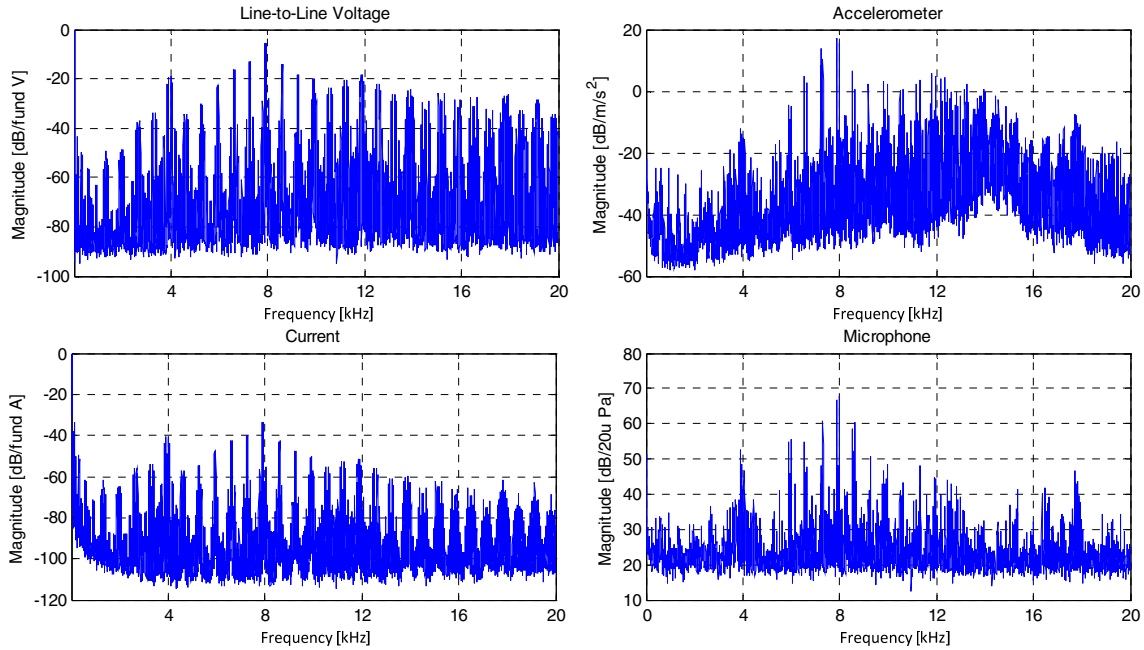

Figure 4-5 Measured spectrum of the line-to-line voltage (top-left), vibrations on the motor shell (top-right), motor current (bottom-left), and acoustic noise (bottom-right), by using two switching frequencies (3.5 and 4.5kHz) on a scheme T_1, T_2, T_2, T_1, T_1, T_2

An alternative solution to decrease the tonality of the acoustic noise generated by inverter controlled electrical motors is to use the FCF-RPWM, which will be discussed in the next section.

4.3 Fixed Carrier Frequency Random PWM

As mentioned in the introduction, the FCF-RPWM methods are preferable due to their easy implementation in closed-loop application, even to retrofit in a prior implemented control algorithm. The FCF-RPWM methods are based on the fact that the position of the active vector region during a carrier period does not influence the fundamental frequency component.

In case of a three phase voltage source inverter (topology presented in section 2.2), where the star point is not connected to the neutral point, randomization of the pulse position cannot be done independently for each phase leg. The current from one phase of the motor only partially depends on the given phase voltage; the motor current is created by the line-to-line voltage. In space vector representation, each connection between the three phase inductivities creates a fixed voltage vector in the *d-q* plane like presented in section 2.3.1. The reposition of the pulses has to be done in such a way to not introduce unwanted voltage vectors. For example, Figure 4-6 presents the situation where the position of a pulse on leg *c* is modified. However, even if the average phase voltage on the leg is not changed, the reposition will introduce a new voltage vector V_{101} and, as a consequence, the resultant voltage vector will not be

identical with the reference voltage vector. This means that, by repositioning the pulse on one phase leg, will affect the fundamental frequency component of the phase current. The distorted fundamental frequency affects the stability of the drive, introducing current and torque ripple.

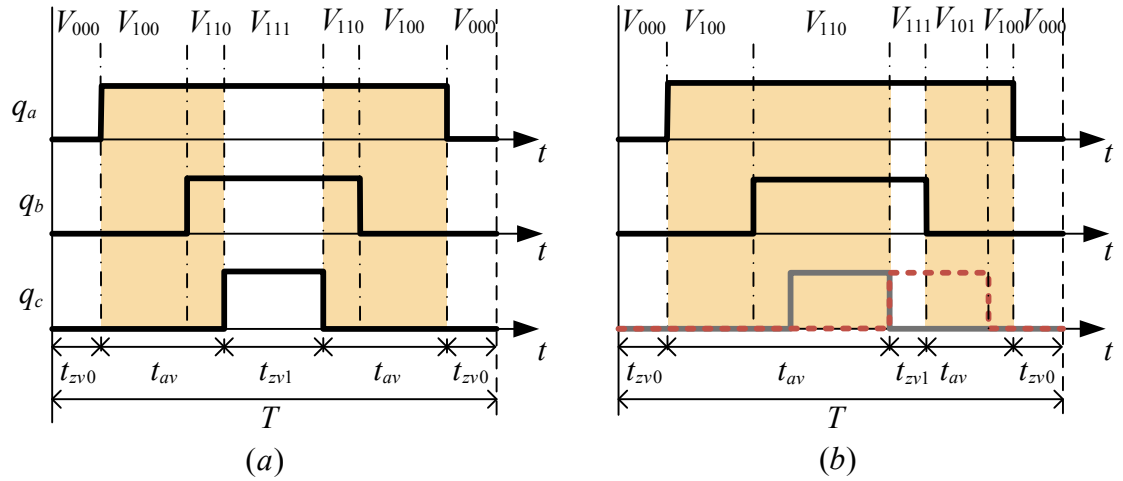

Figure 4-6 Pulse placement during a modulation period using SVM (a), and reposition of the pulse on leg c (b)

As a conclusion, there are two requirements for FCF-RPWM that have to be fulfilled in order to not distort the fundamental of the motor current:

1) the same average voltage space vector has to be generated the in *d-q* plane as it was before randomization
2) the update frequency has to be constant.

4.3.1 Random distribution of the zero sequence vectors

A good acoustic performance can be achieved by randomizing the position of the generated PWM pulses, referred in literature as random pulse position PWM (RPP-PWM) [21, 47, 57]. As presented in Chapter 2, a modulation period can be split in two main regions: region when the load takes the energy from the DC-link (active vectors are generated highlighted in Figure 4-7), and the region when the three legs of the load are connected to the plus or minus of the DC rail (zero vector is generated, no energy is taken from the DC-link). During the active region, two active vectors are usually generated, except the case when the desired reference voltage vector $\bar{U}_s$ is alienated with one of the active vectors. The position of a voltage vector $\bar{U}_s$ in *d-q* plane is defined by the ratio between the applied time-length for the two adjacent active vectors (t_{av1}/t_{av2}). The zero sequence vectors are responsible to reduce the length of the resultant voltage vector $\bar{U}_s$.

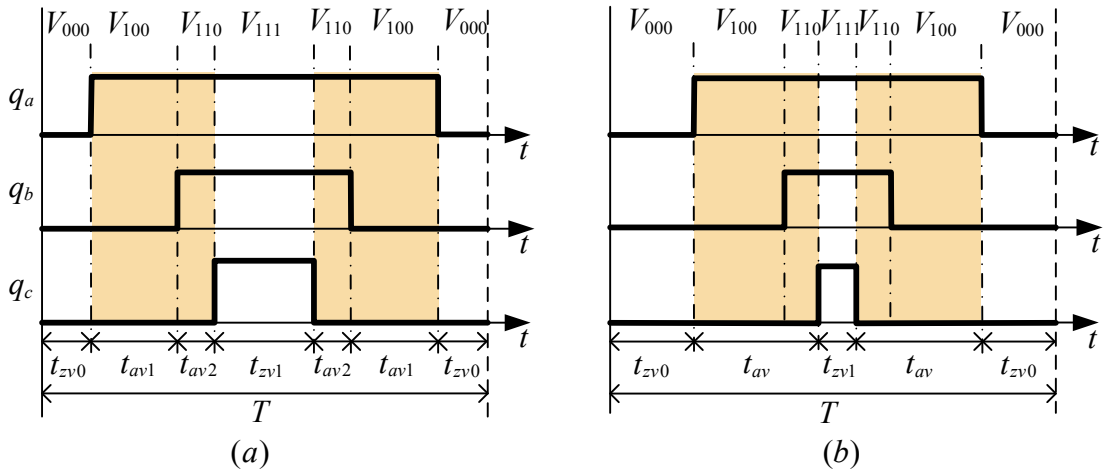

Figure 4-7 Pulse placement during a modulation period when t_{zv0}=t_{zv1} (a), and reposition of the PWM pulses (b)

The choice of a random position for the active vector region, during a modulation period, will not affect the resultant voltage vector $\bar{U}_s$. The random pulse position will introduce a white noise in the acoustic spectra which decreases the tonality from the acoustic noise. The modern modulation methods presented in section 2.3.3 are based on the same principle of redistribution of the zero sequence vectors. As it was presented in [25] and it can be concluded from Chapter 3 as well, each frequency component from the phase voltage spectrum inserts a well defined (in amplitude and frequency) group of harmonic components into the line-to-line voltage, motor current and vibration spectrum. Insertion of these new components into the line-to-line, current and vibration spectra, can reduce the amplitude of the carrier harmonic components, but they will not disappear totally like it is shown for different speeds in Figure 4-8, Figure 4-9, and Figure 4-10. This statement is mathematically proved in Chapter 3.

By increasing the modulation index, the active vector region is extended, and the zero sequence vector regions are decreased. This means that less room remains for the possible pulse positions, decreasing the effectiveness of the randomization for high modulation index, as it is shown in Figure 4-10. With other words, the maximum amplitude of the signal injected in the *cmv* without distorting the fundamental signal is reduced. The mathematical solution for calculation of the line-to-line spectra presented in Chapter 3 shows that the amplitude of each spectral component from the *cmv* is proportional with the amplitude of the group of harmonics created in the line-to-line voltage. Similar conclusion is drawn in [47], where several FCF-RPWM methods are analyzed and compared.

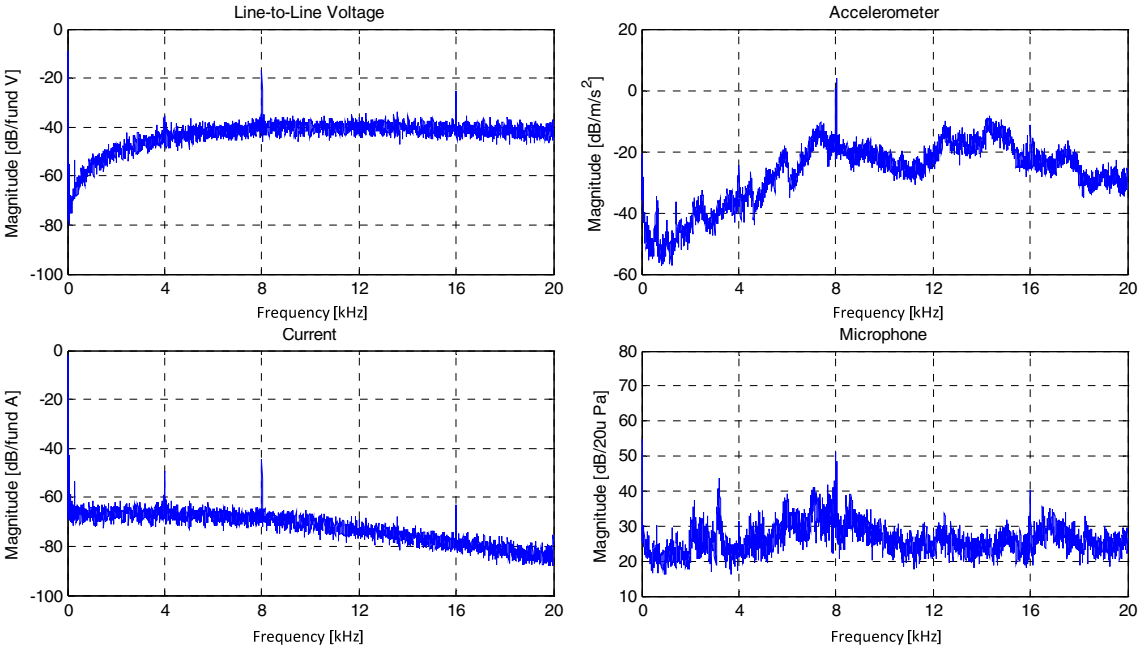

Figure 4-8 Measured spectrum of the line-to-line voltage (top-left), vibrations on the motor shell (top-right), motor current (bottom-left), and acoustic noise (bottom-right), by using RPP-PWM at 10Hz fundamental frequency (modulation index 0.2) and switching frequency of 4kHz

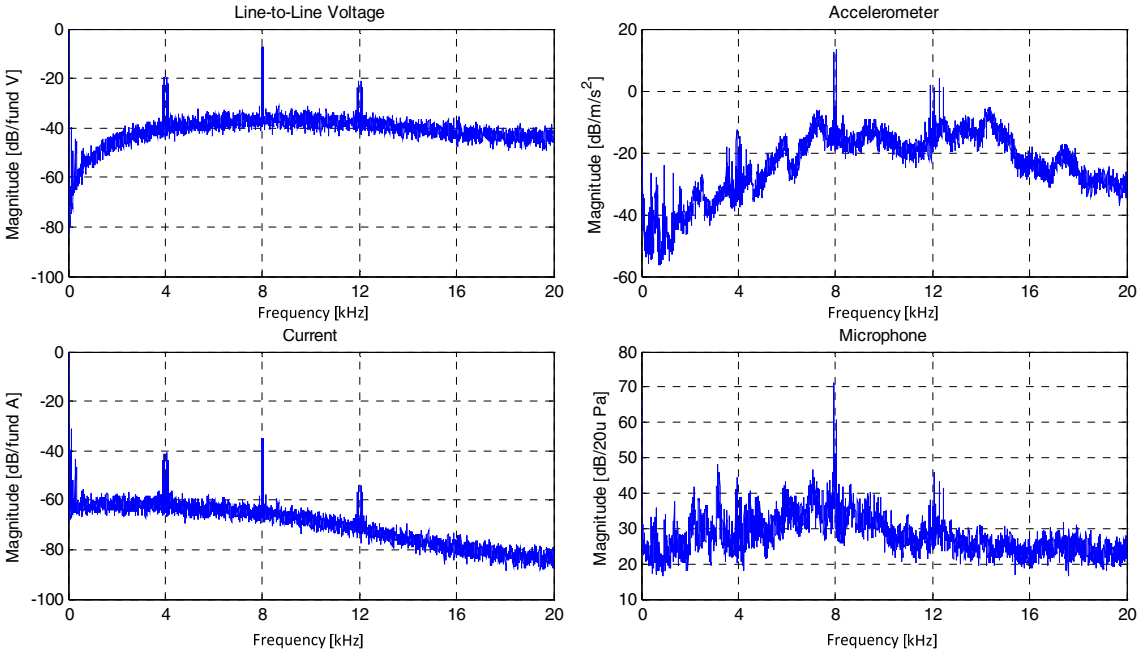

Figure 4-9 Measured spectrum of the line-to-line voltage (top-left), vibrations on the motor shell (top-right), motor current (bottom-left), and acoustic noise (bottom-right), by using RPP-PWM at 25Hz fundamental frequency (modulation index 0.5) and switching frequency of 4kHz

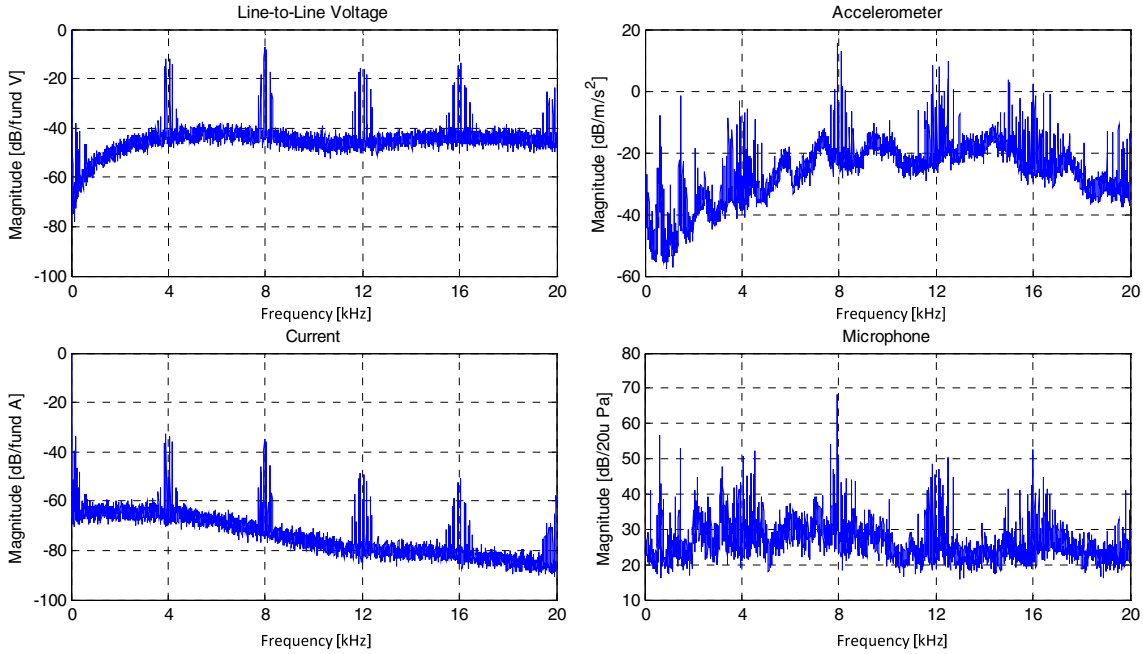

Figure 4-10 Measured spectrum of the line-to-line voltage (top-left), vibrations on the motor shell (top-right), motor current (bottom-left), and acoustic noise (bottom-right), by using RPP-PWM at 40Hz fundamental frequency (modulation index 0.8) and switching frequency of 4kHz

The proposed new FCF-RPWM method, where the spectra of the line-to-line voltage can be shaped, is presented in [58]. The method is based on reposition of the active vector region, (same theory is behind the RPP-PWM method), with the difference that the amplitude and frequency of the signal injected in *cmv* is controlled. As concluded in section 3.3, every frequency component from the *cmv* introduces a well defined set of harmonics into the spectrum of the line-to-line spectra. Having control on the amplitude and frequency of the harmonics injected into the *cmv*, the line-to-line voltage spectrum can be shaped as desired. The spectrum of the line-to-line voltage presented in Figure 4-11 (b) was obtained by randomly varying the frequency of the injected sinusoidal signal in the range of 500-600Hz and 1-1.5kHz. The amplitude of the injected sinusoidal signal corresponding to the lower frequency range was set four times lower than that of the one corresponding to the higher frequency range.

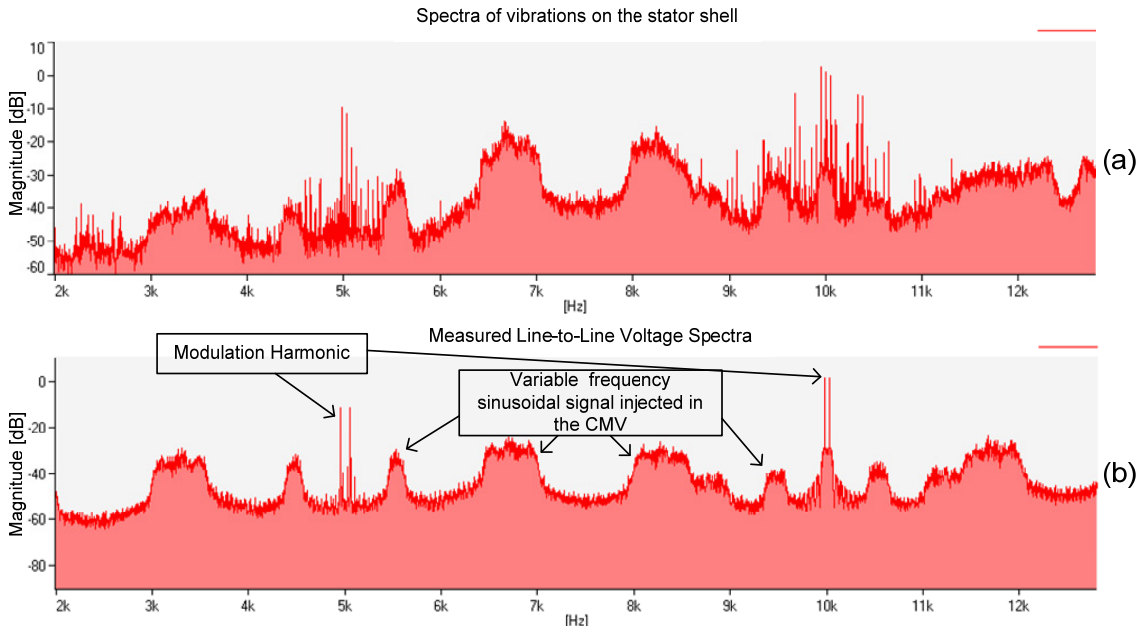

Figure 4-11 Measured spectra of vibrations on the stator shell (a), and l-l voltage using sine wave injection in cmv with randomly selected frequency (b); the frequencies were selected from two defined ranges

As a consequence, the vibration spectra will have similar shape as the line-to-line spectra, shown in the measured vibration spectra from Figure 4-11. A limitation of the method, valid for RPP-PWM, is that the maximum amplitude of the injected sinusoidal signal is inversely proportional to the modulation index. At high modulation index, the time length of the zero vectors is small; in fact the zero-state vectors can even disappear, which results in limited range for replacement of the active vectors.

The digital implementation of the modulator in commercial microcontrollers is usually done by a hardware PWM unit, which was earlier presented in section 2.4. The digital implementation limits the possible position of the active vector region in a modulation period. During an up- or down-counting period (T_{rising} or $T_{falling}$ from Figure 4-12) the switching function $q_{a,b,c}$ can change its state only once; the consequence is that the active region cannot exceed the up- or down-counting period. The reposition of the active vector region can be easily done after the duty ratio is transformed to compare values by adding or subtracting an offset (which value is smaller than half of the time-length of the zero sequence vectors in counter time-base number) to the three compare values.

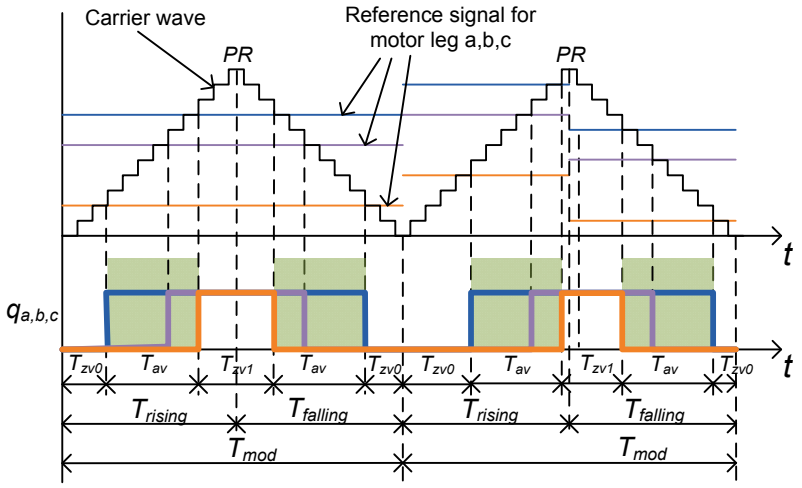

Figure 4-12 Digital implementation of RPP-PWM

4.3.2 Proposed Asymmetric Carrier Random PWM

In the traditional modulation methods like SVM the time-length spent for the up counting mode (T_{rising}) is equal with the time-length spent for the down counting mode ($T_{falling}$) as it is shown in the first modulation period from Figure 4-13.

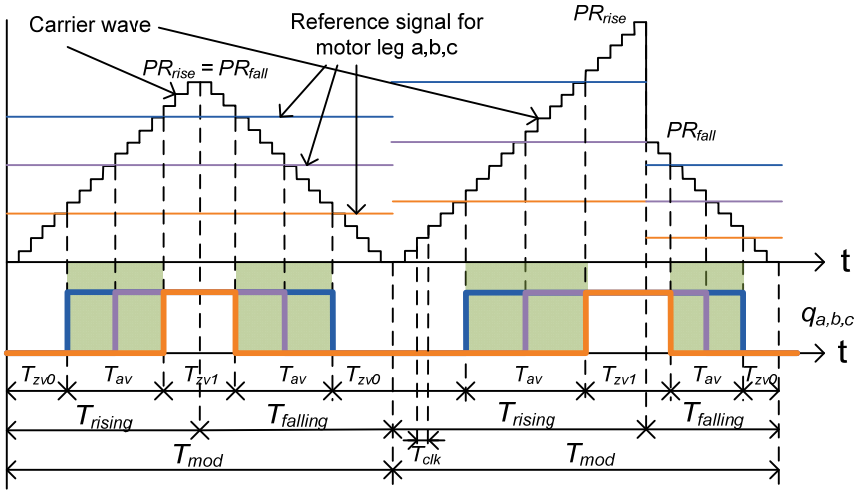

Figure 4-13 PWM carrier waveforms: first modulation period symmetrical carrier wave, in the second modulation period the asymmetric carrier wave

By changing the ratio between the T_{rising} and $T_{falling}$, the voltage vectors generated in the first and the second modulation period will be similar in position and amplitude; the difference is that the resultant voltage vector is created with different switching frequency. Generating the same voltage vectors after randomization as it was before fulfills the second requirement for FCF-RPWM. To fulfill the first requirement for FCF-RPWM the distribution of time-length between the first and second part of the modulation (T_{rising}, $T_{falling}$) is done such that to maintain the modulation period T_{mod}

constant. The following equation has to be fulfilled in order to maintain constant modulation period:

$$T_{mod} = T_{rising} + T_{falling} = constant = \frac{1}{f_{sw}} \tag{4.1}$$

where T_{mod} is the modulation period, T_{rising} is the time-length where the counter is counting up, $T_{falling}$ is the time-length where the counter counts down, and f_{sw} is the switching frequency.

The second modulation period from Figure 4-13 presents the asymmetrical carrier waveform, where the modulation period (T_{mod}) is maintained constant but the distribution of the time-length between T_{rising} and $T_{falling}$ is not equal. Similar results should be obtained by using slope modulation [59-61]. However, that is difficult to implement in a digital environment due to the fact that the time base (T_{clk}) of the counter in a digital PWM module is constant, which results a constant slope for the triangular carrier wave. As it is shown in Figure 4-13, an asymmetrical carrier wave is proposed for digital implementation, which has two different values for the period register: one for the up counting mode and one for the down counting mode.

By choosing a random time-length for T_{rising} or $T_{falling}$ in every modulation period, the time-length spent for the active vector region (highlighted in Figure 4-13) will be randomly varied. With other words, the voltage vector generated in the T_{rising} period is generated with other switching frequency than the voltage vector generated in $T_{falling}$ period. From this point of view the AC-RPWM method can be interpreted as a RCF-PWM, where the update of the new voltage vector is done with constant frequency.

The advantage of AC-RPWM method compared to the RPP-PWM method is that the spread effect of discrete components from the motor current spectra is effective even at high modulation index, where the time spent for generation of the active vectors is larger than the time spent for generation of zero vectors.

A combination of the RPP-PWM and AC-RPWM will result in good performance regardless of the modulation index. Figure 4-14 presents the AC-RPWM with redistributed zero sequence vectors.

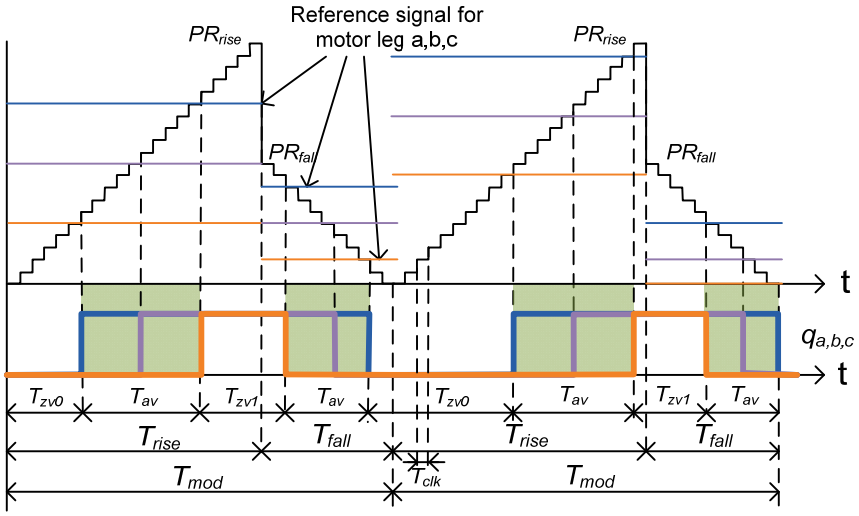

Figure 4-14 SVM ($T_{zv0} = T_{zv1}$) in the first modulation period, and redistribution of the zero vectors ($T_{zv0} \neq T_{zv1}$) in the second

Again, the redistribution of the zero vectors modifies the position of the active vector regions on each half period, which is centered ($T_{zv0} = T_{zv1}$) in case of SVM. In the second modulation period from Figure 4-14 the active vectors have random position ($T_{zv0} \neq T_{zv1}$). From current ripple point of view the optimal position for active vectors is in the middle like it is in case of SVM. The larger current ripple increases the acoustic noise generated by the motor, fact which is confirmed by the measurements presented in Table 4-1. Again, transforming the annoying whistling noise into a white noise can be more pleasant for the human ear. Figure 4-15, Figure 4-16, and

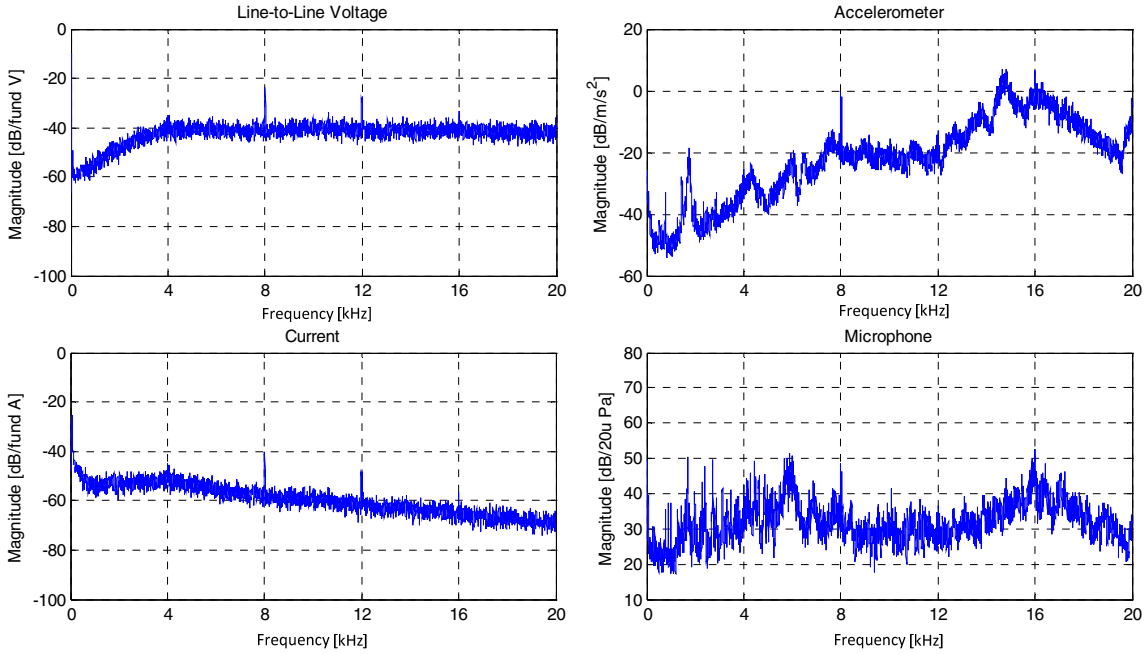

Figure 4-15 Measured spectrum of the line-to-line voltage (top-left), vibrations on the motor shell (top-right), motor current (bottom-left), and acoustic noise (bottom-right), by using AC-RPWM at 10Hz fundamental frequency (modulation index 0.2) and switching frequency of 4kHz

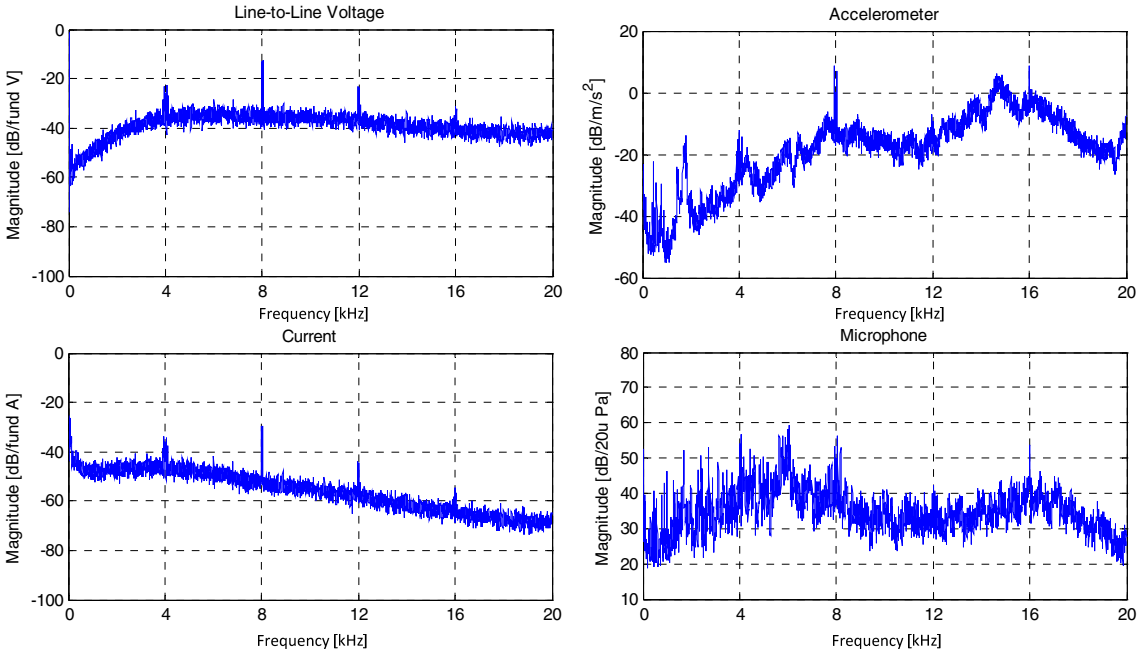

Figure 4-16 Measured spectrum of the line-to-line voltage (top-left), vibrations on the motor shell (top-right), motor current (bottom-left), and acoustic noise (bottom-right), by using AC-RPWM at 25Hz fundamental frequency (modulation index 0.5) and switching frequency of 4kHz

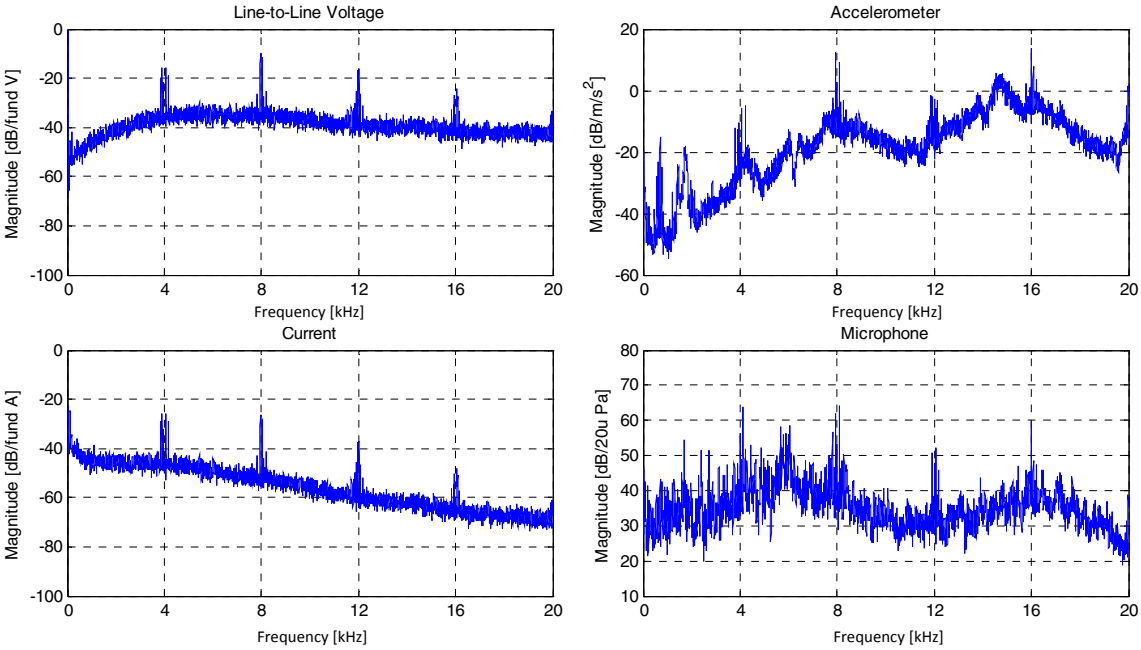

Figure 4-17 Measured spectrum of the line-to-line voltage (top-left), vibrations on the motor shell (top-right), motor current (bottom-left), and acoustic noise (bottom-right), by using AC-RPWM at 40Hz fundamental frequency (modulation index 0.8) and switching frequency of 4kHz

Figure 4-17 present the measured spectra of motor current, line-to-line voltage, vibration and acoustic noise when using AC-RPWM.

By introducing limitations, AC-RPWM can generate similar pulses like most of the existing FCF-RPWM. For example, by random elimination of T_{rising} or $T_{falling}$ for each modulation period, AC-RPWM will work as the oldest FCF-RPWM the so called random lead-lag (RLL-PWM)[62]. RLL-PWM spreads the discrete components from the current spectra, but has very poor current quality, it is not recommended for practical use [54].

Finally, comparing the measured results for the FCF-RPWM methods at low speed, the AC-RPWM shows slightly better performance than RPP-PWM; both modulation techniques perform well, the tonality is nearly disappeared from the acoustic spectra. At medium speed the AC-RPWM performs much better, the amplitude of the discrete components around 8 kHz in the acoustic spectra are reduced with approximately 10dB compared to RPP-PWM and the whistling noise is hard to be distinguished by ear. At high speed the acoustic noise generated by the motor ventilator, bearings etc. introducing extra harmonics in the acoustic spectra, therefore the modulation harmonics become even less evident.

4.3.3 FCF-RPWM in closed-loop applications

The FCF-RPWM methods are easy to implement in open or closed loop motor control schemes. A general motor control block scheme is presented in Figure 4-18 which can run in open- or closed loop. The outcome of the control block is always a calculated reference voltage vector in ***d-q*** plane. This voltage vector ($\bar{U}_s$) is decomposed in two adjoin active voltage vectors, and converted into duty ratios for the PWM module using the SVM block. The FCF-RPWM block is an additional element that makes the randomization of the time-lengths of the active and zero sequence vectors within a modulation period. In case of AC-RPWM the PR_{rising} and $PR_{falling}$ are calculated in this block, and the duty ratios are converted in compare values for the PWM module. The VSC and PWM blocks symbolizes the power switches respectively the hardware of the PWM module from the digital implementation. From the block diagram presented in Figure 4-18 can be seen that the main advantage of the FCF-RPWM is that it is easy to implement in an existing closed or open loop control algorithm. Also a big advantage is that it needs only software modification; there is no need for any additional hardware. As a disadvantage, it can be mentioned that the PWM module has to be updated twice during the modulation period. The control algorithm however can only run once per modulation period.

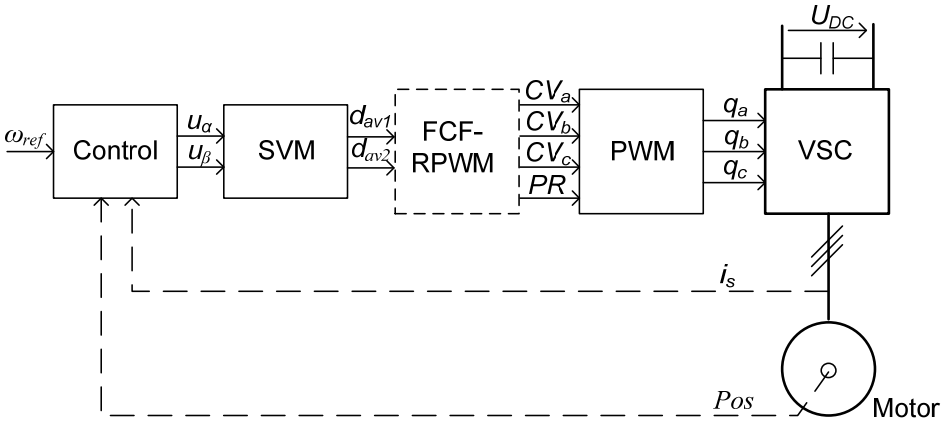

Figure 4-18 Block diagram of a motor control using FCF-RPWM in open and closed loop

The setup used for measurements consists of a 4 kW PMSM with current and position feedback without load. Figure 4-19 presents the closed loop block scheme used to control the PMSM.

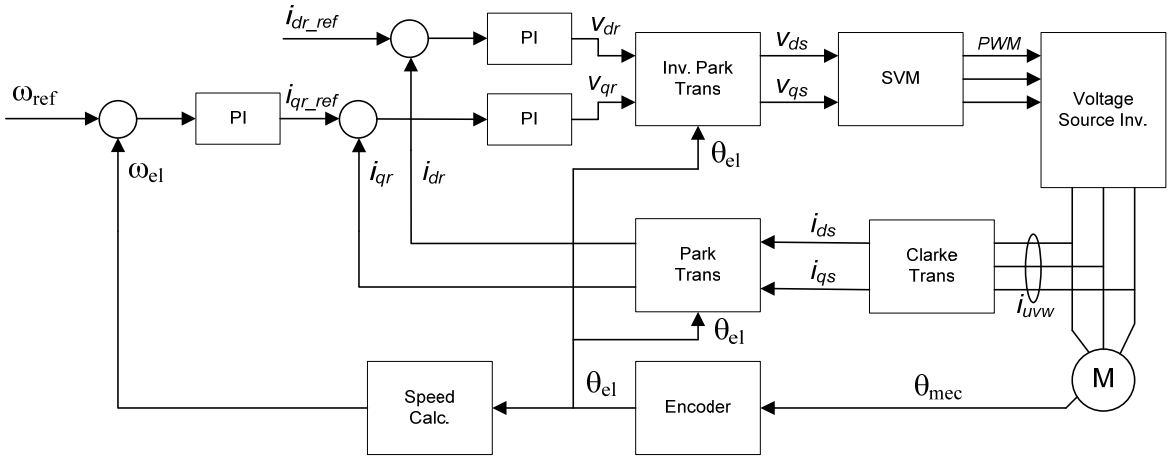

Figure 4-19 Block scheme of the vector control algorithm used to control the 4 kW PMSM

Figure 4-20, Figure 4-21, and Figure 4-22 presents the measured line-to-line voltage, motor current, vibration and acoustic noise of this synchronous motor using field oriented control for 10Hz, 25Hz and respectively 40Hz fundamental frequencies. The new voltage vector is calculated based on the actual motor current and position of the rotor, using field oriented control; therefore an accurate measurement of the motor current is essential. For the experimental validation, the motor current was sampled at the bottom and top of the triangular carrier wave. Some limitations were introduced in the AC-RPWM in order to increase the accuracy of the current sampling, which is described in the next section.

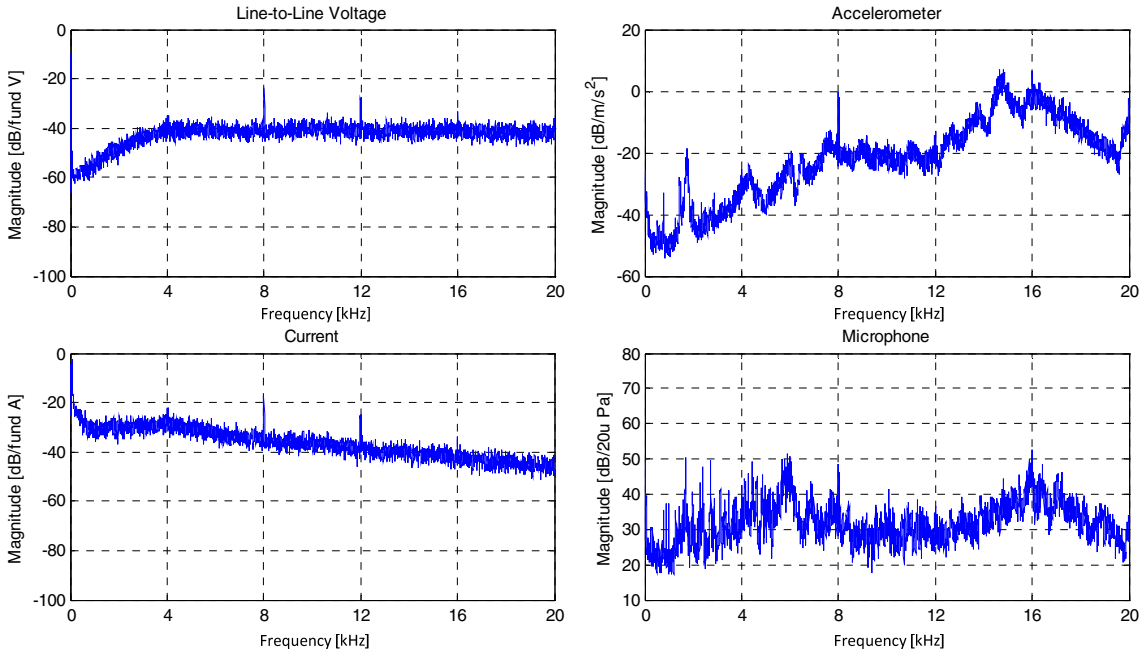

Figure 4-20 Measured spectrum, using field oriented control for PM synchronous motor, of the line-to-line voltage (top-left), vibrations on the motor shell (top-right), motor current (bottom-left), and acoustic noise (bottom-right), by using AC-RPWM at 10Hz fundamental frequency (modulation index 0.2) and switching frequency of 4kHz

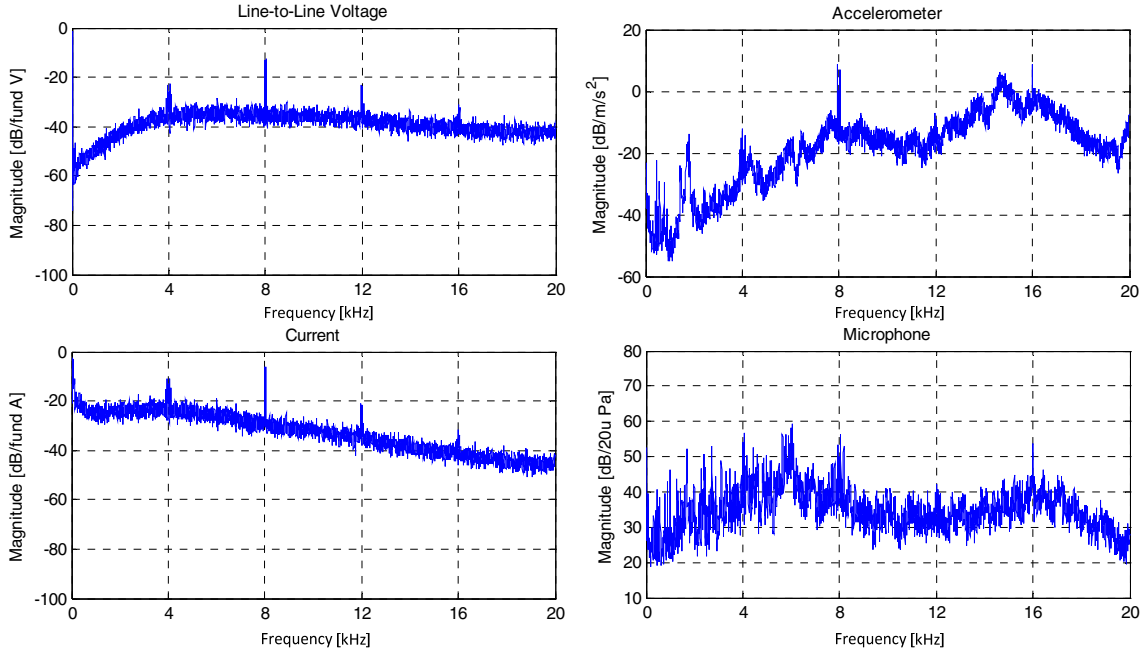

Figure 4-21 Measured spectrum, using field oriented control for PM synchronous motor, of the line-to-line voltage (top-left), vibrations on the motor shell (top-right), motor current (bottom-left), and acoustic noise (bottom-right), by using AC-RPWM at 25Hz fundamental frequency (modulation index 0.5) and switching frequency of 4kHz

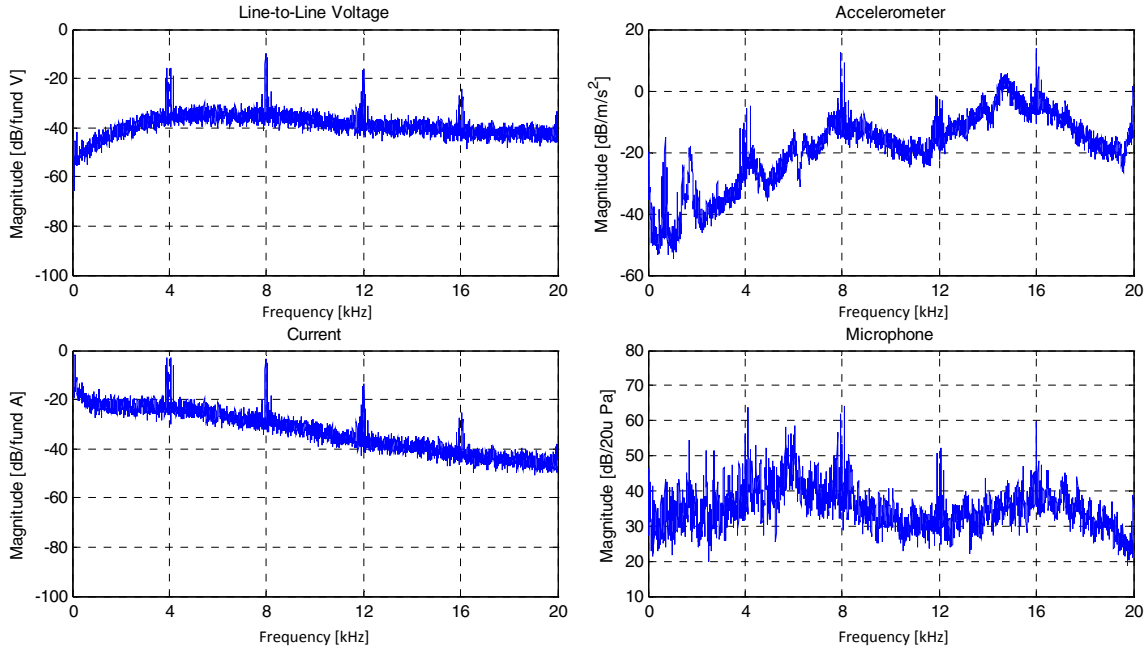

Figure 4-22 Measured spectrum, using field oriented control for PM synchronous motor, of the line-to-line voltage (top-left), vibrations on the motor shell (top-right), motor current (bottom-left), and acoustic noise (bottom-right), by using AC-RPWM at 40Hz fundamental frequency (modulation index 0.8) and switching frequency of 4kHz

The measurements results obtained by field oriented control for PM synchronous motor and the open loop driven asynchronous motor are approximately similar. In Chapter 6, a comparison between the acoustic noise generated by the PM synchronous and asynchronous motors is presented.

4.3.3.1 Current sampling techniques for FCF-RPWM

The current sampling error can cause torque oscillation which deteriorate the performance of the speed control in case of closed loop applications [63, 64]. Usually, the acquisition of the motor currents is done on the top and/or the bottom of the triangular carrier wave [65, 66]. In case of SVM, this means the sampling of the motor current is done in the middle of the time-length in which zero sequence vectors are generated. To quantify the current sampling error, the ideal case was simulated without nonlinearities (like dead time). To obtain current waveforms similar to those in the motor, a simplified circuit was used, shown in Figure 4-23. The impedance of the simplified circuit is similar with the impedance of the motor. Using symmetrical regular sampled SVM method, a balanced three phase sinusoidal voltage can be generated. The *R-L* circuit will act as a first order low pass filter, creating a current with the same fundamental frequency as the phase voltage. To extract the reference current component (pure sinusoidal without ripple) from the current through the inductance, a resonant filter was employed. The advantages of the resonant filter are that its phase shift is

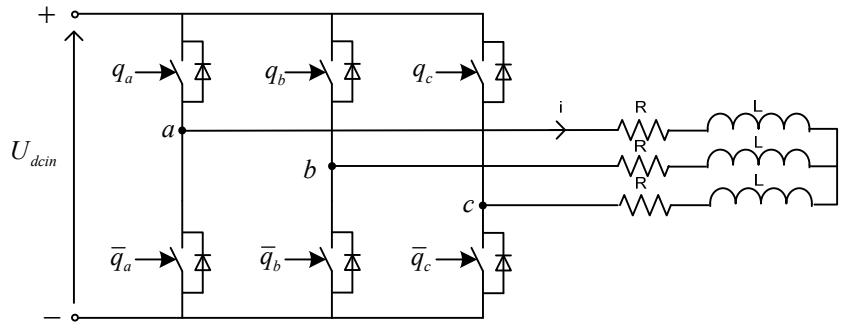

Figure 4-23 Circuit diagram of the three phase converter used for simulation

zero at its resonant frequency (ω_n), and has high attenuation outside of the resonant frequency. The transfer function of the resonant filter is:

$$H(s) = \frac{out}{in}(s) = \frac{k\omega_n s}{s^2 + k\omega_n s + \omega_n^2} \tag{4.2}$$

Subtracting the reference current value from the sampled current value gives the measurement error in the top and bottom of the carrier wave.

Figure 4-24 presents the simulation results of the macro and microscopic scale of the filtered current, the sampled current, and the measurement error.

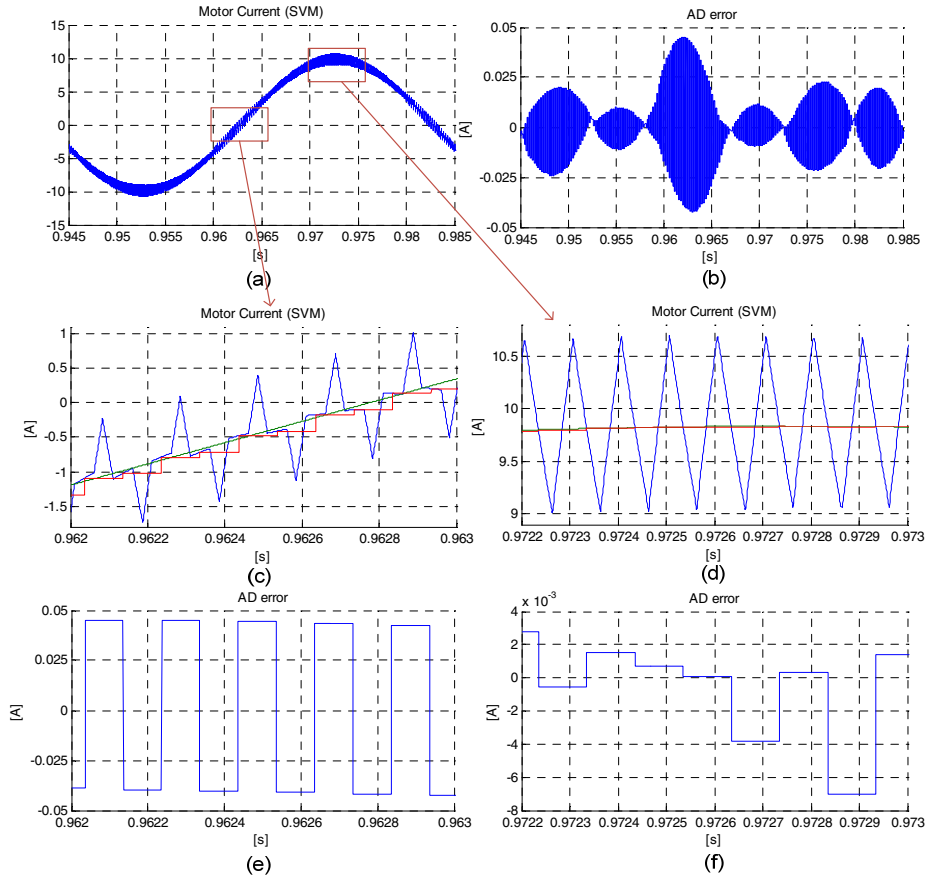

Figure 4-24 Simulation results of the current using SVM with 0.5 modulation index, one fundamental period of the current (a), sampling error during the fundamental (b), zoom in the current plot at zero crossing (c), zoom in the current plot around the maximum of the fundamental (d), zoom in the error plot (e) and (f)

As it can be concluded from Figure 4-24, the sampling error is high when the reference voltage vector is in the middle of a sector, and it is small when the reference voltage vector has the same position as an active vector. This means that, when a voltage vector is created, the sampling in the top and bottom of the triangular carrier has minimal error. At zero crossing, the current has maximum slope, which results in maximum error. Figure 4-24 *(c)* shows that the reference signal is always between the value of the current sampled in the first and second part of the modulation period, when zero vectors are generated. This error is mainly caused by the regular sampling. The maximum error is approximately ±0.05A. For this example (10A nominal current) 15A can be considered as a maximum measurable current, a resolution of 8 bit is enough for analog to digital conversion.

By using RPP PWM method, and by sampling the motor current in the top and bottom of the triangular carrier, the current will not be sampled in the middle of the time spent for generation of the zero sequence vectors which increases the sampling error. This error can be reduced by using the same position for the active vector region in the first and second half of modulation. However, by introducing limitations on the possible position for the active region the spread effect of the discrete components from the motor current spectra is reduced.

Figure 4-25 presents the inductor current in macroscopic time scale when using RPP-PWM and AC-RPWM. The inductor current is sampled in both cases in the middle and in the top of the triangular; the sampled value is subtracted from the filtered current which gives the sampling error. As it was expected, the sampling error increases in case of random modulation. In case of AC-RPWM, the error is slightly smaller than in the case of RPP-PWM. For the random modulation a resolution of 6 bit is enough for analog to digital conversion. In case of applications where this sampling error can cause problems, limitations like maximizing the time-length T_{rising} or $T_{falling}$ for example 80% of the time-length of the modulation period can be introduced. However, this kind of limitations reduces the effectiveness of the randomization.

The usage of a low pass filter and high sampling frequency for current measurement could be a solution. However, the low pass filters affects the phase of the filtered signal which can introduce even higher sampling error. By using a notch filter (like the above presented resonant filter) which does not affect the phase of the current can cause problems by filtering out the low frequency components in the measured current. In this case the current regulators from the closed loop control will not be able to compensate for these unwanted low frequency components.

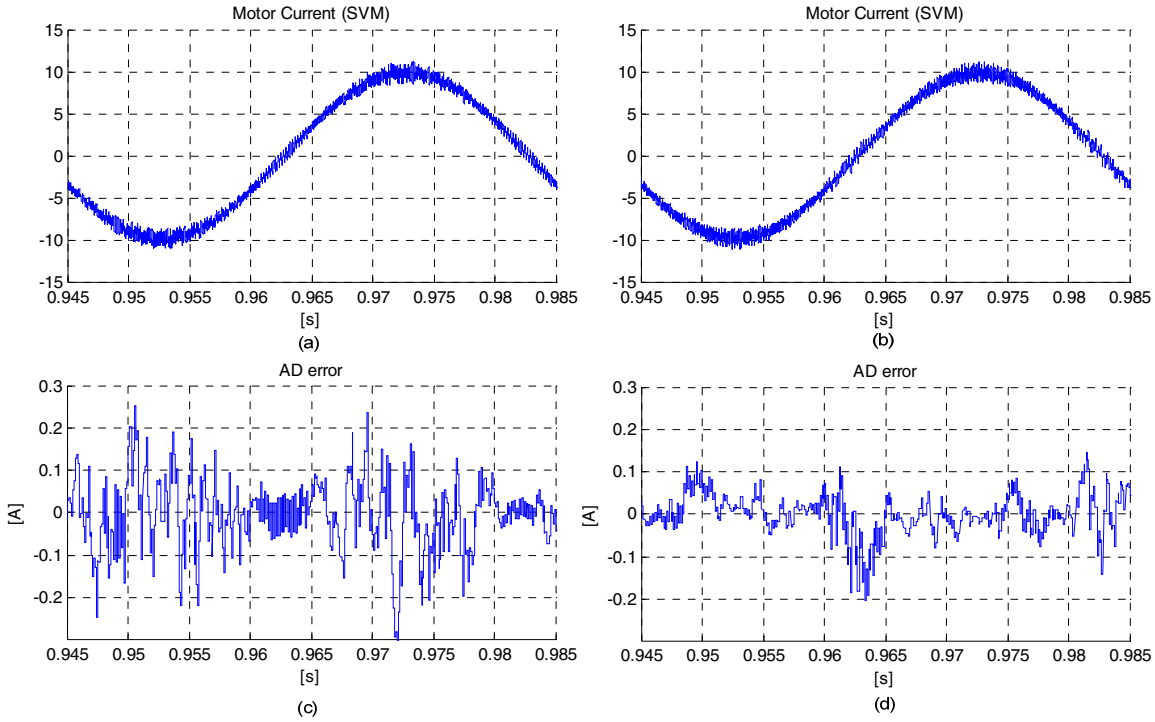

Figure 4-25 Macroscopic time scale of the inductor current (top) and the sampling error (bottom) at 25Hz fundamental, RPP-PWM in the left column and AC-RPWM in the right column

4.4 Comparison of RPWM methods from acoustic point of view

Table 4-1 presents the sound pressure level measured from a distance of one meter at 10 Hz, 25 Hz, and 40 Hz fundamental frequencies. To avoid the acoustic noise generated by the load, the motor was not loaded during the measurements. At low speed, the randomization increases the sound pressure level with around 7-10 dB. At higher speed the difference between the methods decreases to around 1-2 dB, higher for RPWM. The opinion of the author is that the flat spectrum acoustic noise is more pleasant in spite of the fact that the sound pressure level is slightly increased by randomization.

From the randomization effectiveness point of view, the RCF-PWM method has the best performance, totally spreading the discrete components from the acoustic spectra. However, it is difficult to implement into closed-loop control applications. The FCF-PWM methods overcome this limitation, but the modulation harmonics are not totally spread. From the presented FCF-RPWM methods, the most effective was the AC-RPWM.

Fundamental frequency	SVM (4kHz)	RCF-PWM (3-5kHz)	Scheme (3.5;4.5;4.5;3.5;3.5;4.5 kHz)	3.5kHz and 4.5kHz random	RPP-PWM 4kHz	AC-RPWM 4kHz
	sound pressure level in [dBA]					
10Hz	53	60.5	63.3	60.3	59	61.5
25Hz	64	66	63	66	65	67
40Hz	66.5	66	66.6	66.7	67	67.2

Table 4-1 Measurement of the sound pressure level

4.5 Summary

Several modulation methods, which transform the whistling acoustic noise generated by PWM fed electrical motors into a white noise, has been presented in this chapter. Two new FCF-RPWM modulation methods have been proposed, the AC-RPWM and a RPP-PWM method, which shape the spectra of the line-to-line spectra. From acoustic point of view it is very subjective to decide which modulation method is the best. The author's opinion is that the flat spectrum, with a sound like white noise, is less annoying than SVM.

Apart from the acoustic performance of the random modulation, the implementation of the methods was analyzed as well. In closed loop applications, the calculation of the new voltage vector is mainly based on the sampling of the motor currents; therefore a possible error in the motor current sampling can cause instability or control error. The sampling error caused by the randomization, error which can be reduced by introducing some limitations, has been analyzed. However, the limitations reduce the effectiveness of spreading the discrete components from the acoustic spectra.

Chapter 5

Modeling of the ventilation system

In this chapter three methods to model the frequency response of a complex structure like the ventilation system are presented. The first method uses a force impulse (hammer excitation) to excite the structure. The second method is based on injection of a sinusoidal current in one phase of the motor with variable frequency. The third method is based on random PWM.

5.1 Introduction

As presented in the previous chapter, the acoustic noise generated by an inverter fed electrical motor is mainly generated by the modulation. Usually, the stator shell of an electrical motor can be considered as a cylinder, which is contracted and released by the radial forces. The natural frequency of the stator can be expressed in patterns per circumference as it is shown in Figure 5-1.

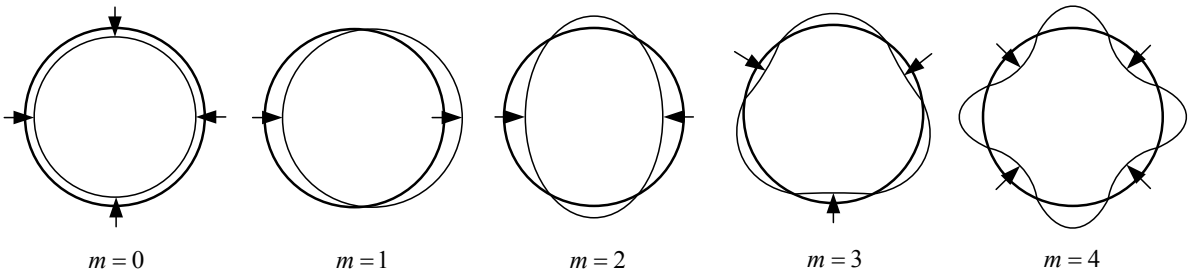

Figure 5-1 Modes of the stator core vibration

In electrical motors the radial force is larger than the tangential (approximately 10 times higher [45]); this radial force transforms the cylindrical shell into a kind of loudspeaker, converting the frequency components present in the force spectra into a sound. Several methods were proposed in the literature to analytically or numerically determine the radiated acoustic noise. There are two main methods to determine the

analytical model, one is based on the spherical model [67, 68] and the second one is based on the cylindrical model [69, 70]. A general description of the noise sources in electrical motors can be found in [3, 71]. The vibro-acoustic analysis estimates the frequencies of the spectral components very well, but the estimation for the magnitude of the frequency components is not very precise [45]. Moreover, in case of motor constructions, which have an irregular shape, these idealized models are not applicable. The numerical methods, like finite element modeling of the machines [72] give a better estimation for the magnitude of the electromagnetic force. The analysis based on finite elements has the advantage of including the influence of magnetic saturation, the effect of end shields etc. in the vibration spectra. A big disadvantage of the finite element analysis is that creating a vibro-analysis in high frequency range requires a large number of elements and long computation time. In case of a complex drive system where the load has to be considered as well, the design of a finite element model is a very time consuming process.

In this chapter the sound generation in a Dantherm ventilation system is analyzed, equipped with a VEM asynchronous motor. Being the whole ventilation system too complex to be analyzed by using finite element modeling, the frequency response of the system to motor current in terms of vibrations is established by using measurements. The reason why the vibrations and not the acoustic noise are considered is that the measurements were made in a room with echo. The echo has influences on the acoustic measurements; therefore they would only be valid for the actual environment.

As the motor is the main source of vibrations, the stand alone motor is analyzed first. Next, the analysis is extended to the ventilation system.

5.2 Determination of the structure response

To measure the frequency response of the structure of the motor and the ventilation system, three methods were chosen: hammer excitation, sine sweep and random PWM. Generally speaking, the system response can be characterized as a ratio between the spectrum of the output signal and the spectrum of the input signal. To get a view on the structure response in a frequency range, the input signal spectrum should contain each frequency component from that range. The equipment used for measurements was a B&K pulse FFT analyzer equipped with an impact hammer (type 8206) with a force transducer attached to its head, an accelerometer (type 4503) and B&K PULSE LabShop software.

Figure 5-2 presents the flowchart of a classic spectra measurement process and the determination of the frequency response.

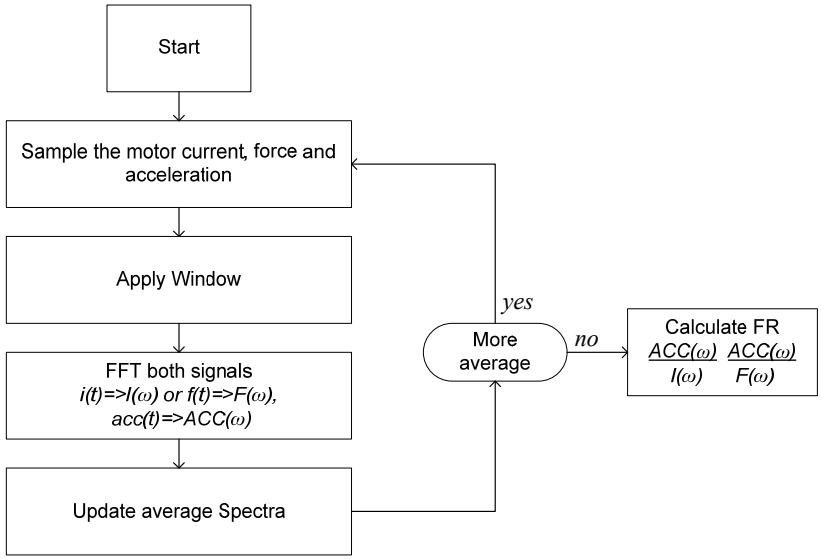

Figure 5-2 Block scheme of the measurement process of the frequency response between vibrations and motor current or impact force

For the standalone measurements, the motor was lifted with a crane in order to exclude the contact with the floor. To exclude the effect of the crane structure, a rubber ring was used like it is shown in left picture from Figure 5-3. The accelerometer was screwed into the stator shell, minimizing in this way the contact damping between the motor and accelerometer.

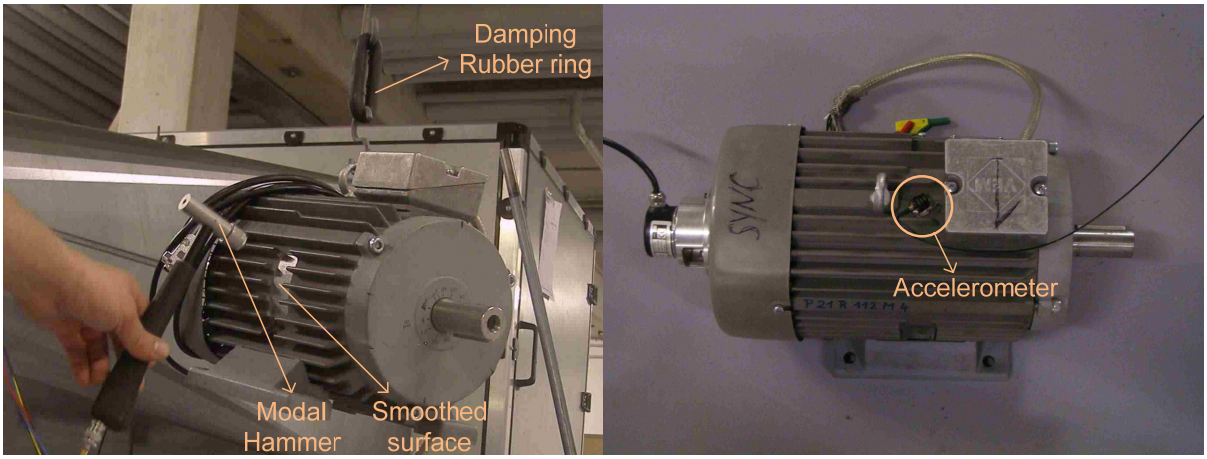

Figure 5-3 Smoothed stator surface of the motor (left), and placement of the accelerometer on the surface of the stator

5.2.1 Hammer Excitation

A standard approach to measure the mechanical response is to excite the structure with a force impulse, using a modal hammer, and measure the response of the structure with an accelerometer. The impact testing is fast, convenient, and low cost procedure to determine the frequency response of the structure. In ideal case the input force signal should last for an infinitely small duration only, and stay at zero for the rest of the window time period. In this ideal case the input signal will have constant amplitude in the frequency domain, which means all the vibration modes will be

equally excited. In reality, this ideal excitation signal cannot be produced, but by hitting the structure with a hammer creates an impulse force which replicates quite well the ideal excitation signal. The shape of the force waveform depends on the type of tip used for the hammer. Hard tips, for example made out of aluminum, generate a narrow pulse; soft tips like plastic or rubber generate wider pulses. The spectrum of the impulse force in case of plastic tip is presented in Figure 5-4 (d). In this case the amplitude of the spectral components is approximately constant in the range of 0-2kHz, which gives the possibility of modal analysis up to 2 kHz. By installing aluminum tip, this range can be extended up to around 3 kHz, but the amplitude of the spectral components will be low. By installing rubber tip, the frequency range is reduced to several hundreds of Hz, but their amplitudes are going to be higher compared to the case of aluminum tip.

To minimize the noise from the impulse force and vibration spectra, exponential windowing was used (red signal form Figure 5-4 (a) and (c)) for the time domain signal. The exponential window does not affect the non-zero data from the window time period, but it removes the noise from the rest of the time. Being the impact and response very short, it fits in one time window, there was no need for averaging.

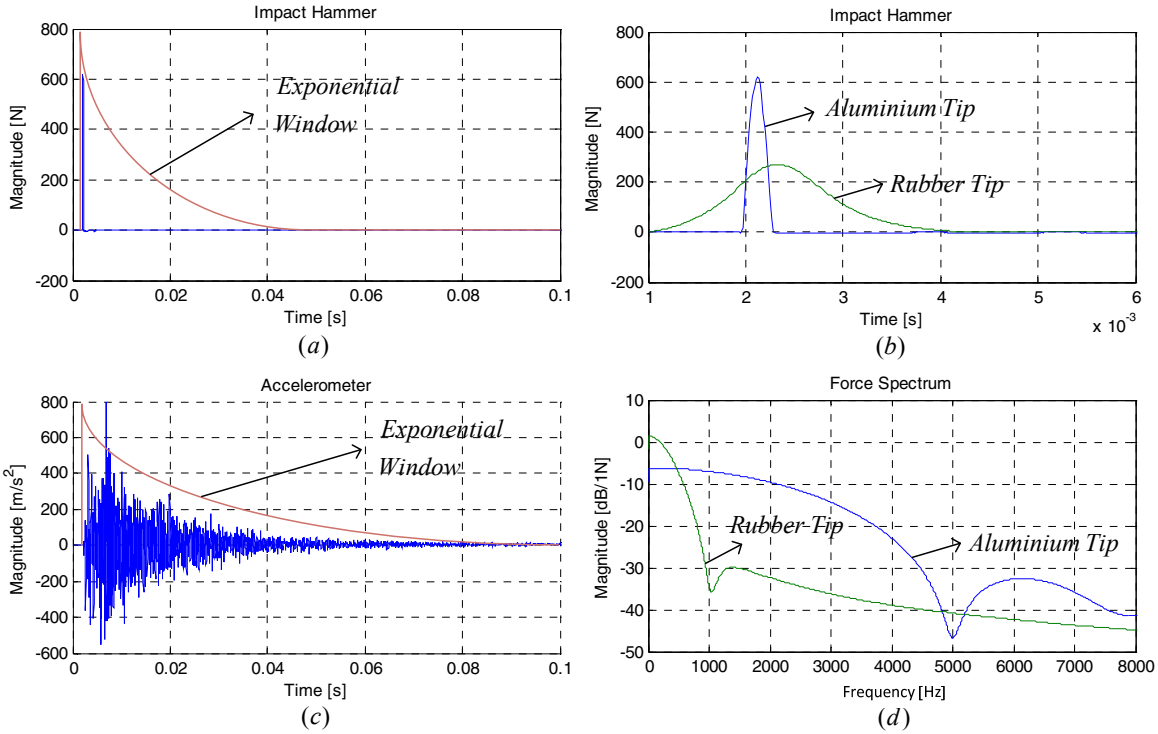

Figure 5-4 Impact force waveform (a), zoom in time domain force waveform (b), vibration waveform (c), and spectrum of the impact force (d)

5.2.1.1 Measurements of the frequency response of the motor using hammer excitation

A part of the stator surface was smoothed, making possible to hit the enclosure close to the yoke of the stator, like it is shown in Figure 5-3. Figure 5-4 presents the frequency response obtained by using an impact hammer. As it can be seen from the zoomed spectra from Figure 5-5, the structure of the motor is sensible to frequency components around 1.8 kHz, but in the switching frequency range (from 2 kHz to 10 kHz) the spectrum is quite flat. Due to the limitation of the hammer excitation method, the structure is excited only in the low frequency range, giving a response in the range between several hundreds of Hz up to 5 kHz.

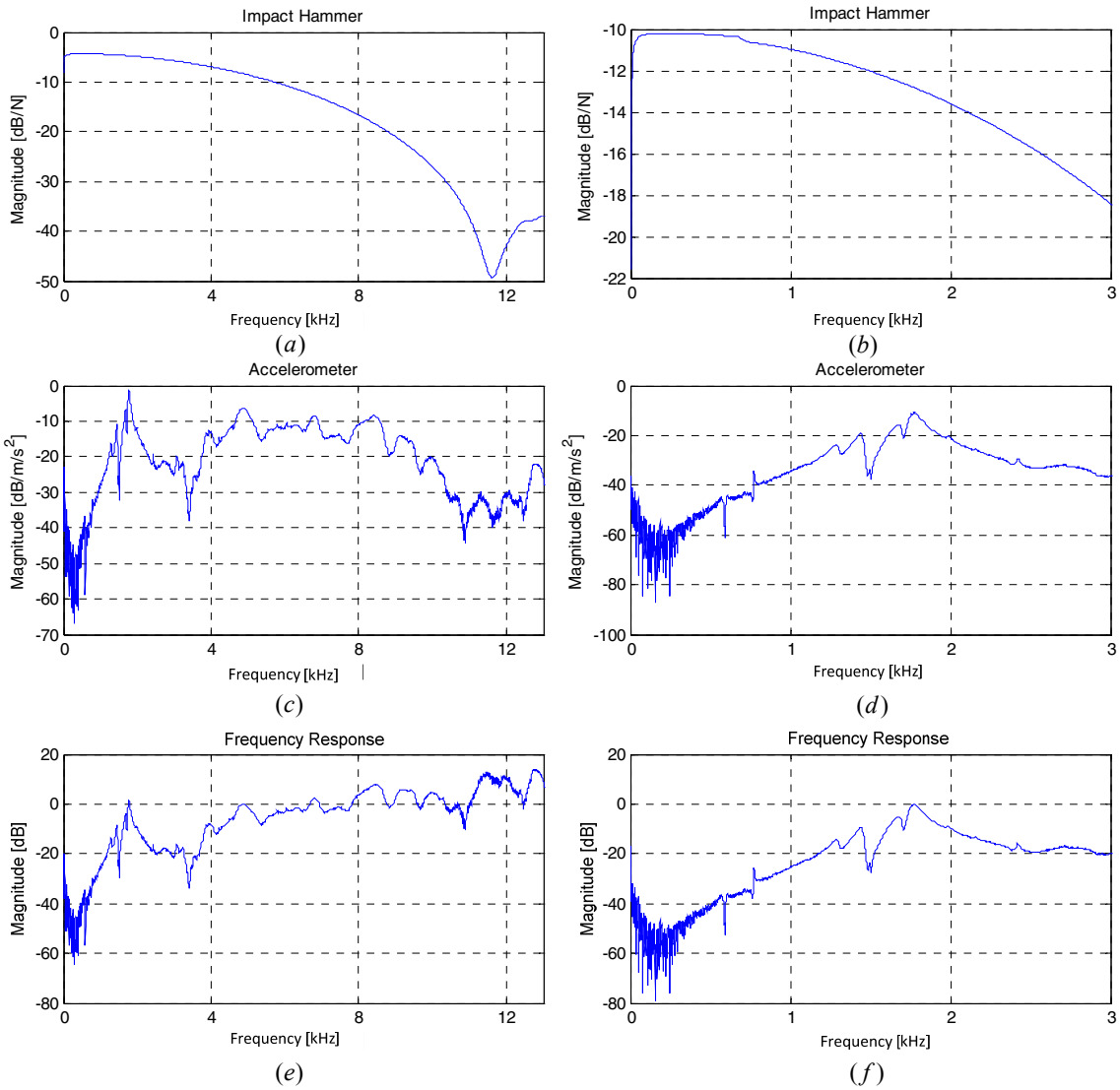

Figure 5-5 Measurement of the frequency response of the motor structure to the impact force. The left column shows measurements with aluminum tip, while the right column shows measurements for the case when plastic tip was used

5.2.1.2 Measurements of the frequency response of the ventilation system using hammer excitation

The frequency response of the ventilation system to a force impact was measured when the accelerometer was placed in two different points. The impact force excitation was made on the same smoothed area from the surface of the motor.

For the first set of measurements the accelerometer was mounted on the surface of the stator (on the same place where the stand alone measurements were made). The measurement results are shown in the left column from Figure 5-6. By comparing the results from the left column from Figure 5-6 with the results when the motor was suspended (Figure 5-5), can be concluded that the frequency response is similar. This means the enclosure of the ventilator has a minor effect on the resonances from the motor.

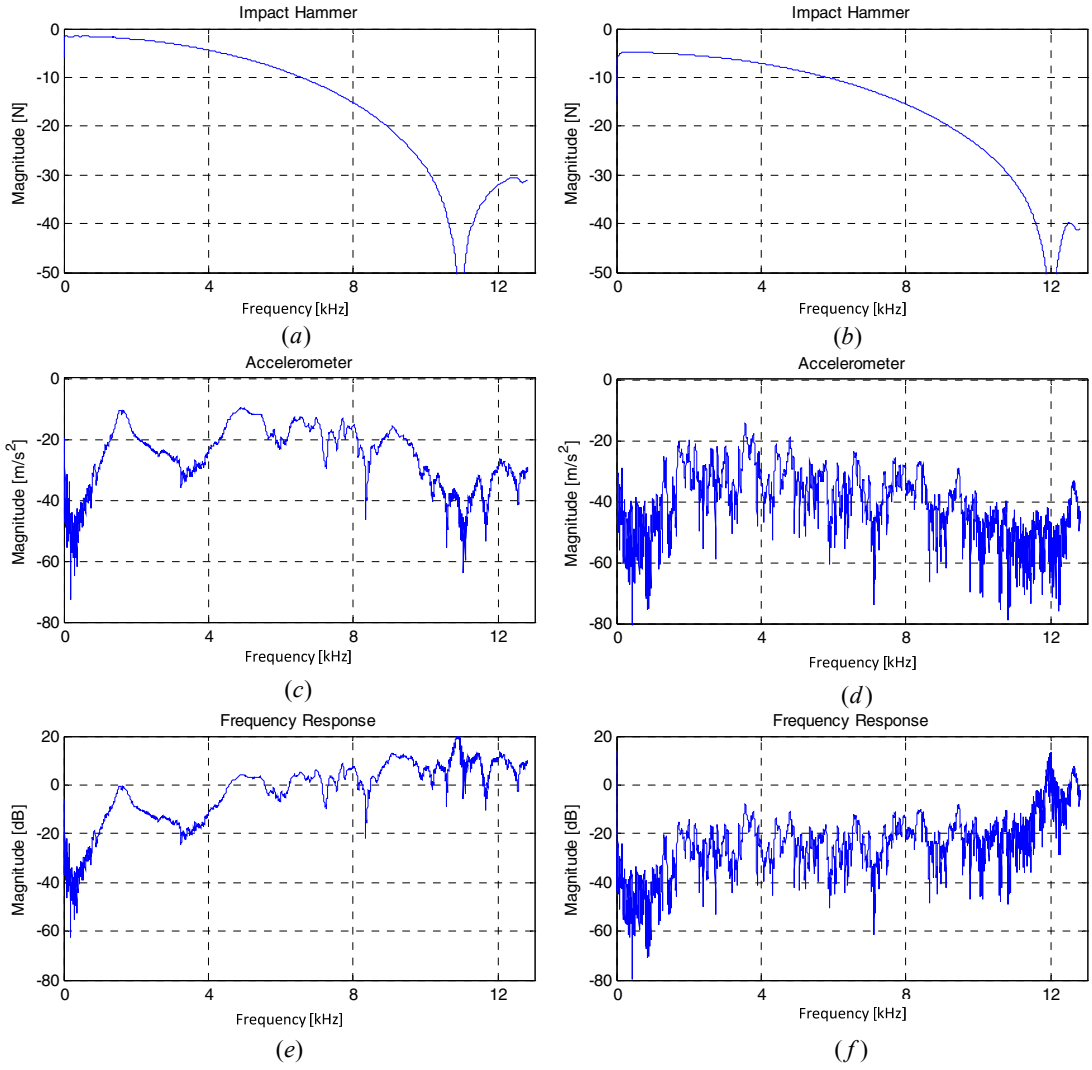

Figure 5-6 Measurement of the frequency response between the impact force and the frame of the ventilation system, in the left column (a, c, e), for which the accelerometer was placed on the frame of the stator. For the measurements in the right column (b, d, f) the accelerometer was mounted on the bottom of the ventilation enclosure

For the second set of measurements the accelerometer was placed on the ventilators enclosure as it can be seen in the picture from Figure 5-7. By exciting the motor with a force impact and by measuring the response on the ventilator enclosure, gives information about the transfer of the vibrations between the motor and the enclosure.

To damp the mechanical oscillations in the ventilation system, a spring is installed between the motor and the ventilator enclosure, shown in the picture from Figure 5-7. This spring works as a low pass filter, damping the high frequency vibrations (in the range of switching frequency). The low excitation level in the switching frequency region results in a frequency response with flat spectrum as it shown in the right column from the measurements is Figure 5-6.
A big disadvantage of using hammer excitation is that it is difficult to hit the structure with the same power on the same place.

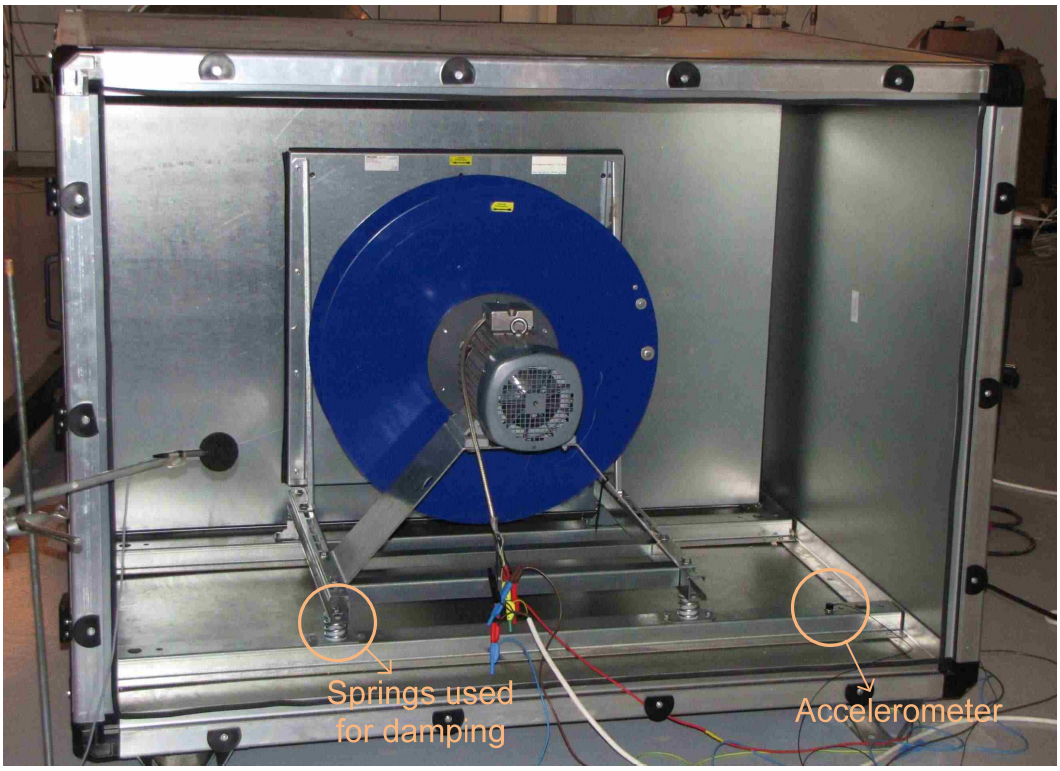

Figure 5-7 Placement of the accelerometer on the frame of the ventilation system

5.2.2 Sine sweep

As it was presented in the previous section, the hammer excitation has a limited frequency range for high energy density, or low energy density over a wide spectrum. Another solution to analyze the frequency response of the system in the range of the full audible domain (20 Hz-20 kHz) is to use a shaker. The shaker test takes longer time but the reliability is better, due to the controllable parameters (amplitude, frequency) of the excitation force.

The current through the motor coils creates a radial force in the motor, therefore it can be used to substitute the shaker; the structure will be excited by the radial force from the air-gap. Moreover, in the electrical drive applications it is difficult to

measure the force from the air-gap, it is more useful to determine the frequency response between the motor current and vibration. Figure 5-8 presents the scheme used for determination of the frequency response between motor current and vibration. It should be noticed here that there is no linear relationship between the current and vibration; the algebraic form of the transfer function between motor current and vibrations is difficult to be determined. The goal of this sine sweep measurement is to find the resonances in the structure.

A Philips PM 5132 type signal generator was set to generate a sinusoidal wave which sweeps from 1 kHz to 16 kHz. A Crown Macro-Tech 5000VZ type linear amplifier was used to amplify the signal from the signal generator. The maximum current through the motor windings was limited by the power amplifier to around 1.5A (20% of the motor nominal current). The sine sweep function from the signal generator has constant amplitude, this results in decreased amplitude of the motor current for high frequencies. The spectrum of the motor current and spectrum of vibration on the motor shell was measured using B&K Pulse multi analyzer.

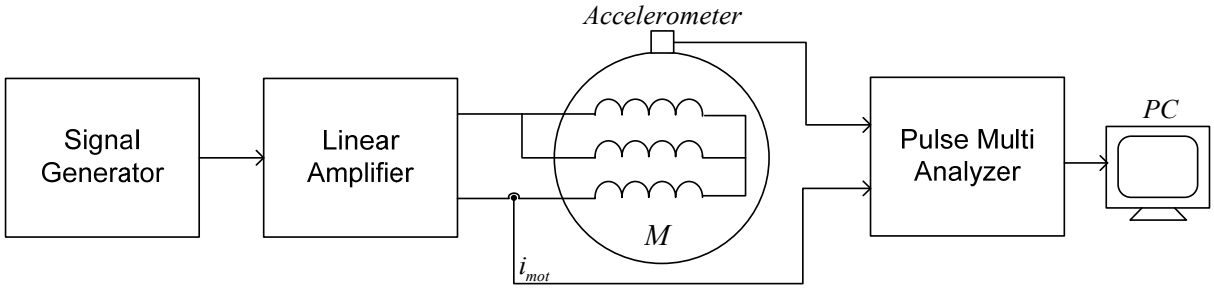

Figure 5-8 Simplified setup structure used for determination of the frequency response between the motor current and vibration

The measurements take a relatively long time (few minutes) compared to the hammer test which was more or less instantaneous. To obtain the spectrum of the motor current and vibrations, windowing and averaging was used. For windowing, Hanning window was used, and for the average calculation linear mode was used, which gives equal emphasis on all samples during the measurement.

5.2.2.1 Measurements of the frequency response of the motor using sine sweep technique

The stand alone motor was lifted up with a crane in order to exclude the contact with other bodies which can influence the frequency response of the structure. Figure 5-9 presents the measured current and vibration spectra as well as the measured frequency response. The frequency response obtained by using sine sweep shows two separate resonance peaks at around 1.5 kHz and 1.7 kHz. The spectra obtained by sine sweep technique compared to the one resulted by hammer excitation are close, showing

that the motor structure is sensible in the frequency range of 1 to 2 kHz. In the switching frequency region (2 kHz to 10 kHz) the sine sweep method shows a resonance at 6 kHz. However, the current waveform is noisy after 6 kHz. When comparing the two spectra, the different scaling and the difference between the points where the force is applied should be taken in consideration.

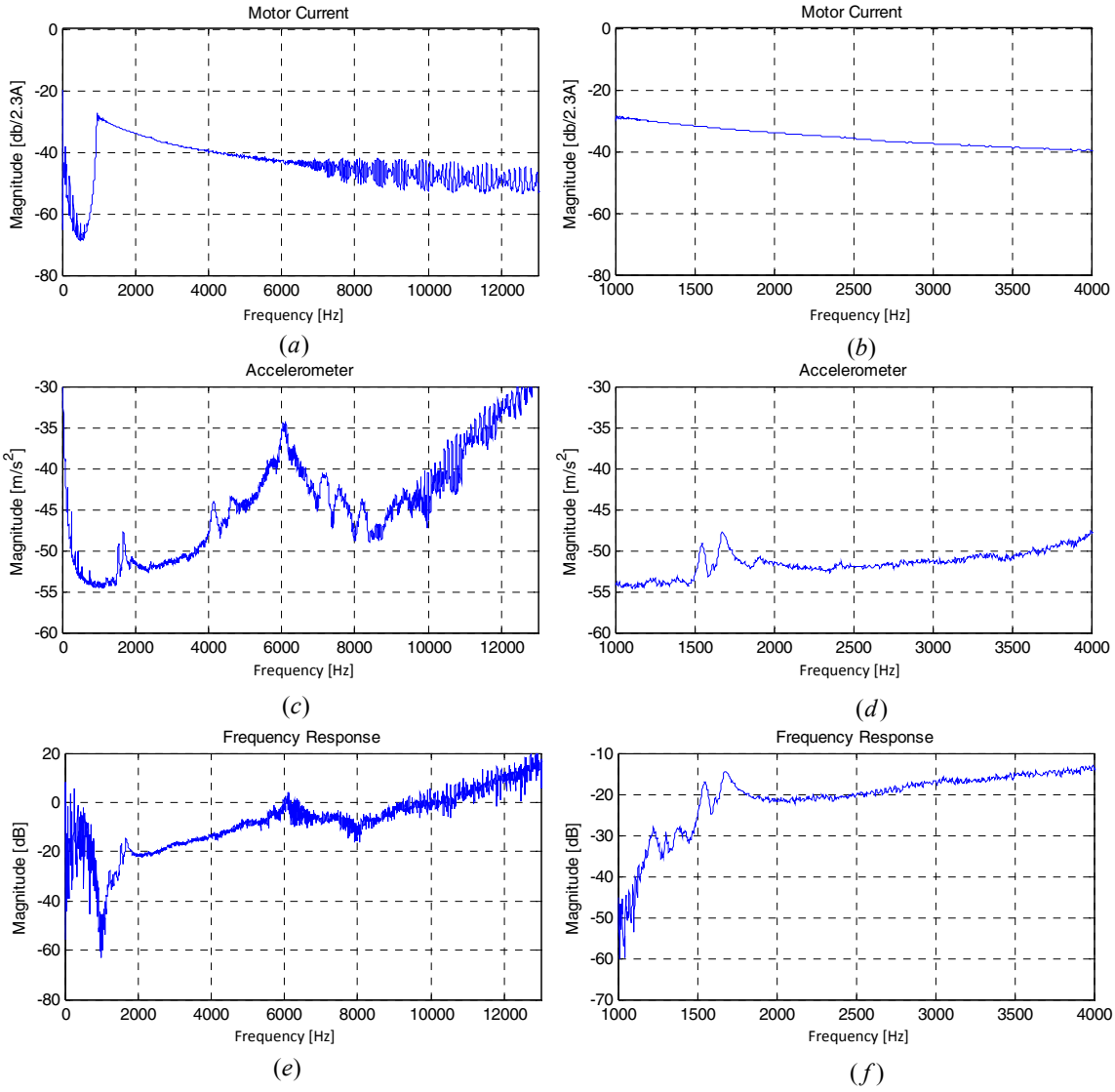

Figure 5-9 Measured frequency response of the stand alone motor to a sine sweep current in the left column the analyzed frequency range is between 2kHz and 12kHz; in the right column the analyzed frequency range is between 1kHz and 4kHz

5.2.2.2 Measurements of the frequency response of the ventilation system using sine sweep technique

After installing the motor into the ventilation system, the resonance around 1.6 kHz appears in the vibration spectra, as it is shown in the measurement results from Figure 5-10. However, the resonant frequency component was not present in the spectrum when the accelerometer was installed on the frame of the ventilation enclosure.

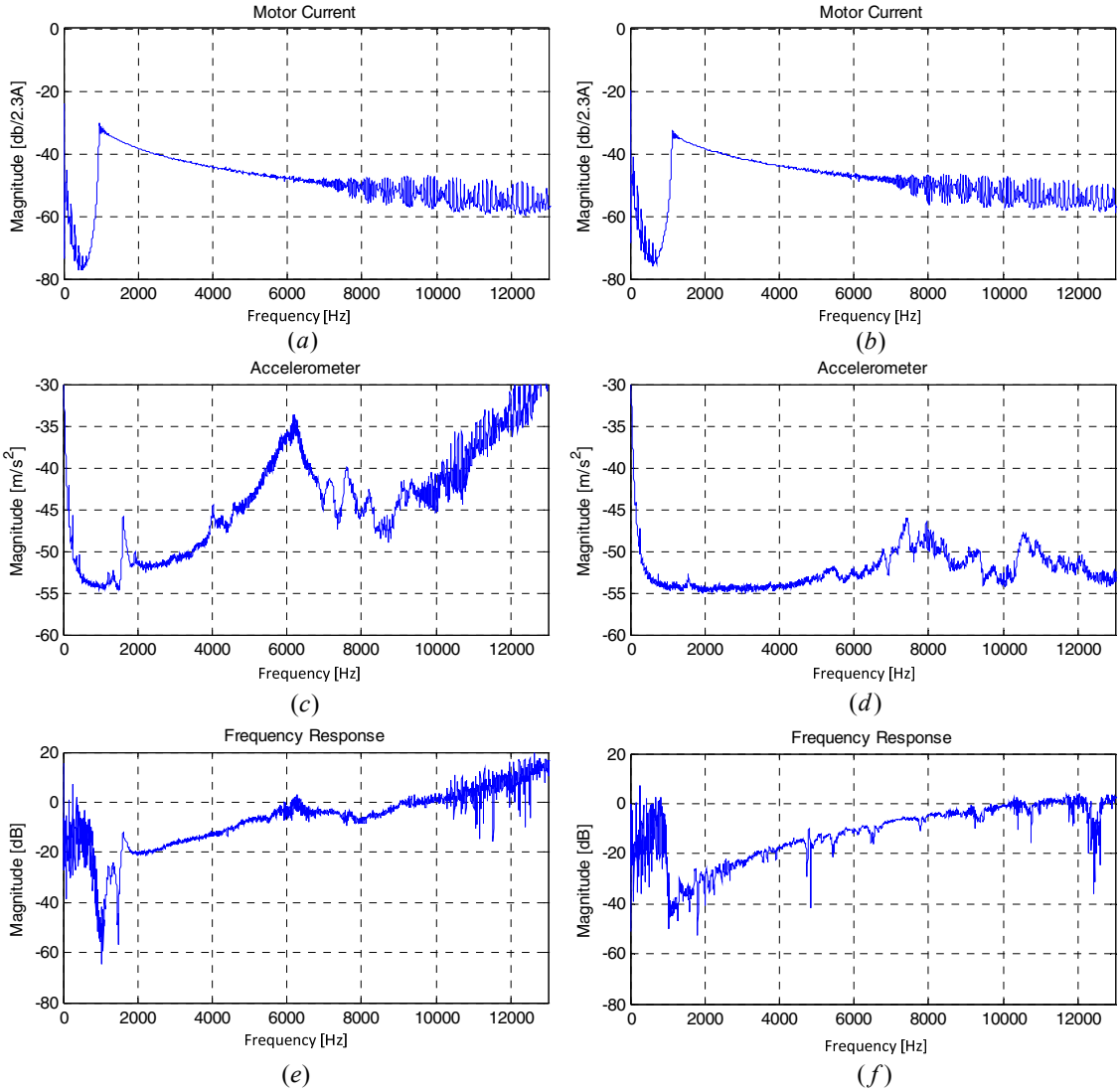

Figure 5-10 Measured frequency response of the ventilation system to a sine sweep current, left column accelerometer placed on the motor, right column the accelerometer mounted on the bottom of the ventilation enclosure

5.2.3 Random PWM

As it was presented in detail in Chapter 4, random variation of the switching frequency spreads the discrete frequency components from the acoustic spectra caused by the modulation in a wider frequency range. Having flat spectrum of the motor current in the audio range, the created radial force will also contain all the frequency compo-

nents in this range, without having a significant influence to the normal drive operation. A previous work was done in [73], where the idea of using RPWM for determination of the mechanical resonances in an asynchronous motor is presented. The same idea is used in [74] to measure the relatively high natural frequencies of an induction motor.

From the RPWM techniques presented in the previous chapter the RCF-PWM method was selected to be used for measuring the frequency response of the structure. The switching frequency varies randomly for each modulation period in the range between 3 kHz to 5 kHz.

5.2.3.1 Measurements of the frequency response of the electrical motor by using RPWM

In case of the stand alone motor, the frequency response was measured while the motor was rotating with 750 RPM. Figure 5-11 presents the frequency response between the motor current and vibrations. The measurement result is in concordance with the hammer and sine sweep method, the motor is sensible to the frequency components between 1 kHz and 2 kHz. The vibration spectrum has more components in the low frequency range compared to the spectrum obtained with sine sweep and hammer excitation methods. When RPWM method is used, the noise sources like bearings, balancing, cooling fan and non-uniform air-gap introduces extra frequency components compared to the sine sweep and impulse force methods.

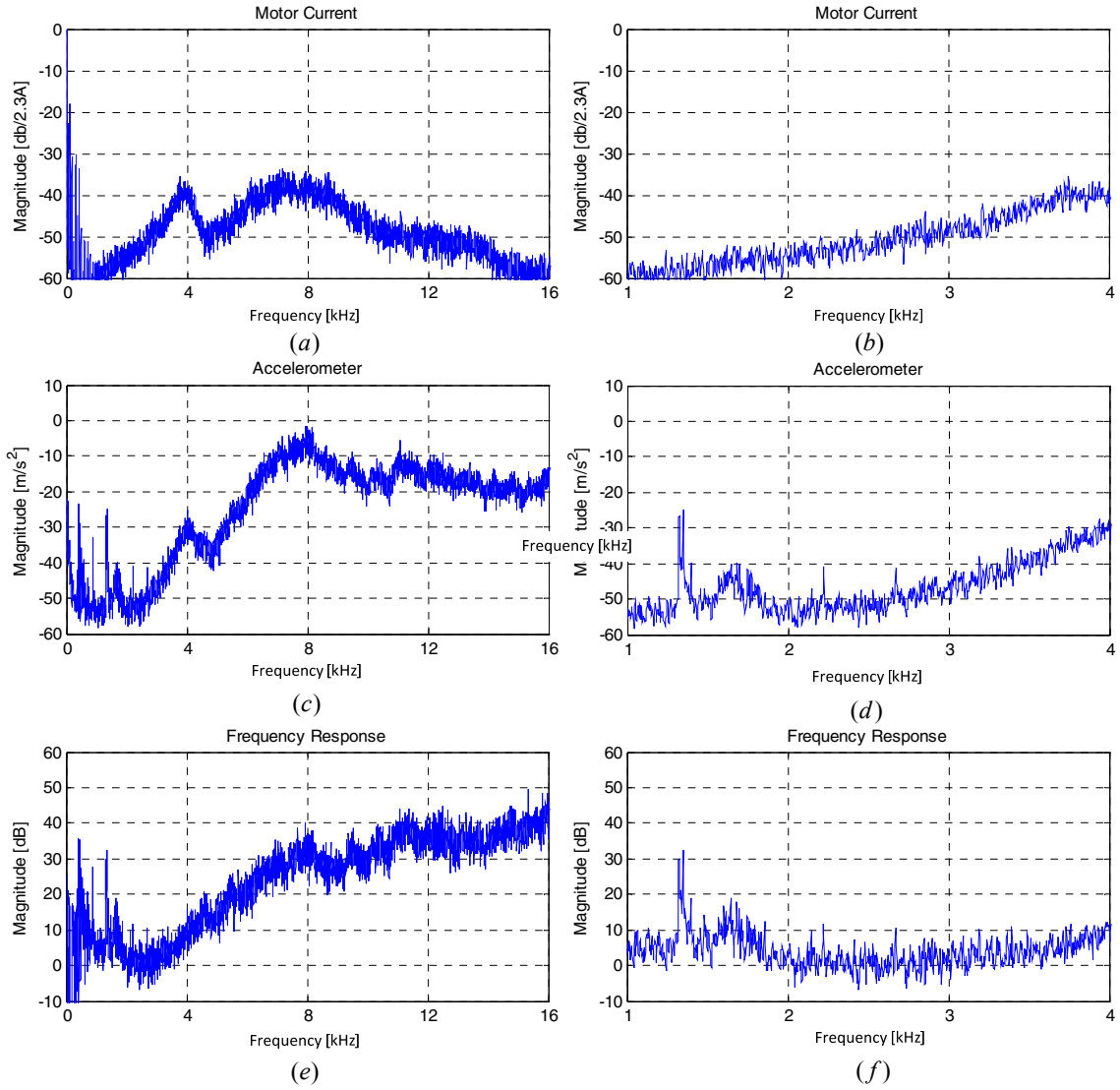

Figure 5-11 Measured frequency response of the stand alone motor when RCF-PWM technique is used, left column the frequency range is between 0-16 kHz, right column is a zoom in the spectrum in range of 0-4 kHz

5.2.3.2 Measurements of the frequency response of the ventilation system using RPWM

The frequency response was measured for two different fundamental frequencies. The left column from Figure 5-12 shows the measurement results when the motor rotates at half of the nominal speed (750 RPM); the measurements shown in the right hand side column were made at a rotor speed of 1350 RPM.

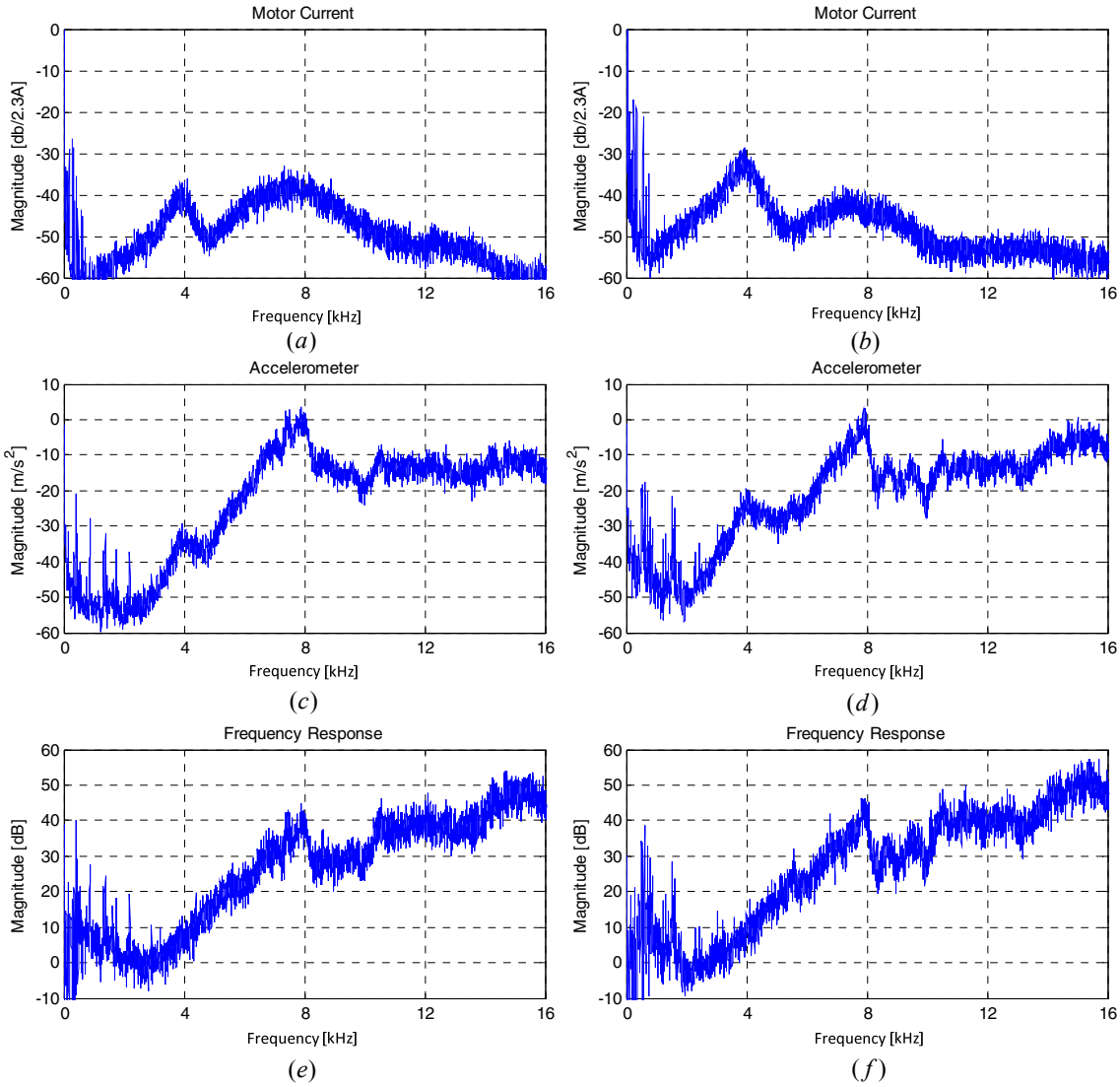

Figure 5-12 Measured frequency response of the ventilation system when RCF-PWM technique is used, the accelerometer is placed on the motor shell, left column the motor rotates at 750 RPM (25Hz fundamental), right column the motor rotates at 1350 RPM (45Hz fundamental)

All three methods show that a resonance in the range of 1 kHz and 2 kHz is present, while no clear resonances can be seen in the switching frequency range. The measurement from Figure 5-13 presents the case when the accelerometer was placed on the frame of the ventilator.

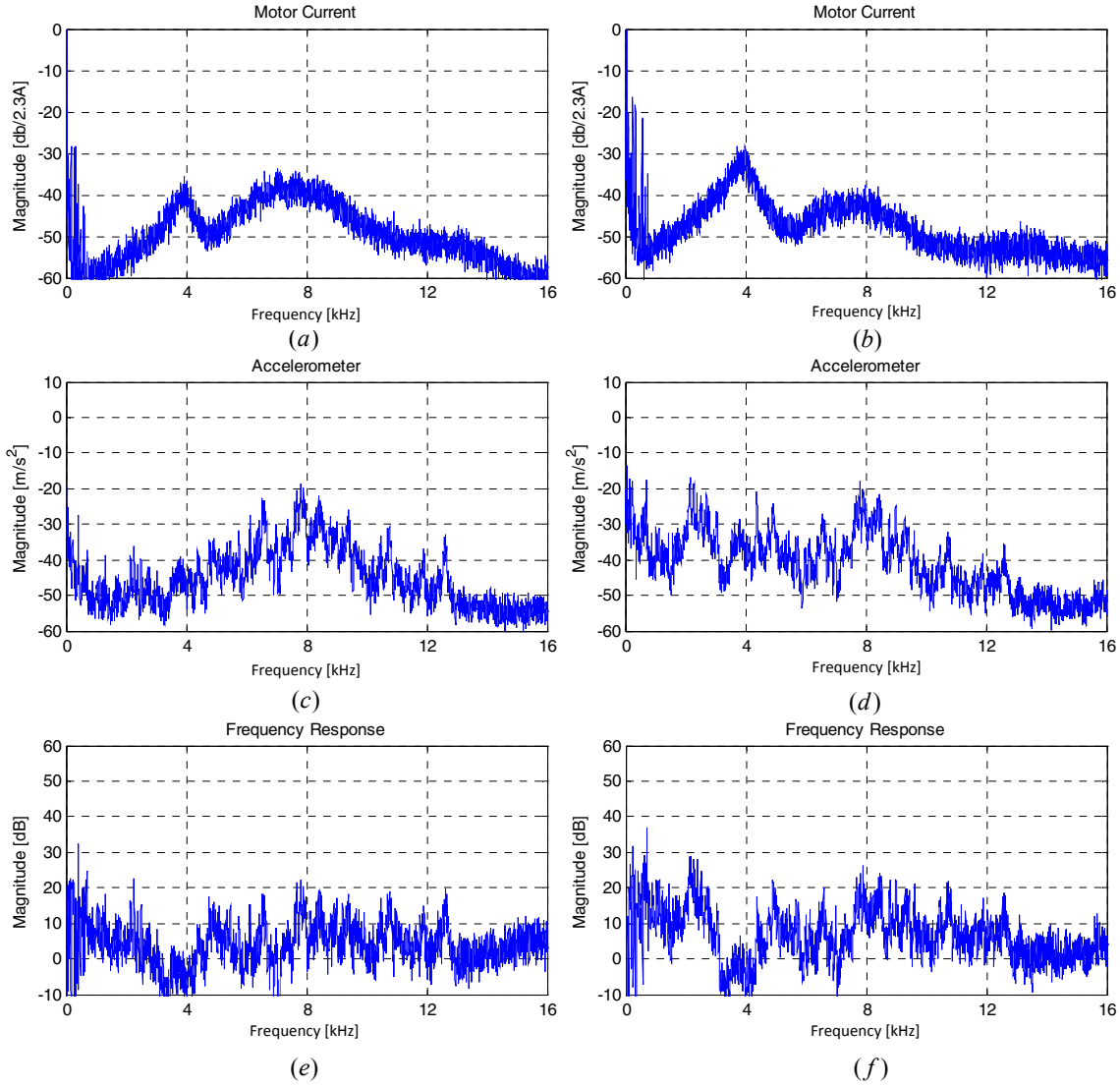

Figure 5-13 Measured frequency response of the ventilation system when RCF-PWM technique is used the accelerometer was mounted on the bottom of the ventilation enclosure, left column the motor rotates at 750 rot/min (25Hz), right column the motor rotates at 1350 rot/min (45Hz)

5.3 Summary

In this chapter three methods were presented to measure the frequency response of the stand alone motor and the frequency response of a ventilation system.
The first method was based on exciting the structure with a force impact by hitting the structure with an impact hammer. The hammer excitation is a very popular method used for modal analysis. However, this method has a limited bandwidth; the frequency response that can be determined by this method lies in the range of 0-5kHz. Another limitation of the hammer excitation technique is that the force can be applied only on the outer surface of the stator. The control over the amplitude and position of the force is also limited.

The second method is based on the injection of a sinusoidal current into the motor coils. This current will create a force similar to the radial force from the normal operation of the motor. To excite all the frequency components, the sinusoidal signal was varying in a defined frequency range, creating a 'sine sweep'. Being difficult to measure the force from the air-gap in electrical motors, a solution is to establish a relation between the motor current and the vibrations on the frame of the motor rather than a relation between the force and vibration. An advantage of sine sweep method compared to the hammer excitation method is that it can be used to measure the frequency response for the whole audible range. Another advantage is that the structure is excited with a force inside the air gap, which is similar to the force at normal operation.

The third method is based on random PWM. When the motor is controlled with random PWM inverter, the current spectrum is flat; this will result in a flat spectrum for the radial force as well. The flat force spectrum excites all the frequency components from the system. An advantage of the RPWM method compared to sine sweep and hammer excitation methods is that it gives the possibility to analyze the whole structure during normal operation.

It is difficult to compare the results obtained with the three methods due to their different nature. In the first method the force was applied in the outer surface of the stator, while in the second and third methods the exciting force was created inside the motor, in the air-gap. When the second method is used acoustic noise sources caused by bearings, balancing, cooling fan and non-uniform air-gap are not excited. During normal operation this acoustic noise sources create new frequency components in the vibration spectra, which are present when RPWM is used as excitation method.

The main goal of analyzing the frequency response of the entire drive was to find the resonances in the structure, and to develop modulation techniques that can avoid exciting these resonant frequencies. The measurements presented in this chapter show that the chosen ventilation system had no resonances in the range of the switching frequency.

Chapter 6

Acoustic noise measurement of the ventilation system

This chapter presents the measurement results of the proposed modulation technique (see Chapter 4) on a ventilation system. A comparison between an asynchronous and synchronous motor from acoustic point of view is also presented.

6.1 Introduction

HVAC applications usually do not require high shaft-torque dynamics, the focus is mostly on efficiency and acoustic noise. In modern HVAC applications the control of the electrical motor is usually done by a PWM based inverter. The acoustic noise generated by the PWM penetrates in the whole mechanical structure of the HVAC application, creating sometimes intolerable noise. For example in case of a ventilation system, where usually the motor is placed outside the building, the whistling noise caused by PWM can be transmitted into the building through the ducts. In order to measure the acoustic noise propagation in the ducts, an experimental test setup has been built, where the long ducts have been emulated by a special anechoic termination.

To increase the efficiency of the HVAC applications a new trend is to replace the less efficient asynchronous motor with a highly efficient PM synchronous motor. To maintain the stability of PMSM a closed loop control is needed. The proposed AC-RPWM in Chapter 4 can be a good alternative to spread the discrete components from the acoustic spectra for the closed loop control algorithm. The acoustic performance of the two different motor constructions (synchronous and asynchronous) is also analyzed and compared in this chapter.

6.2 Acoustic performance of the ventilation system driven by an Asynchronous motor

The airflow inside the duct and inside the motor area affects the acoustic measurements. In order to overcome the direct contact of the air with the membrane of the microphone, a special foam ball was installed at the tip of the microphone as shown in Figure 6-1.

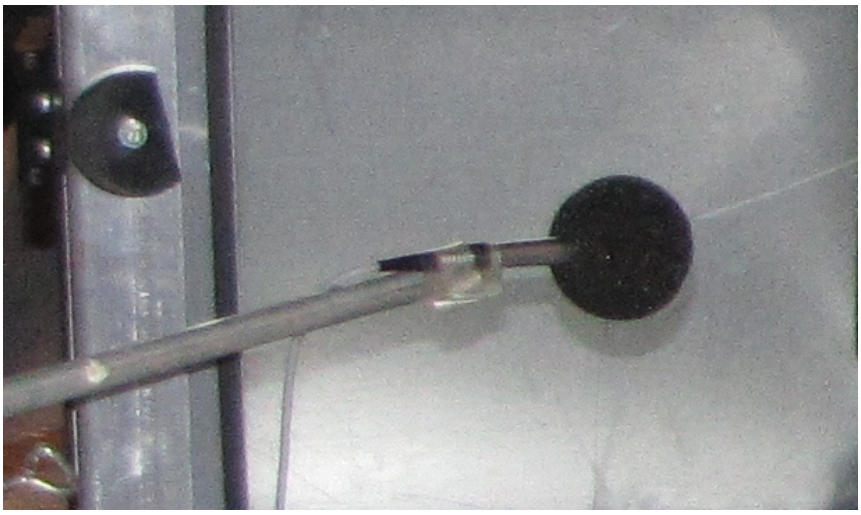

Figure 6-1 Microphone with the foam ball used for the acoustic measurements

As previously mentioned, a special anechoic termination was constructed on the ventilation system conform the Danish standard (EN ISO 5136) [75], in order to simulate the acoustic noise propagation in long ducts . In Figure 6-2 the schematic of the anechoic termination is presented. The purpose of the anechoic termination is to create a sufficient gradual change in the duct area to suppress the reflections of the sound waves back in the duct.

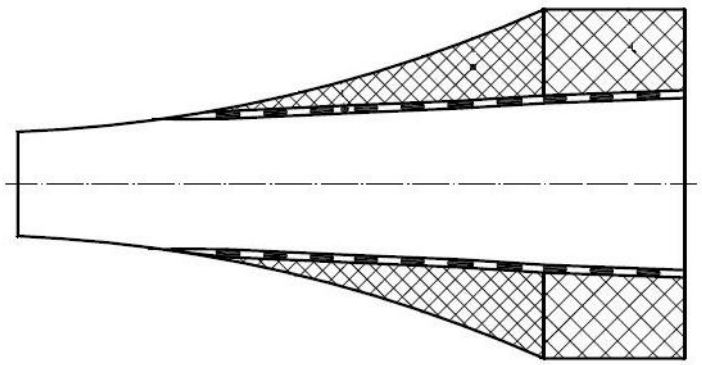

Figure 6-2 Schematic of the anechoic termination for the ventilation system

Finally, the test system used for the acoustic measurements is shown in the Figure 6-3.

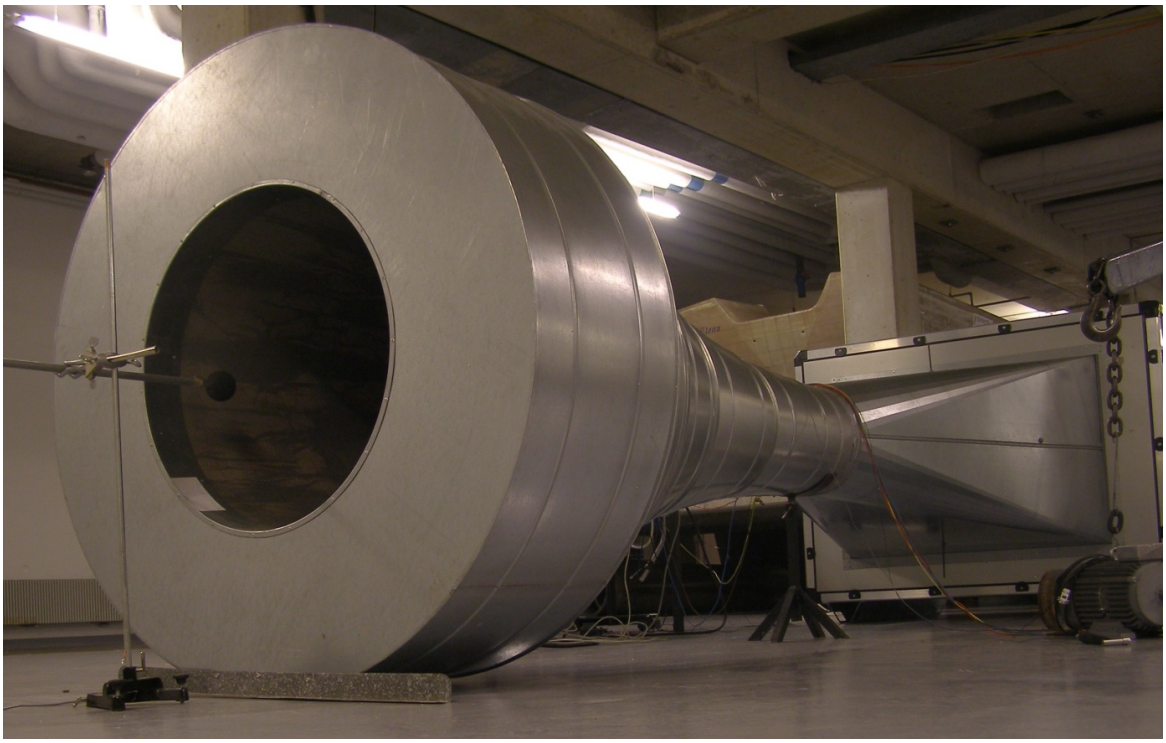

Figure 6-3 Anechoic termination for the ventilation system

The acoustic noise, vibration, and the motor current were measured when the fan was driven by open loop U/f motor control algorithm. Four different modulation methods were tested; the measurement of each modulation method is grouped in a study case. For each modulation method three operating points were chosen: at 150RPM (5Hz fundamental), at 750RPM (25Hz fundamental), and at 1350RPM (45Hz fundamental).

6.2.1 Study case 1:

SVM at a speed of 150RPM:

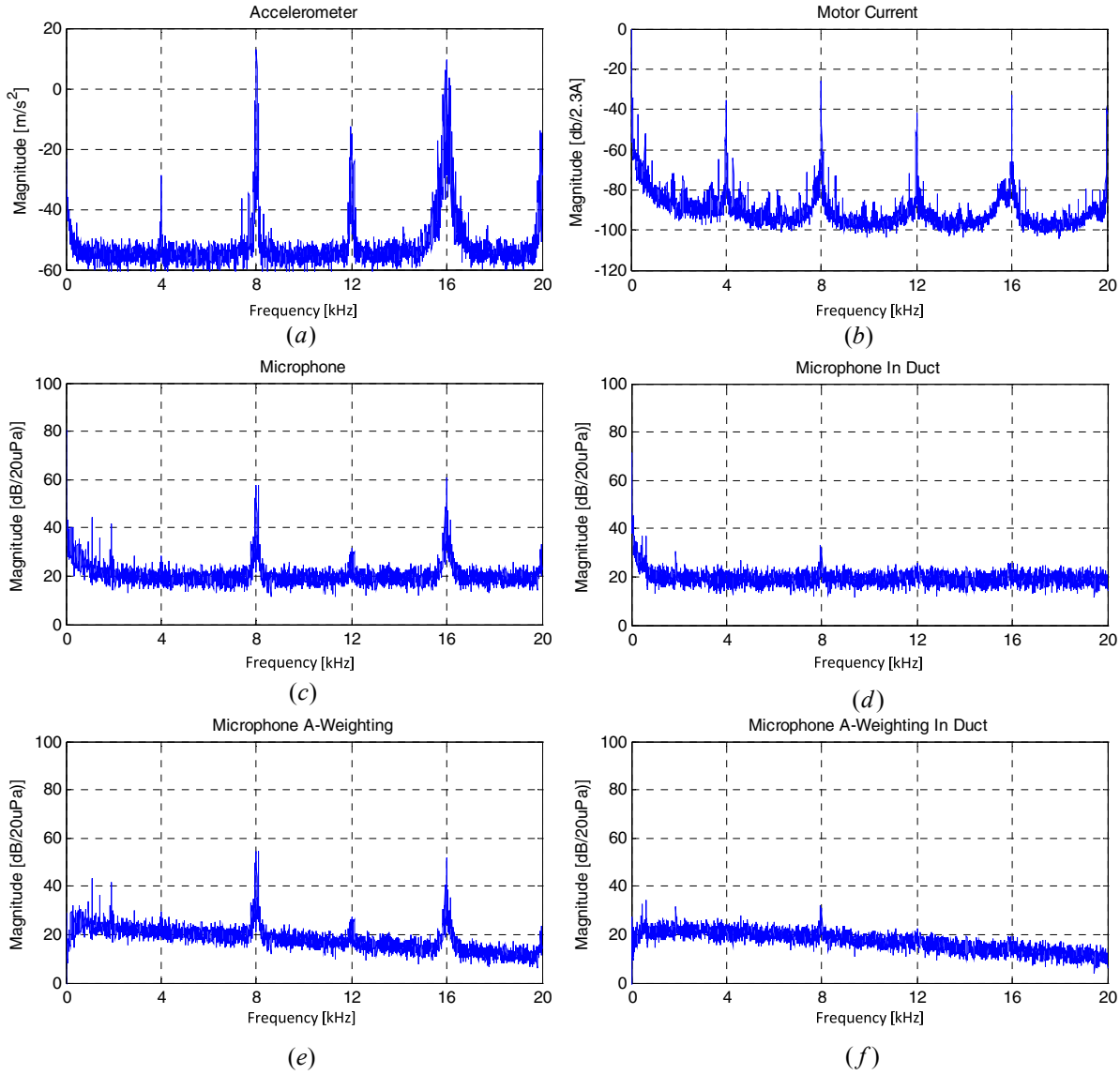

Figure 6-4 Measured spectra of: vibrations on the motor shell (a), motor current (b), acoustic noise near the ventilation system (c), acoustic noise inside the duct (d), A-weighted acoustic noise near the ventilation system (e), and A-weighted acoustic noise inside the duct (f) by using SVM at a speed of 150RPM

SVM at a speed of 750RPM:

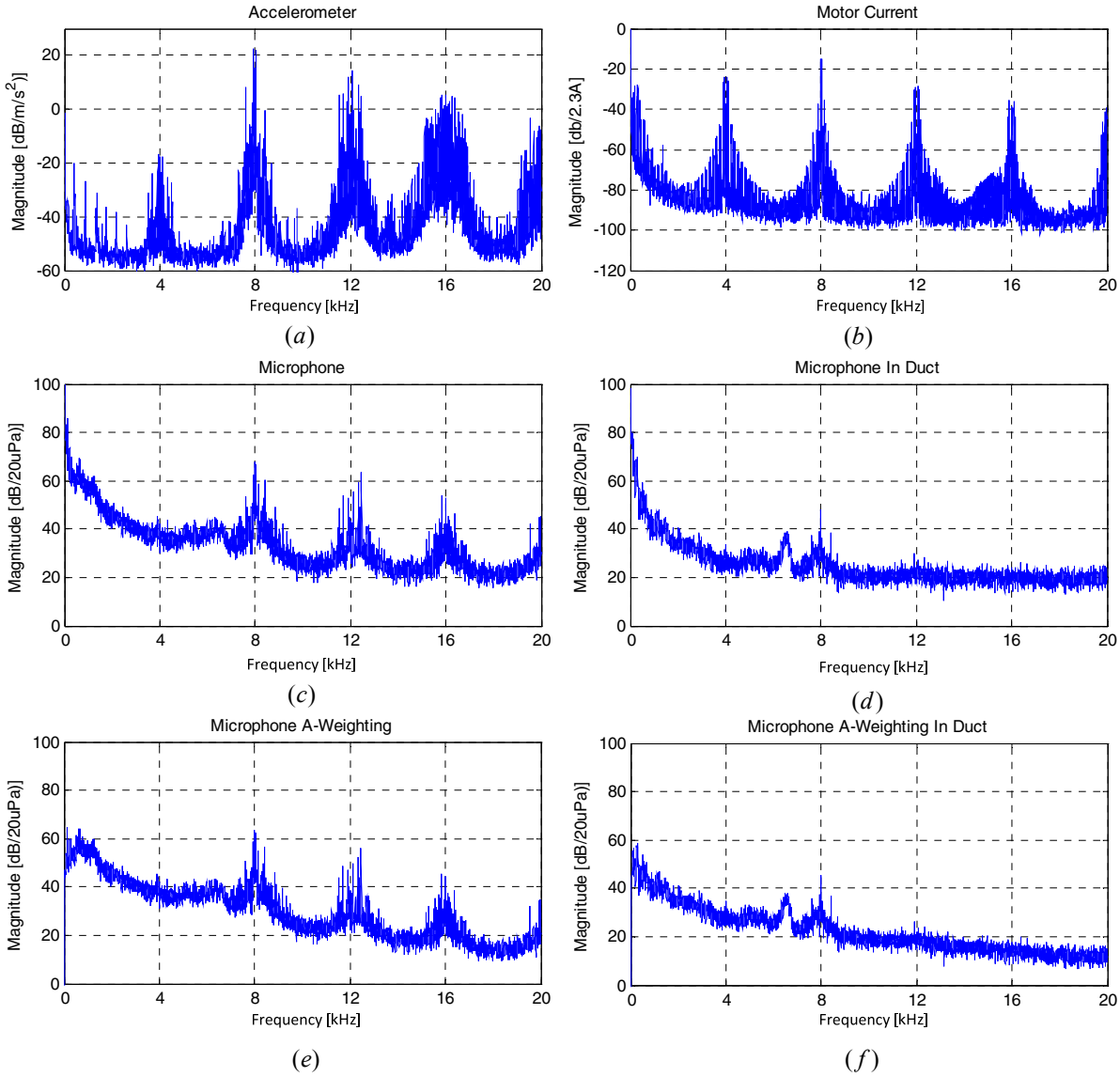

Figure 6-5 Measured spectra of: vibrations on the motor shell (a), motor current (b), acoustic noise near the ventilation system (c), acoustic noise inside the duct (d), A-weighted acoustic noise near the ventilation system (e), and A-weighted acoustic noise inside the duct (f) by using SVM at a speed of 750RPM

SVM at a speed of 1350RPM:

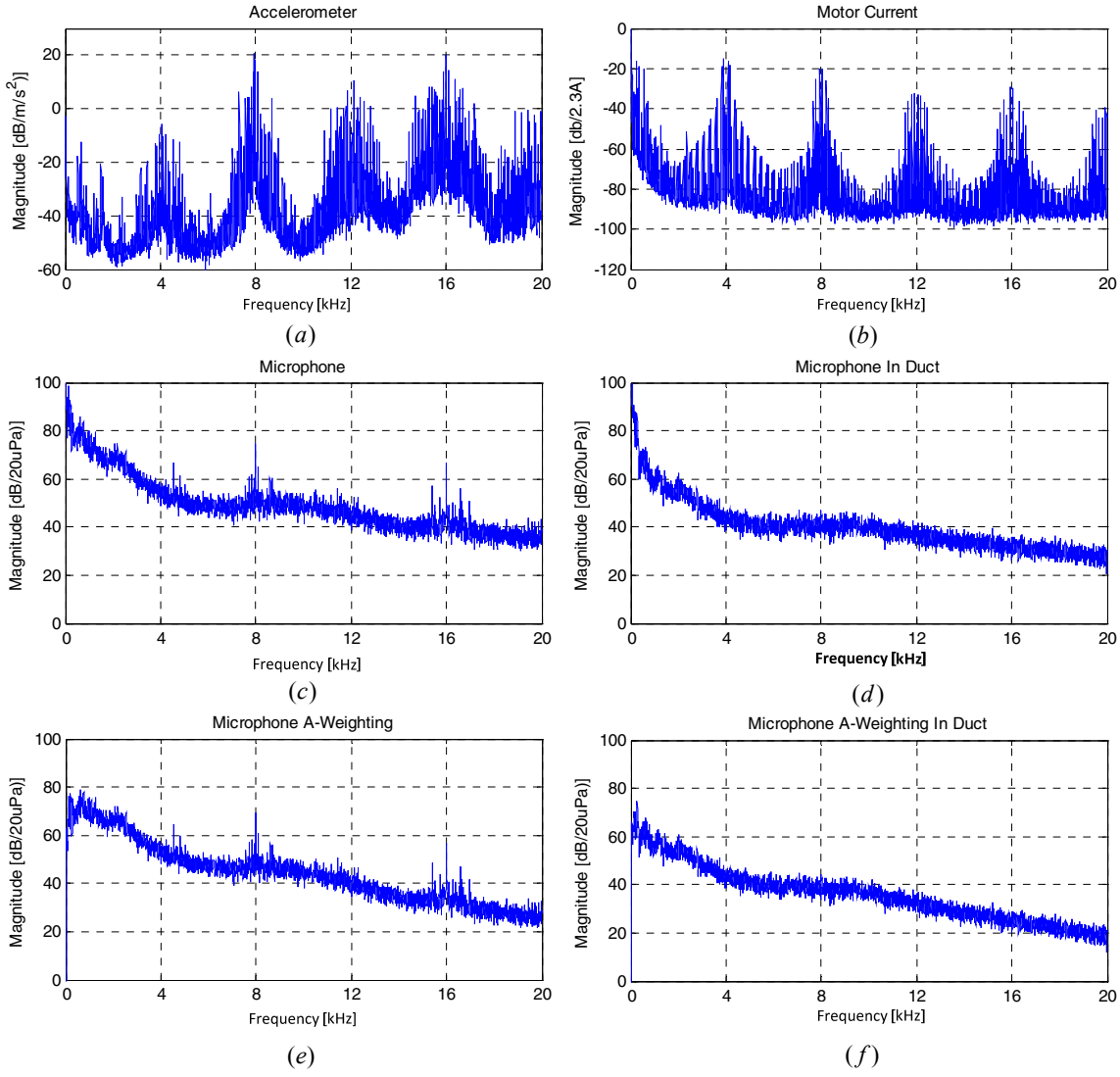

Figure 6-6 Measured spectra of: vibrations on the motor shell (a), motor current (b), acoustic noise near the ventilation system (c), acoustic noise inside the duct (d), A-weighted acoustic noise near the ventilation system (e), and A-weighted acoustic noise inside the duct (f) by using SVM at a speed of 1350RPM

As can be seen in Figure 6-4, Figure 6-5, and Figure 6-6 the discrete components are present in all of the measured spectra of the motor current, vibration and acoustic noise. At 150RPM and 750RPM the discrete components caused by the modulation are present in the acoustic spectra measured inside the duct with an amplitude of 10-30dB. This means that the whistling noise is transmitted inside the ventilated area through the ducts. As the mathematical analysis of the acoustic spectra presented in Chapter 3 shows, at high speed (above RPM) the discrete components are not concentrated close to the modulation frequency, and the sideband components have also higher amplitude. This wider distribution of the discrete components together with the increased back-

ground white noise, mainly created by the airflow, overpower the discrete components from the acoustic spectra. At 750RPM the airflow introduces a spectral component around 5 kHz in the acoustic spectra measured inside the duct. This spectral component has an amplitude of 35 dB, and is present in all the measurements with the same amplitude, at the speed of 750RPM.

6.2.2 Study case 2:

RCF-PWM at a speed of 150RPM:

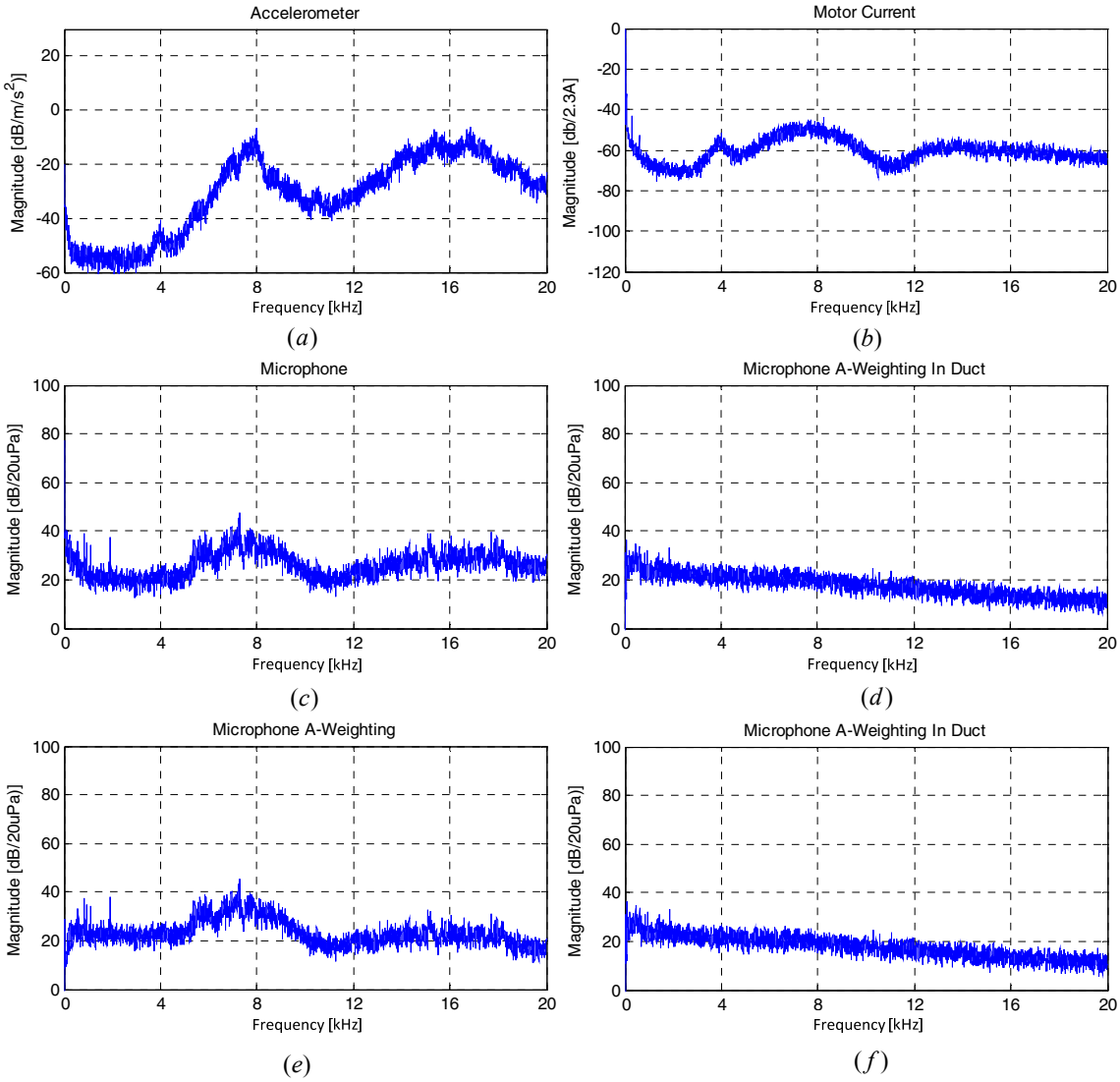

Figure 6-7 Measured spectra of: vibrations on the motor shell (a), motor current (b), acoustic noise near the ventilation system (c), acoustic noise inside the duct (d), A-weighted acoustic noise near the ventilation system (e), and A-weighted acoustic noise inside the duct (f) by using RCF-PWM at a speed of 150RPM

RCF-PWM at a speed of 750RPM:

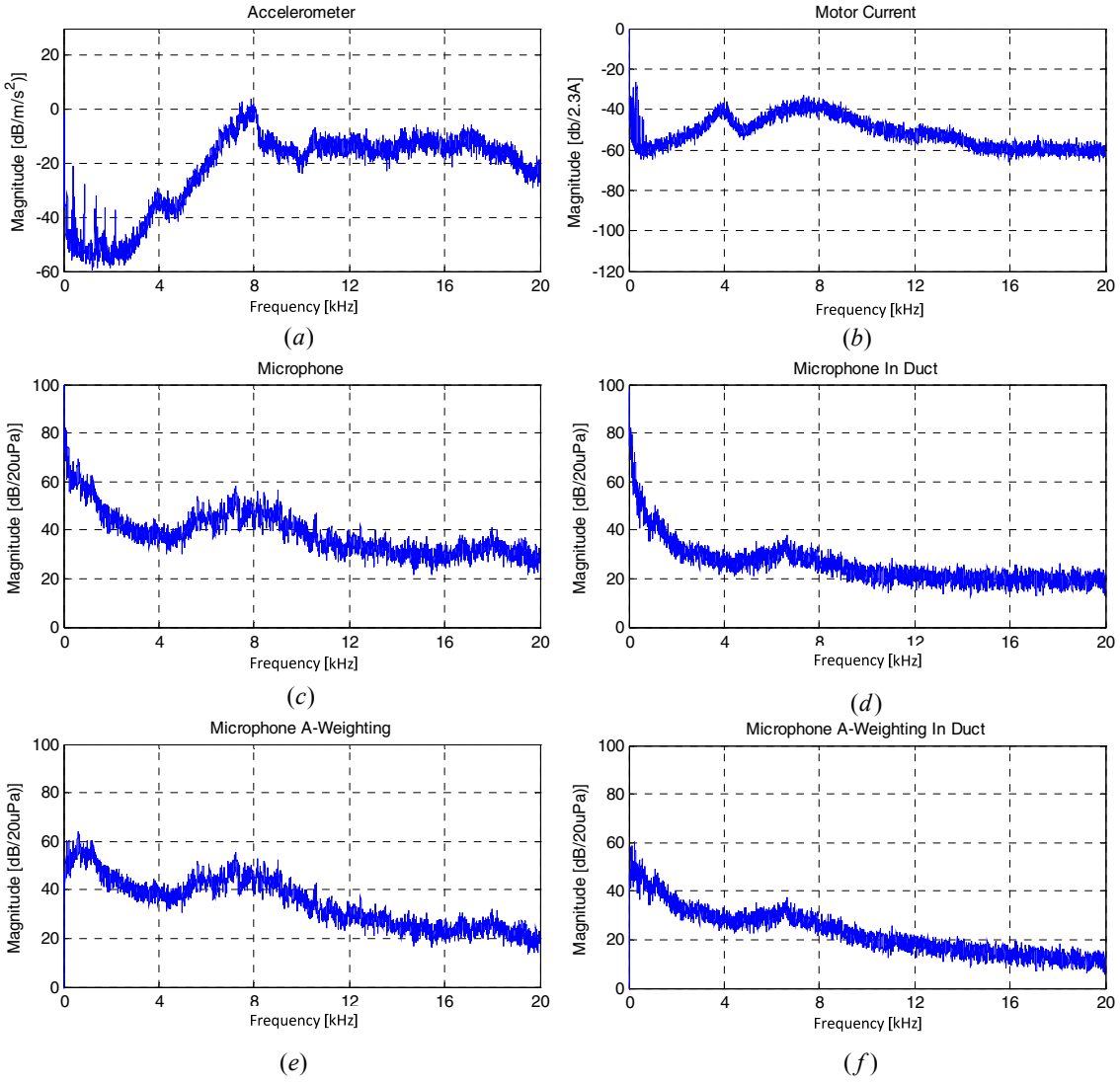

Figure 6-8 Measured spectra of: vibrations on the motor shell (a), motor current (b), acoustic noise near the ventilation system (c), acoustic noise inside the duct (d), A-weighted acoustic noise near the ventilation system (e), and A-weighted acoustic noise inside the duct (f) by using RCF-PWM at a speed of 750RPM

RCF-PWM at a speed of 1350RPM:

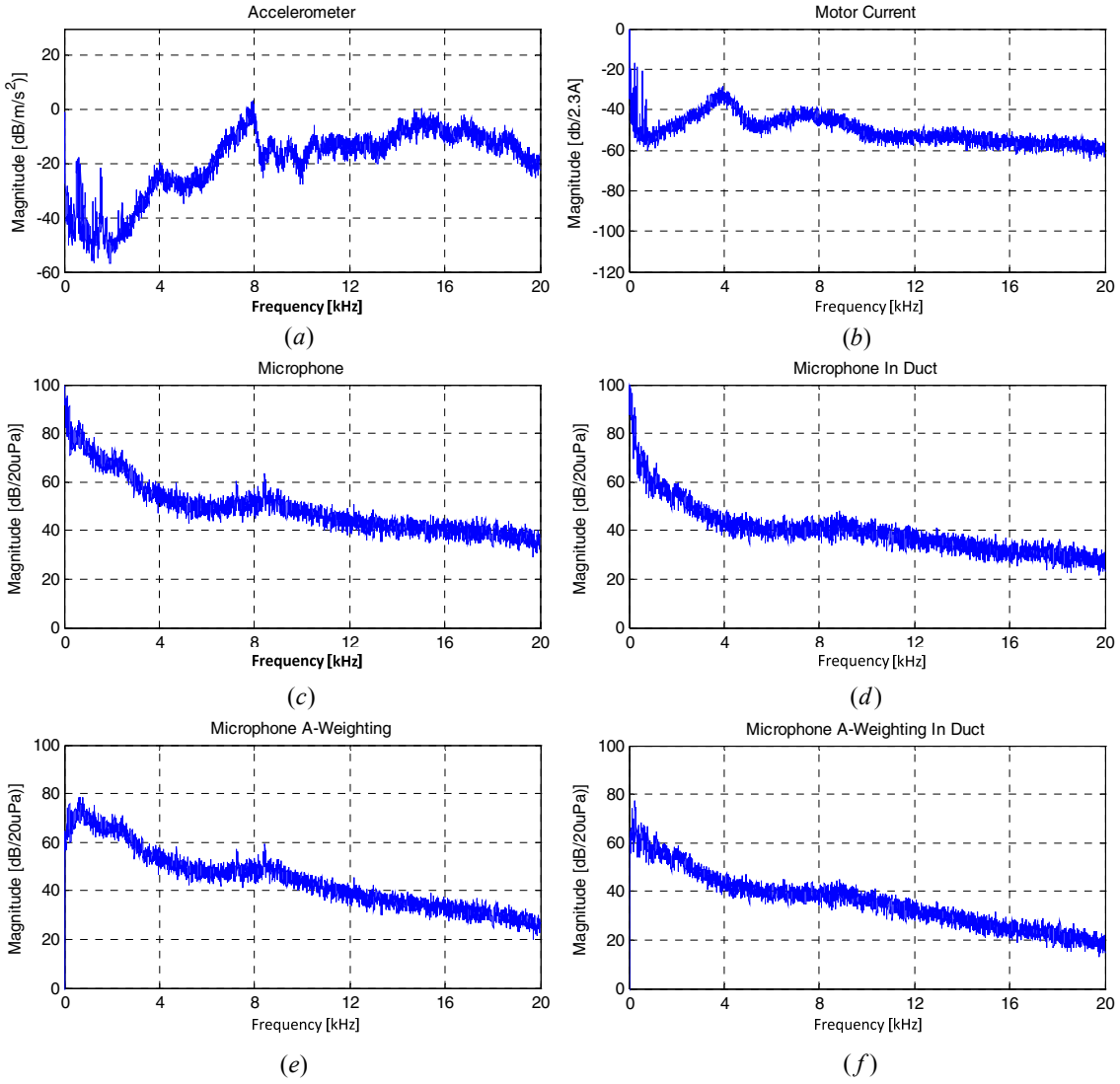

Figure 6-9 Measured spectra of: vibrations on the motor shell (a), motor current (b), acoustic noise near the ventilation system (c), acoustic noise inside the duct (d), A-weighted acoustic noise near the ventilation system (e), and A-weighted acoustic noise inside the duct (f) by using RCF-PWM at a speed of 1350RPM

The oldest modulation technique, which was developed in order to ameliorate the acoustic noise generated by modulation, performs very well for the analyzed ventilation system. The measurement results presented in Figure 6-7, Figure 6-8, and Figure 6-9 shows that the discrete components disappear from the spectrum, independently on the fundamental frequency. The method is a good alternative due to easy to implementation in open loop applications, but in case of closed loop applications it creates problems.

Next, the FCF-RPWM methods are tested, methods which are easy to integrate in closed loop applications. As it was mentioned in the first study case, at a speed of 750RPM, the airflow introduces a frequency component in the acoustic spectra meas-

ured inside the duct. This frequency component remains present when RCF-PWM is used, but it is not distinguishable, because of the increased noise level in its neighborhood, caused by the spread switching harmonics.

6.2.3 Study case 3:

RPP-PWM at a speed of 150RPM:

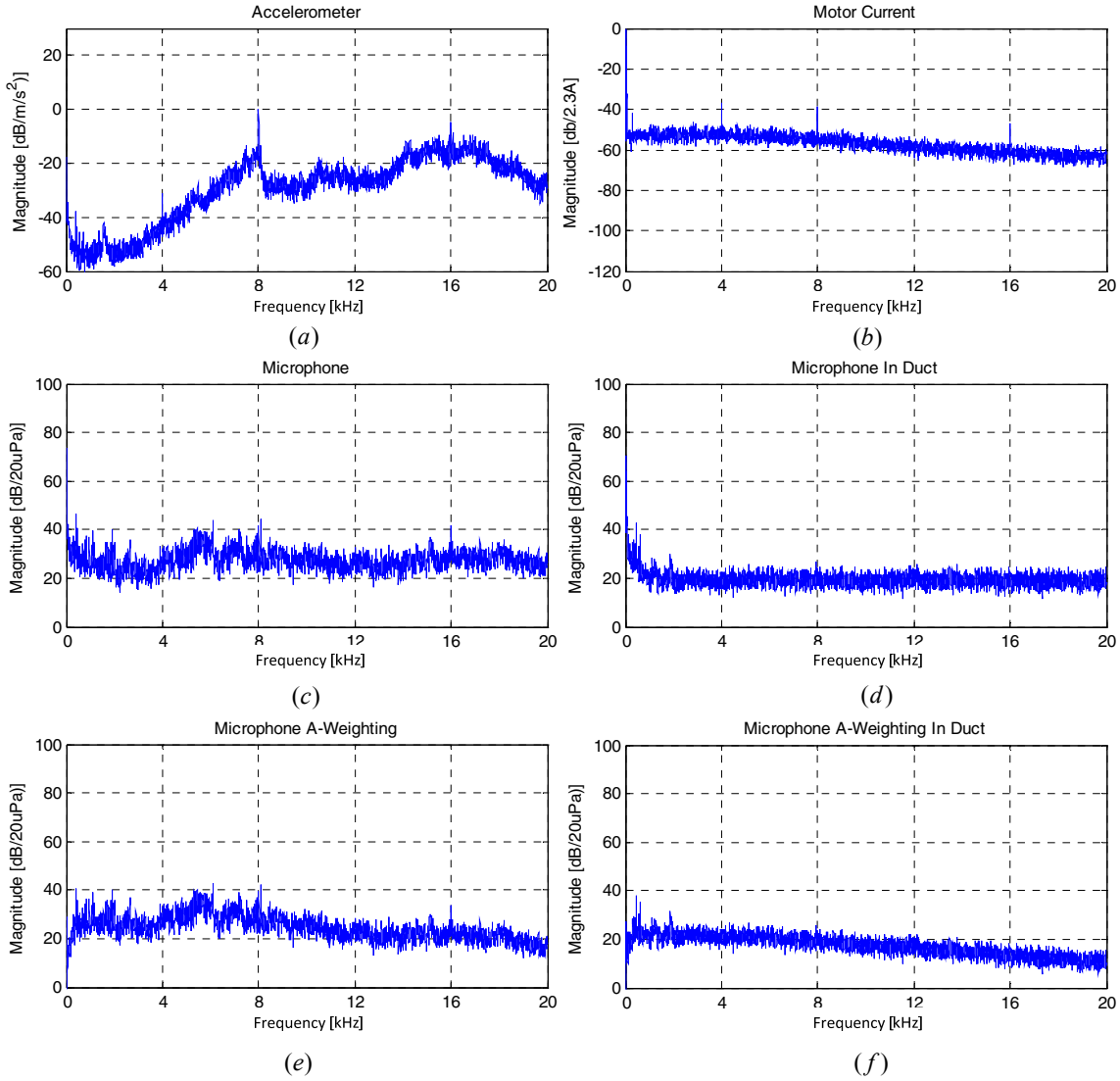

Figure 6-10 Measured spectra of: vibrations on the motor shell (a), motor current (b), acoustic noise near the ventilation system (c), acoustic noise inside the duct (d), A-weighted acoustic noise near the ventilation system (e), and A-weighted acoustic noise inside the duct (f) by using RPP-PWM at a speed of 150RPM

RPP-PWM at a speed of 750RPM:

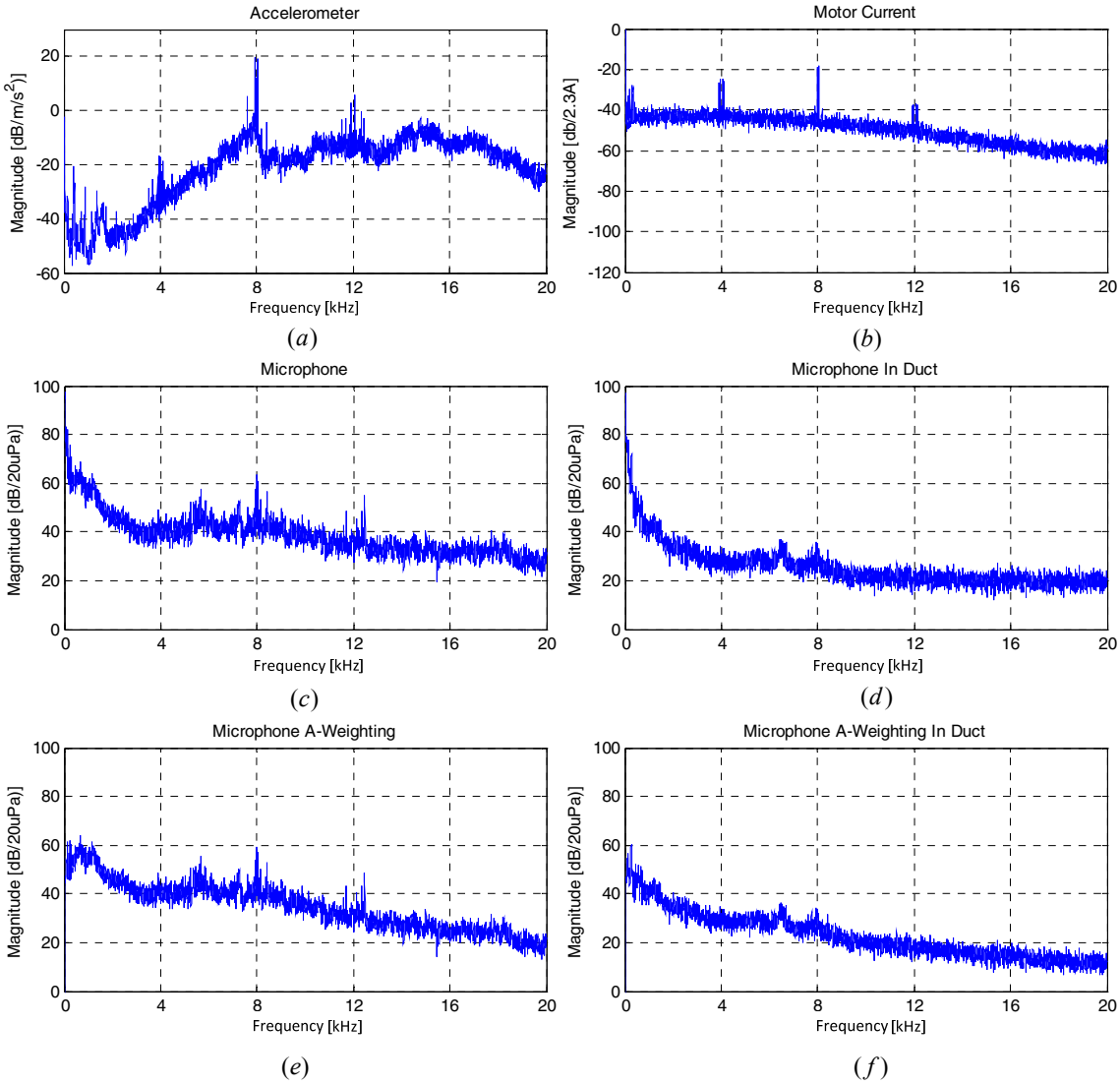

Figure 6-11 Measured spectra of: vibrations on the motor shell (a), motor current (b), acoustic noise near the ventilation system (c), acoustic noise inside the duct (d), A-weighted acoustic noise near the ventilation system (e), and A-weighted acoustic noise inside the duct (f) by using RPP-PWM at a speed of 750RPM

RPP-PWM at a speed of 1350RPM:

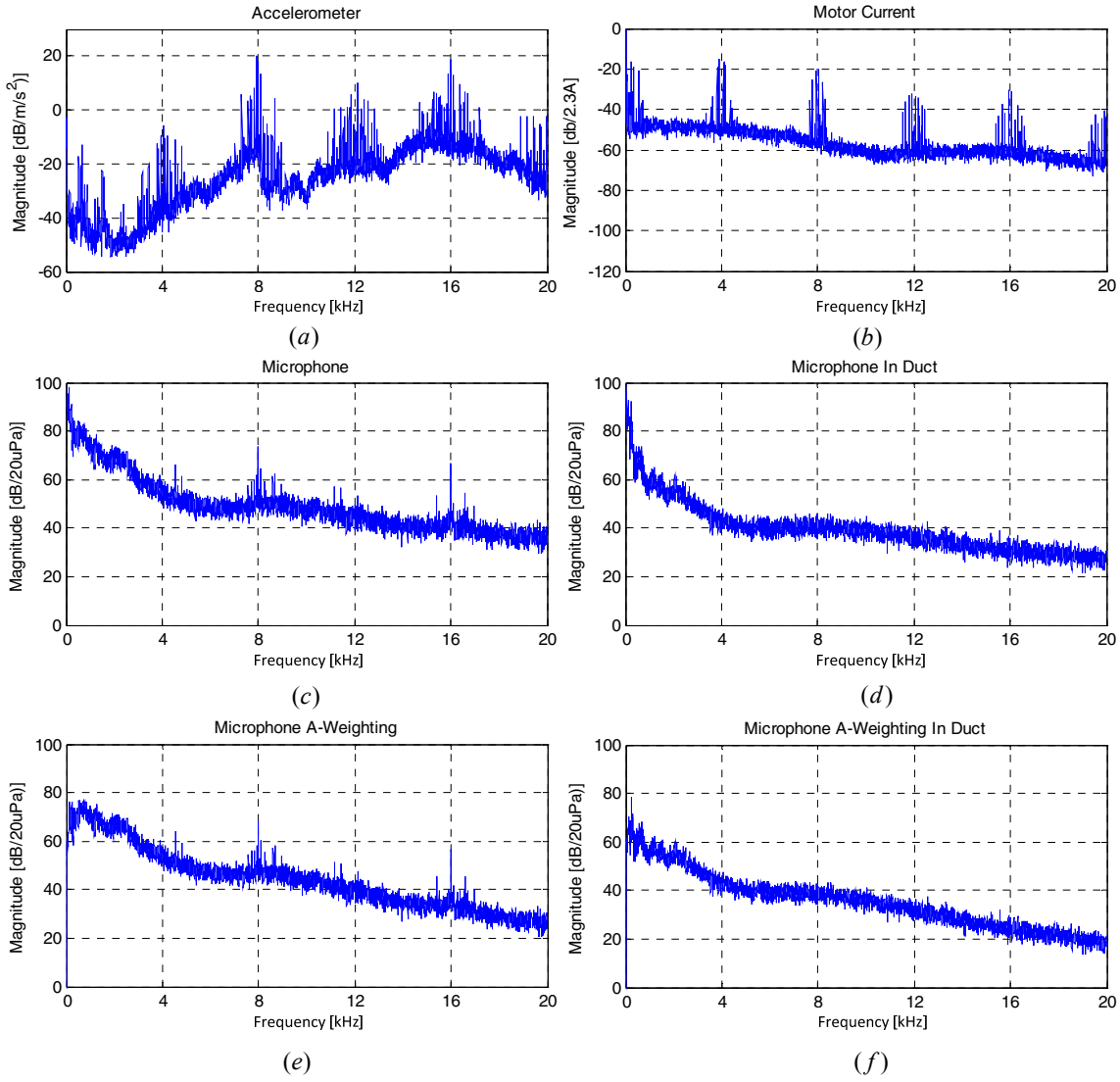

Figure 6-12 Measured spectra of: vibrations on the motor shell (a), motor current (b), acoustic noise near the ventilation system (c), acoustic noise inside the duct (d), A-weighted acoustic noise near the ventilation system (e), and A-weighted acoustic noise inside the duct (f) by using RPP-PWM at a speed of 1350RPM

The RPP-PWM method is only effective at low fundamental frequency; the discrete components are nearly disappeared in the measurements at 150RPM from Figure 6-10. From the measurements at 750RPM (Figure 6-11) can be seen that the discrete components start to show their presents. By increasing the speed above 750RPM, the airflow starts to increase rapidly due to the exponential relation between the rotor speed and airflow rate. The noise produced by the airflow therefore overpowers the acoustic noise generated by the inverter. In conclusion, the annoying whistle noise is decreased by RPP-PWM when the ventilation system runs at low speed, and is over-

powered by the airflow noise at nominal speed. However, at around half the nominal speed, the discrete components are present in the acoustic spectra.

6.2.4 Study case 4:

AC-RPWM at a speed of 150RPM:

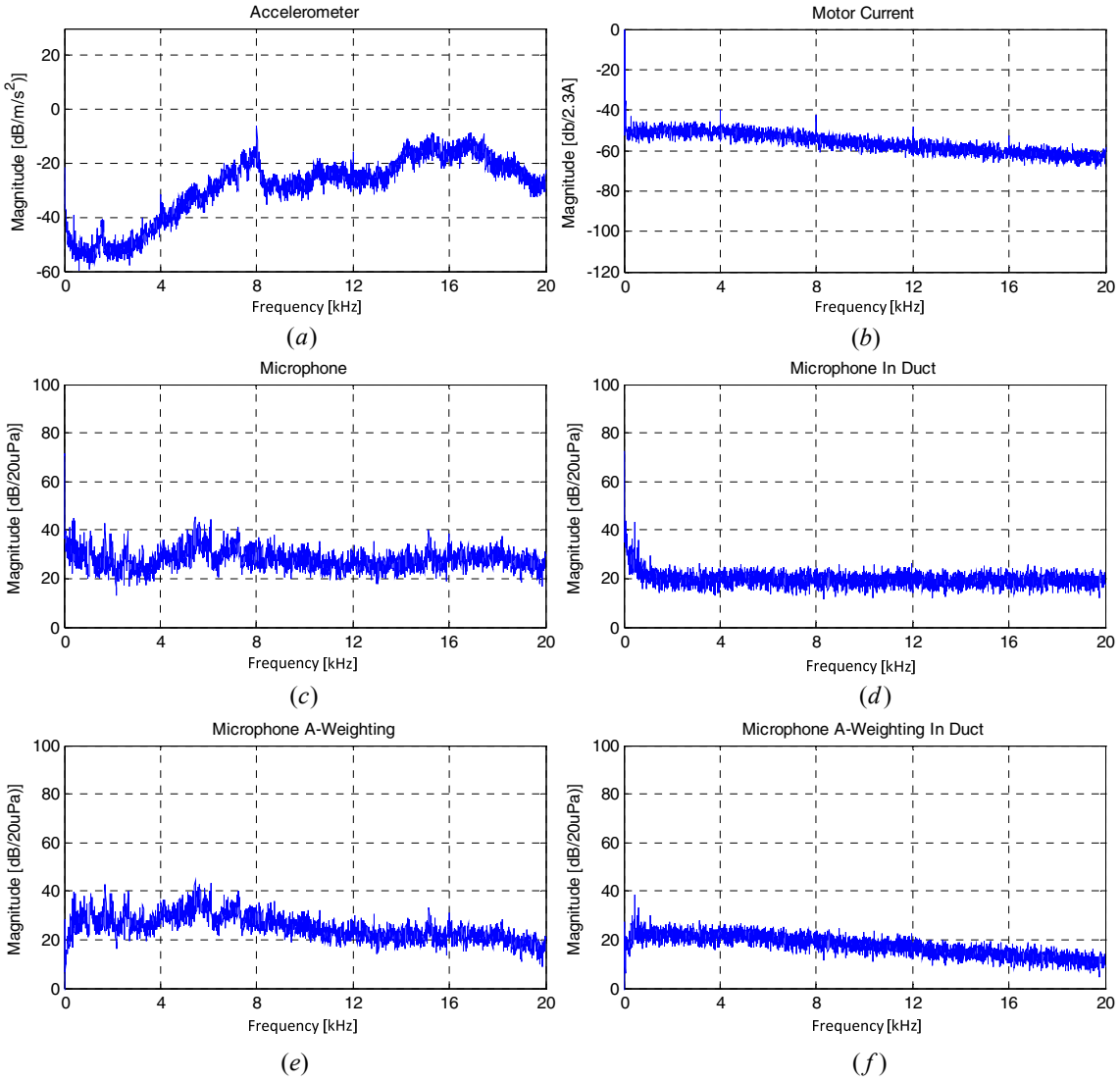

Figure 6-13 Measured spectra of: vibrations on the motor shell (a), motor current (b), acoustic noise near the ventilation system (c), acoustic noise inside the duct (d), A-weighted acoustic noise near the ventilation system (e), and A-weighted acoustic noise inside the duct (f) by using AC-RPWM at a speed of 150RPM

AC-RPWM at a speed of 750RPM:

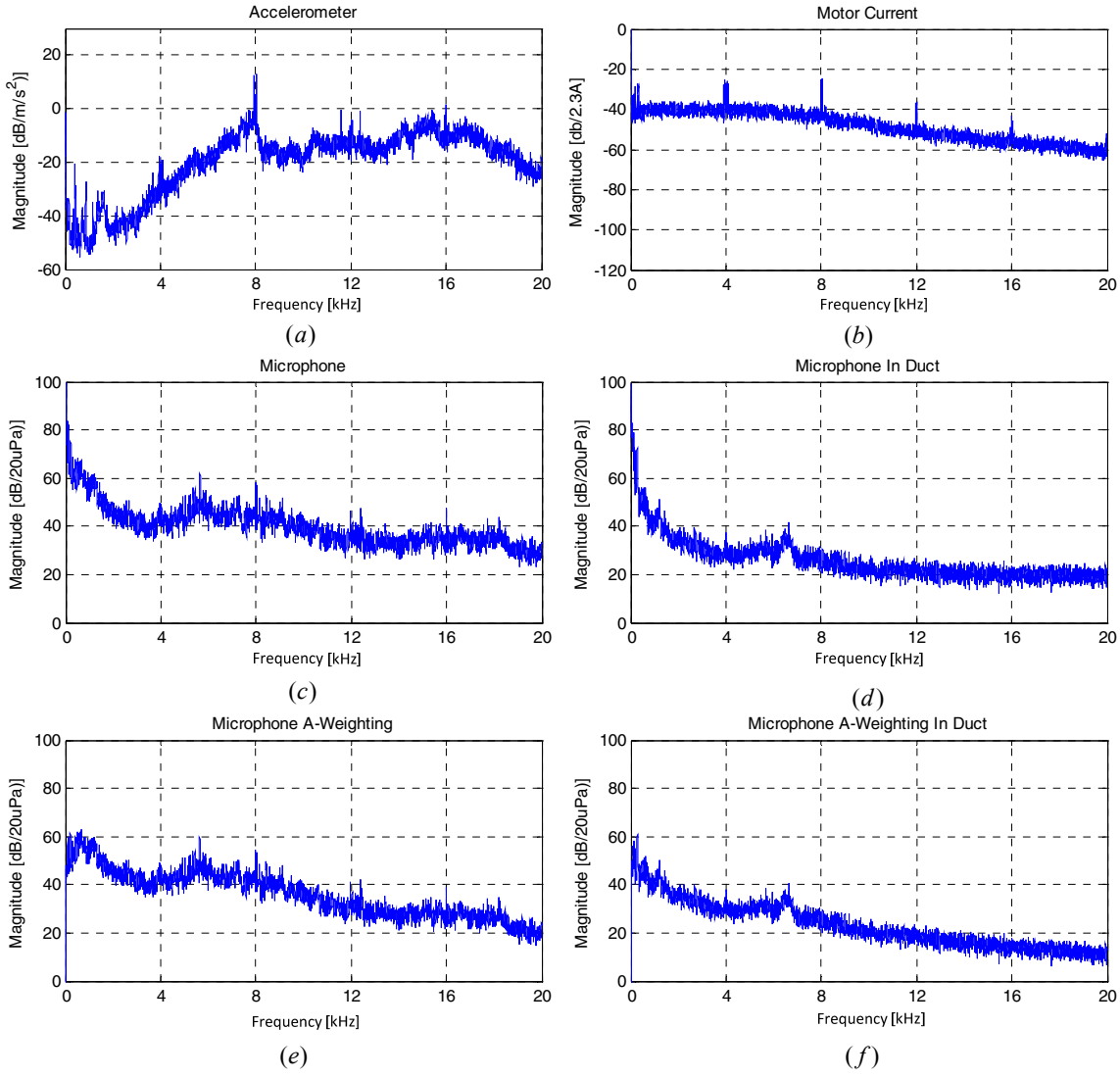

Figure 6-14 Measured spectra of: vibrations on the motor shell (a), motor current (b), acoustic noise near the ventilation system (c), acoustic noise inside the duct (d), A-weighted acoustic noise near the ventilation system (e), and A-weighted acoustic noise inside the duct (f) by using AC-RPWM at a speed of 750RPM

AC-RPWM at a speed of 1350RPM:

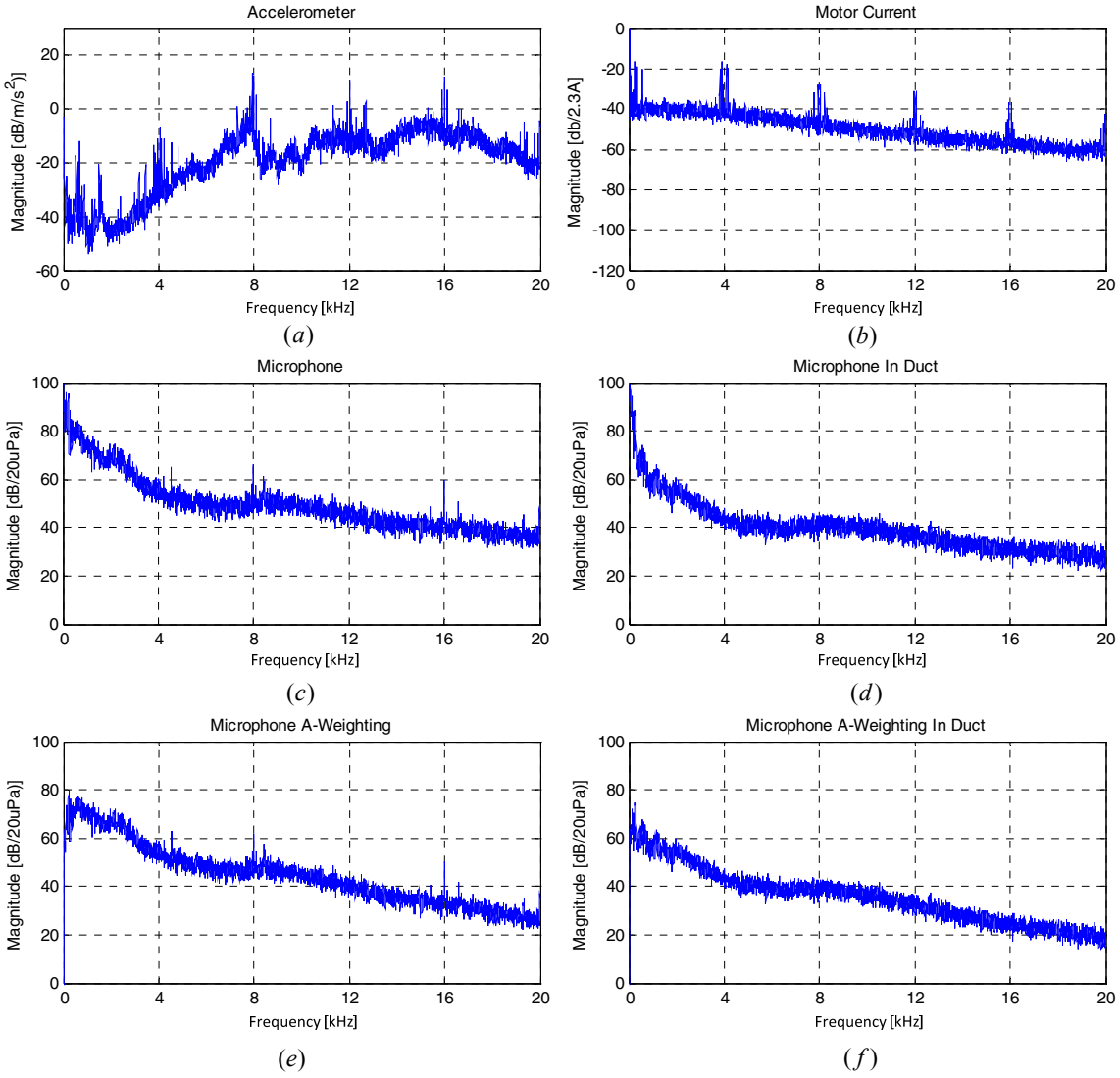

Figure 6-15 Measured spectra of: vibrations on the motor shell (a), motor current (b), acoustic noise near the ventilation system (c), acoustic noise inside the duct (d), A-weighted acoustic noise near the ventilation system (e), and A-weighted acoustic noise inside the duct (f) by using AC-RPWM at a speed of 1350RPM

The advantage of the AC-RPWM compared to RPP-PWM is that the discrete components cannot be distinguished from the background noise even around half the nominal speed. The performance of AC-RPWM is approximately the same as the performance of the RCF-PWM, which means the whistling noise created by the modulation is not audible at any speed.

6.3 PMSM versus Asynchronous motor from acoustic point of view

The efficiency of the permanent magnet synchronous motors is higher compared to the asynchronous motors, creating a trend to replace the asynchronous motor from the HVAC applications. In this section the acoustic behavior of the synchronous motor compared to the very popular asynchronous motor is analyzed.

The main difference between a PMSM and an asynchronous motor consist in the construction of the rotor. In case of PMSM the rotor field is generated by permanent-magnets thus the rotor does not need external energy. In most of the cases, the asynchronous motors are equipped with a squirrel-cage rotor.

Due to the fact the acoustic noise generated by electrical motors depends on their mechanical structure, it is difficult to compare two motors with different structure form acoustic noise point of view. To minimize the difference between the structures of the motors, two identical asynchronous motors have been used, having the squirrel-cage rotor exchanged to a permanent magnet rotor in one of them. Figure 6-16 presents a picture of the synchronous and asynchronous motors used for the experiments. As it can be seen from the picture, there is no visible difference between the two motors.

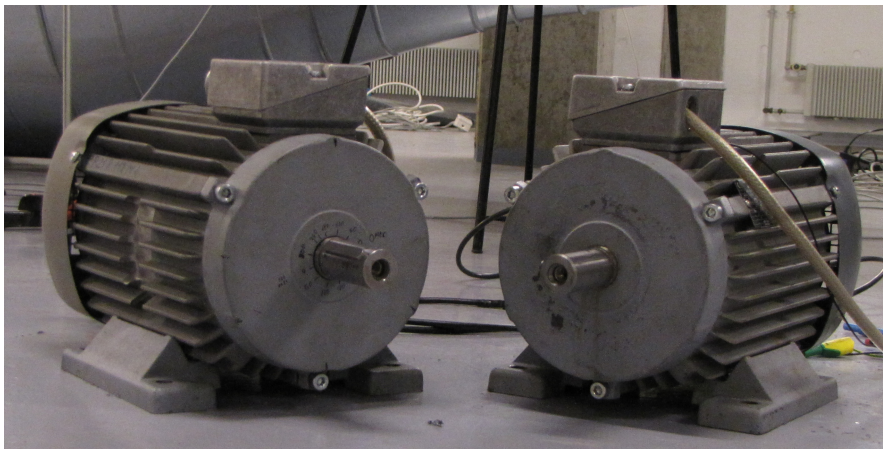

Figure 6-16 Synchronous motor (left), Asynchronous motor (right)

The mechanical structure of the motor can be characterized by measuring the frequency response of the vibrations to a flat spectrum current excitation, technique presented in details in the previous chapter. Figure 6-17 presents the measured frequency response of the two motors, when the motors are excited by using RPWM technique. As it was concluded in [45, 76], the rotor coupled to the stator through the end-shield introduces some new frequency components, mainly into the low frequency range of the acoustic spectra. The main focus in this thesis is on the modulation frequency region (2-10 kHz), where the frequency responses of the two motors are similar. Moreover, the human ear has high attenuation on the perception of the low frequency noise. It can be concluded here that the response of the two motor structures to a force excitation is similar.

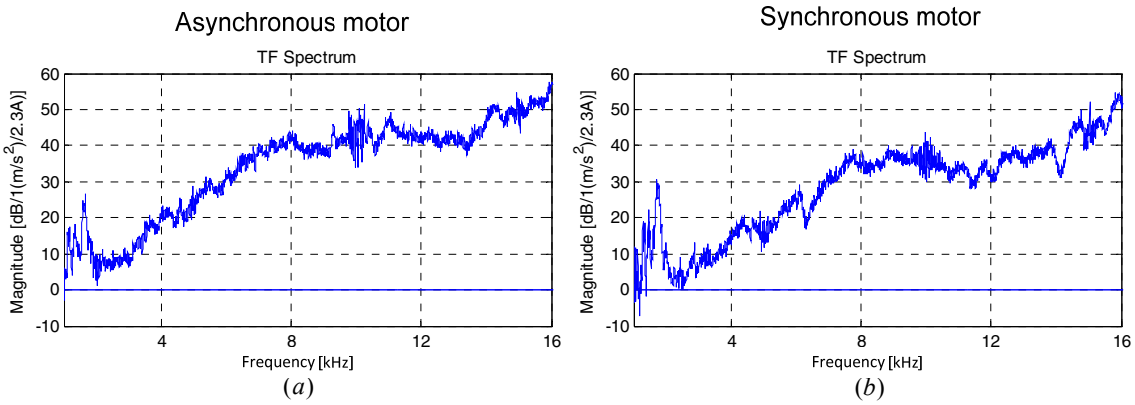

Figure 6-17 Frequency response of the asynchronous (a) and the synchronous motor (b)

For the experimental tests the asynchronous motor was driven by an open loop U/f algorithm. Because the PM synchronous motor is not stable in open loop U/f control, field oriented motor control was implemented, the block scheme was presented in Figure 4-19 . From acoustic point of view, there is minimal difference between the U/f and field oriented control strategies. The motors were tested without load. To obtain the similar current waveform the PM synchronous magnet motor was over-magnetized. This low frequency current component (25 and 50 Hz) does not change the sound of the motor.

Another factor that can have an influence on the acoustic spectra is the increased current ripple, which is around 1.5 times larger in case of the synchronous motor as it can be seen in Figure 6-18.

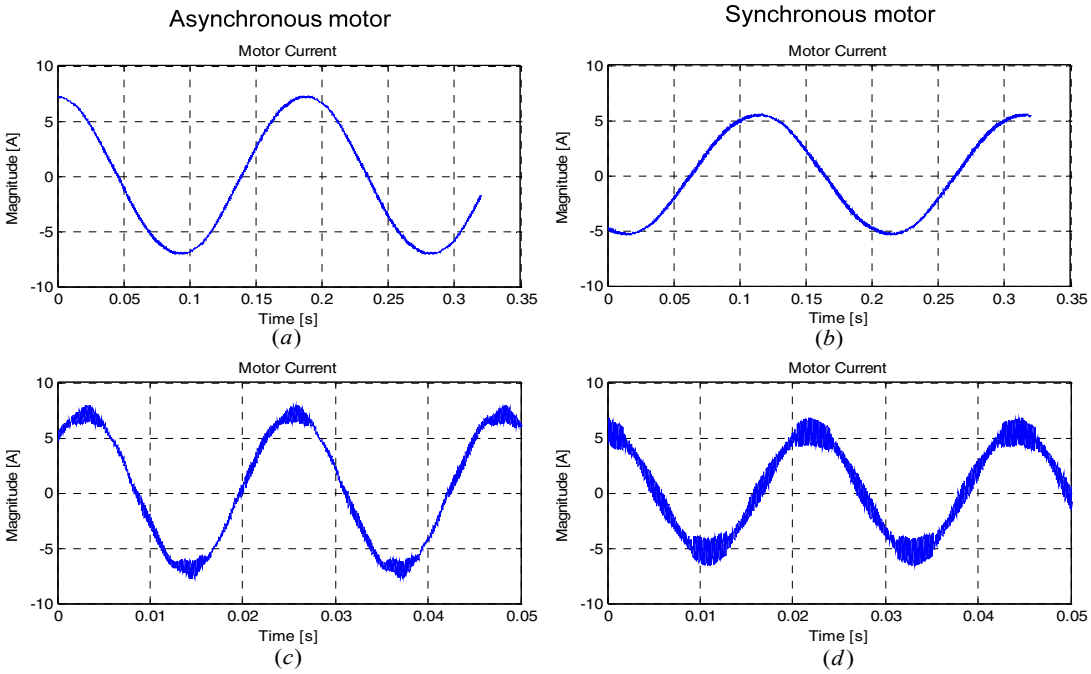

Figure 6-18 Measured motor current in time domain: asynchronous motor with 5Hz fundamental frequency (a), synchronous motor with 5Hz fundamental frequency (b), asynchronous motor with 45Hz fundamental frequency (c), and synchronous motor with 45Hz fundamental frequency (d)

Both of the motors have two pole pairs, at nominal speed the frequency of the current is 50Hz. This 50Hz low frequency component in the current spectra creates a frequency component at 100Hz in the acoustic spectra. The human ear can hardly hear this 100Hz low frequency component, which means that the acoustic noise generated by the motors is mainly characterized by the extra current ripple caused by the modulation.

As presented in section 3.4, the vibrations on the motor shell are mainly caused by the radial force [33], which depends on the current in the windings. By using the simplified setup presented in section 3.4, and neglecting the nonlinearities, the force in the air-gap of the coil can be calculated with:

$$f = \frac{L^2 \cdot i^2}{2 \cdot \mu_0 \cdot A \cdot N^2} \tag{6.1}$$

where f is the radial force, μ_0 – magnetic permeability, A -cross sectional area of the magnetic path, N – number of wire turns, L – inductance.
The current from the coil can be expressed in function of the inductivity and voltage like:

$$U = L\frac{di}{dt} \Leftrightarrow i = \frac{1}{L}\int U dt \tag{6.2}$$

where U – is the voltage applied on the inductor.
Substituting (6.2) into (6.1):

$$f = \frac{L^2\left(\frac{1}{L}\int U dt\right)^2}{2 \cdot \mu_0 \cdot A \cdot N^2} = \frac{\left(\int U dt\right)^2}{2 \cdot \mu_0 \cdot A \cdot N^2} \tag{6.3}$$

Differentiating (6.3) in order to get the force ripple gives:

$$\frac{df}{dt} = \frac{\frac{d\left(\int U dt\right)^2}{dt}}{2 \cdot \mu_0 \cdot A \cdot N^2} = \frac{2 \cdot U \cdot \int U dt}{2 \cdot \mu_0 \cdot A \cdot N^2} \tag{6.4}$$

Equation (6.4) shows that the force ripple does not depend on the increased length of the air-gap in the coil. With other words, by increasing the air-gap, the inductance of the coil is decreased, which causes larger current ripple. However, in the same time the increased air-gap reduces the amplitude of the force, canceling the effect of the increased current ripple. Due to the fact the permeability of the permanent magnets is very close to the permeability of the air, it can be considered that in case of synchronous motor the air gap is larger with the thickness of the permanent magnets than the air gap from the asynchronous motor. Again, the presented statement is valid only for the ideal case. Nevertheless, the measurement results from Figure 6-19, Figure 6-20, and Figure 6-21 validate this statement. The acoustic noise generated by the analyzed PM synchronous motor is approximately the same as the noise generated by the

asynchronous motor; it is hard to distinguish by listening with ear, which motor operates.

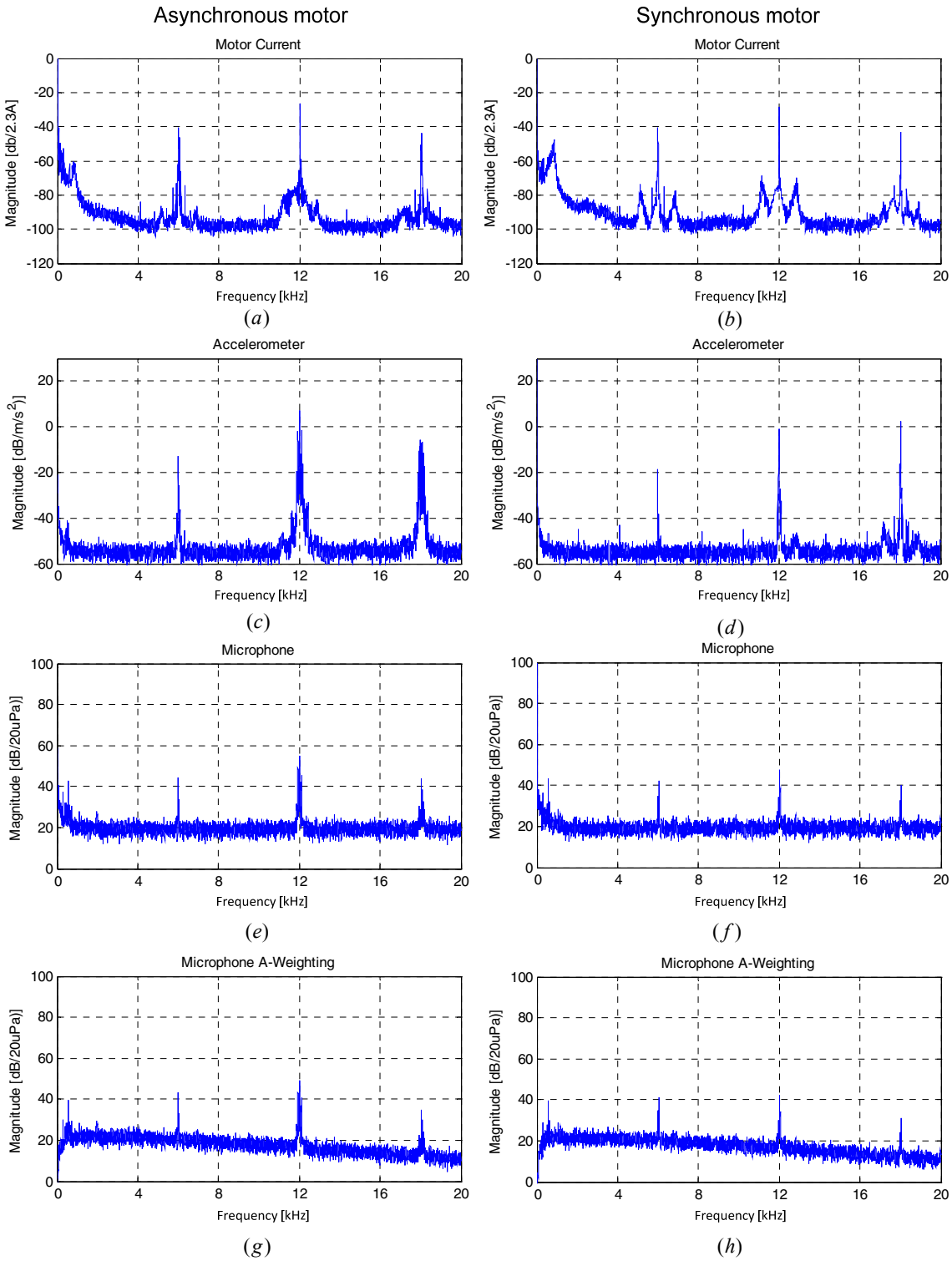

Figure 6-19 Measured spectrum of the motor current, vibration and acoustic noise at 150RPM on the asynchronous motor (left column) and synchronous motor (right column)

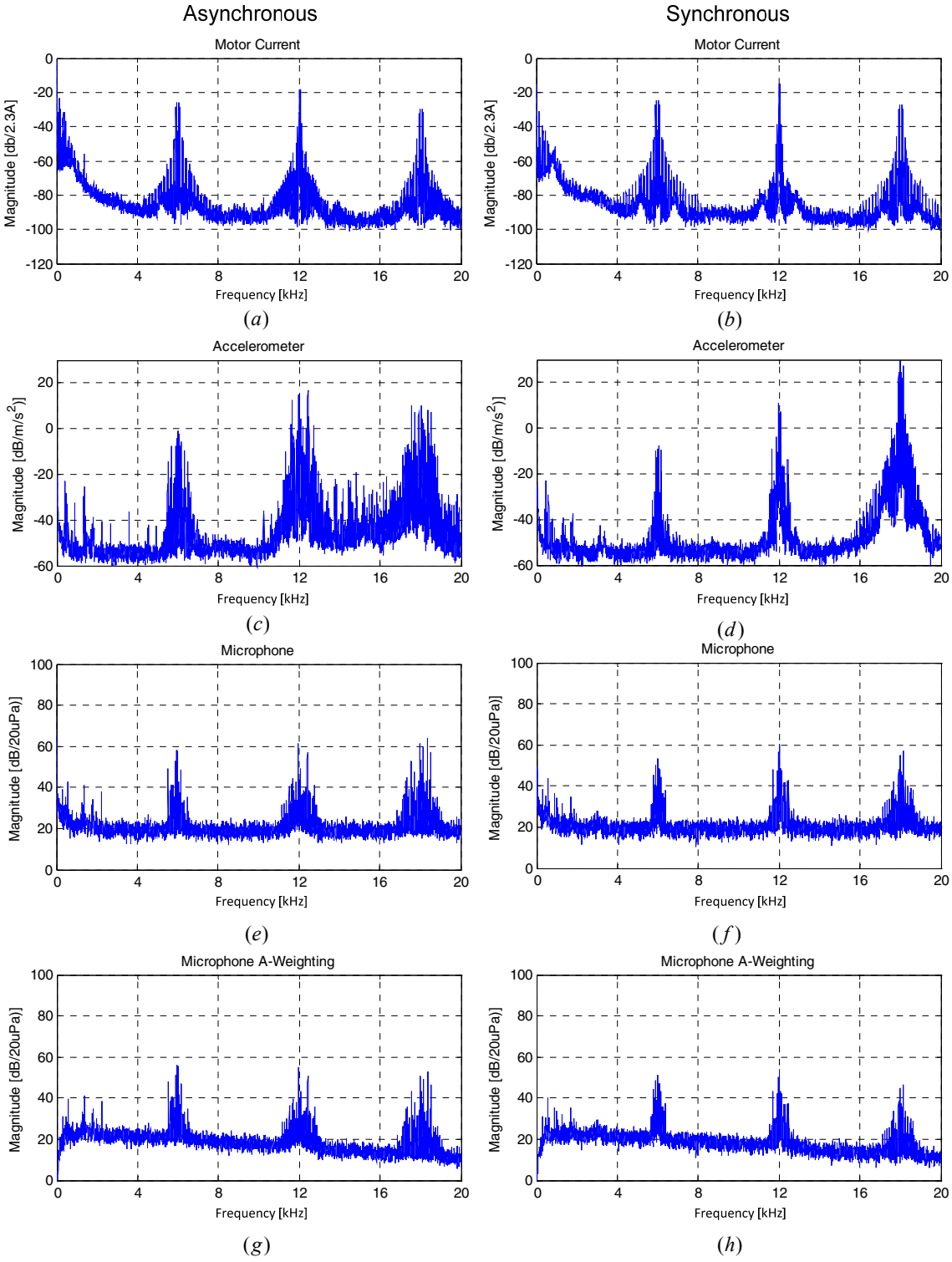

Figure 6-20 Measured spectrum of the motor current, vibration and acoustic noise at 750RPM on the asynchronous motor (left column) and synchronous motor (right column)

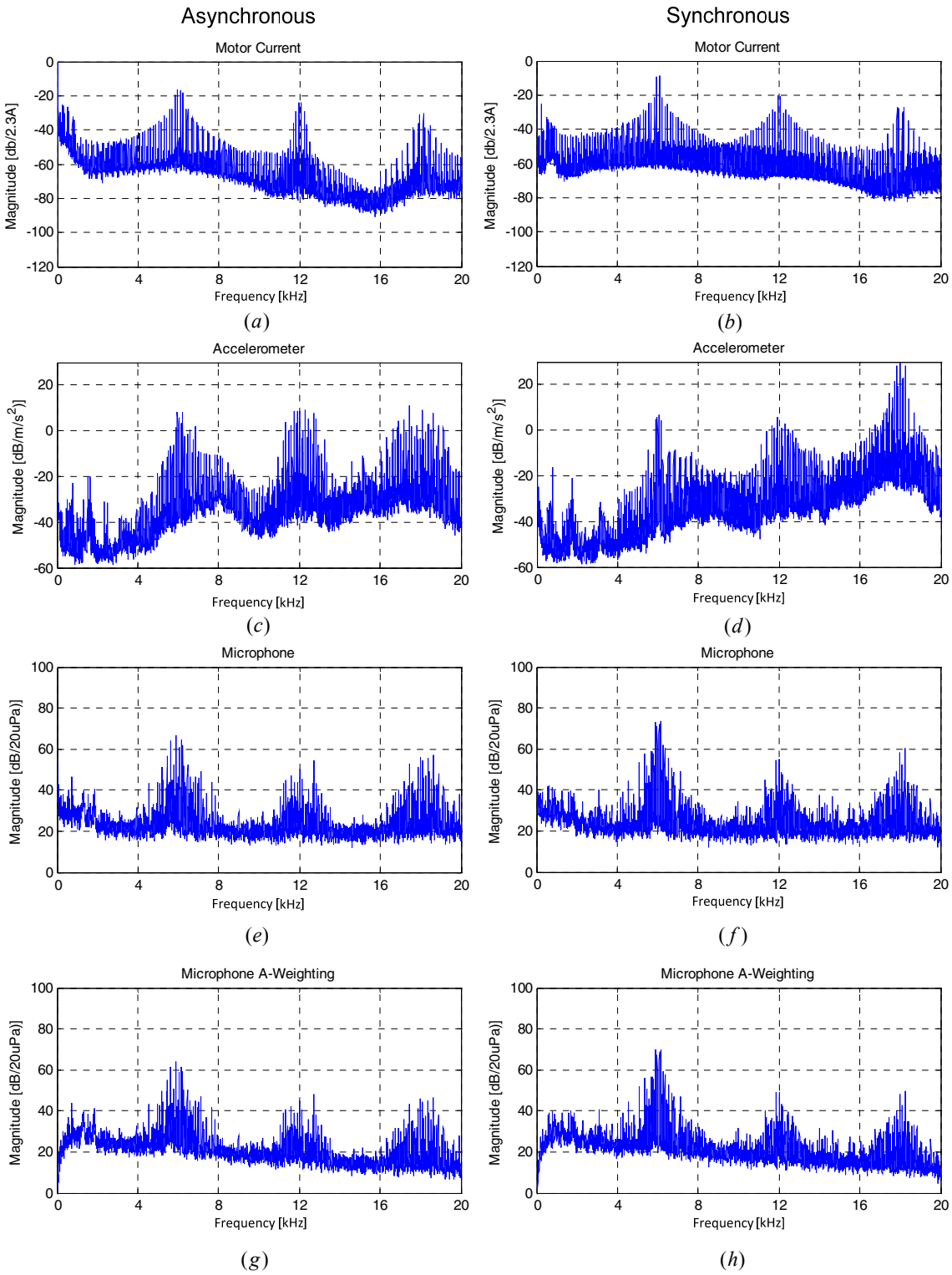

Figure 6-21 Measured spectrum of the motor current, vibration and acoustic noise at 1350RPM on the asynchronous motor (left column) and synchronous motor (right column)

6.4 Summary

In this chapter the acoustic performance of a ventilation system driven by random PWM inverter was presented. A special anechoic termination was installed on the ventilation system to simulate the acoustic noise transmitted into the ducts. The whistling noise generated by the SVM technique is present in both part of the ventilation system: near the motor and in the duct as well. By using the random modulation method presented in Chapter 4, the whistling noise disappears from the acoustic spectra.

The airflow in the ventilation system creates a strong acoustic noise similar to white noise. However, as the random modulation spreads the discrete components from the acoustic spectra, its generated noise is also similar to white noise. Therefore, the noises generated by random modulation and by the airflow merge together, giving the sensation of eliminating the discrete components from the acoustic spectra.

The analysis of the acoustic noise generation in the PM synchronous and asynchronous motors leads to the conclusion that their acoustic performance is virtually identical. This statement was validated by measurements, concluding that it is difficult to distinguish by ear, which motor operates.

Chapter 7

Acoustic noise analysis of Slim DC-link drives

This chapter deals with the acoustic noise generated by a slim DC-link inverter driven motor. A DC-link voltage compensation method is proposed, method which reduces the oscillation between the line inductance and DC-link capacitor. Moreover, using the proposed modulation method the 300Hz component from the acoustic spectra caused by the low DC-link capacitor is eliminated.

7.1 Introduction

A new trend in HVAC drives is to reduce the DC-link capacitance in order to improve cost effectiveness. PWM AC drives with a passive front-end are typically equipped with an electrolytic capacitor in the DC-link giving a robust performance. For applications with low demands on EMC and shaft performance, (typically HVAC application) drives equipped with a small DC-link capacitance are emerging. These are referred to as Slim DC-link (AC) drives.

A reduced DC-link capacitance enables the usage of film capacitors instead of electrolytic capacitors without compromising the physical size of the capacitor bank. Besides being able to tolerate the DC-link current ripple, a film capacitor has to be large enough to ensure that the resonant frequency of the DC-link is lower than the desired minimum switching frequency of the inverter [77]. The maximum resonant frequency is given by the minimum line impedance and the film capacitance.

Film capacitors are interesting because of their long lifetime [78, 79]. Also, the low loss of the film capacitor eases the thermal management of the drive. The main advantage is the reduced harmonic content of the line currents without needing inductive elements [79] giving a low total harmonic distortion (THD). The 5th and 7th harmonics are attenuated effectively, at the expense of increased higher harmonics as

described by the partially weighted harmonic distortion (PWHD). Slim DC-link AC drives do not comply with European harmonic standards, unless extra line-side inductance is installed [77]. Also, line-injected current harmonics at the switching-frequency level is an issue, motivating installation of extra line-side inductance.

The reduced DC-link capacitance leads to a high DC-link voltage ripple at six times the line frequency, which creates torque ripple on the motor shaft and acoustic noise. Papers [78, 80] present modulation methods to compensate for the large ripple voltage assuming a stiff grid. At a weak grid, or when installing additional line inductance to reduce high-frequency effects, the tendency for resonance between the DC-link capacitor and the line-side inductance is amplified by such modulation techniques giving potential instability [81-83].

In this chapter, a new DC-link compensation method for slim DC-link drives operated on a soft grid is proposed. The method addresses the instability tendency of the DC-link, while giving a reduced low-frequency motor torque ripple, resulting also in lower acoustic noise. The oscillation between the line inductance and the DC-link capacitor is damped, and the line-current THD is maintained around 31%. The proposed DC-link compensation method can be used for both scalar and vector control.
The large voltage ripple from the DC-link inserts a frequency component at six times the grid frequency into the current spectra resulting in a loud acoustic noise. The proposed new compensation method reduces the amplitude of this component, while maintaining the stability of the drive.

7.2 DC-link voltage analysis

Simple models of the passive front-end of a slim DC-link drive are sketched in Figure 7-1 (a) and Figure 7-1 (b) [77, 81]. The models of the DC-link show that an *L-C* resonant circuit is formed by the DC-link capacitor and the line inductors. L_{gph} and R_{gph} from Figure 7-1 (a) are the total inductance and resistance per phase at the line side. Any EMC-filter impedance of the drive is included in L_{gph} and R_{gph}.

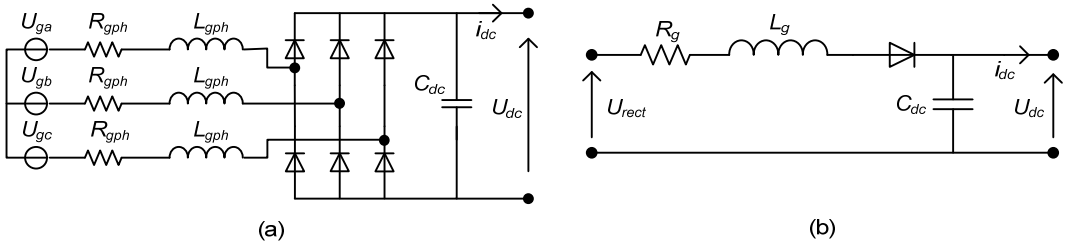

Figure 7-1 Line, rectifier and DC-link: 3-phase (a), and simplified (b) model.

During operation of the diode rectifier, only two phases conduct per time interval. Hence, the total inductance and resistance seen from the DC-link is given by (1). ESR_{Cdc} is the series resistance of the DC-link capacitor C_{dc}. R_d is the series resistance of a rectifier diode.

$$L_g = 2 \cdot L_{gph}, \quad R_g = 2(R_{gph} + R_d) + ESR_{Cdc} \tag{7.1}$$

The resonant frequency of the DC-link is given by L_g and C_{dc}.

$$f = \frac{1}{2\pi\sqrt{C_{dc} L_g}} \quad [Hz] \tag{7.2}$$

This resonant frequency can vary between 100Hz and several kHz [77], and L_g-C_{dc} oscillation increases the THD and PWHD of the line current. Fig. 2 shows a simulation of a 4kW drive equipped with a 10µF DC-link capacitor (500%) and a 1.1mH line inductance (1%). The percentage values of L_g and C_{dc} are given by (7.3).

$$\begin{aligned} L_g\% &= 100\frac{2\pi f_{line} L_g}{z_{base}}, \quad z_{base} = \frac{n_{ph}\eta_{tot} U_{phase}^2}{P_{shaft}} \\ C_{dc}\% &= 100\frac{1}{2\pi f_{line} 2C_{dc} z_{base}} \end{aligned} \tag{7.3}$$

where f_{line} is the line frequency (50Hz), U_{phase} is the phase voltage of the grid (230V), P_{shaft} is the rated motor shaft power, η_{tot} is the system efficiency set to 0.8, and n_{ph} is the number of grid phases (3).

As seen in Figure 7-2, the oscillation between L_g-C_{dc} appears both in the DC-link voltage and the line current(s).

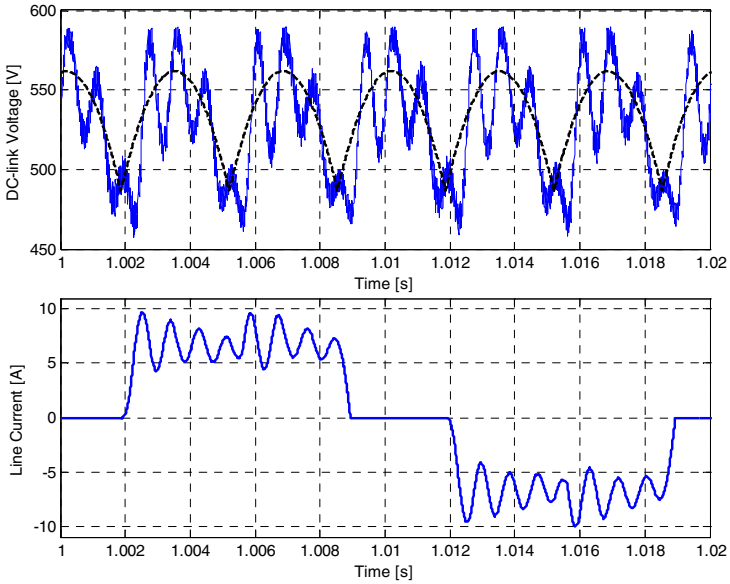

Figure 7-2 Simulated DC link voltage (top) and line current (bottom)

The DC-link voltage contains three main components.

1. Rectified component due to rectification of the three-phase line (Figure 7-2 top – dashed line). The frequency of the rectified component is 300 Hz at a 50Hz grid.

2. Resonant component due to L_g-C_{dc} oscillation.

3. Switching-frequency component. From a DC-link compensation perspective it is not important.

7.3 DC-link voltage compensation ensuring active damping of rectifier side

Traditional compensation of the DC-link voltage ripple is reported in [84], given by (7.4). The scheme removes the rectified component of the DC-link voltage from the motor voltages.

$$U_{dccomp} = U_{cont} \frac{U_{dcref}}{U_{dcmeas}} \tag{7.4}$$

where U_{dccomp} is the amplitude of the compensated voltage vector, U_{cont} is the amplitude of the voltage vector set by the motor-control algorithm, U_{dcref} is the reference DC-link voltage, and U_{dcmeas} is the measured DC-link voltage.

The method proposed in this chapter, aiming at ensuring the DC-link stability while using (7.4), is inspired by the fact that a time delay exists between the sampling instant of U_{dcmeas}, and the time instant when U_{dccomp} is applied to the motor. This is illustrated in the flowchart in Figure 7-3 (a), showing the sequence of traditional DC-link voltage compensation.

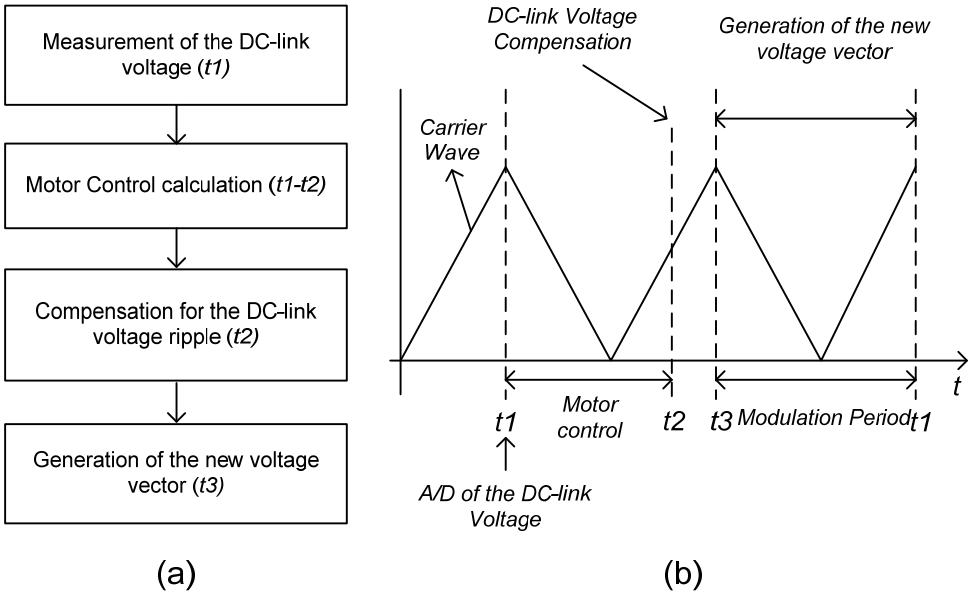

Figure 7-3 Flowchart of DC link compensation method (a), and its timing diagram (b)

The sample delay is usually one to two switching periods (Figure 7-3 (b)). In case of a slim DC-link drive fed by an ideal 400V/50Hz grid, the peak-to-peak DC-link voltage ripple is 75V or 14% of the average DC-link voltage. Having the compensation voltage delayed by two samples, at a switching frequency of 6kHz as shown in Figure 7-4, the voltage error in the compensation will be ±25V (±4.5%).

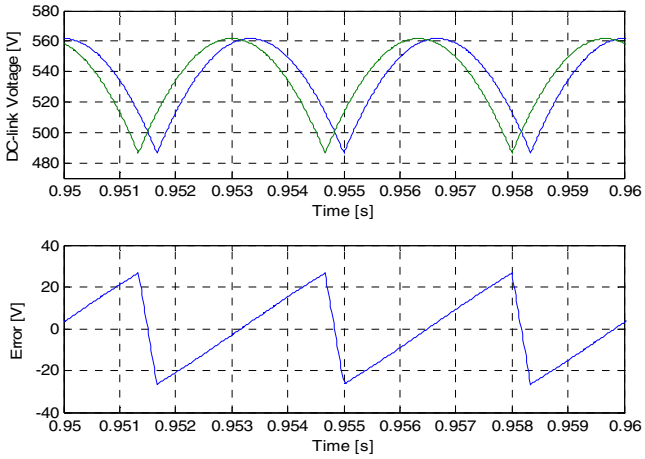

Figure 7-4 Compensation error for the rectified component with two-sample delay in the compensation loop

This means that (7.4) cannot give a perfect result. Figure 7-5 shows the DC-link voltage and the voltage used for the compensation with and without a sample delay.

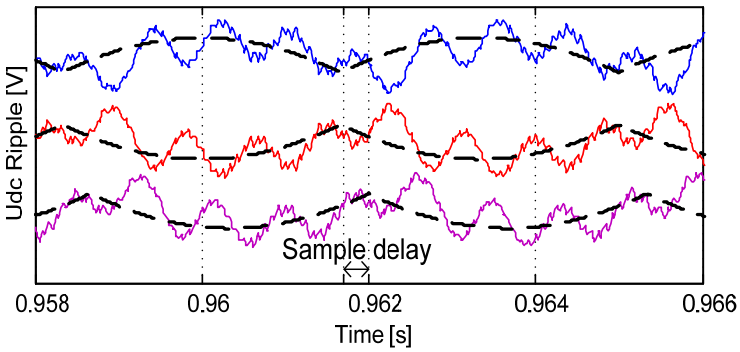

Figure 7-5 Simulated results for DC-link voltage, top: dashed line is the rectified voltage component, full line is the DC-link voltage, middle: compensation voltage without delay, bottom: compensation voltage with two-sample delay

In the ideal case, using (7.4) without a delay, a perfect result would be achieved, given that the over-modulation range of the PWM is avoided. The side effect would be maximum amplification of the L_g-C_{dc} oscillation. That is, when the DC-link voltage goes up, the modulation index, being proportional to U_{dccomp}, is decreased. Decreasing the modulation index, the inverter will take less energy from the DC-link, allowing the voltage to increase even more. Likewise, when the DC-link voltage goes down, (7.4) increases the modulation index. Consequently, more energy is taken from the DC-link, decreasing the voltage even more. Hence, traditional DC-link compensation makes the inverter load appear to be a negative resistance seen from the rectifier in a steady-state operating point. This negative damping reduces the effect of the natural resistive damping in the (7.5) rectifier side. Hence, from a L_g-C_{dc} oscillation perspective, it is more safe not to compensate for the DC-link voltage ripple at all. But in this case the rectified component will have a negative effect on the motor performance. The current controllers from the closed loop applications can compensate for the current ripple

caused by the rectified component from the DC-link voltage. However, the bandwidth of the control algorithm has to be high enough to compensate for the rectified component. The high bandwidth requires also high switching frequency which increases losses in the inverter.

According to [83], the rectifier side is damped, if (7.6) is fulfilled. Equation (7.6) is considered to be a rule-of-thumb.

$$C_{dc} > \frac{P_{shaft} L_g}{\eta_{tot} R_g U_{dc}^2} \tag{7.6}$$

Some examples in terms of the needed capacitor size at 4kW ensuring the DC-link stability are given below. Feeding the drive by a 500kVA/400V/50Hz distribution transformer (stiff grid) the series impedance per phase is about (3.5+j15.5) mΩ, when assuming a short line cable. A 250kVA transformer equals (8.4+j27.6)mΩ. A 100kVA transformer equals (27+j59) mΩ. Assuming that a 4 kW slim DC-link drive contributes to R_g by around 100mΩ (capacitor, diodes, EMC-filter), the DC-link capacitor should be larger than 16, 26 and 45μF respectively (300, 200 and 100%). In case of adding a 1% inductor (1.1mH with 100mΩ series resistance) between the grid and the drive, the capacitor size should be 125μF (40%). A 40% capacitance is realistic by using electrolytic capacitors only. From the above examples it may be deduced that, slim DC-link drives (C_{dc} >>40%) suffer dominantly from poor damping on soft grids. Hence, the compensation method presented in this chapter is aimed at operation on soft grids and/or operation with line inductors. In these cases the method provides active damping for the film-capacitor-based DC-link.

The proposed method is based on delaying the resonant component of the DC link voltage with half a resonant period, while the rectified component is left unchanged. The 180° phase shift of the resonant component transforms the impact of (7.4) on it into active damping. In order to calculate the right delay for the resonant component, its period must be identified (delay-calculation block in Figure 7-6).

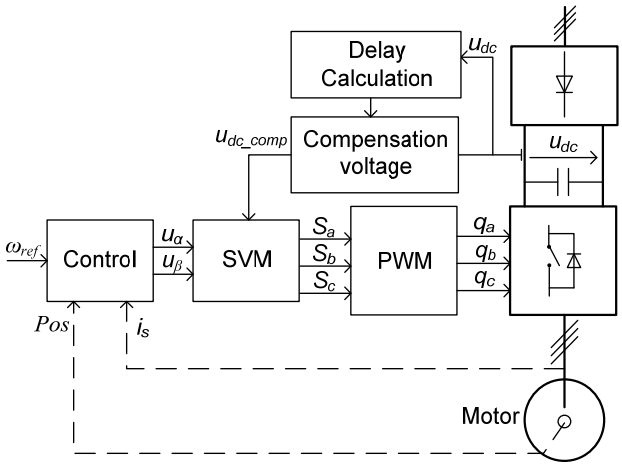

Figure 7-6 Control algorithm of DC-link voltage compensation using delay in the compensation loop (dashed lines = feedback for closed-loop control)

By using a digital band-pass filter, the rectified component can be isolated from the DC-link voltage. Subtracting the rectified component from the DC-link voltage gives the resonant component and the DC component. This combined signal is delayed by half a resonant period. The simulated steps in Figure 7-7, contained in the compensation-voltage block in Figure 7-6, visualizes the isolation procedure, the phase shift of the combined signal and the reconstructed DC-link voltage U_{dccomp} by adding the rectified component and the delayed combined signal.

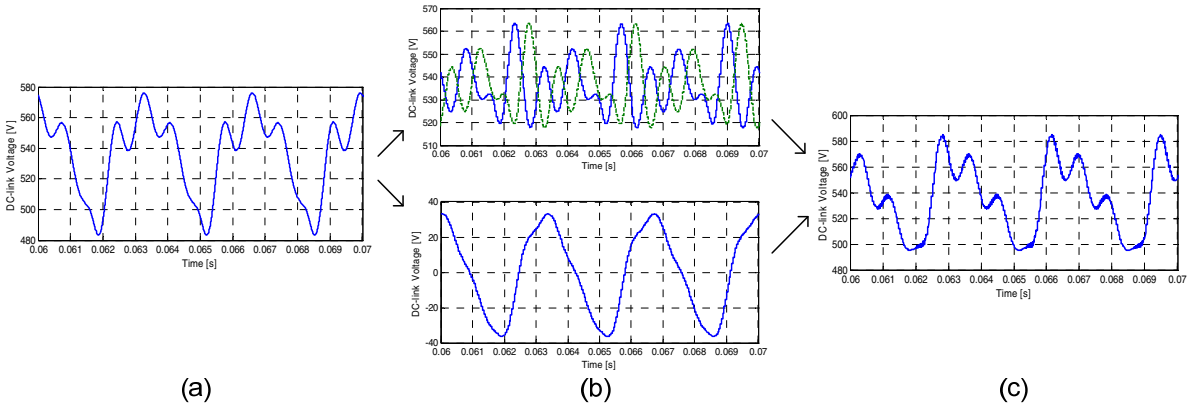

Figure 7-7 Simulation results: Initial DC-link voltage (a); DC-link voltage with extracted rectified component (top - full line without, dashed line with half period delay, bottom - rectified component) (b), and reconstructed compensation signal with delayed resonance (c)

Regarding the proposed method two conditions must be fulfilled.

1. The frequency of the resonant component must be at least two times higher than the rectified component to ensure a proper separation.
2. The sample rate of the U_{dccomp} routine should be at least five times higher than the frequency of the resonant component.

Hence, at a 50Hz line and a sample rate of 14kHz the upper limit of the line inductance for a 4kW drive with a 500% capacitor is around 3.5mH (3.5%). The lower limit of the inductance is about 160µH (0.16%). Outside these limits the rectifier stability is governed by the natural damping of the hardware (7.6). As may be deduced, the sample frequency must be increased as the film capacitor is reduced, to ensure the stability by software. This means extra controller costs.

Figure 7-6 sketches the overall control algorithm. The sample rate of the U_{dccomp} routine was set to be twice the switching frequency of the slim DC-link drive. The control block in Figure 7-6 may range from simple scalar control to advanced vector-oriented control. The SVM block contains space-vector-oriented duty-cycle calculations including (7.4). The duty cycles are input to the PWM block controlling the six switching elements of the inverter. In the following, these blocks are executed at a 7kHz switching rate (modulation period, see Figure 7-3). The delay-calculation and the

compensation-voltage blocks run at 2·7000 = 14 kHz, meaning that the input signal U_{dcmeas} is sampled in the start and in the middle of the modulation period. Hence, the right half of any modulation period is available for preparing the duty cycles for the following switching period. That is, the calculations can be initiated, when U_{dccomp} is available in the middle of the modulation period. In terms of the rectified component this gives a one switching-period delay.

For installations with varying grid impedance, the delay-calculation block must run continuously during operation. Else, it is needed in a start-up calibration phase only.

7.4 Experimental results

A ventilation system, equipped with a 4kW induction motor fed by a VLT® AutomationDrive FC 302 from Danfoss Drives A/S, has been used for experimental tests. The DC-link capacitance of the drive was decreased to 10µF (500%), and the built-in DC-chokes were removed. The vibration of the motor shell has been measured using a Bruel & Kjaer Pulse Multi-analyzer type 3560. Motor and line currents were measured applying oscilloscope equipment from Tektronix. In order to emulate a soft grid, inductors were installed at the line side.

A first set of measurements was recorded at a total line inductance of about 0.5% (0.5mH) (Figure 7-8). A second set of measurements was recorded at a line inductance of about 1% (1.15mH) (Figure 7-9). The frequency of the L-C oscillation between the line inductors and DC-link capacitor is 1.6 kHz and 1.1 kHz respectively, which is well below the 14 kHz sample rate (factor of 8).

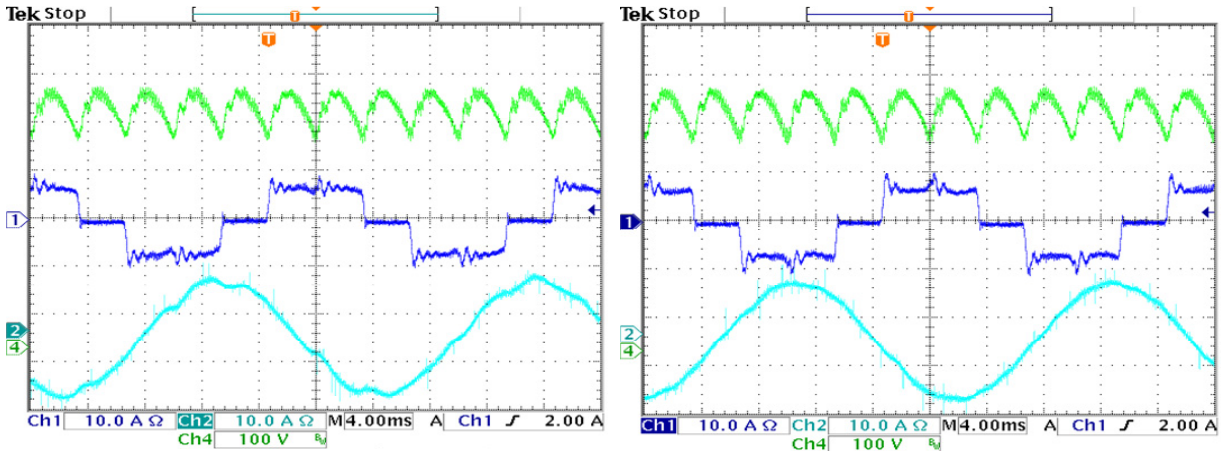

Figure 7-8 Measured line and motor currents at 0.5% line inductance, 7kHz switching frequency, 45Hz fundamental frequency without (left), and with (right) DC-link compensation with delay

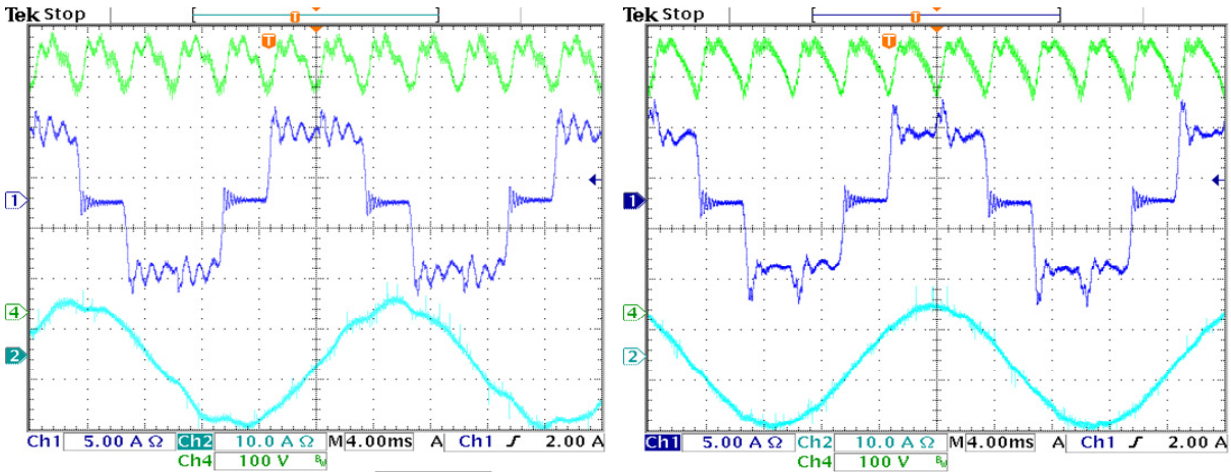

Figure 7-9 Measured line and motor currents at 1% line inductance, 7kHz switching frequency, 45Hz fundamental frequency without (left), and with (right) DC-link compensation with delay

Figure 7-10 presents the worst-case scenario from a resonance perspective, when the resonant component of U_{dccomp} is in phase with the actual resonant component of the DC-link voltage.

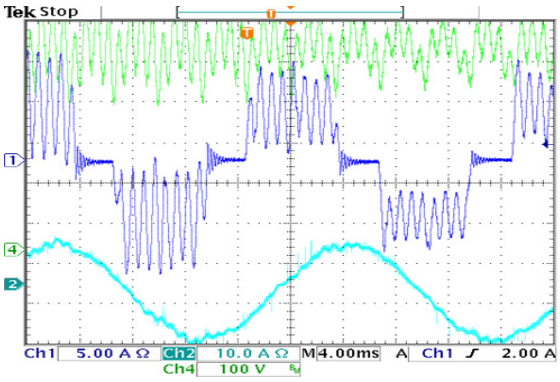

Figure 7-10 Measured line and motor currents with 1% line inductance, switching frequency of 7kHz, fundamental frequency of 45Hz. Resonant component in compensation signal in phase with resonant component of DC-link voltage

As it can be seen from Figure 7-5, this may occur if the sample delay in the DC-link compensation matches the period of the uncontrolled resonant component. Table 1 shows the THD and PWHD of the line current and the THD of the motor current.

Line Inductance		THD of the Line Current [%]	PWHD of the Line Current [%]	THD of the Motor Current [%]
0.5%	Compensation	32.5	72	4.7
	No Compensation	31	74.5	7.2
1%	Compensation	31.5	58	4.5
	No Compensation	31	64	7
	Compensation in phase	60	180	6

Table 2 Measured THD and PWHD of the line and motor currents

The line current THD is approximately the same (31-32%) except for the case, when the resonant components of the compensation and measured DC link voltage are in phase. The reduction of the PWHD is better at a 1% line inductor, because the need for active damping is highest in this case. The measurements were recorded at a fundamental frequency of 45Hz and U_{dcref}=530V. Increasing the speed over 45Hz, at a constant U/f-ratio, the drive enters in over-modulation. At over-modulation it is not possible to compensate for the DC-link voltage ripple due to saturation of the modulation index. Hence, the slim DC-link drive cannot give full output voltage, while maintaining a stable DC-link on a soft grid.

Fig. 11 presents the measured vibration spectra on the motor shell in case of a 1% line inductor at 45Hz. If no DC-link voltage compensation is applied, a 300Hz component appears in the motor currents. The result is increased vibration of the motor shell and increased acoustic noise. By compensating the DC-link voltage according to the method proposed in this chapter, the vibrations at 300Hz are reduced with around 20dB. The L_g-C_{dc} oscillation does not influence the acoustic performance of the drive.

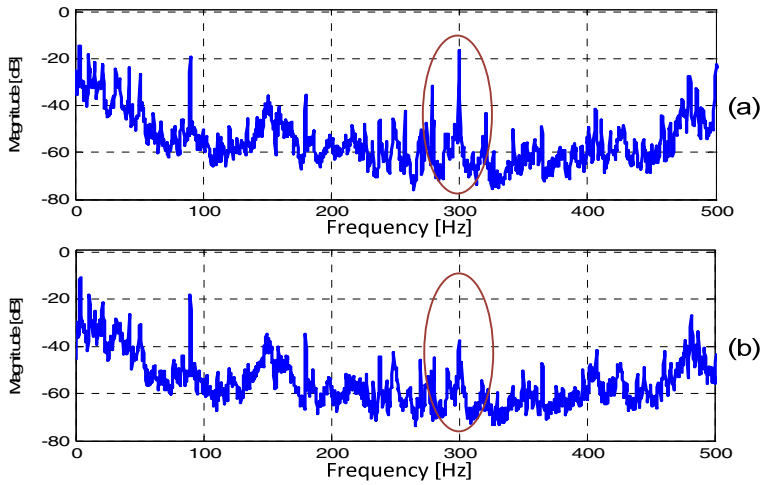

Figure 7-11 Measured vibration spectra on the motor shell without compensation (a), and with the proposed DC-link compensation (b)

7.5 Summary

A new DC-link voltage compensation method for drives equipped with a small DC-link capacitor, usually used in HVAC applications, was proposed in this chapter. The method is useful for poorly damped slim DC-link drives fed by a soft grid. The compensation removes the 300Hz DC-link voltage ripple from the voltages applied to the motor, while at the same time providing active damping of the DC-link resonances.

Measurements showed that the PWHD of the line currents was reduced from 64% to 58%, while the THD was maintained below 32%. Another advantage of the proposed method is that it can be used for both open- and closed-loop control schemes, as it operates independently from the control loop.

Motor-vibration measurements indicate that the acoustic performance of a slim DC-link drive is affected by the large 300Hz DC-link voltage ripple. Using the proposed compensation method, the 300Hz component in the vibration spectrum of the motor shell was reduced by 21dB.

Chapter 8

Conclusions and future research

This chapter summarizes the work which has been carried out through the PhD project. The chapter ends with an outlook to further research.

8.1 Summary of the thesis

The work presented in this report deals with the acoustical performance of the electrical drives fed by a PWM based inverter.

The first introductive chapter presented the motivation, objectives, limitations and a small introduction in electrical motor drive acoustics. In this chapter the main contributions of the author to the work made for this thesis are highlighted.

In the second chapter a general overview on the conversion of a DC voltage into an AC voltage using power electronics has been presented. First, the basic inverter topologies, especially the three-phase voltage-source inverter have been reviewed. Second, the pulse generation mechanism which includes the basics of the modulation theory is described. In this chapter the importance of the signal injection in the common mode voltage is described as well. The difference between the modern PWM techniques can be reduced to the shape of the common mode voltage.

The third chapter presented a new way to mathematically estimate the spectrum of the line-to-line voltage and the spectrum of the acoustic noise generated by an inverter fed electrical motor. The single mathematical expression proposed in this chapter can be used for modulation methods where an arbitrary signal is injected into the common mode voltage;

The fourth chapter gave an overview of the most popular method used to decrease the annoyance of the acoustic noise generated by electrical motors, the random PWM (RPWM). In general, the carrier based random PWM techniques can be divided in two main categories: random carrier frequency PWM and fixed carrier frequency (FCF) RPWM. The random carrier frequency (RCF) PWM technique has the advantage of efficient spreading of the discrete components from the acoustic spectra. The

main disadvantage of this modulation method is that it creates difficulties in closed loop applications. The FCF-RPWM overcomes this disadvantage of the RCF-PWM; however, the spreading effect of the discrete components from the acoustic spectra at high modulation index is poor. The proposed new modulation method called AC-RPWM alloys the advantages of the FCF-RPWM and RCF-PWM in that it provides good spreading effect of the discrete frequency components and it easily integrates in closed-loop control systems.

Furthermore, an implementation method for the AC-RPWM that aims to reduce the effects of the current sampling error on the control algorithm was proposed. An analysis of the sampling error for both the FCF and AC-RPWM has also been presented in this chapter.

In the next chapter the modeling of the ventilation system was presented. In this chapter the frequency response of the stand alone motor and the frequency response of the ventilation system were tested in three different ways. First, the very popular hammer excitation method is used, method which has the disadvantage of exciting the system up to maximum 10kHz. The second method to measure the frequency response of the system was a sinusoidal current sweep; the current was injected through one of the motor coils. By using this method the frequency range can be extended to the full acoustic range. The third method gives the possibility to analyze the system during normal operation. For this method RPWM technique was used. RPWM creates a flat spectrum for the motor current, with the consequence of a good excitation for the whole drive system in the acoustic frequency range.

Being the acoustics a very important issue in heating, ventilation and air-conditioning (HVAC) applications, Chapter 6 presented the acoustic measurements on a ventilation system. The measurements showed that the discrete components in the voltage spectrum caused by the modulation are present in the acoustic noise spectrum generated by the ventilation system. Moreover, the whistling noise is transmitted through the ducts in the ventilated place. By using RPWM these discrete components are spread, blending into the strong background noise caused by the airflow. To increase the efficiency of the HVAC application a new trend is to replace the less efficient asynchronous motor to a more efficient synchronous motor. The measurements showed that the acoustic performance of the two motor is approximately similar.

Chapter 7 gave an analysis of the acoustic noise generated by a slim DC-link driven motor. In this chapter a new DC-link voltage compensation method was proposed, that reduces the oscillation between the line inductance and the DC-link capacitor. Moreover, using the proposed modulation method the 300Hz component from the acoustic spectra caused by the low DC-link capacitor is eliminated.

8.2 Conclusions

Based on the results presented in this thesis the author considers the main objectives of the PhD work were achieved.

The mathematical expression presented in the third chapter shows that each frequency component from the common mode voltage introduces a well defined group of harmonics in the acoustic spectra.

Using the new random PWM method presented in the forth chapter and confirmed by the measurements made on the ventilation system presented in the sixth chapter, the whistling noise can be minimized having a small overhead on the control algorithm of the motors.

In case of complex drive systems, especially when the structure is constructed from many small components, it is difficult to model the whole system by using for example finite element modeling. Random PWM method can be used to measure the frequency response of the whole drive system, method presented in chapter 5. The advantage of the method is: it can give an image about the whole audible frequency range; it is a fast and inexpensive method to find the dominant frequency components in the entire dive while operating.

From the comparison between the synchronous and asynchronous motor presented in Chapter 6 can be concluded that the generated acoustic noise is approximately the same in amplitude and distribution frequency components in both motors.

Finally, using the compensation method for slim DC drives presented in Chapter 7, the 300Hz component from the acoustic spectra can be reduced considerably, while the performance of the drive is maintained.

8.3 Future work

The research topics for future work in the opinion of the author are:

- Implement and analyze the performance of the presented modulation methods for more different applications.
- The current sampling method should be improved for the proposed random PWM technique for closed loop applications where high shaft-torque is required.
- To avoid the high current ripple caused by the proposed modulation method some limitations should be introduced. A study on these limitations should increase the value of the modulation method.
- Development of a new control algorithm for slim DC drives, which makes the drive to be compatible with the international standards.

Bibliography

[1] M. P. Kazmierkowski, R. Krishan, and F. Blaabjerg, *Control in Power Electronics*, 2002.

[2] P. Vijayraghavan and R. Krishnan, "Noise in electric machines: a review," *Industry Applications, IEEE Transactions on,* vol. 35, pp. 1007-1013, 1999.

[3] P. L. Timar, "Noise and Vibration of Electrical Machines," Budapest: Akadémiai Kiadó, 1989.

[4] S. J. Yang, "Low-noise electrical motors," Oxford: Clarendon Press 1981.

[5] S. R. Bowes, S. Grewal, and D. Holliday, "Simplified ultrasonic regular-sampled PWM technique," *Electronics Letters,* vol. 36, pp. 854-855, 2000.

[6] J. E. Gilliam, J. A. Houldsworth, and L. Hadley, "Variable speed induction motor with integral ultrasonic PWM inverter," in *Applied Power Electronics Conference and Exposition, 1988. APEC '88. Conference Proceedings 1988., Third Annual IEEE*, 1988, pp. 92-96.

[7] T. H. Nishimura and P. G. Maranesi, "Ultrasonic carrier PWM converter employing IGBT in the near future," in *Telecommunications Energy Conference, 1989. INTELEC '89. Conference Proceedings., Eleventh International*, 1989, pp. 20.7/1-20.7/5 vol.2.

[8] J. A. Ferreira, P. Dorland, and F. G. de Beer, "An active in-line notch filter for reducing acoustic noise in drives," in *Industry Applications Conference, 2004. 39th IAS Annual Meeting. Conference Record of the 2004 IEEE*, 2004, p. 141.

[9] J. T. Boys and P. G. Handley, "Spread spectrum switching: low noise modulation technique for PWM inverter drives," *Electric Power Applications, IEE Proceedings B,* vol. 139, pp. 252-260, 1992.

[10] J. R. Hassall and K. Zaveri, "Acoustic noise measurement," Glostrup, Denmark: Larsen & Son A/s, 1988.

[11] "MATLAB Getting Started Guide," *The Mathworks, Inc. 3 Apple Hill Drive Natick, MA 01760-2098 [online www.mathworks.com]*, 2008.

[12] "PLECS Piece-Wise Linear Electrical Circuit Simulator User Manual," *2nd ed., PLEXIM Gmbh, Technoparkstrasse 1 8005 Zurich Switzerland [online www.plexim.com]*, 2008.

[13] Holmes D. G. and L. T. A., *Pulse Width Modulation for Power Converters: Principles and Practice*: John Wiley &Sons, Inc., 2003.

[14] H. W. van der Broeck and H. C. Skudelny, "Analytical analysis of the harmonic effects of a PWM AC drive," *Power Electronics, IEEE Transactions on,* vol. 3, pp. 216-223, 1988.

[15] P. F. Seixas, M. A. Severo Mendes, P. Donoso-Garcia, and A. M. N. Lima, "A space vector PWM method for three-level voltage source inverters," in *Applied Power Electronics Conference and Exposition, 2000. APEC 2000. Fifteenth Annual IEEE*, 2000, pp. 549-555 vol.1.

[16] A. M. Hava, R. J. Kerkman, and T. A. Lipo, "Simple analytical and graphical methods for carrier-based PWM-VSI drives," *Power Electronics, IEEE Transactions on,* vol. 14, pp. 49-61, 1999.

[17] A. Schonung and H. Stemmler, "Static frequency changers with subharmonic control in conjunction with reversible variable speed ac drives," *Brown Boveri Rev.,* pp. 555-577, 1964.

[18] J. Holtz, "Pulse width modulation for electronic power conversion," *Proceedings of the IEEE,* vol. 82, pp. 1194-1214, 1994.

[19] H. W. van der Broeck, H. C. Skudelny, and G. V. Stanke, "Analysis and realization of a pulsewidth modulator based on voltage space vectors," *Industry Applications, IEEE Transactions on,* vol. 24, pp. 142-150, 1988.

[20] S. Ogasawara, H. Akagi, and A.Nabae, "A novel PWM scheme of voltage source inverter based on space vector theory," *European Power Electron. Conf.Rec., Aachen, Germany,* pp. 1197-1202, 1989.

[21] V. Blasko, "Analysis of a hybrid PWM based on modified space-vector and triangle-comparison methods," *Industry Applications, IEEE Transactions on,* vol. 33, pp. 756-764, 1997.

[22] A. M. Hava, R. J. Kerkman, and T. A. Lipo, "A high-performance generalized discontinuous PWM algorithm," *Industry Applications, IEEE Transactions on,* vol. 34, pp. 1059-1071, 1998.

[23] J. W. Kolar, H. Ertl, and F. C. Zach, "Influence of the modulation method on the conduction and switching losses of a PWM converter system," *Industry Applications, IEEE Transactions on,* vol. 27, pp. 1063-1075, 1991.

[24] J. A. Houldsworth and D. A. Grant, "The Use of Harmonic Distortion to Increase the Output Voltage of a Three-Phase PWM Inverter," *Industry Applications, IEEE Transactions on,* vol. IA-20, pp. 1224-1228, 1984.

[25] L. Mathe, P. R. Omand, and J. K. Pedersen, "Shaping the spectra of the line-to-line voltage using signal injection in the common mode voltage," *IEEE conference proceedings,* 2009.

[26] W. R. Bennett, "New results in the calculation of modulation products," *The Bell System Technical Journal,* vol. 12, pp. 228-243, April 1933.

[27] H. S. Black, "Modulation theory," N. Y. Van Nostrand, Ed., 1953.

[28] s. Bowes and B. M. Bird, "Novel approach to the analisys and synthesis of modulation processes in power converters," *IEE Procededings (London),* vol. 122, pp. 507-513, May 1975.

[29] J. T. Boys and P. G. Handley, "Harmonic analysis of space vector modulated PWM waveforms," *Electric Power Applications, IEE Proceedings B,* vol. 137, pp. 197-204, 1990.

[30] D. Heng, L. Helle, B. Yin, and K. B. Larsen, "A General Solution for Theoretical Harmonic Components of Carrier Based PWM Schemes," in *Applied Power Electronics Conference and Exposition, 2009. APEC 2009. Twenty-Fourth Annual IEEE*, 2009, pp. 1698-1703.

[31] Holmes G. D. , "A general analytical method for determining the theoretical harmonic components of carrier based PWM strategies," in *Industry Applications Conference, 1998. Thirty-Third IAS Annual Meeting. The 1998 IEEE*, 1998, pp. 1207-1214 vol.2.

[32] J. F. Moynihan, M. G. Egan, and J. M. D. Murphy, "Theoretical spectra of space-vector-modulated waveforms," *Electric Power Applications, IEE Proceedings -,* vol. 145, pp. 17-24, 1998.

[33] F. J. Gieras, C. Wang, and J. C. S. Lai, *Noise of Polyphase Electric Motors*: CRC / Taylor & Francis, 2006.

[34] R. Krishnan and P. Vijayraghavan, "State of the art: acoustic noise in switched reluctance motor drives," in *Industrial Electronics Society, 1998. IECON '98. Proceedings of the 24th Annual Conference of the IEEE*, 1998, pp. 929-934 vol.2.

[35] P. Pillay and W. Cai, "An investigation into vibration in switched reluctance motors," *Industry Applications, IEEE Transactions on,* vol. 35, pp. 589-596, 1999.

[36] S. P. Verma and A. Balan, "Determination of radial-forces in relation to noise and vibration problems of squirrel-cage induction motors," *Energy Conversion, IEEE Transaction on,* vol. 9, pp. 404-412, 1994.

[37] W. C. Lo, C. C. Chan, Z. Q. Zhu, X. Lie, D. Howe, and K. T. Chau, "Acoustic noise radiated by PWM-controllel induction machine drives," *Industrial Electronics, IEEE Transactions on,* vol. 47, pp. 880-889, 2000.

[38] N. Hashemi, R. Lisner, and D. G. Holmes, "Acoustic noise reduction for an inverter-fed three-phase induction motor," in *Industry Applications Conference, 2004. 39th IAS Annual Meeting. Conference Record of the 2004 IEEE*, 2004, pp. 2030-2035 vol.3.

[39] C. Wang, A. Astfalck, and J. C. S. Lai, "Sound power radiated from an inverter-driven induction motor: experimental investigation," *Electric Power Applications, IEE Proceedings -,* vol. 149, pp. 46-52, 2002.

[40] C. Wang and J. C. S. Lai, "Sound power radiated from an inverter-driven induction motor. Part 3: statistical energy analysis," *Electric Power Applications, IEE Proceedings -,* vol. 152, pp. 619-626, 2005.

[41] C. Wang, J. C. S. Lai, and A. Astfalck, "Sound power radiated from an inverter driven induction motor II: Numerical analysis," *Electric Power Applications, IEE Proceedings -,* vol. 151, pp. 341-348, 2004.

[42] L. Mathe, U. Jakobsen, P. O. Rasmussen, and J. K. Pedersen, "Analysis of the vibration spectrum based on the input voltage spectrum," in *Energy Conversion Congress and Exposition, 2009. ECCE 2009. IEEE*, 2009, pp. 220-225.

[43] P. O. Rasmussen, J. H. Andreasen, and E. C. LaBrush, "Interlaminated damping - a method for reduction of vibration and acoustic noise for switched reluctance machines?," in *Industry Applications Conference, 2005. Fourtieth IAS Annual Meeting. Conference Record of the 2005*, 2005, pp. 1531-1539 Vol. 3.

[44] A. M. Trzynadlowski, F. Blaabjerg, J. K. Pedersen, R. L. Kirlin, and S. Legowski, "Random pulse width modulation techniques for converter-fed drive systems-a review," *Industry Applications, IEEE Transactions on,* vol. 30, pp. 1166-1175, 1994.

[45] C. Wang, "Vibro-acoustic Analysis of Inverter Driven Induction Motors," University of New South Wales, 1998.

[46] T. G. Habetler and D. M. Divan, "Acoustic noise reduction in sinusoidal PWM drives using a randomly modulated carrier," in *Power Electronics Specialists Conference, 1989. PESC '89 Record., 20th Annual IEEE*, 1989, pp. 665-671 vol.2.

[47] M. M. Bech, F. Blaabjerg, and J. K. Pedersen, "Random modulation techniques with fixed switching frequency for three-phase power converters," in *Power Electronics Specialists Conference, 1999. PESC 99. 30th Annual IEEE*, 1999, pp. 544-551 vol.1.

[48] A. M. Trzynadowski, M. M. Bech, F. Blaabjerg, J. K. Pedersen, R. L. Kirlin, and M. Zigliotto, "Optimization of switching frequencies in the limited-pool random space vector PWM technique for inverter-fed drives," in *Applied Power Electronics Conference and Exposition, 1999. APEC '99. Fourteenth Annual*, 1999, pp. 1013-1018 vol.2.

[49] A. M. Trzynadlowski, K. Borisov, L. Yuan, and Q. Ling, "A novel random PWM technique with low computational overhead and constant sampling frequency for high-volume, low-cost applications," *Power Electronics, IEEE Transactions on,* vol. 20, pp. 116-122, 2005.

[50] J. K. Pedersen and F. Blaabjerg, "Implementation and test of a digital quasi-random modulated SFAVM PWM in a high performance drive system," in *Industrial Electronics, Control, Instrumentation, and Automation, 1992. 'Power Electronics and Motion Control'., Proceedings of the 1992 International Conference on*, 1992, pp. 265-270 vol.1.

[51] J. K. Pedersen, F. Blaabjerg, and P. S. Frederiksen, "Reduction of acoustic noise emission in AC-machines by intelligent distributed random modulation," in *Power Electronics and Applications, 1993., Fifth European Conference on*, 1993, pp. 369-375 vol.4.

[52] H. Kragh, F. Blaabjerg, and J. K. Pedersen, "Reduce of the acoustic noise effect from PWM-VSI inverter controlled AC-drives by music and random modulation," in *Power Conversion Conference, 1993. Yokohama 1993., Conference Record of the*, 1993, pp. 85-92.

[53] S. Ueda, K. Honda, T. Ikimi, M. Hombu, and A. Ueda, "Magnetic noise reduction technique for an AC motor driven by a PWM inverter," *Power Electronics, IEEE Transactions on,* vol. 6, pp. 470-475, 1991.

[54] M. M. Bech, J. K. Pedersen, and F. Blaabjerg, "Field-oriented control of an induction motor using random pulsewidth modulation," *Industry Applications, IEEE Transactions on,* vol. 37, pp. 1777-1785, 2001.

[55] G. A. Covic and J. T. Boys, "Noise quieting with random PWM AC drives," *Electric Power Applications, IEE Proceedings -,* vol. 145, pp. 1-10, 1998.

[56] H. C. Chen, Y. C. Chang, and C. K. Huang, "Development of optimised carrier sequence in MCU-based random-frequency PWM," *Electric Power Applications, IET,* vol. 1, pp. 43-48, 2007.

[57] M. M. Bech, "Analysis of Random Pulse-Width Modulation Techniques For Power Electronic Converters," R. T. A/S, Ed. Skive, Denmark, 2000.

[58] L. Mathe, P. O. Rasmussen, and J. K. Pedersen, "Shaping the spectra of the line-to-line voltage using signal injection in the common mode voltage," in *Industrial Electronics, 2009. IECON '09. 35th Annual Conference of IEEE*, 2009, pp. 1288-1293.

[59] D. H. John C. Salmon, "Slope Modulation in Inverter Circuits," 1989.

[60] C. M. Liaw and Y. M. Lin, "Random slope PWM inverter using existing system background noise: analysis, design and implementation," *Electric Power Applications, IEE Proceedings -,* vol. 147, pp. 45-54, 2000.

[61] J. C. Salmon, "A new `slope-modulated' PWM strategy for implementation in a single chip gate array," in *Industry Applications Society Annual Meeting, 1988., Conference Record of the 1988 IEEE*, 1988, pp. 388-394 vol.1.

[62] S. Legowski, J. Bei, and A. M. Trzynadlowski, "Analysis and implementation of a grey-noise PWM technique based on voltage space vectors," 1992, pp. 586-593.

[63] C. Dae-Woong and S. Seung-Ki, "Analysis and compensation of current measurement error in vector-controlled AC motor drives," *Industry Applications, IEEE Transactions on,* vol. 34, pp. 340-345, 1998.

[64] D. Antic, J. B. Klaassens, and W. Deleroi, "Side effects in low-speed AC drives," in *Power Electronics Specialists Conference, PESC '94 Record., 25th Annual IEEE*, 1994, pp. 998-1002 vol.2.

[65] V. Blasko, V. Kaura, and W. Niewiadomski, "Sampling of discontinuous voltage and current signals in electrical drives: a system approach," in *Industry Applications Conference, 1997. Thirty-Second IAS Annual Meeting, IAS '97., Conference Record of the 1997 IEEE*, 1997, pp. 682-689 vol.1.

[66] S. Yo-Chan, S. Seung-Ho, and S. Seung-Ki, "Analysis and compensation of current sampling error in AC drive with discontinuous PWM," in *Applied Power Electronics Conference and Exposition, 1999. APEC '99. Fourteenth Annual*, 1999, pp. 795-799 vol.2.

[67] F. W. Carter, "Magnetic noise in dynamo-electric machines," *Engineering,* pp. 548-51 and 579-81, 1932.

[68] H. Jordan, "Approximate calculation of the noise produced by squirrel cage motors," *Engineering Digest,* pp. 222-6, 1949.

[69] P. L. Alger, "The nature of induction machines," *Gordon and Breach, London,* 1965.

[70] E. Erdelyi, "Predetermination of the sound levels of magnetic noise in medium induction motors," *PhD. Thesis,* 1955.

[71] S. J. Yand, "Low-noise electrical motors," Oxford: Clarendon Press 1981.

[72] A. Yahiaoui and F. Bouillault, "2D and 3D numerical computation of electrical parameters of an induction motor," *Magnetics, IEEE Transactions on,* vol. 30, pp. 3690-3692, 1994.

[73] F. Blaabjerg, J. K. Pedersen, E. Ritchie, and P. Nielsen, "Determination of mechanical resonances in induction motors by random modulation and acoustic measurement," *Industry Applications, IEEE Transactions on,* vol. 31, pp. 823-829, 1995.

[74] Z. Q. Zhu, L. Xu, and D. Howe, "Influence of mounting and coupling on the natural frequencies and acoustic noise radiated by a PWM controlled induction machine," in *Electrical Machines and Drives, 1999. Ninth International Conference on (Conf. Publ. No. 468)*, 1999, pp. 164-168.

[75] DanishStandard, "Acoustics - Determination of sound power radiated into a duct by fans and other air-moving devices - In-duct method," *DS/EN ISO 5136:2009,* 2009.

[76] Z. Q. Zhu and D. Howe, "Effects of end-shields and rotor on natural frequencies and modes of stator of small electrical machines," in *Electrical Machines and Drives, 1989. Fourth International Conference*, 1989, pp. 232-236.

[77] H. R. Andersen, T. Ruimin, and K. Cai, "3-phase AC-drives with passive front-ends with focus on the slim DC-link topology," in *Power Electronics Specialists Conference, 2008. PESC 2008. IEEE*, 2008, pp. 3248-3254.

[78] X. Chen and M. Kazerani, "Space Vector Modulation Control of an AC-DC-AC Converter With a Front-End Diode Rectifier and Reduced DC-link Capacitor," *Power Electronics, IEEE Transactions on,* vol. 21, pp. 1470-1478, 2006.

[79] H. Saren, O. Pyrhonen, K. Rauma, and O. A. L. O. Laakkonen, "Overmodulation in Voltage Source Inverter with Small DC-link Capacitor," in *Power Electronics Specialists Conference, 2005. PESC '05. IEEE 36th*, 2005, pp. 892-898.

[80] H. Saren, O. Pyrhonen, J. Luukko, O. A. L. O. Laakkonen, and K. A. R. K. Rauma, "Verification of frequency converter with small DC-link capacitor," in *Power Electronics and Applications, 2005 European Conference on*, 2005, p. 10 pp.

[81] M. Hinkkanen, L. Harnefors, and J. Luorni, "Control of induction motor drives equipped with small DC-Link capacitance," in *Power Electronics and Applications, 2007 European Conference on*, 2007, pp. 1-10.

[82] M. Hinkkanen and J. Luomi, "Induction motor drives equipped with diode rectifier and small DC-link capacitance," in *Industrial Electronics Society, 2005. IECON 2005. 31st Annual Conference of IEEE*, 2005, p. 6 pp.

[83] K. Pietilainen, L. Harnefors, A. Petersson, and H. P. Nee, "DC-Link Stabilization and Voltage Sag Ride-Through of Inverter Drives," *Industrial Electronics, IEEE Transactions on,* vol. 53, pp. 1261-1268, 2006.

[84] J. K. Pedersen, F. Blaabjerg, J. W. Jensen, and P. A. T. P. Thogersen, "An ideal PWM-VSI inverter with feedforward and feedback compensation," in *Power Electronics and Applications, 1993., Fifth European Conference on*, 1993, pp. 501-507 vol.5.

Appendix A

Data for the VEM Asynchronous motor used in the ventilation system

Rated power	4 [kW]
Rated voltage	400 [V_{rms}]
Rated current	8.8 [A_{rms}]
Rated frequency	50 [Hz]
Rated torque	25.5 [Nm]
Rated speed	1435 [rpm]
Number of poles	4
Rotor inertia	0.009 [kg m^2]
Stator resistance	1.3 [Ohm]
Rotor resistance	1.43 [Ohm]
Stator leakage inductance	5.7 [mH]
Rotor leakage inductance	5.6 [mH]
Magnetizing inductance	146 [mH]

Data for the VEM Synchronous motor used in the ventilation system

Rated power	4 [kW]
Rated voltage	400 [V_{rms}]
Rated current	7.6 [A_{rms}]
Rated frequency	50 [Hz]
Rated torque	25.5 [Nm]
Maximum torque	42 [Nm]
Rated speed	1500 [rpm]
Number of poles	4
Rotor inertia	0.009 [kg m^2]

Stator resistance	1.1 [Ohm]
Back EMF	188V/1000rpm
Stator leakage inductance	11.32 [mH]

Data for the ABB asynchronous motor used for standalone measurements

Rated power	2.2 [kW]
Rated voltage	400 [V_{rms}]
Cos(φ)	0.8
Rated frequency	50 [Hz]
Rated torque	14.5 [Nm]
Rated speed	1450 [rpm]
Number of poles	2
Rotor inertia	0.0086 [kg m^2]

Stator resistance	2.34 [Ohm]
Rotor resistance	1.43 [Ohm]

Stator leakage inductance	12 [mH]
Rotor leakage inductance	15 [mH]
Magnetizing inductance	365 [mH]

Appendix B

Published papers

(Listed in chronological order)

[P1] Laszlo Mathe, Uffe Jakobsen, Peter Omand Rasmussen, John K. Pedersen, Institute of Energy Technology; Aalborg University; Aalborg, Denmark

"Analysis of the Vibration Spectrum Based on the Input Voltage Spectrum"

Proc. of ECCE 2009, ISBN: 978-1-4244-2893-9, pp. 220 – 225

Analysis of the Vibration Spectrum Based on the Input Voltage Spectrum

Laszlo Mathe, Uffe Jakobsen, Peter Omand Rasmussen, John K. Pedersen
Institute of Energy Technology; Aalborg University; Aalborg, Denmark
lam@iet.aau.dk

Abstract —**Pulse width modulation, present in most drives, gives rise to harmonics in the current and this generates radial forces that cause vibrations in the motor shell. This paper derives an analytical expression for the estimation of the spectrum of the radial force in a machine with an air gap, based on the spectrum of the applied voltage. The measurements show that the spectral components are caused mainly by the modulation, which agrees with the results from the analytical solution. A method to determine the dominant frequency components from the radial force spectrum based on current measurements is also presented.**

I. INTRODUCTION

Noise from an electric machine may arise due to mechanical, aerodynamic, electronic and magnetic sources [1]. The magnetic source and the mechanical structure interact due to the magnetic forces and the frequency response of the mechanical structure [2, 3]. It is well known that the normal components of the current dependent forces are significantly larger than the tangential components [2].

The standard approach for vibration analysis is to use DFT on the measured signals, rather than an analytical solution to find the spectra. The drawback of using DFT is that it is limited by its inputs: windowing will introduce sidelobes in the frequency domain, and aliasing will introduce non-existing frequency components. The magnitude of the signal will be influenced by the limits of the analogue to digital conversion, the physical setup of the measurements, and external noise. An analytical solution is not affected by the previously mentioned factors in its prediction of the spectral components.

A previous analytical approach for treating pulse width modulation (PWM) effects on AC-drives was presented in [4], however radial forces were not considered in that paper. The radial forces were considered also regarding harmonics in the magnetic air gap flux in [5], without an evaluation of the effects from PWM. However, at low speed, switching frequency is the dominant source of the acoustic noise generated by the machine [6, 7]. The effects from PWM were considered with regards to the radial force in [6], but the authors did not treat analytically the relationship between PWM and radial force. Radial force prediction and calculation for a PWM driven asynchronous motor using finite-element method (FEM) can be found in [8-10]. A very comprehensive overview of harmonic analysis of PWM is described in [11], where the focus is on the voltage spectrum and not radial force spectrum.

From vibration and acoustic noise point of view it is important to know the origin of the individual frequency components from their spectra, to avoid/minimize the excitation of the resonances of the entire drive system. Although in this paper the complex construction of a rotating machine was simplified to a coil, the simulations using finite-element method (FEM) and measurements show very good coincidence on the vibration spectra with an asynchronous motor. Based on the above-mentioned simplification, this paper introduces an analytical method for determining the frequency components of the normal force spectra caused by PWM. The method is based on the analytical description of the PWM-generated line to line voltage. A graphical presentation of the analytical solution is then compared to the measurements on a simplified setup and on an induction motor.

II. ANALYTICAL DETERMINATION OF THE FORCE SPECTRA

Based on [11], the line to line voltage spectrum of a there phase asymmetrical regularly sampled sine-triangle modulation can be expressed as:

$$V_{ll}(t)=\frac{4\sqrt{3}V_{dc}}{\pi}J_1\left(\frac{\omega_o}{\omega_c}\frac{\pi}{2}M\right)cos\left(\omega_o t+\frac{\pi}{6}\right)+$$
$$\frac{8V_{dc}}{\pi}\sum_{m=1}^{\infty}\sum_{n=-\infty}^{\infty}\left(\begin{array}{l}\frac{1}{q}J_n\left(q\frac{\pi}{2}M\right)sin\left((m+n)\frac{\pi}{2}\right)\times\\ sin\left(n\frac{\pi}{3}\right)cos\left((m\omega_c+n\omega_0)t-n\frac{\pi}{3}+\frac{\pi}{2}\right)\end{array}\right) \quad (1)$$

where: V_{dc} – DC-link voltage; M – Modulation index; ω_o – Modulated frequency; ω_c – Carrier frequency; J – Bessel function; m - Carrier frequency component; n - sideband harmonics of the carrier frequency; $q=m+n\left(\frac{\omega_0}{\omega_c}\right)$ for asymmetrical regular sampled PWM

Using equation (1) the analytical form of the spectrum of the normal force can be approximated. The normal force f in a not saturated coil is given by:

$$f=\frac{\psi^2}{2\mu_0 AN^2}=\frac{L^2}{2\mu_0 AN^2}\cdot i^2=k\cdot i^2 \quad (2)$$

where ψ – magnetic flux, μ_0 – magnetic permeability, A - cross sectional area of the magnetic path, N – number of wire turns, L – inductance, k – constant in time;

Since all the parameters in an ideal coil are constant, (noted as k in (2)) they can be ignored and thus represents a normalized spectra.

The flux can be expressed in function of the line voltage, ignoring nonlinearities and the phase resistances:

$$\psi(t) \simeq \int V_{ll}(t)dt \tag{3}$$

Expressing the flux by integrating the voltage equation (1) in function of time:

$$\psi(t) = \int V_{ll}dt = \frac{4\sqrt{3}V_{dc}}{\pi\omega_0} J_1\left(\frac{\omega_o}{\omega_c}\frac{\pi}{2}M\right)\sin\left(\omega_o t + \frac{\pi}{6}\right) + \frac{8V_{dc}}{\pi}\sum_{m=1}^{\infty}\sum_{n=-\infty}^{\infty}\left(\begin{array}{l}\frac{1}{q(m\omega_c + n\omega_o)} J_n\left(q\frac{\pi}{2}M\right)\times \\ \sin\left((m+n)\frac{\pi}{2}\right)\sin\left(n\frac{\pi}{3}\right)\times \\ \cos\left((m\omega_c + n\omega_o)t - n\frac{\pi}{3}\right)\end{array}\right) \tag{4}$$

Substituting the flux equation (4) in (2), the force equation becomes:

$$f(t) = \left(\begin{array}{l}\sqrt{\frac{1}{2\mu_0 AN^2}}\frac{4\sqrt{3}V_{dc}}{\pi\omega_0} J_1\left(\frac{\omega_o}{\omega_c}\frac{\pi}{2}M\right)\sin\left(\omega_o t + \frac{\pi}{6}\right) + \\ \sqrt{\frac{1}{2\mu_0 AN^2}}\frac{8V_{dc}}{\pi}\sum_{m=1}^{\infty}\sum_{n=-\infty}^{\infty}\left(\begin{array}{l}\frac{1}{q(m\omega_c + n\omega_o)} J_n\left(q\frac{\pi}{2}M\right)\times \\ \sin\left((m+n)\frac{\pi}{2}\right)\sin\left(n\frac{\pi}{3}\right)\times \\ \cos\left((m\omega_c + n\omega_o)t - n\frac{\pi}{3}\right)\end{array}\right)\end{array}\right)^2 \tag{5}$$

Recalling the amplitude values of the fundamental and the harmonic components from the force equation:

$$\begin{cases} Fund = \sqrt{\frac{1}{2\mu_0 AN^2}}\frac{4\sqrt{3}V_{dc}}{\pi\omega_0} J_1\left(\frac{\omega_o}{\omega_c}\frac{\pi}{2}M\right) \\ Harm_{(m,n)} = \sqrt{\frac{1}{2\mu_0 AN^2}}\frac{8V_{dc}}{\pi q(m\omega_c + n\omega_o)}\times \\ \qquad J_n\left(q\frac{\pi}{2}M\right)\sin\left((m+n)\frac{\pi}{2}\right)\sin\left(n\frac{\pi}{3}\right) \end{cases} \tag{6}$$

The force equation becomes:

$$f(t) = \left(\begin{array}{l} Fund\cdot\sin\left(\omega_o t + \frac{\pi}{6}\right) + \\ \sum_{m=1}^{\infty}\sum_{n=-\infty}^{\infty}\left(Harm_{(m,n)}\cdot\cos\left(\begin{array}{l} m\omega_c t + \\ n\left(\omega_o t - \frac{\pi}{3}\right)\end{array}\right)\right)\end{array}\right)^2 \tag{7}$$

In case of other modulation methods like space vector modulation (SVM), third-harmonic reference injection or discontinuous PWM (DPWM), equation (6) will be expanded with further harmonic components as they are described in [11].

Expanding the square and by using the trigonometric identities, (7) is transformed into:

$$\begin{aligned} f(t) = {} & Fund^2\frac{1-\cos\left(2\left(\omega_o t + \frac{\pi}{6}\right)\right)}{2} + \\ & \sum_{m=1}^{\infty}\sum_{n=-\infty}^{\infty}\left(\begin{array}{l} Fund\cdot Harm_{(m,n)}\times \\ \sin\left(\begin{array}{l}\left(m\omega_c + (n+1)\omega_0\right)t + \\ (1-2n)\frac{\pi}{6}\end{array}\right) \\ Fund\cdot Harm_{(m,n)}\times \\ \sin\left(\begin{array}{l}\left((1-n)\omega_0 - m\omega_c\right)t + \\ (2n+1)\frac{\pi}{6}\end{array}\right)\end{array}\right) + \\ & \sum_{m=1}^{\infty}\sum_{i=1}^{m}\sum_{n=-\infty}^{\infty}\sum_{j=-\infty}^{\infty}\left(\begin{array}{l} Harm_{(m,n)}Harm_{(i,j)}\times \\ \left(\begin{array}{l}\cos\left(\begin{array}{l}\left(\begin{array}{l}(i-m)\omega_c + \\ (j-n)\omega_o\end{array}\right)t + \\ (n-j)\frac{\pi}{3}\end{array}\right) + \\ \cos\left(\begin{array}{l}\left(\begin{array}{l}(i+m)\omega_c + \\ (j+n)\omega_o\end{array}\right)t - \\ (n+j)\frac{\pi}{3}\end{array}\right)\end{array}\right)\end{array}\right) + \\ & \sum_{m=1}^{\infty}\sum_{n=-\infty}^{\infty}\sum_{j=n+1}^{\infty}\left(\begin{array}{l} Harm_{(m,n)}Harm_{(m,j)}\times \\ \left(\begin{array}{l}\cos\left((j-n)\omega_o t + (n-j)\frac{\pi}{3}\right) + \\ \cos\left(\begin{array}{l}\left(2m\omega_c + (n+j)\omega_o\right)t - \\ (n+j)\frac{\pi}{3}\end{array}\right)\end{array}\right)\end{array}\right) + \\ & \sum_{m=1}^{\infty}\sum_{n=-\infty}^{\infty}\left(\frac{\left(Harm_{(m,n)}\right)^2\times \cos\left(2m\omega_c t + 2n\left(\omega_o t - \frac{\pi}{3}\right)\right) + 1}{2}\right) \end{aligned} \tag{8}$$

Comparing the voltage equation (1) with the force equation (8), it can be concluded that:

1. the frequency of the fundamental force component will have double the frequency compared to the fundamental in the voltage spectrum

2. Since the force is proportional to the squared voltage, this gives rise to a convolution in the frequency domain. The second, the third, and the fourth line from equation (8) are the result of this convolution.

III. Simplified Experimental Setup for Evaluation of the Vibration Spectra

To isolate the effect of the PWM on the vibration spectra from the vibrations caused by the complex structure of the motor, a simplified setup with no moving parts was used. The behavior of the normal force in the induction motor can be approximated with a single coil shown in Fig. 1, as it was done similarly in [12], for a switched reluctance motor. To have the same shape of the current in the coil as in one phase of an induction motor, the coil was connected to the inverter together with two resistors as shown in Fig. 3. The transfer function between the current of the coil and the vibration on the frame of the coil depends on the mechanical structure of the coil. This transfer function has been determined using Random PWM (RPWM) [13]. RPWM has the property to distribute the discrete frequency components from the current spectrum creating a spectrum close to white noise. The current with a spectrum like white noise equally excites all the frequency components, giving the response of the mechanical structure to them in term of vibrations. The transfer function from phase current to shell vibrations of the asynchronous motor presented in Fig. 4 was measured in the same way. The advantage to determine the transfer function of the mechanical structure by measurements is that it gives a real picture about the entire mechanical system.

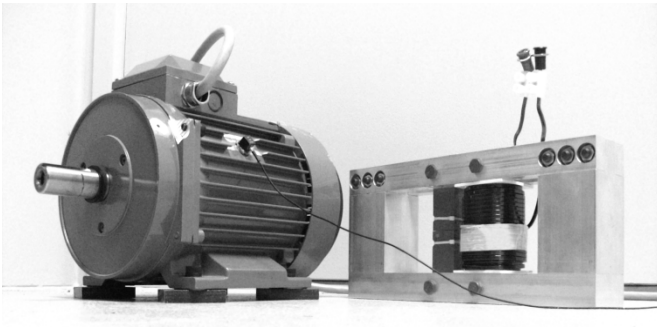

Fig. 1 The motor and coil used for measurements

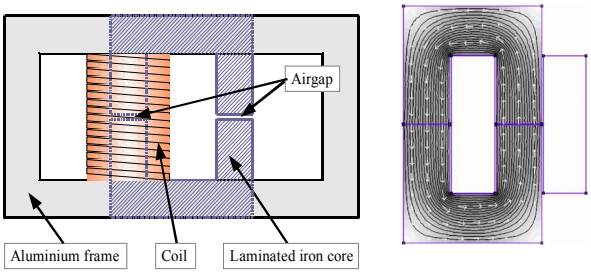

Fig. 2 On the left is shown two u-cores with an 0.8 mm air gap, and a coil to excite this core with 80 turns and 3 mH inductance. The core has a cross sectional area of 6 cm^2. The acceleration sensor is placed on the aluminum frame. The right side is a result from a FEM simulation of the magnetic circuit.

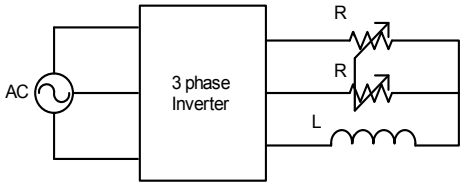

Fig. 3 Experimental setup schematic for the coil fed by an inverter

To calculate the normal force in the air gap acting on the laminated iron core of the coil, FEM simulation was set up as shown in Fig. 2. Stepping through various current levels a look up table was generated. Since vibrations comes from the acceleration on the shell of the coil, and $F = m \cdot a$ the, force is proportional to the vibrations. The normalized force spectrum is thus equal to the normalized acceleration spectrum.

IV. Experimental Validation

For experimental tests, the 2.2 kW asynchronous motor and the coil was used driven by a 2.2 kW Danfoss FC302 VLT three phase inverter. The current and vibrations on the motor/coil frame were measured with a Bruel and Kjaer Pulse Multi-analyzer type 3560. Asymmetrical regular sampled sine-triangular modulation was used for the measurements. The switching frequency was set to 5kHz, while the fundamental frequency of the current was 35Hz.

Fig. 5 presents the results of vibration spectra obtained by different methods: calculated analytically, using a current to force look-up table and by measuring the vibration on the frame of the coil. The theoretical spectra components of the vibrations created by the PWM can be seen in Fig. 5 (a) and (b). To compare the calculated and measured spectra the transfer function of the mechanical structure of the coil was added in Fig. 5 (c) and (d). The measured and calculated spectra were normalized to the maximum amplitude from their respective spectra.

To show the coincidence between the calculated and measured spectra Fig. 6 and Fig. 7 presents a zoom in the spectra around 10 kHz respectively 5 kHz.

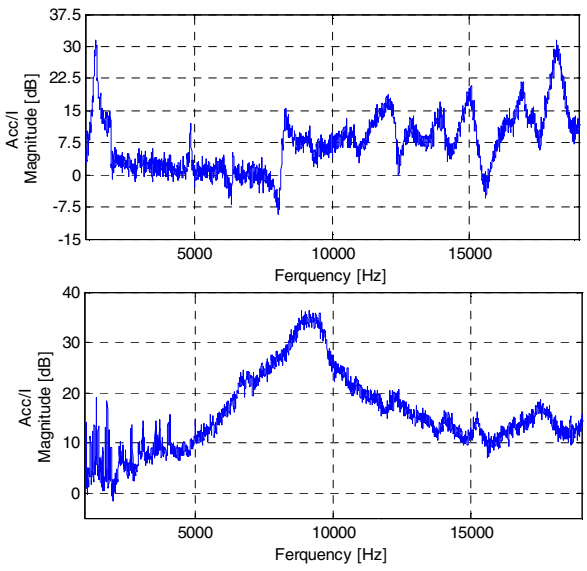

Fig. 4 Measured transfer function between current and acceleration of the mechanical structure: in the top for the coil, in the bottom for the motor

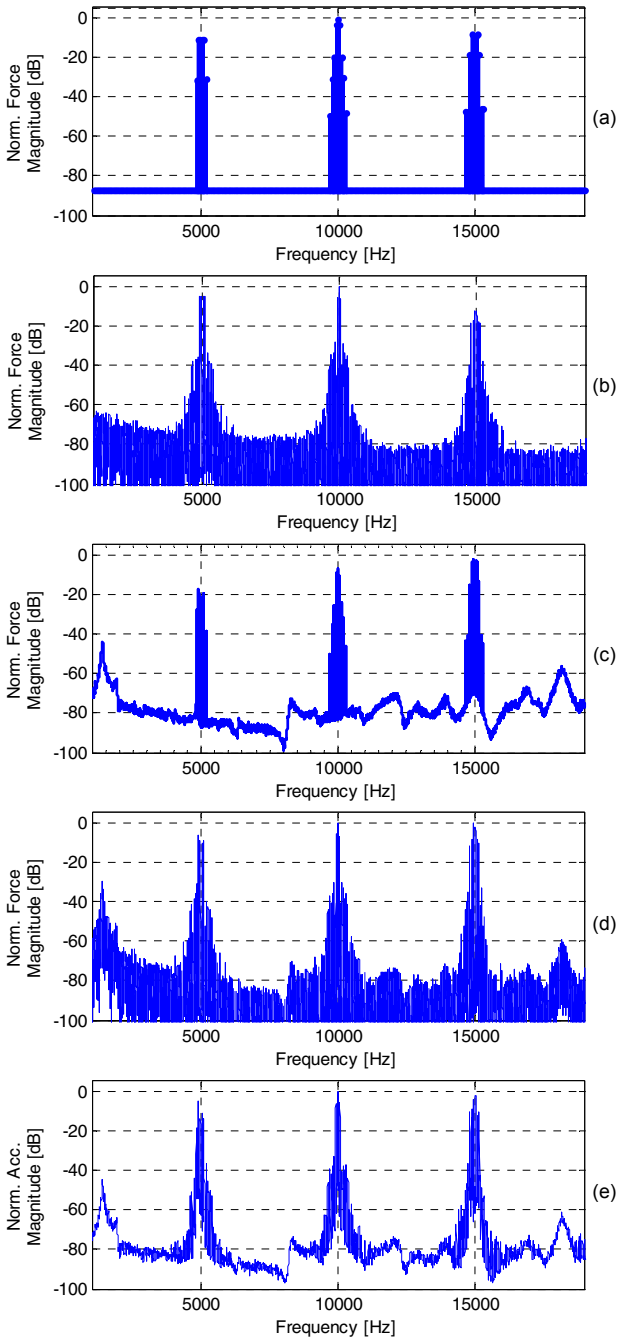

Fig. 5 The normalized vibration spectra on the frame of the coil: (a) analytical calculated spectra, (b) spectra derived using the current to force look-up table, (c) analytical calculated spectra adjusted with the transfer function of the mechanical structure, (d) Simulation using force look-up table adjusted with the transfer function of the mechanical structure (e) measured spectra

Fig. 8 presents the calculated and measured spectra for the asynchronous motor. For the spectra given by the analytical calculations (Fig. 8 (a)), the current – to – vibration transfer function of the motor has been considered. The prediction of the force spectra in the asynchronous motor using (2) is shown in Fig. 8 (b). Using (2) with the measured phase current from the rotating asynchronous motor as input, the

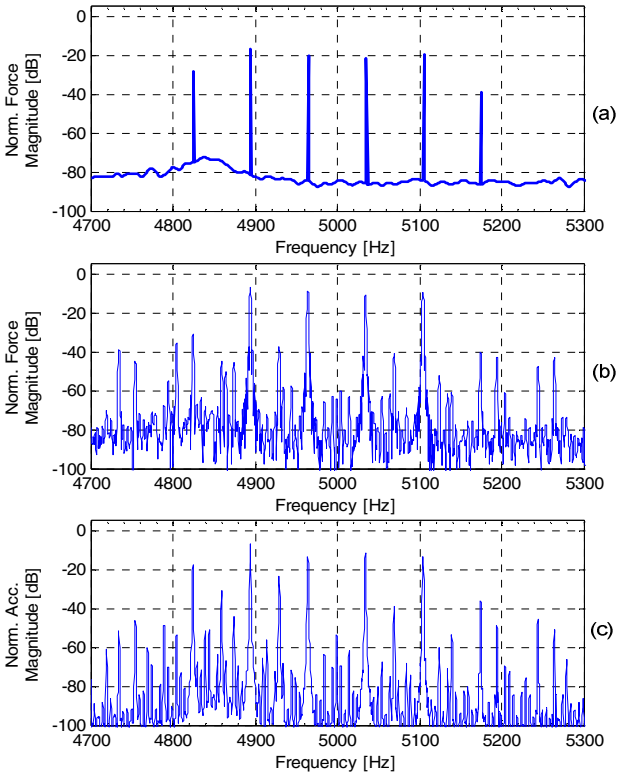

Fig. 6 Zoom in vibration spectra of the coil at 5kHz: (a) analytically calculated spectra, (b) vibration spectra using force look-up table, (c) measured vibration spectra

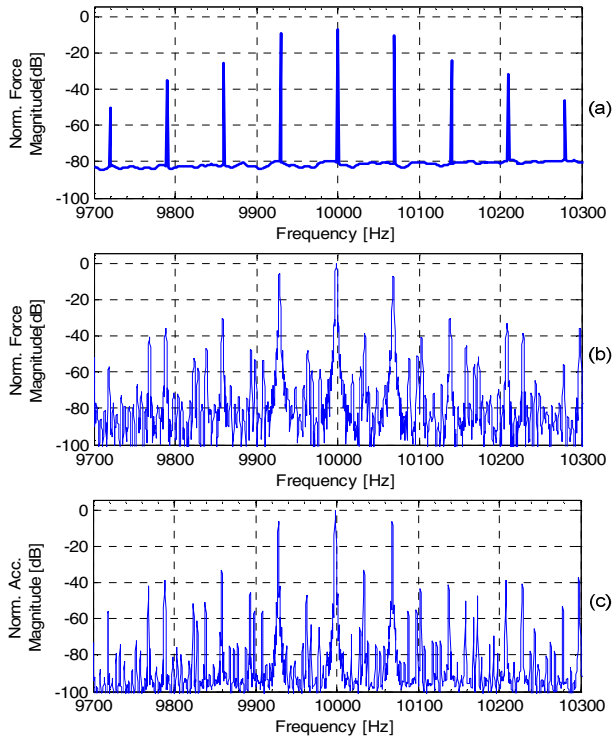

Fig. 7 Zoom in vibration spectra of the coil at 10kHz: (a) analytically calculated spectra, (b) vibration spectra using force look-up table, (c) measured vibration spectra

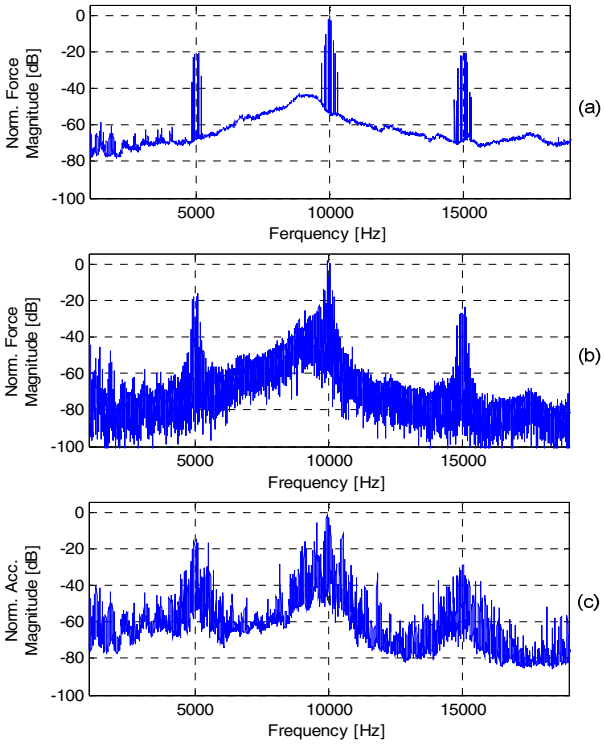

Fig. 8 The normalized spectra of vibrations on the motor shell: (a) analytically calculated spectra, (b) vibration spectra using force look-up table, (c) measured vibration spectra

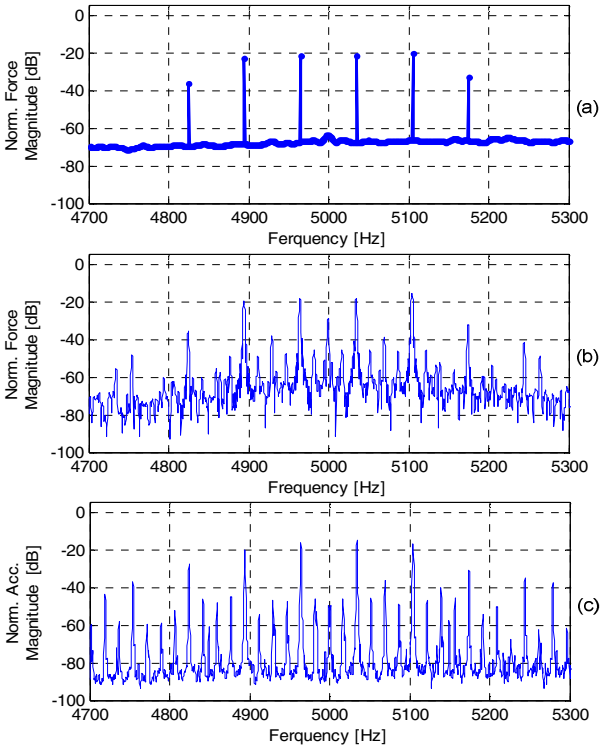

Fig. 9 Zoom in vibration spectra on the motor shell at 5kHz: (a) analytically calculated spectra, (b) vibration spectra using force look-up table, (c) measured vibration spectra

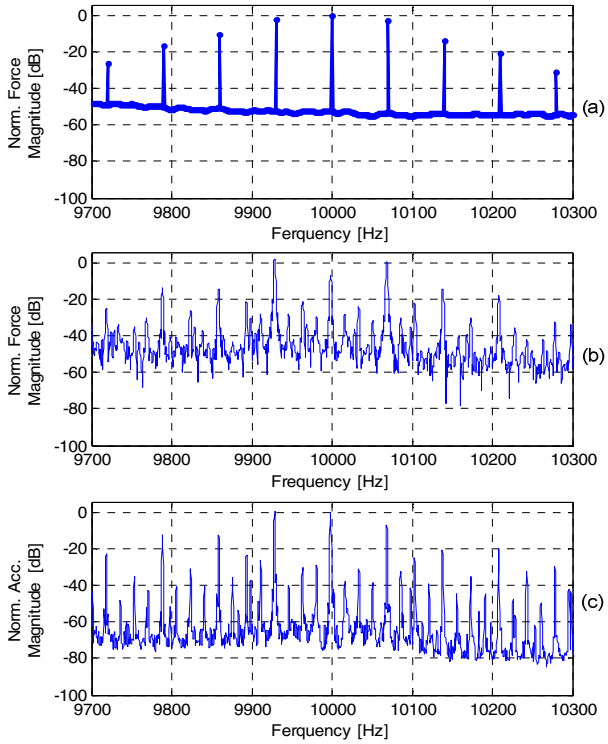

Fig. 10 Zoom in vibration spectra on the motor shell at 10 kHz: (a) analytically calculated spectra, (b) vibration spectra using force look-up table, (c) measured vibration spectra

equivalent force in the air gap of an imaginary coil was calculated and normalized. The spectrum of the force was calculated using DFT with a Hanning windowing function, the same as was used in vibration measurements on the motor shell.

As it can be seen on Fig. 8, the predicted spectra from both the analytical solution and from the FEM model, shows good agreement with the measured acceleration on the shell of the induction motor.

Although the mechanical structure of the motor is completely different from the structure of the coil used for FEM model, the spectra of the vibration around the switching frequency shows very good match.

The magnitude of vibrations on the motor and coil are influenced by mechanical parameters [12], measurement errors, and limitations of the DFT, but the main spectral components from the analytical solution fits the measured results as it is shown on the zoomed spectra. The resolution of the measurements for the zoomed spectra was increased; this is the reason why the base level of the full spectra is higher than the base level of the zoomed spectra.

V. Conclusions

New methods for predicting the spectral components of the normal force in a machine with an air gap have been presented in this paper. This prediction was achieved using a simplified setup. One solution is to analytically calculate the spectral components of the vibrations based on the analytical

solution of the line to line voltage generated by PWM. The second solution to predict the vibrations spectra is based on the measured phase current of the motor, which is fed into a current to force look-up table of the simplified system.

The measurements show that the dominant spectral components in an asynchronous motor are caused mainly by the modulation, which agrees well with the results obtained from the analytical solution and simulation based on the current to force look-up table. The advantage of the analytical method is that it allows isolating spectral components caused by the PWM even in mechanically complex drive system. The method can be applied to other than sin-triangular PWM strategies to evaluate their performance in terms of radial force. The experiments show that vibrations caused by the PWM are dominant irrespective if the PWM was applied to the coil or the induction motor.

VI. Acknowledgment

The authors would like to thank for Danfoss Drives for supporting this work.

References

[1] F. J. Gieras, C. Wang, and J. C. S. Lai, *Noise of Polyphase Electric Motors*: CRC / Taylor & Francis, 2006.

[2] R. Krishnan and P. Vijayraghavan, "State of the art: acoustic noise in switched reluctance motor drives," in *Industrial Electronics Society, 1998. IECON '98. Proceedings of the 24th Annual Conference of the IEEE*, 1998, pp. 929-934 vol.2.

[3] P. Pillay and W. Cai, "An investigation into vibration in switched reluctance motors," *Industry Applications, IEEE Transactions on,* vol. 35, pp. 589-596, 1999.

[4] H. W. van der Broeck and H. C. Skudelny, "Analytical analysis of the harmonic effects of a PWM AC drive," *Power Electronics, IEEE Transactions on,* vol. 3, pp. 216-223, 1988.

[5] S. P. Verma and A. Balan, "Determination of radial-forces in relation to noise and vibration problems of squirrel-cage induction motors," *Energy Conversion, IEEE Transaction on,* vol. 9, pp. 404-412, 1994.

[6] W. C. Lo, C. C. Chan, Z. Q. Zhu, X. Lie, D. Howe, and K. T. Chau, "Acoustic noise radiated by PWM-controllel induction machine drives," *Industrial Electronics, IEEE Transactions on,* vol. 47, pp. 880-889, 2000.

[7] N. Hashemi, R. Lisner, and D. G. Holmes, "Acoustic noise reduction for an inverter-fed three-phase induction motor," in *Industry Applications Conference, 2004. 39th IAS Annual Meeting. Conference Record of the 2004 IEEE*, 2004, pp. 2030-2035 vol.3.

[8] C. Wang, J. C. S. Lai, and A. Astfalck, "Sound power radiated from an inverter driven induction motor II: Numerical analysis," *Electric Power Applications, IEE Proceedings -,* vol. 151, pp. 341-348, 2004.

[9] C. Wang and J. C. S. Lai, "Sound power radiated from an inverter-driven induction motor. Part 3: statistical energy analysis," *Electric Power Applications, IEE Proceedings -,* vol. 152, pp. 619-626, 2005.

[10] C. Wang, A. Astfalck, and J. C. S. Lai, "Sound power radiated from an inverter-driven induction motor: experimental investigation," *Electric Power Applications, IEE Proceedings -,* vol. 149, pp. 46-52, 2002.

[11] D. G. Holmes and T. A. Lipo, *Pulse Width Modulation for Power Converters: Principles and Practice*: John Wiley &Sons, Inc., 2003.

[12] P. O. Rasmussen, J. H. Andreasen, and E. C. LaBrush, "Interlaminated damping - a method for reduction of vibration and acoustic noise for switched reluctance machines?," in *Industry Applications Conference, 2005. Fourtieth IAS Annual Meeting. Conference Record of the 2005*, 2005, pp. 1531-1539 Vol. 3.

[13] A. M. Trzynadlowski, F. Blaabjerg, J. K. Pedersen, R. L. Kirlin, and S. Legowski, "Random pulse width modulation techniques for converter-fed drive systems-a review," *Industry Applications, IEEE Transactions on,* vol. 30, pp. 1166-1175, 1994.

[P2] Laszlo Mathe, Peter Omand Rasmussen, John K. Pedersen,
Institute of Energy Technology; Aalborg University; Aalborg, Denmark

"Shaping the spectra of the line-to-line voltage using signal injection in the common mode voltage"

Proc. of IECON 2009, ISBN: 978-1-4244-4648-3*, pp.* 1288 - 1293

Shaping the spectra of the line-to-line voltage using signal injection in the common mode voltage

Laszlo Mathe, Peter Omand Rasmussen, John K. Pedersen
Institute of Energy Technology; Aalborg University; Aalborg, Denmark
lam@iet.aau.dk

Abstract — A drawback of Pulse Width Modulation in electrical drives is the high harmonic content of the line to line voltages, which gives rise to Electro-Magnetic Interference and acoustic noise. By injection of a signal into the common mode voltage, the fundamental is not affected, but new frequency components are introduced in the line to line voltage spectrum. This paper introduces a new analytical method for estimation of the line to line voltage spectrum, where sinusoidal signal is injected into the common mode voltage. Based on the analytical calculations, also a new fixed carrier frequency quasi-random PWM method is proposed. The advantage of the proposed random PWM method is that the acoustical noise generated by the drive can be improved, without exciting the electrical and mechanical resonances of the full drive system. A graphical representation is also presented, where during a fundamental period the distribution of the zero vectors can be tracked.

I. Introduction

In most of the variable speed drives, a pulse width modulated (PWM) converter is used for generation of three phase voltages for an electrical motor. The advantage of power converters based on PWM is that, it can generate controllable magnitude and frequency voltage with high efficiency. A drawback of PWM based converters is the high harmonic content of the generated voltages, which gives rise to electro-magnetic interference (EMI) and acoustic noise in a motor.

The carrier based sine-triangle PWM method generates a train of pulses for the power switches from an inverter, based on the comparison between a high frequency triangular and a sinusoidal reference signal. By adding the 3rd harmonic to the phase voltages the linear range of the modulation index can be extended by 15% [1]. The modulation index is the normalized fundamental voltage. Another method to generate the pulses for the power switches is called Space Vector Modulation (SVM) [2]. The difference between SVM and sine-triangle method with 3rd harmonic added is that, in case of SVM, the added signal is triangular. Injection of the same signals into the phase voltages does not affect the fundamental of the line-to-line (*l-l*) voltage [3], but it will introduce some new high frequency components into its spectrum. From vector generation point of view, the injection of a signal into the Common Mode Voltage (CMV), changes the time distribution between the zero-state vectors V_{000} and V_{111}. A study, regarding to the distribution of the time length of the applied zero vectors can be found in [4]. The replacement of the zero-state vectors in a random manner gives rise to several fixed carrier frequency (FCF) random PWM (RPWM) methods [5], which are very popular because of their easy implementation in drives with closed loop control. The advantage of spreading the spectrum of the voltages and currents of the motor is that the EMI and acoustical performance of the drive [6] can be improved. The uniform distribution of the spectrum achieved using RPWM has the drawback of exciting the electrical or mechanical resonances of the drive system [7]. The new FCF quasi RPWM method proposed in this paper has the advantage to control the composition of the spectrum, in a way to avoid those frequency components which may excite the electrical or mechanical resonances on the drive system.

So far, general analytical description of the harmonic contents in the *l-l* voltage, caused by the upper harmonic of the fundamental signal injected in the CMV has not been found in the literature, except for the third-harmonic injection. This paper introduces a new analytical method to determine the amplitude and frequency components of the *l-l* voltage spectrum using sinusoidal signal injection in the CMV. A new graphical representation of the three reference voltages, where the distribution of the zero vectors during a fundamental period can be tracked, is also presented.

II. Analogy between representation of one period of fundamental signal in polar coordinates and SVM representation

A two level voltage source converter, (Fig. 1) is built using power transistors. The binary switching functions (q_a, q_b, q_c) describe the state of each switch in time. The converter presented in Fig. 1 can operate on eight different states; on each state one voltage vector is generated, called basic voltage vectors.

During a modulation period using SVM, seven basic voltage vectors are generated as it can be seen in Fig. 2 (a). These basic vectors can be classified as active vectors (AV), when the load takes the energy from the DC-link, and zero vectors (ZV) when the output legs of converter are connected together to plus or minus of U_{dc} (no energy is taken from the DC-link). The six active vectors can be represented in α-β reference frame as in Fig. 2 (b).

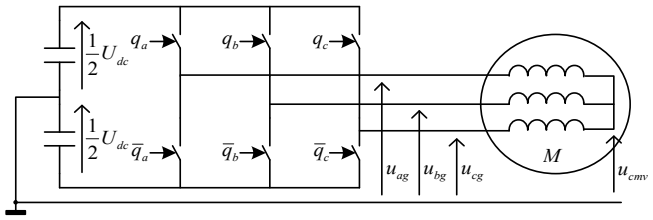

Fig. 1 Three phase voltage-source converter

In Fig. 2 (a) the regions where active vectors were generated, are highlighted.

A graphical interpretation of the voltage space vector in α-β plane can be seen in Fig. 2 (b). The generated $\bar{U}_s$ voltage space vector can be decomposed in two adjoin basic vector with the following equations:

$$\begin{cases} \bar{U}_s = d_{av1} \cdot \bar{V}_x + d_{av2} \cdot \bar{V}_y \\ d_{av1} = \sqrt{3} \dfrac{|U_s|}{U_{dc}} \sin(\gamma) \\ d_{av2} = \sqrt{3} \dfrac{|U_s|}{U_{dc}} \sin(\dfrac{\pi}{3} - \gamma) \end{cases} \quad (1)$$

where the duty ratios d_{av1} and d_{av2} are the ratio between the time-length of the applied vector and the modulation period T, V_x and V_y are adjoin basic vectors. The relation between the time interval of the AV's and duty ratios can be written as:

$$\begin{cases} t_{av1} = d_{av1} T \\ t_{av2} = d_{av2} T \end{cases} \quad (2)$$

From the generated fundamental l-l voltage point of view, the time distributions of zero-state vectors between V_{000} and V_{111} are not relevant; they are not represented in SVM representation in α-β plane (Fig. 2 (b)).

Distribution of the zero vectors using sine-triangle comparison and SVM during a period of the fundamental reference signal is shown in Fig. 3. The power transistors are switched when one from the three target reference signals (Fig. 3) is intersecting the triangular carrier waveform. The amplitude of the reference sinusoidal signal (modulation index) was set to 0.7.

Fig. 3 (b) presents the reference signals, which were obtained by adding a triangular signal to the reference signals from Fig. 3 (a). Similar reference signals can be obtained using SVM, where during a fundamental period the t_{z0} and t_{z1}

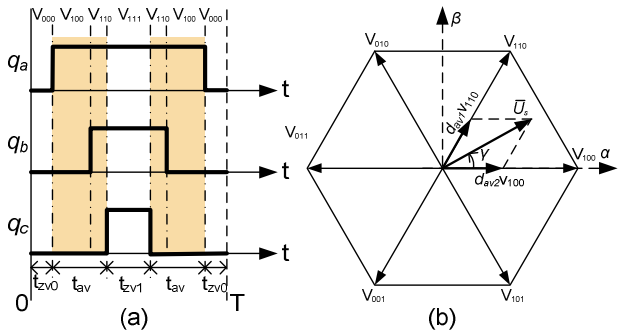

Fig. 2 Representation of a generated vector (a) as switching function for the power switches, (b) SVM representation of the generated voltage vector in α-β plane

are always set to be equal.

The advantage of this kind of reference signals is that the linear range of the modulation index can be extended by 15%. From Fig. 3 (a) and (b) it can be seen that having the same modulation index, the time t_{z1min} is shorter in case of sine-triangular method than in case of SVM. This shows that the maximum modulation index in linear range using SVM is extended 15% compared to sine-triangular method.

The time coordinate representation of the fundamental period from Fig. 3 (b) is presented in Fig. 4 (a) in polar coordinates. In polar coordinates representation, the intersection of the radius at an angle γ with the curves drawn by the three phase voltages gives the individual time components (t_{z0}, t_{av1}, t_{av2}, t_{z1}). The relation between time components obtained by the intersection of the radius with the reference signals and the resultant voltage vector is given by (1) and (2). This relation between radius and voltage vector shows analogy using polar coordinates and SVM representation in α-β plane like in Fig. 4. The benefit of using representation in polar coordinates, is to make the time distribution between the two zero-state vectors visible.

The maximum amplitude which can be reached by the active vector (eliminating the zero-state vectors) in polar

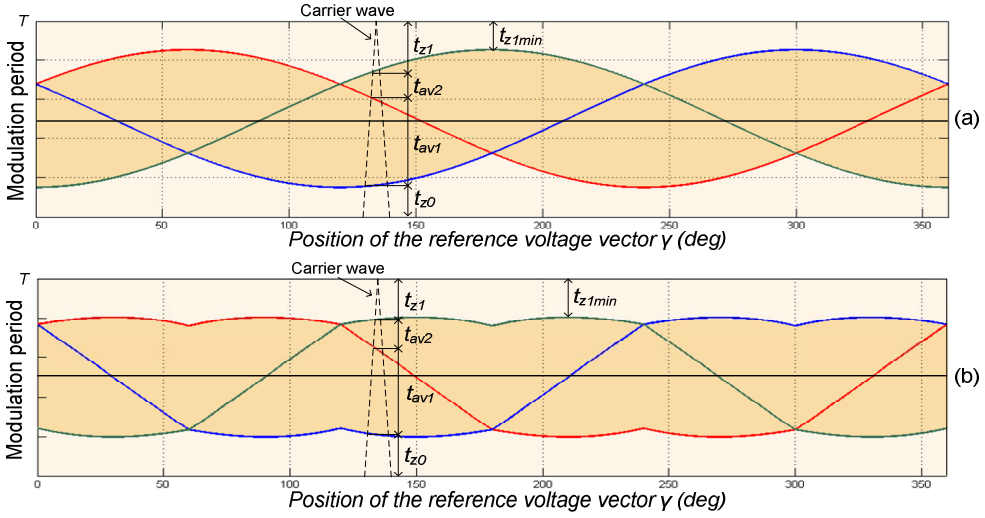

Fig. 3 Representation of phase voltages using (a) sine-triangular modulation, (b) SVM during a period of the fundamental signal

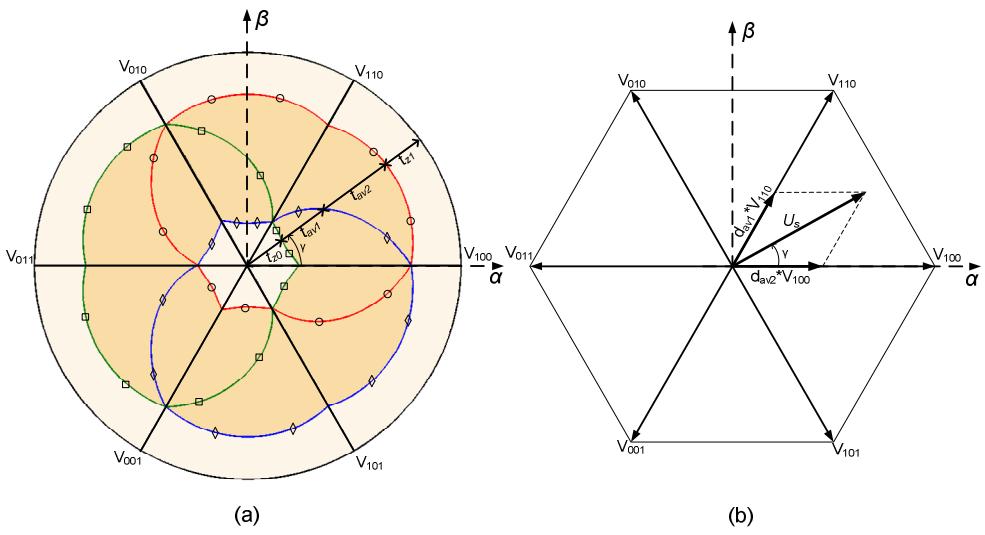

Fig. 4 (a) representation of the phase voltages using polar coordinates (b) representation using voltage space vector

representation, is a circle. Transformation of the time length of the active vector to duty ratios using (2), and representation as vectors like in Fig. 4 (b) transforms the circle in a hexagon. When a signal is injected into the CMV, each phase voltage curve should draw one closed curve, which should be inside the circle from Fig. 4 (a), otherwise the fundamental *l-l* voltage will be distorted.

III. Injection of a Sinusoidal Signal into the Common Mode Voltage

As presented in the introduction, adding the same signal to all the three phase voltages, the fundamental *l-l* voltage will not be affected. The equations of the three phase reference voltages with the injected sinusoidal signal are:

$$\begin{cases} u_{ag} = U_{dc}(M\cos(\omega_0 t) + M_z \sin(z\omega_0 t)) \\ u_{bg} = U_{dc}(M\cos(\omega_0 t - \frac{2\pi}{3}) + M_z \sin(z\omega_0 t)) \\ u_{cg} = U_{dc}(M\cos(\omega_0 t + \frac{2\pi}{3}) + M_z \sin(z\omega_0 t)) \end{cases} \quad (3)$$

where u_{ag} is the phase to ground voltage of phase *A*, *M* is the modulation index, M_z is the amplitude of the injected harmonic, while *z* is the number of the fundamentals upper harmonic.

The *l-l* output voltages can be calculated from eq. (3), and they are given by the differences between the phase leg voltages:

$$\begin{cases} u_{ab} = u_{ag} - u_{bg} = M\sqrt{3}U_{dc}\cos(\omega_0 t + \frac{\pi}{6}) \\ u_{bc} = u_{bg} - u_{cg} = M\sqrt{3}U_{dc}\cos(\omega_0 t - \frac{\pi}{2}) \\ u_{ca} = u_{zg} - u_{ag} = M\sqrt{3}U_{dc}\cos(\omega_0 t + \frac{5\pi}{6}) \end{cases} \quad (4)$$

It can be noticed that the injected signal in phase to ground voltages disappears from (4). Injecting a sine wave with the amplitude of $M_z=0.15M$ and frequency of $f=7\omega_o t$ into the CMV (*M* and ω_o same as it was for SVM from Fig. 4), the plot of the three phase voltages in polar and Cartesian coordinates becomes as presented in Fig. 5.

Representation of the modulation with the 7th harmonic injection in *α-β* plane, presented for SVM in Fig. 4 (b), will not differ from the representation of the same modulation without the 7th harmonic injected.

The injection of the 7th harmonic spreads the position of the active vector in a carrier period, which results in a higher motor current ripple and reduces the linear range of the modulation index. The advantage of injecting such a signal in CMV is that new frequency components appears in the *l-l* voltage spectrum, which may improve the EMC and the acoustical performance of the motor [6].

IV. Determination of the *l-L* Voltage Spectrum Using Double Fourier Series

A mathematical approach for determination of the Fourier spectrum of the phase or *l-l* voltages generated by PWM is described in [8]. From the Fourier transform theory of decomposition, a time varying signal *f(t)* can be expressed as an infinite series of sine and cosine harmonic components:

$$f(t) = \frac{a_0}{2} \sum_{m=-\infty}^{\infty} \left(a_m \cos(m\omega t) + b_m \sin(m\omega t)\right) \quad (5)$$

where a_m and b_m are the amplitudes of each individual frequency component and they can be determined using a Fourier integral:

$$\begin{cases} a_m = \frac{1}{T}\int_{-\frac{T}{2}}^{\frac{T}{2}} f(t)\cdot\cos(m\omega t)dt \\ b_m = \frac{1}{T}\int_{-\frac{T}{2}}^{\frac{T}{2}} f(t)\cdot\sin(m\omega t)dt \end{cases} \quad (6)$$

A PWM switching signal is generated by the combination of a reference signal (usually sinusoidal) and a carrier waveform

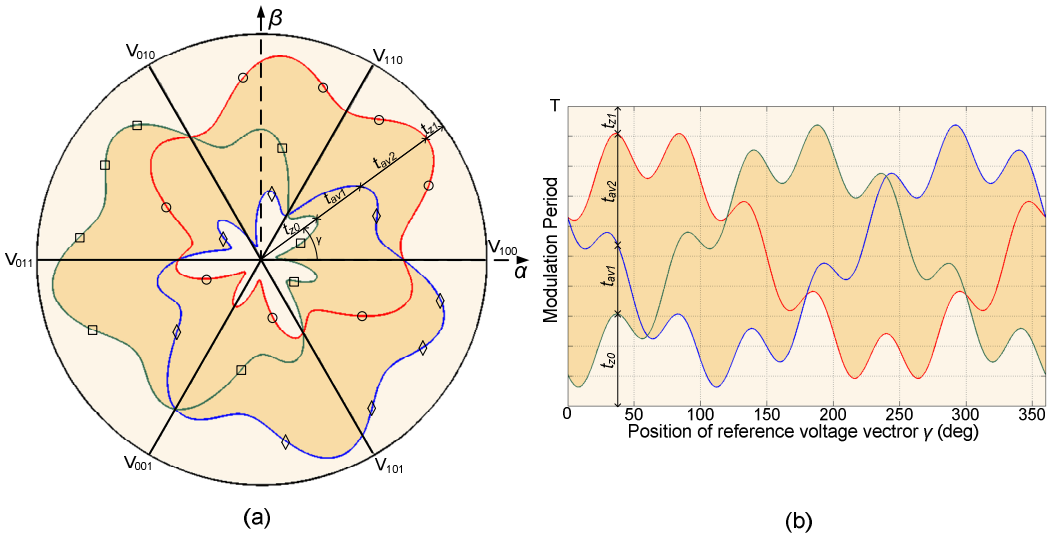

Fig. 5 Phase to ground voltage with the 7th harmonic injected during a fundamental period: (a) polar coordinates (b) Cartesian coordinates

(usually triangular). Mathematically the description of a PWM signal, which is generated by the comparison of two time variable functions can be described as:

$$\begin{cases} f(t) = f(x(t), y(t)) \\ x(t) = \omega_c t + \theta_c, y(t) = \omega_o t + \theta_o \end{cases} \quad (7)$$

where ω_c is the carrier angular frequency, ω_0 is the fundamental angular frequency, while θ_c and θ_o are the phase offsets.

The expansion in Fourier harmonics of the PWM switching function can be done by using the extension of (5) for a double variable function called double Fourier series method. The general equation of a decomposed PWM signal in harmonics as [3] is:

$$\begin{aligned} f(t) = \frac{A_{00}}{2} + \sum_{n=1}^{\infty}\begin{pmatrix} A_{0n}\cos\left(n(\omega_0 t+\theta_o)\right)+ \\ B_{0n}\sin\left(n(\omega_0 t+\theta_o)\right)\end{pmatrix}+ \\ \sum_{m=1}^{\infty}\begin{pmatrix} A_{m0}\cos\left(m(\omega_c t+\theta_c)\right)+ \\ B_{m0}\sin\left(m(\omega_c t+\theta_c)\right)\end{pmatrix}+ \\ \sum_{m=1}^{\infty}\sum_{\substack{n=-\infty \\ n\neq 0}}^{\infty}\begin{pmatrix} A_{mn}\cos\left(m(\omega_c t+\theta_c)+n(\omega_0 t+\theta_o)\right)+ \\ B_{mn}\sin\left(m(\omega_c t+\theta_c)+n(\omega_0 t+\theta_o)\right)\end{pmatrix} \end{aligned} \quad (8)$$

where the amplitude of the harmonic components can be defined as:

$$A_{mn} + jB_{mn} = \frac{U_{dc}}{\pi^2}\int_{-\pi}^{\pi}\int_{-\frac{\pi}{2}(1+M\cos(y)+M_z\cos(z\cdot y))}^{\frac{\pi}{2}(1+M\cos(y)+M_z\cos(z\cdot y))} e^{j(ny+qx)}dxdy \quad (9)$$

for a sinusoidal signal injected into the CMV. By setting $q = m + n(\omega_0/\omega_c)$ the equation becomes valid for a regular sampled asymmetrical modulation, while $q = m$ represents the case of a natural sampled modulation.

In (8) and (9), m is the carrier index variable, n is the baseband index variable.

Solving the double integral from (9), the closed-form solution can be expressed like:

$$A_{mn} + jB_{mn} = \frac{4U_{dc}}{q\pi}\left(\begin{array}{l} J_0\left(q\frac{\pi}{2}M\right)J_0\left(q\frac{\pi}{2}M_z\right)\sin(q\frac{\pi}{2})\Big|_{n=0} + \\ J_0\left(q\frac{\pi}{2}M_z\right)\sum_{k=1}^{\infty}\begin{pmatrix} J_k\left(q\frac{\pi}{2}M\right)\times \\ \sin\left((q+k)\frac{\pi}{2}\right)\end{pmatrix}\Big|_{k=|n|} + \\ J_0\left(q\frac{\pi}{2}M\right)\sum_{h=1}^{\infty}\begin{pmatrix} J_h\left(q\frac{\pi}{2}M_z\right)\times \\ \sin\left((q+h)\frac{\pi}{2}\right)\end{pmatrix}\Big|_{M_z h=|n|} \\ \sum_{k=1}^{\infty}\sum_{h=1}^{\infty}\begin{pmatrix} J_k\left(q\frac{\pi}{2}M\right)\times \\ J_h\left(q\frac{\pi}{2}M_z\right)\times \\ \sin\left((q+k+h)\frac{\pi}{2}\right)\end{pmatrix}\Big|_{\substack{k+M_z h=|n| \\ k-M_z h=|n| \\ M_z h-k=|n|}} \end{array}\right) \quad (10)$$

where k and h are the index values of Jacobi-Anger expansion.

From (10), only those amplitude values have to be considered, where n, k and h fulfills the conditional limitations. For calculation of one amplitude value, an infinite summation of the Bessel function terms is required. However, considering the rapid roll off of the Bessel functions, it is enough to calculate only for the first 10 terms of h and k sums [3]. Fig. 6 (c) presents a graphical representation of the *l-l* voltage spectrum expressed by eq. (10).

V. MEASUREMENTS AND VALIDATION

To show the coincidence between the measured and analytically calculated spectra, Fig. 6 presents the spectrum of the *l-l* voltage around 10kHz for a 25Hz fundamental, with 30th harmonic (750Hz) injected sinusoidal signal and a 5kHz carrier wave frequency. The setup used for measurements consists a 2.2kW asynchronous motor driven by a 2.2kW Danfoss FC302 VLT. The *l-l* voltage and vibration on the motor shell were measured with a Bruel and Kjaer Pulse Multi-analyzer type 3560.

When comparing the theoretical calculations with the experimental results, should be taken into consideration that for the measured results discrete Fourier transform (DFT) was used. The drawback of using DFT is that the windowing will introduce sidelobes in the frequency domain; aliasing will introduce non-existing frequency components. The magnitude of the spectral components will be influenced by the limits of the analogue to digital (A/D) conversion and by the external noise.

Injection of the harmonic into the CMV slightly reduces the amplitude of the carrier and its sideband harmonics. The maximum frequency of the sine wave which can be injected in the CMV is given by:

$$z_{\max} = \frac{f_{sw}}{2 f_{fund}} \qquad (11)$$

where f_{sw} is the switching frequency, f_{fund} is the frequency of the fundamental signal.

Adding the same sinusoidal signal to the three phase voltages, will introduce a group of harmonic components as shown in Fig. 6 (c) with the amplitude and frequency dependent only on the injected sinusoidal signal.

By varying the frequency of the injected signal in the CMV in a random manner, the active vectors are going to have random position during the modulation period, which gives rise to similar voltage spectrum as FCF-RPWM methods. As it was shown in Fig. 6, by injection of a sinusoidal signal in the CMV with a defined amplitude and frequency, several well defined amplitude and frequency components appears in the *l-l* voltage spectrum. Having control on the amplitude and frequency of the injected harmonics in the CMV, the *l-l* voltage spectrum can be predicted using (10) and shaped as it is desired. The spectrum of the *l-l* voltage from Fig. 7 was obtained by varying the frequency of the injected sinusoidal signal randomly in the range of 500-600Hz and 1-1.5kHz. The amplitude of the injected sinusoidal signal in the CMV corresponding to the lower frequency range was set four times lower than that of the corresponding higher frequency range.

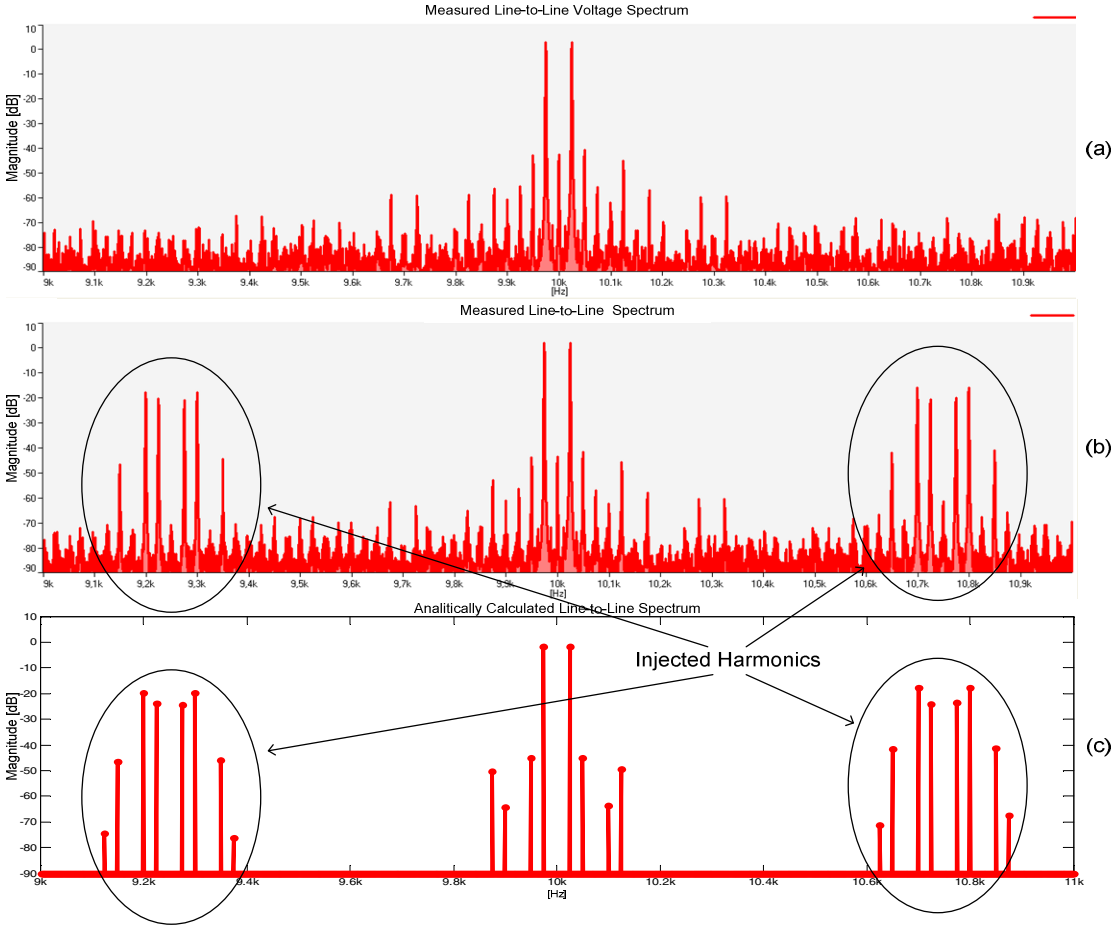

Fig. 6 Sine-triangle PWM *l-l* voltage spectra: (a) measured results with no harmonic injected, (b) measured results with 30th harmonic injected, (c) analytically calculated spectrum; All dB values referenced to magnitude of sine wave fundamental

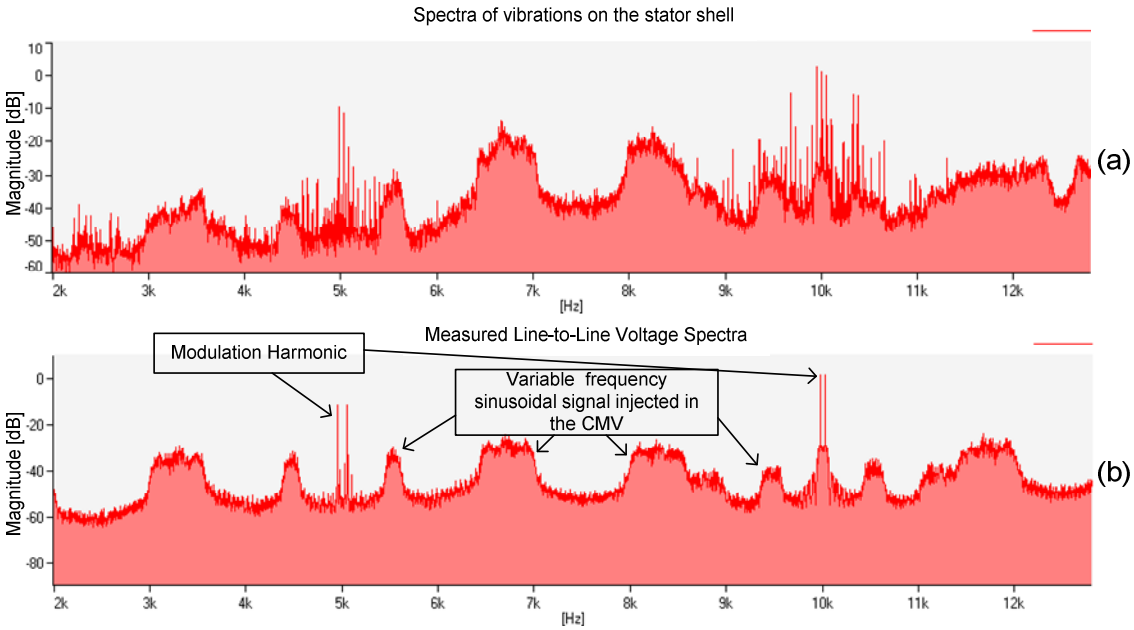

Fig. 7 Measured spectra of (a) vibrations on the stator shell (dB/1.0m/s^2), (b) *l-l* voltage using sine wave injection in CMV with randomly selected frequency (dB values referenced to magnitude of sine wave fundamental); the frequencies were selected from two defined ranges

A limitation of the method is that the maximum amplitude of the injected sinusoidal signal is inversely proportional to the modulation index. At high modulation index, the time length of the zero vectors is small; in fact the zero-state vectors can even disappear, which results in limited range for replacement of the active vectors.

VI. Conclusions

A new fixed carrier frequency quasi random PWM method has been presented and analyzed in this paper. The measured results show that the unwanted frequency components, which may excite electrical or mechanical resonances, can be avoided. This method offers full control over the spectra of the line-to-line voltage, and therefore the acoustical characteristics of the entire drive.

An analytical method for calculation of the spectra of the line-to-line voltage has also been presented. The harmonic spectra calculated analytically shows an excellent agreement with the experimentally measured spectra.

The graphical interpretation of the phase voltages presented in this paper, visualize the distribution of the zero vectors during a fundamental period. The authors hope that this new way of representation of the phase voltages, will be useful for understanding the link between the zero-state vector placement and common mode voltage.

VII. Acknowledgment

The authors would like to thank for Danfoss Drives for supporting this work.

References

[1] J. A. Houldsworth and D. A. Grant, "The Use of Harmonic Distortion to Increase the Output Voltage of a Three-Phase PWM Inverter," *Industry Applications, IEEE Transactions on,* vol. IA-20, pp. 1224-1228, 1984.

[2] H. W. van der Broeck, H. C. Skudelny, and G. V. Stanke, "Analysis and realization of a pulse width modulator based on voltage space vectors," *Industry Applications, IEEE Transactions on,* vol. 24, pp. 142-150, 1988.

[3] G. D. Holmes and T. A. Lipo, "Pulse Width Modulation for Power Converters: Principles and Practice," USA: John Wiley &Sons, Inc., 2003.

[4] V. Blasko, "Analysis of a hybrid PWM based on modified space-vector and triangle-comparison methods," *Industry Applications, IEEE Transactions on,* vol. 33, pp. 756-764, 1997.

[5] M. M. Bech, F. Blaabjerg, and J. K. Pedersen, "Random modulation techniques with fixed switching frequency for three-phase power converters," *Power Electronics, IEEE Transactions on,* vol. 15, pp. 753-761, 2000.

[6] A. M. Trzynadlowski, M. Zigliotto, S. Bolognani, and M. M. Bech, "Reduction of the electromagnetic interference conducted to mains in inverter-fed AC drives using random pulse width modulation," in *Industry Applications Conference, 1998. Thirty-Third IAS Annual Meeting. The 1998 IEEE*, 1998, pp. 739-744 vol.1.

[7] G. A. Covic and J. T. Boys, "Noise quieting with random PWM AC drives," *Electric Power Applications, IEE Proceedings -,* vol. 145, pp. 1-10, 1998.

[8] Holmes G. D. , "A general analytical method for determining the theoretical harmonic components of carrier based PWM strategies," in *Industry Applications Conference, 1998. Thirty-Third IAS Annual Meeting. The 1998 IEEE*, 1998, pp. 1207-1214 vol.2.

[P3] Laszlo Mathe[1], Florin Lungeanu[2], Peter Omand Rasmussen[1], John K. Pedersen[1]

[1] Institute of Energy Technology; Aalborg University; Aalborg, Denmark

[2] Danfoss Drives; Graasten, Denmark

"Asymmetric Carrier Random PWM"

Proc. of ISIE 2010, ISBN: 978-1-4244-6391-6, pp. 1236 - 1241

Asymmetric Carrier Random PWM

Laszlo Mathe[1], Florin Lungeanu[2], Peter Omand Rasmussen[1], John K. Pedersen[1]
[1] Institute of Energy Technology; Aalborg University; Aalborg, Denmark
[2]Danfoss Drives; Graasten, Denmark
lam@iet.aau.dk

Abstract — This paper presents a new fixed carrier frequency random PWM method, where a new type of carrier wave is proposed for modulation. Based on the measurements, it is shown that the spread effect of the discrete components from the motor current spectra is very effective independent of the modulation index. The flat motor current spectrum generates an acoustical noise close to the white noise, which may improve the acoustical performance of the drive. The new carrier wave is easy to implement digitally, without employing any external circuits. The modulation method can be used in open, as well as in closed loop motor control applications.

I. Introduction

To reach controllability, high efficiency and dynamic performance in electrical drives, power electronic converters based on ON/OFF control of power switches are employed. To control the power switches from the converter, several modulation methods were proposed from which pulse width modulation (PWM) method is one of the most encountered technique. A drawback of this method is that it gives rise to discrete frequency components in the current spectrum which leads to electro-magnetic interference (EMI) and acoustic noise in the drive. A cost effective strategy to distribute the discrete components from the current spectrum of the motor is random PWM (RPWM). Several concepts of RPWM strategies can be found in the literature [1], which can be classified from the point of view of switching frequency in two main categories:

a) Random Carrier Frequency PWM (RCF-PWM)

b) Fixed Carrier Frequency Random PWM (FCF-RPWM)

The spread of the discrete components from the motor current spectrum using RCF-PWM is more effective compared to FCF-RPWM method [2] [3]. In most of the practical applications the control algorithm is synchronized with the switching frequency, variable switching frequency gives implementation difficulties for closed loop applications [4]. Usually the FCF-RPWM methods are based on the fact that the redistribution of the zero vectors does not have effect on the fundamental but changes the motor current spectra [5] [6]. In publication [7] several FCF-RPWM methods are analyzed and compared, concluding that the methods where the position of the pulses were randomized (RPP-PWM) has good performance only at low fundamental. A RCF-PWM method where the slope of the carrier wave varies randomly in each half modulation period can be found in [8] [9]. In [10] the authors introduce a limitation on the variable slope modulation method to realize a new FCF-RPWM method. On this method the slopes of each triangular sides of the carrier wave are chosen in order to maintain constant modulation period. A drawback of variable slope modulation is that external circuits are used to generate the PWM pulses.

This paper proposes a new FCF-RPWM method called Asymmetric Carrier RPWM (AC-RPWM). The advantage of the new AC-RPWM method compared to the other FCF-RPWM methods is that it has good performance for both low and high modulation index. A digital implementation is also proposed in the paper, requiring no external circuits.

II. Fixed Carrier Frequency Random PWM

In a conventional construction of an inverter Fig. 1(a) six active vectors and two zero sequence vectors can be generated. The six active voltage vectors represented in α-β plane Fig. 1(c) form a hexagon, where each active vector points in the corner of the hexagon. When one of the six active vectors is generated the load takes the energy from the DC-link, forming a circuit from the load impedances like is shown in Fig. 1(c). The generation of the zero sequence vector is done by connection of the three legs of the load to the plus (V_{111}) or minus (V_{000}) of the DC rail. The position of a voltage vector U_s in α-β plane is defined by the ratio between the applied time-length for the two adjoin active vectors. The zero sequence vectors are responsible to reduce the amplitude of the resultant voltage vector U_s. During a modulation period where triangular carrier wave is used two voltage vectors with arbitrary amplitude and position in α-β plane can be generated. The first one is generated when the carrier wave is rising (T_{rising}), the second one is generated when the carrier wave is falling ($T_{falling}$).

The fundamental requirement of FCF-RPWM is to have constant update frequency and to generate the same voltage vector in α-β plane as it was before randomization. Because the distribution of zero sequence vectors (V_{111}, V_{000}) does not have any influence on the generated fundamental voltage vector [6], the time-length distribution of the zero vectors can vary randomly. This randomization gives a random position for the active region (shadowed area in Fig. 1(b)) during the first and second part of the modulation period.

By choosing random position for the pulses on each leg will not fulfill the second requirement for FCF-RPWM. For example, by using symmetrical modulation (the voltage vector is updated once per modulation period) in the first and second part of the modulation period the same resultant voltage vector is generated. Fig. 2 presents the effect of reposition of the pulse on one phase. With full line are represented the pulses using symmetrical modulation for the legs named q_a, q_b and q_c, with dashed line is presented the

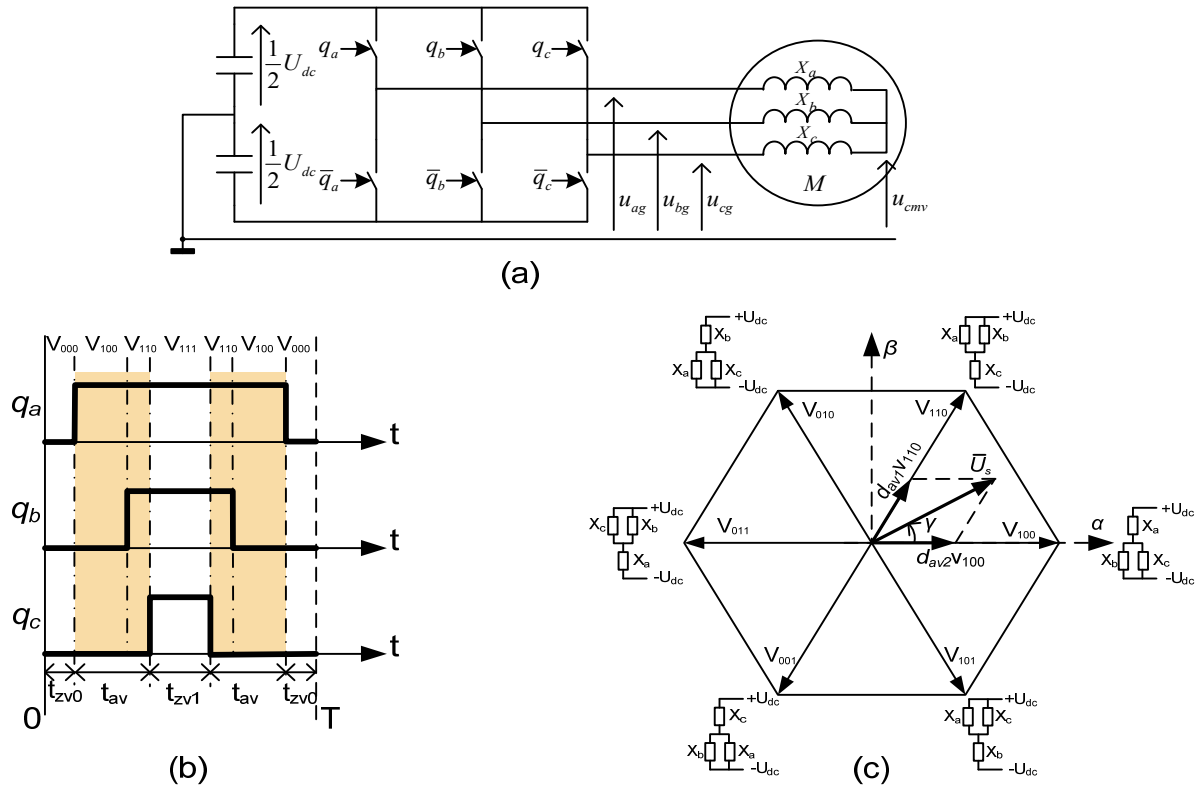

Fig. 1 Three-phase voltage-source converter (a) Circuit diagram, (b) Switching function during one period of the carrier (c) Space vector diagram in α-β plane

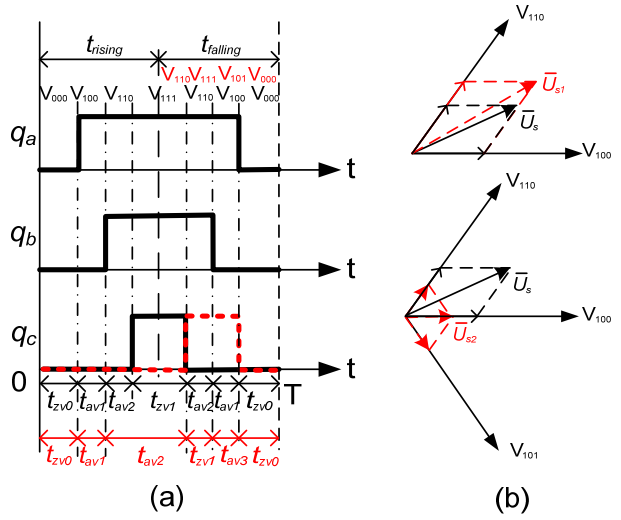

Fig. 2 Reposition of the pulse position in one leg. (a) pulses generated by symmetrical modulation (full line), changed position of the pulse on leg c (broken line), (b) vector diagram of the generated voltage vectors in the top first part of the modulation, in the bottom second part of modulation

reposition of the pulse for leg q_c. The average voltage during modulation period on leg q_c is the same, independently of the pulse position. Fig. 2 (b) shows the representation of the generated voltage vectors in α-β plane for the both cases symmetrical modulation and with reposition of the pulse on one leg. The generated voltage vectors U_s, U_{s1} and U_{s2} differs in amplitude and position in α-β plane, which means the fundamental component is distorted by the randomized pulse position. The distorted fundamental affects the stability of the drive, introducing current and torque ripple. Usually the three phases of the motor are in delta or star connection, the current through one phase depends on the current on the other two phases. As a consequence, the PWM pulses have to be synchronized to have controllability of the motor current on each individual phase of the motor. It can be concluded that the position of a pulse cannot be changed in arbitrary manner.

III. Description of the Proposed Modulation Method

The PWM unit (used for motor control) from a commercial microcontroller usually consists: an up-down counter, three Compare Registers (CR), and a Period Register (PR). An up-down counter is used for generation of the carrier wave for the PWM unit. In the traditional modulation methods like Space Vector Modulation (SVM) the time-length for up counting mode (T_{rising}) is equal with the time-length for down counting mode ($T_{falling}$) as it is shown in the first modulation period from Fig. 3.

By changing the ratio between the T_{rising} and $T_{falling}$ the resultant voltage vectors generated in the first and the second modulation period will be similar in position and amplitude; the difference is that the resultant voltage vector is created with different modulation frequency. Generating the same voltage vectors after randomization as it was before, fulfills the second requirement for FCF-RPWM described in the previous paragraph. To fulfill the first requirement for FCF-RPWM the distribution of time-length between the first and second part of the modulation (T_{rising}, $T_{falling}$) is done on such a

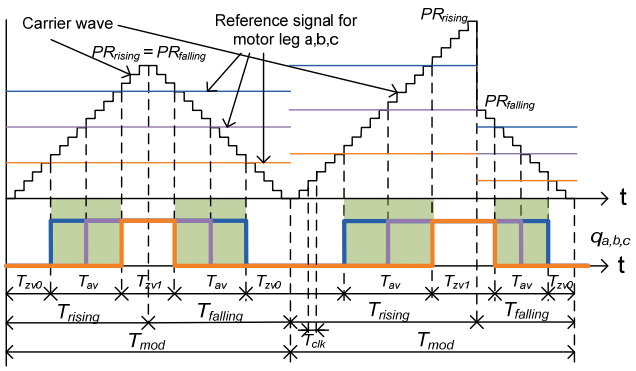

Fig. 3 PWM carrier waveforms: first modulation period symmetrical carrier wave, in the second modulation period the asymmetric carrier wave

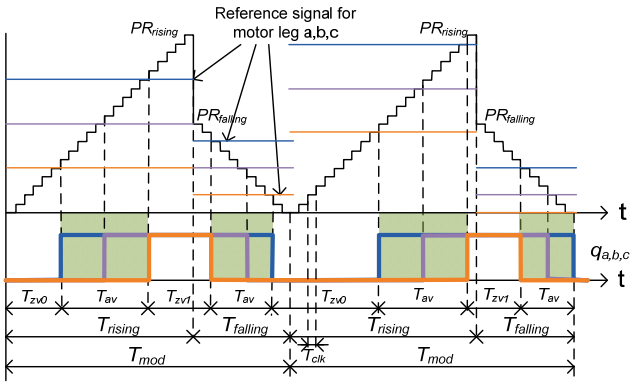

Fig. 4 First modulation period SVM ($T_{zv0} = T_{zv1}$), Redistribution of the zero vectors ($T_{zv0} \neq T_{zv1}$)

way to maintain the modulation period T_{mod} constant. The following equation has to be fulfilled to maintain constant modulation period:

$$T_{mod} = T_{rising} + T_{falling} = constant = \frac{1}{f_{sw}} \quad (1)$$

where T_{mod} is the modulation period, T_{rising} is the time-length where the counter is counting up, $T_{falling}$ is the time-length where the counter counts down, and f_{sw} is the switching frequency.

The second modulation period from Fig. 3 presents the asymmetrical carrier waveform, where the modulation period (T_{mod}) is maintained constant but the distribution of the time-length between T_{rising} and $T_{falling}$ is not equal. Having constant time base (T_{clk}) for the counter used in PWM module from a digital implementation, the slope of the triangular wave cannot be changed. However, by varying the slope of the triangular carrier wave similar pulses can be generated [8, 9]. As it is shown in Fig. 3 for digital implementation of the asymmetrical carrier wave two different values are used for the period register, creating an asymmetrical carrier wave for modulation.

By choosing in every modulation period a random time-length for T_{rising} or $T_{falling}$ the time-length for the active vector region (highlighted in Fig. 3) will vary randomly. With other words, the voltage vector generated in the T_{rising} period is generated with other switching frequency than the voltage vector generated in $T_{falling}$ period. From this point of view the AC-RPWM method can be interpreted as a RCF-PWM, where the update of the new voltage vector is done with constant frequency. The spread effect of discrete components from the motor current spectra using this method is effective at high modulation index, where the time spent for generation of the active vectors is lager than the time spent for generation of zero vectors.

For low modulation index very good spread effect of the discrete component generated by modulation can be reach by redistributing the time-length of the zero sequence vectors. As it was presented in the introduction the redistribution of the time-length between the zero vectors affects the current ripple without having any influence on the fundamental component [5]. Redistribution of the zero vectors modifies the position of the active vector region (highlighted in Fig. 4) in the rising and falling modulation period as it is presented in Fig. 4. In the first modulation period from Fig. 4 both active regions are centered ($T_{zv0} = T_{zv1}$). In the second modulation period the active vectors are replaced ($T_{zv0} \neq T_{zv1}$). From current ripple point of view the optimal position for active vectors is in the middle like it is used in SVM. The increased current ripple cause louder acoustic noise in the motor, but transforms the whistling noise into a white noise which sad more pleasant for the human ear. Table 1 presents the measured A-weighted sound pressure level using different modulation methods. The drive used for this measurement is presented in Experimental results section.

Fund. freq.	SVM (4kHz)	RCF PWM (3-5kHz)	RPP PWM 4kHz	AC RPWM 4kHz
SPL	[dBA]	[dBA]	[dBA]	[dBA]
10Hz	53	60.5	59	61.5
25Hz	64	66	65	67
40Hz	66.5	66	67	67.2

Table 1 Measured Sound Pressure Level (SPL) of different modulation strategies and fundamental frequency

IV. Digital Implementation of AC-RPWM

In Fig. 5 a general block scheme of a typical motor control in open or closed loop is presented. The control block can run in open (no feedback) or closed loop where the current and position of the rotor can be used as a feedback. The outcome of the control block is always a calculated reference voltage vector in α-β plane. This voltage vector (U_s from Fig. 1 (c)) is

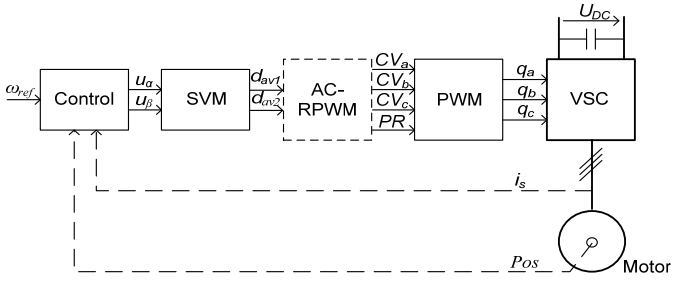

Fig. 5 Block diagram of a motor control using AC-RPWM in open and closed loop

decomposed in two adjoin active vectors, and the duty ratio is calculated usually using the Space Vector Modulator (SVM) block. The AC-RPWM block is an additional block which makes the randomization of the active and zero sequence vectors time-length from a modulation period. In this block the PR_{rising} and $PR_{falling}$ is also calculated, and the duty ratios are converted in compare values for the PWM module. The VSC and PWM blocks symbolizes the power switches and the hardware part from the PWM module from the digital implementation. From the block diagram presented in Fig. 5 it can be seen that the main advantage of the AC-RPWM is the easy implementation in an existing closed or open loop control algorithm. A big advantage of the proposed method is also that it can be realized in software without using any additional hardware. As a disadvantage it can be mentioned that the PWM module has to be updated twice during the modulation period.

V. Experimental Results

For experimental results a 2.2 kW asynchronous motor was used, driven by a 2.2 kW Danfoss VLT® AutomationDrive FC 302. The motor current and vibration on the motor frame were measured with a Bruel and Kjaer Pulse Multi-analyzer type 3560. Fig. 6 and Fig. 7 presents the measured spectra of the vibration and the phase current of the asynchronous motor at 10, 25 and 45 Hz fundamental frequency.

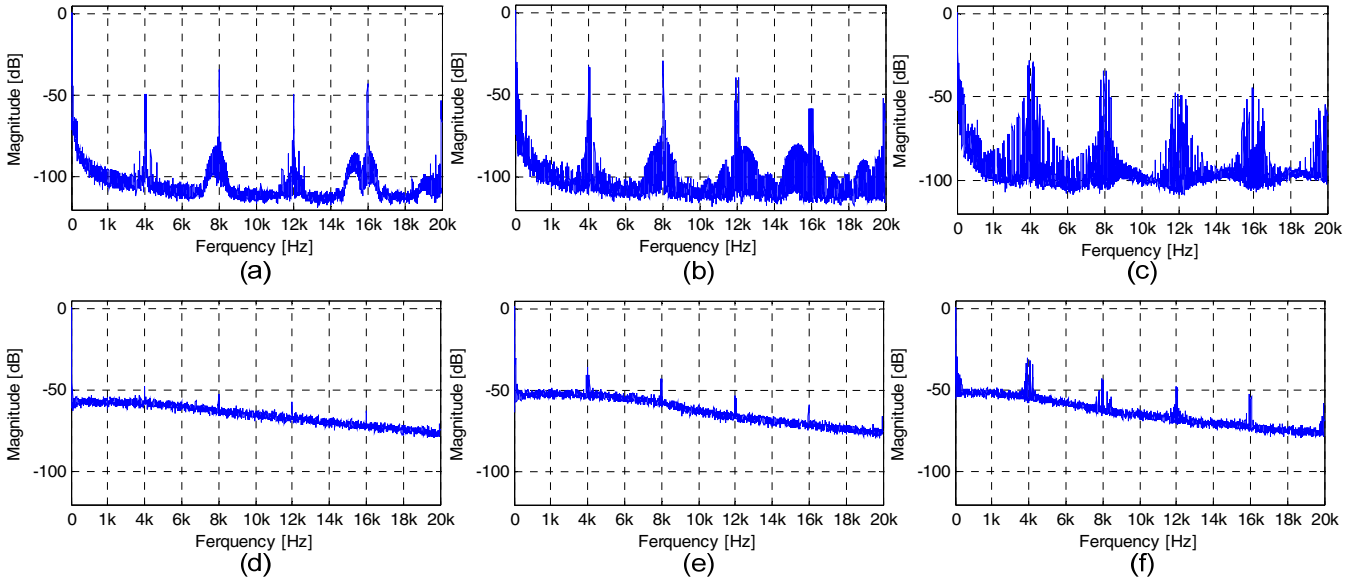

Fig. 6 Measured phase current of the motor, (a) SVM with 10Hz fundamental, (b) SVM with 25Hz fundamental, (c) SVM with 45Hz fundamental, (d) AC-RPWM with 10Hz fundamental, (e) AC-RPWM with 25Hz fundamental, (f) AC-RPWM with 45Hz fundamental,

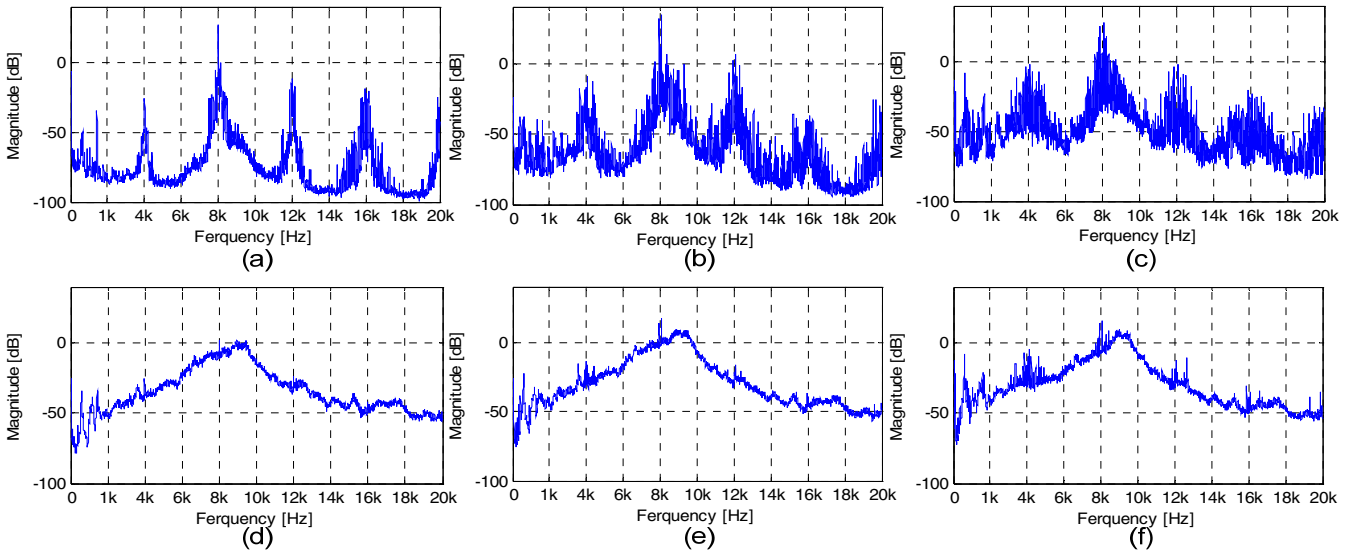

Fig. 7 Measured vibrations on the motor shell, (a) SVM with 10Hz fundamental, (b) SVM with 25Hz fundamental, (c) SVM with 45Hz fundamental, (d) AC-RPWM with 10Hz fundamental, (e) AC-RPWM with 25Hz fundamental, (f) AC-RPWM with 45Hz fundamental

As the spectrum shows, at low fundamental frequency the discrete components are almost eliminated, and at high frequency they are present because of the hardware requirements like dead time and minimum pulse width filter. However, they can hardly be distinguished from the background acoustic noise of the motor close to full speed. The current ripple is minimal in case of SVM, by using AC-RPWM this ripple is increased which leads to higher acoustic noise. Still, by eliminating the discrete components from the vibration spectra, the subjective noise may be reduced in case of AC-RPWM.

VI. Current Sampling

The current sampling error can cause torque oscillations that deteriorate the performance of the speed control in case of closed loop applications [11, 12]. Usually, the acquisition of the motor currents is done on the top and/or the bottom of the triangular carrier wave [12, 13]. In case of SVM this means the sampling of the motor current is done in the middle of the time-length of the PWM period since zero sequence vectors are generated. One way to quantify the current sampling error is to filter the current signal, (in steady state conditions), in order to obtain the fundamental component. For this purpose, a second order resonant filter has been used. It has the advantage of zero phase shift at its resonant frequency, and high attenuation for all other frequencies. The sampling error is calculated by subtracting the actual current value in the top and bottom of the carrier wave from the fundamental value (filtered current). This error is transformed in percentage of the peak of the nominal current. (Fig. 8 bottom).

Fig. 8 presents the simulation results of the motor current in macroscopic time scale by using SVM and AC-RPWM modulation methods. The used motor control algorithm was a U/f open loop control. As it was expected, the sampling error increases with a few percent in case of AC-RPWM. For those applications where this sampling error can cause problems, limitations can be introduced. For example the time-length of T_{rising} or $T_{falling}$ can be maximized to not exceed 80% of the modulation period. However, these kinds of limitations reduce the effectiveness of the randomization.

VII. Conclusions

A new fixed carrier random PWM method called Asymmetric Carrier Random PWM has been presented and analyzed in this paper. The modulation method has fixed update frequency, which has the advantage of easy implementation on an existing open or closed loop motor control, without using any additional hardware. The measurements show that the AC-RPWM method effectively spreads the discrete components of the current and vibration spectra independent of the modulation index. A drawback of the proposed modulation method can be the increased current sampling error.

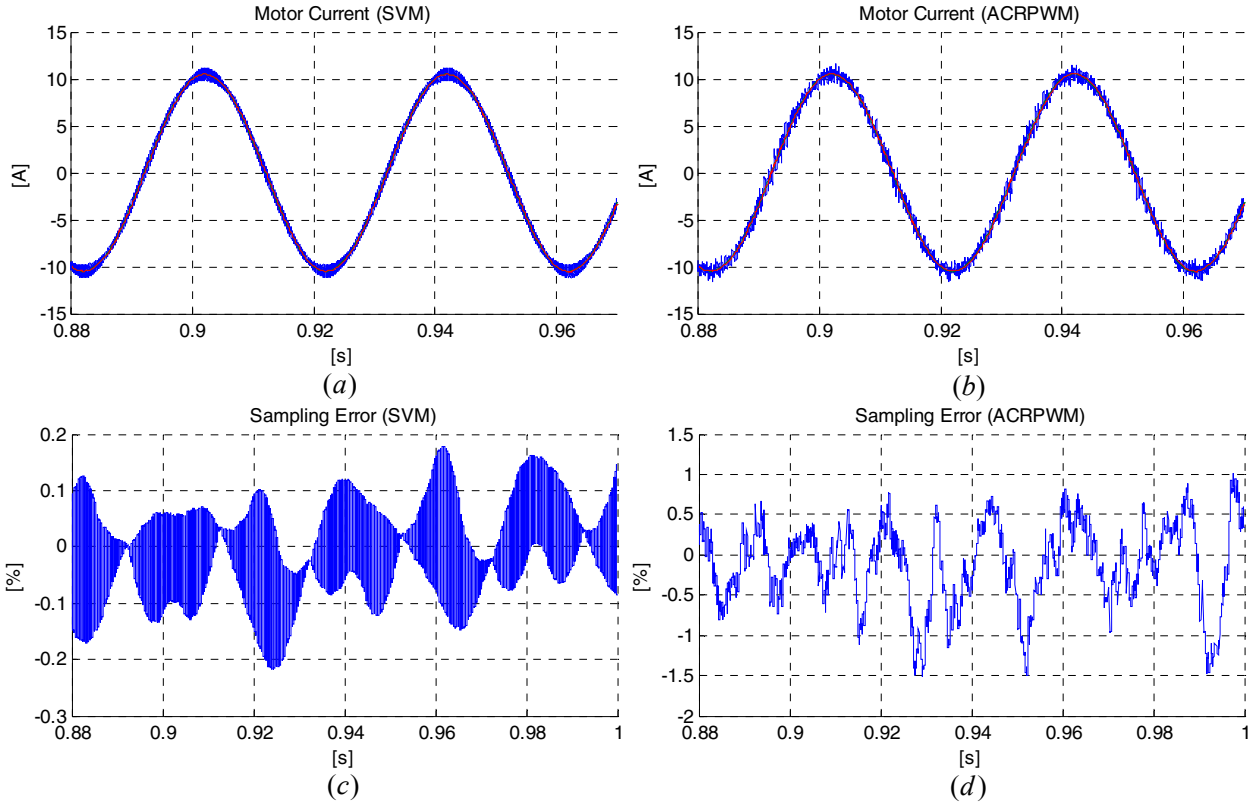

Fig. 8 Simulated results of the motor current in the top and the sampling error in the bottom at 25Hz fundamental frequency, for the plot (a) and (b) the modulation method was SVM, for (b) and (c) the modulation method was AC-RPWM

REFERENCES

[1] M. M. Bech, "Analysis of Random Pulse-Width Modulation Techniques For Power Electronic Converters," *PhD thesis,* 2000.

[2] A. M. Trzynadlowski, F. Blaabjerg, J. K. Pedersen, R. L. Kirlin, and S. Legowski, "Random pulse width modulation techniques for converter-fed drive systems-a review," *Industry Applications, IEEE Transactions on,* vol. 30, pp. 1166-1175, 1994.

[3] M. M. Bech, F. Blaabjerg, A. M. Trzynadlowski, and K. P. John, "Comparative Investigation of Random PWM Techniques with Variable Switching Frequency and Pulse Position for Inverter-fed Induction Motors," *EPE '97 : 7th European Conference on Power Electronics and Applications, 8-10 September 1997, Trondheim, Norway,* 1997.

[4] M. M. Bech, J. K. Pedersen, and F. Blaabjerg, "Field-oriented control of an induction motor using random pulse width modulation," *Industry Applications, IEEE Transactions on,* vol. 37, pp. 1777-1785, 2001.

[5] V. Blasko, "Analysis of a hybrid PWM based on modified space-vector and triangle-comparison methods," *Industry Applications, IEEE Transactions on,* vol. 33, pp. 756-764, 1997.

[6] G. D. Holmes and T. A. Lipo, "Pulse Width Modulation for Power Converters: Principles and Practice," USA: John Wiley &Sons, Inc., 2003.

[7] M. M. Bech, F. Blaabjerg, and J. K. Pedersen, "Random modulation techniques with fixed switching frequency for three-phase power converters," *Power Electronics, IEEE Transactions on,* vol. 15, pp. 753-761, 2000.

[8] C. M. Liaw and Y. M. Lin, "Random slope PWM inverter using existing system background noise: analysis, design and implementation," *Electric Power Applications, IEE Proceedings -,* vol. 147, pp. 45-54, 2000.

[9] J. C. Salmon, "A new `slope-modulated' PWM strategy for implementation in a single chip gate array," in *Industry Applications Society Annual Meeting, 1988., Conference Record of the 1988 IEEE*, 1988, pp. 388-394 vol.1.

[10] L. P. Luis Graces, Vinh T. N'Guyen Phuoc, "Inverter Control Device," *U.S. Patent 5,552,980,* 1996.

[11] D. Antic, J. B. Klaassens, and W. Deleroi, "Side effects in low-speed AC drives," in *Power Electronics Specialists Conference, PESC '94 Record., 25th Annual IEEE*, 1994, pp. 998-1002 vol.2.

[12] V. Blasko, V. Kaura, and W. Niewiadomski, "Sampling of discontinuous voltage and current signals in electrical drives: a system approach," in *Industry Applications Conference, 1997. Thirty-Second IAS Annual Meeting, IAS '97., Conference Record of the 1997 IEEE*, 1997, pp. 682-689 vol.1.

[13] S. Yo-Chan, S. Seung-Ho, and S. Seung-Ki, "Analysis and compensation of current sampling error in AC drive with discontinuous PWM," in *Applied Power Electronics Conference and Exposition, 1999. APEC '99. Fourteenth Annual*, 1999, pp. 795-799 vol.2.

[P4] Laszlo Mathe[1, 2], Henrik Rosendal Andersen[1], Radu Lazar[1], Mihai Ciobotaru[2]

[1] Institute of Energy Technology; Aalborg University; Aalborg, Denmark

[2] Danfoss Drives; Graasten, Denmark

"DC-Link Compensation Method for Slim DC Link Drives Fed by Soft Grid"

Proc. of ISIE 2010, ISBN: 978-1-4244-6391-6, pp. 1218 - 1223

DC-Link Compensation Method for Slim DC-Link Drives Fed by Soft Grid

Laszlo Mathe[1, 2], Henrik Rosendal Andersen[1], Radu Lazar[1], Mihai Ciobotaru[2]
[1] Danfoss Drives A/S, Graasten, Denmark
[2] Department of Energy Technology, Aalborg University, Aalborg, Denmark
lam@iet.aau.dk, HRA@danfoss.com

***Abstract* – Slim DC-link PWM (AC) drives for low-performance applications are emerging on the market. Such drives equipped with a small DC-link capacitance exhibit instability tendencies, if installed on a soft line, giving a degraded performance. The total harmonic distortion (THD) and the partially weighted harmonic distortion (PWHD) of the line current are degraded, if resonance between the line impedance and the DC-link capacitance occurs. Likewise, the motor performance is affected negatively giving extra torque ripple, vibration and acoustic-noise emission. This paper proposes a novel DC-link compensation method, which ensures the stability of the slim DC-link on a soft grid. The proposed compensation method may be used for open- and closed-loop control schemes, requiring a small overhead in the digital implementation.**

I. INTRODUCTION

PWM AC drives with a passive front-end are typically equipped with an electrolytic capacitor in the DC-link giving a robust performance. For applications with low demands on EMC and shaft performance drives equipped with a small DC-link capacitance are emerging. These are referred to as Slim DC-link (AC) drives.

A reduced DC-link capacitance enables the usage of film capacitors instead of electrolytic capacitors without compromising the physical size of the capacitor bank. Besides being able to tolerate the DC-link current ripple, a film capacitor has to be large enough to ensure that, the resonant frequency of the DC-link is lower than the desired minimum switching frequency of the inverter [1]. The maximum resonant frequency is given by the minimum line impedance and the film capacitance.

Film capacitors are interesting because of their long lifetime [2, 3]. Also, the low loss of the film capacitor eases the thermal management of the drive. The main advantage is the reduced harmonic content of the line currents without needing inductive elements [3] giving a low total harmonic distortion (THD). The 5^{th} and 7^{th} harmonics are attenuated effectively, at the expense of increased higher harmonics as described by the partially weighted harmonic distortion (PWHD). Slim DC-link AC drives do not comply with European harmonic standards, unless extra line-side inductance is installed [1]. Also, line-injected current harmonics at the switching-frequency level is an issue, motivating installation of extra line-side inductance.

The reduced DC-link capacitance leads to a high DC-link voltage ripple at six times the line frequency, which creates torque ripple on the motor shaft. Papers [2, 4] present modulation methods to compensate for the large ripple voltage assuming a stiff grid. At a soft grid, or when installing additional line inductance to reduce high-frequency effects, the tendency for resonance between the DC-link capacitor and the line-side inductance is amplified by such modulation techniques giving potential instability [5-7].

In this paper, a new DC-link compensation method is presented for slim DC-link drives operated on a soft grid. The method addresses the instability tendency of the DC-link while giving a reduced low-frequency motor-torque ripple. The oscillation between the line inductance and the DC-link capacitor is damped, and the line-current THD is maintained around 31%. The proposed DC-link compensation method can be used for both scalar and vector control. An analysis of motor vibration (acoustic-noise indicator) generated by the slim DC-link drive is presented also.

II. DC-LINK VOLTAGE ANALYSIS

Simple models of the passive front-end of a slim DC-link drive are sketched in *Fig. 1* (a) and *Fig. 1* (b) [1, 5]. The models of the DC-link show that, an *L-C* resonant circuit is formed by the DC-link capacitor and the line inductors. L_{gph} and R_{gph} from *Fig. 1* (a) are the total inductance and resistance per phase at the line side. Any EMC-filter impedance of the drive is included in L_{gph} and R_{gph}.

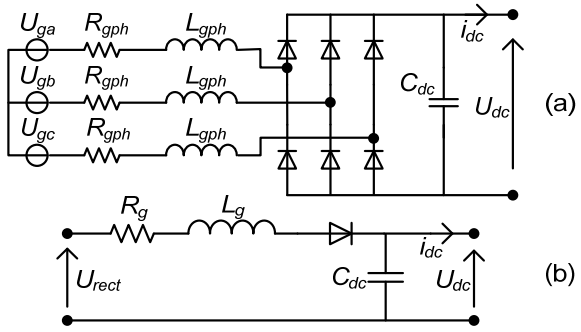

Fig. 1 Models DC-link (a) 3-ph. model (b) simplified model

During operation of the diode rectifier two phases conduct per time interval only. Hence, the total inductance and resistance seen from the DC-link is given by (1). ESR_{Cdc} is the series resistance of the DC-link capacitor C_{dc}. R_d is the series resistance of a rectifier diode.

$$L_g = 2 \cdot L_{gph}, \quad R_g = 2(R_{gph} + R_d) + ESR_{Cdc} \quad (1)$$

The resonant frequency of the DC-link is given by L_g *and* C_{dc}.

$$f = \frac{1}{2\pi\sqrt{C_{dc} L_g}} \quad [Hz] \quad (2)$$

This resonant frequency can vary between 100Hz and several kHz [1]. L_g-C_{dc} oscillation increases the THD and PWHD of the line current. Fig. 2 shows a simulation of a 4kW drive equipped with a 10µF DC-link capacitor (500%) and a 1.1mH line inductance (1%). The percentage values of L_g and C_{dc} are given by (3).

$$L_g\,\% = 100\frac{2\pi f_{line} L_g}{z_{base}}, \quad z_{base} = \frac{n_{ph}\eta_{tot} U_{phase}^2}{P_{shaft}}$$
$$C_{dc}\,\% = 100\frac{1}{2\pi f_{line} 2C_{dc} z_{base}} \quad (3)$$

f_{line} is the line frequency (50Hz), U_{phase} is the phase voltage of the line (230V), P_{shaft} is the rated motor shaft power, η_{tot} is the system efficiency set to 0.8, and n_{ph} is the number of line phases (3).

As seen in Fig. 2, the oscillation between L_g-C_{dc} appears both in the DC-link voltage and the line current(s). The DC-link voltage contains three main components.

1. Rectified component due to rectification of the three-phase line (*Fig. 2* top – dashed line). The frequency of the rectified component is 300 Hz at a 50Hz line.
2. Resonant component due to L_g-C_{dc} oscillation.
3. Switching-frequency component. From a DC-link compensation perspective not important.

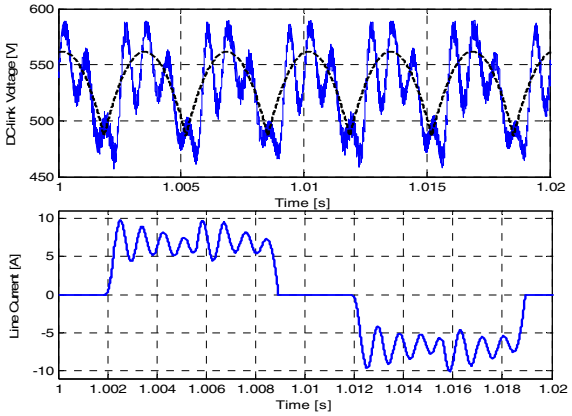

Fig. 2 Simulated DC link voltage (top) & line current (bottom)

III. DC-LINK VOLTAGE COMPENSATION ENSURING ACTIVE DAMPING OF RECTIFIER SIDE

Traditional compensation of the DC-link voltage ripple is reported in [8]. The method is given by (4). The scheme removes the rectified component of the DC-link voltage from the motor voltages.

$$U_{dccomp} = U_{cont}\frac{U_{dcref}}{U_{dcmeas}} \quad (4)$$

U_{dccomp} is the amplitude of the compensated voltage vector, U_{cont} is the amplitude of the voltage vector set by the motor-control algorithm, U_{dcref} is the reference DC-link voltage, and U_{dcmeas} is the measured DC-link voltage.

The proposed method in this paper, aiming at ensuring the DC-link stability while using (4), is inspired by the fact that, a time delay exists between the sampling instant of U_{dcmeas} and the time instant, when U_{dccomp} is applied to the motor. This is illustrated in the flowchart in Fig. 3 (a), showing the sequence of traditional DC-link voltage compensation. Usually the sample delay is one to two switching periods (Fig. 3 (b)). In case of a slim DC-link drive fed by an ideal 400V/50Hz grid, the peak-to-peak DC-link voltage ripple is 75V or 14% of the average DC-link voltage. By having the compensation voltage delayed by two samples, at a switching frequency of 6kHz as shown in Fig. 5, the voltage error in the compensation will be 50V (9%) still. This means that, (4) cannot give a perfect result. Fig. 4 shows the DC-link voltage and the voltage used for the compensation with and without a sample delay. In the ideal case, using (4) without a delay, a perfect result would be achieved, given that the overmodulation range of the PWM is avoided. The side effect would be maximum amplification of the L_g-C_{dc} oscillation. That is, when the DC-link voltage goes up, the modulation index, being proportional to U_{dccomp}, is decreased. Decreasing the modulation index, the inverter will take less energy from the DC-link, allowing the voltage to increase even more.

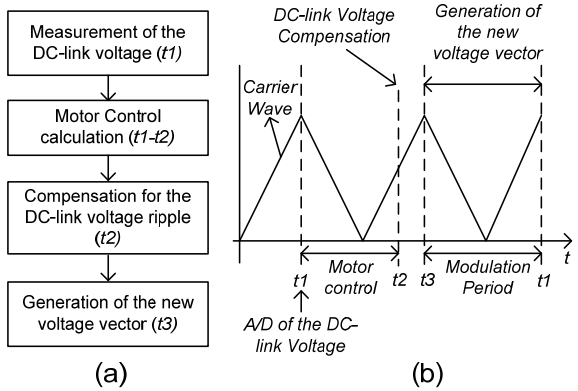

Fig. 3 DC-link compensation (a) flowchart of compensation method, (b) timing diagram of DC-link compensation

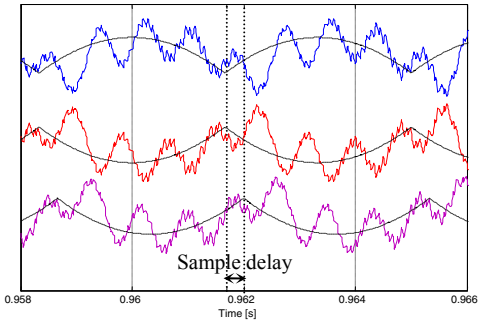

Fig. 4 Simulated results for DC-link voltage, top: dashed line= rectified voltage component, full line=DC-link voltage, middle: compensation voltage without delay, bottom: compensation voltage with two-sample delay

Likewise, when the DC-link voltage goes down, (4) increases the modulation index. Consequently, more energy is taken from the DC-link, decreasing the voltage even more. Hence, traditional DC-link compensation makes the inverter load appear to be a negative resistance seen from the rectifier in a steady-state operating point. This is forced, negative damping reducing the effect of the natural resistive damping in the rectifier side. Hence, from a L_g-C_{dc} oscillation perspective, it is more safe not to compensate for the DC-link voltage ripple at all. But in this case the rectified component will have a negative effect on the motor performance.

According to [7], the rectifier side is damped, if (5) is fulfilled. (5) is considered to be a rule-of-thumb.

$$C_{dc} > \frac{P_{shaft} L_g}{\eta_{tot} R_g U_{dc}^2} \qquad (5)$$

Some examples are given below in terms of the needed capacitor size at 4kW ensuring the DC-link stability. Feeding the drive by a 500kVA/400V/50Hz distribution trafo (stiff grid) the series impedance per phase is about (3.5+j15.5)mΩ, when assuming a short line cable. A 250kVA trafo equals (8.4+j27.6)mΩ. A 100kVA trafo equals (27+j59)mΩ. Assuming a 4 kW slim DC-link drive contributes to R_g by around 100 mΩ (capacitor, diodes, EMC-filter), the DC-link capacitor should be larger than 16, 26 and 45μF respectively (300, 200 and 100%). In case of adding a 1% inductor (1.1mH with 100mΩ series resistance) between the grid and the drive, the capacitor size should be 125μF (40%). A 40% capacitance is realistic by using electrolytic capacitors only. From the above examples it may be deduced that, slim DC-link drives (C_{dc} >>40%) suffer from poor damping on soft grids dominantly. Hence, the compensation method presented in this paper is aimed at operation on soft grids and/or operation with line inductors. In these cases the method provides active damping for the film-capacitor-based DC-link.

The proposed method is based on delaying the resonant component of the DC link voltage with half a

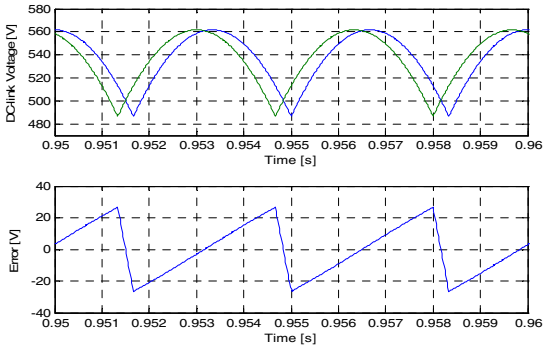

Fig. 5 Compensation error for the rectified component with two-sample delay in the compensation loop

resonant period, while the rectified component is left unchanged. The 180° phase shift of the resonant component transforms the impact of (4) on it into active damping. In order to calculate the right delay for the resonant component, its period must be identified (delay-calculation block in Fig. 7).

By using a digital band-pass filter the rectified component is isolated from the DC-link voltage. Subtracting the rectified component from the DC-link voltage gives the resonant component and the DC component. This combined signal is delayed by half a resonant period. The simulated steps in Fig. 6, contained in the compensation-voltage block in Fig. 7, visualizes the isolation procedure, the phase shift of the combined signal and the reconstructed DC-link voltage U_{dccomp} by adding the rectified component and the delayed combined signal.

Regarding the proposed method two items must be fulfilled.

1. The frequency of the resonant component must be two times larger than the rectified component to ensure a proper separation.
2. The sample rate of the U_{dccomp} routine should be at least five times higher than the frequency of the resonant component.

Hence, at a 50Hz line and a sample rate of 14kHz the upper limit of the line inductance for a 4kW drive with a 500% capacitor is around 3.5mH (3.5%). The lower limit of the inductance is about 160μH (0.16%). Outside these limits the rectifier stability is governed by the natural damping of the hardware (5). As may be deduced, the sample frequency must be increased, as the film capacitor is reduced, to ensure the stability by software. This means extra controller costs.

Fig. 7 sketches the overall control algorithm. In a preferred embodiment the sample rate of the U_{dccomp} routine is two times the switching frequency of the slim DC-link drive. The control block in Fig. 7 may range from simple scalar control to advanced vector-oriented control.

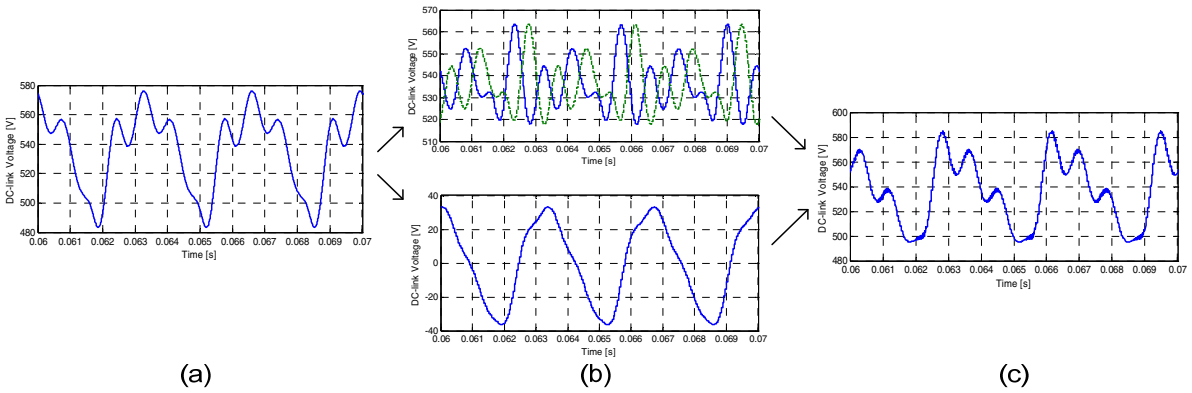

Fig. 6 Simulation results: (a) DC-link voltage; (b) in the top DC-link voltage with extracted rectified component (full line without, dashed line with half period delay) and in the bottom rectified component (c) reconstructed compensation signal with delayed resonance

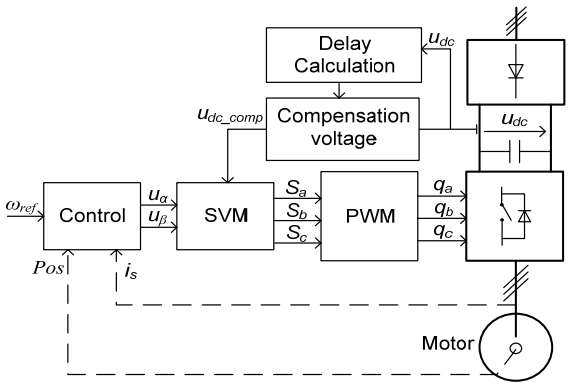

Fig. 7 Control algorithm of DC-link voltage compensation using delay in the compensation loop (dashed lines = feedback for closed-loop control)

The SVM block contains space-vector-oriented duty-cycle calculations including (4). The duty cycles are input to the PWM block controlling the six switching elements of the inverter. In the following, these blocks are executed at a 7kHz switching rate (modulation period, see Fig 3). The delay-calculation block and the compensation-voltage block run at 2·7k = 14kHz, meaning that the input signal U_{dcmeas} is AD-converted in the start and in the middle of the modulation period. Hence, the right half of any modulation period is available for preparing the duty cycles for the following switching period. That is, the calculations can be initiated, when U_{dccomp} is available in the middle of the modulation period. In terms of the rectified component this gives a one switching-period delay.

For installations with varying grid impedance, the delay-calculation block must run continuously during operation. Else, it is needed in a start-up calibration phase only.

IV. EXPERIMENTAL RESULTS

A ventilation system, equipped with a 4kW induction motor fed by a VLT® AutomationDrive FC 302 from Danfoss Drives A/S, has been used for experimental tests. The DC-link capacitance of the drive was decreased to 10µF (500%), and the built-in DC-chokes were removed. The vibration of the motor shell has been measured using a Bruel & Kjaer Pulse Multi-analyzer type 3560. Motor and line currents were measured applying oscilloscope equipment from Tektronix. In order to emulate a soft grid, inductors were installed at the line side.

A first set of measurements was recorded at a total line inductance of about 0.5% (0.5mH) (Fig. 9). A second set of measurements was recorded at a line inductance of about 1% (1.15mH) (Fig. 10). The frequency of the *L-C* oscillation between the line inductors and DC-link capacitor is 1.6kHz and 1.1kHz respectively, which is well below the 14kHz sample rate (factor 8).

Fig. 8 presents the worst-case scenario from a resonance perspective, when the resonant component of U_{dccomp} is in phase with the real resonant component of the DC-link voltage. As may deduced from Fig. 4, this may occur, if the sample delay in the DC-link compensation matches the period of the uncontrolled resonant component. Table 1 shows the THD and PWHD of the line current and the THD of the motor current. The line current THD is approximately the same (31-32%) except for the case, when the resonant component is in phase. The reduction of the PWHD is best at a 1% line inductor, because the need for active damping is highest in this case. The measurements were recorded at a fundamental frequency of 45Hz and U_{dcref}=*530V*. Increasing the speed over 45Hz, at a constant U/f-ratio, the drive enters overmodulation. At overmodulation it is not possible to compensate for the DC-link voltage ripple due to saturation of the modulation index. Hence, the slim DC-link drive cannot give full output voltage, while maintaining a stable DC-link on a soft grid.

Fig. 11 presents the measured vibration spectra on the motor shell in case of a 1% line inductor at 45Hz. If no DC-link voltage compensation is applied, a 300Hz component appears in the motor currents. The result is increased vibration of the motor shell and increased acoustic noise. By compensating the DC-link voltage

according to the proposed method in this paper, the vibrations are reduced by around 20db at 300Hz.

V. Conclusions

A new DC-link voltage compensation method for drives equipped with a small DC-link capacitor was reported in this paper. The method is useful for poorly damped slim DC-link drives fed by a soft grid. The compensation removes the 300Hz DC-link voltage ripple in the PWM voltages for the motor, while at the same time providing active damping of the DC-link.

Measurements showed that, the PWHD of the line currents was reduced from 64% to 58%, while the THD was maintained below 32%. Another advantage of the proposed method is that, it can be used for both open- and closed-loop control schemes, as it operates independently on the control loop.

Motor-vibration measurements indicate that, the acoustic performance of a slim DC-link drive is affected by the large 300Hz DC-link voltage ripple. Using the proposed compensation method, the 300Hz component in the vibration spectrum of the motor shell was reduced by 21db.

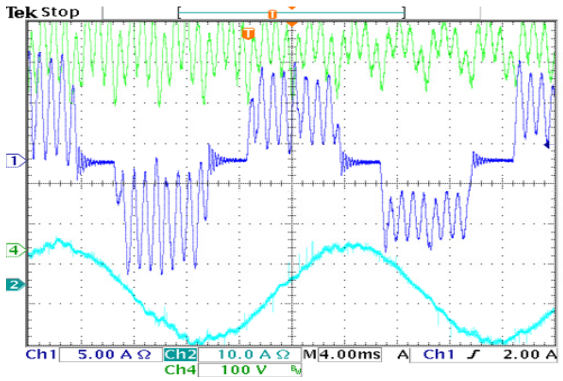

Fig. 8 Measured line & motor currents with 1% line inductance, switching frequency of 7kHz, fundamental frequency of 45Hz. Resonant component in compensation signal in phase with resonant component of DC-link voltage

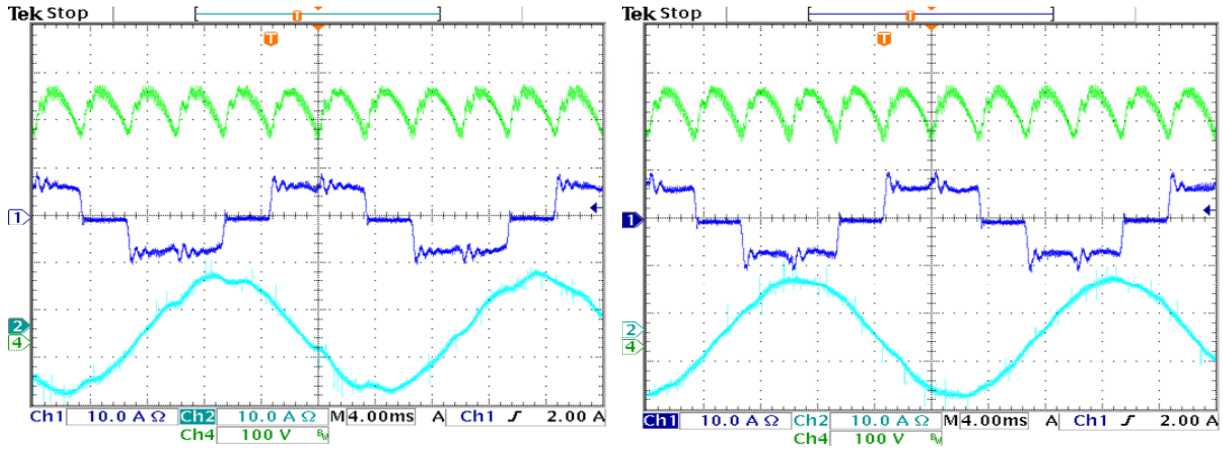

Fig. 9 Measured line & motor currents at 0.5% line inductance, 7kHz switching frequency, 45Hz fundamental frequency without (left), and with (right) DC-link compensation with delay

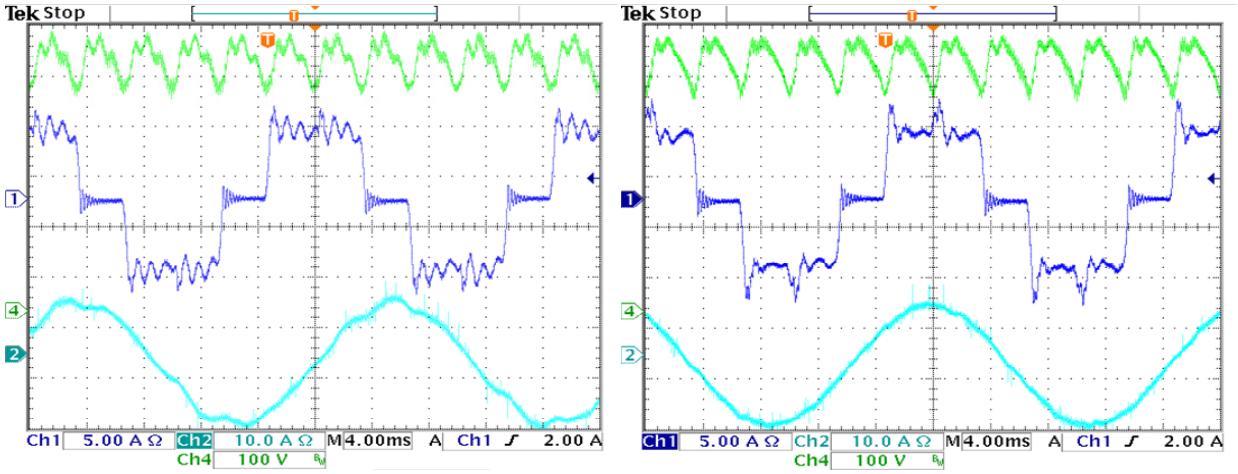

Fig. 10 Measured line & motor currents at 1% line inductance, 7kHz switching frequency, 45Hz fundamental frequency without (left), and with (right) DC-link compensation with delay

Line Inductance		THD of the Line Current [%]	PWHD of the Line Current [%]	THD of the Motor Current [%]
0.5%	Compensation	32.5	72	4.7
	No Compensation	31	74.5	7.2
1%	Compensation	31.5	58	4.5
	No Compensation	31	64	7
	Compensation in phase	60	180	6

Table 1 Measured THD and PWHD of the line and motor currents

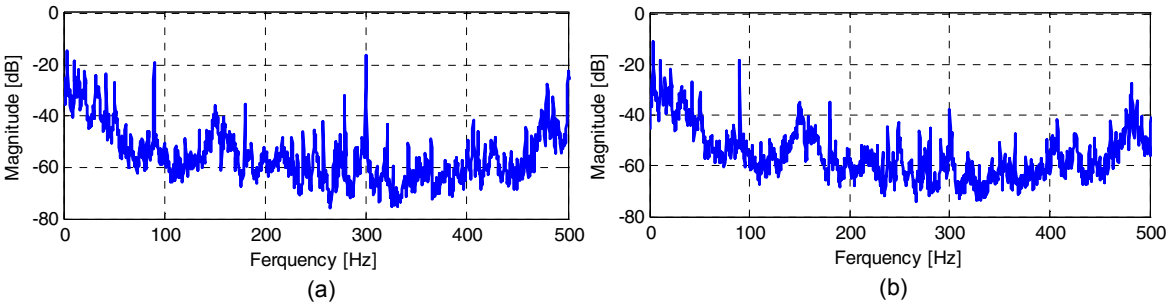

Fig. 11 Measured vibration spectra on the motor shell without delay (a), and with delay (b) in DC-link compensation loop

REFERENCES

[1] H. R. Andersen, T. Ruimin, and K. Cai, "3-phase AC-drives with passive front-ends with focus on the slim DC-link topology," in *Power Electronics Specialists Conference, 2008. PESC 2008. IEEE*, 2008, pp. 3248-3254.

[2] X. Chen and M. Kazerani, "Space Vector Modulation Control of an AC-DC-AC Converter With a Front-End Diode Rectifier and Reduced DC-link Capacitor," *Power Electronics, IEEE Transactions on,* vol. 21, pp. 1470-1478, 2006.

[3] H. Saren, O. Pyrhonen, K. Rauma, and O. A. L. O. Laakkonen, "Overmodulation in Voltage Source Inverter with Small DC-link Capacitor," in *Power Electronics Specialists Conference, 2005. PESC '05. IEEE 36th*, 2005, pp. 892-898.

[4] H. Saren, O. Pyrhonen, J. Luukko, O. A. L. O. Laakkonen, and K. A. R. K. Rauma, "Verification of frequency converter with small DC-link capacitor," in *Power Electronics and Applications, 2005 European Conference on*, 2005, p. 10 pp.

[5] M. Hinkkanen, L. Harnefors, and J. Luorni, "Control of induction motor drives equipped with small DC-Link capacitance," in *Power Electronics and Applications, 2007 European Conference on*, 2007, pp. 1-10.

[6] M. Hinkkanen and J. Luomi, "Induction motor drives equipped with diode rectifier and small DC-link capacitance," in *Industrial Electronics Society, 2005. IECON 2005. 31st Annual Conference of IEEE*, 2005, p. 6 pp.

[7] K. Pietilainen, L. Harnefors, A. Petersson, and H. P. Nee, "DC-Link Stabilization and Voltage Sag Ride-Through of Inverter Drives," *Industrial Electronics, IEEE Transactions on,* vol. 53, pp. 1261-1268, 2006.

[8] J. K. Pedersen, F. Blaabjerg, J. W. Jensen, and P. A. T. P. Thogersen, "An ideal PWM-VSI inverter with feedforward and feedback compensation," in *Power Electronics and Applications, 1993., Fifth European Conference on*, 1993, pp. 501-507 vol.5.